MTG-IRS Level 1 Algorithm Theoretical Basis Document

Doc.No. : EUM/RSP/TEN/16/878765
Issue : v2 e-signed
Date : 19 November 2021
WBS/DBS :

EUMETSAT
Eumetsat-Allee 1, D-64295 Darmstadt, Germany
Tel: +49 6151 807-7
Fax: +49 6151 807 555
http://www.eumetsat.int

Page left intentionally blank

Document Change Record

Issue / Revision	*Date*	*DCN. No*	*Changed Pages / Paragraphs*
Version 1D	20 April 2017		First version
Version 1E			Correction of various typos and errors in the text The spectral sampling of the L1 products is indicated to be the one of the instrument (i.e. better than 0.625 cm^{-1}) Changed the term “FIM transmission” by “FIM reflectivity”. Changed the notation “τ_{υ}^{FIM}” in “ρ_{υ}^{FIM}” The possibility of combining uniformisation and spectral calibration is indicated Removal of the image calibration section pending investigations on the subject Update of the post-processing section: PC and scene analysis, introduction of the scene heterogeneity index Complete rewriting of the monitoring section, now split into online and offline functions
Version 1F			Completion of section 5.5 on the “imager mode calibration” Added the section on the spectrum re-centring by phase gradient Updated the section Uniformization Added an appendix on the spectral grids
V2	11/2021		P. Dussarrat Revision of all sections except the offline monitoring. - New section on processing grids: 5.1.3 - New description of the SRF model: 5.4 - Description of the RTF uniformisation processing: 5.3.5 - All online monitoring sections 6. have been re-written following the IDPF-S v3 update.

Table of Contents

List of Figures

List of Tables

1 INTRODUCTION

1.1 Purpose

This document describes the algorithm theoretical basis for the level-1[1] (L1) radiance processing, as it shall be derived from the Meteosat Third Generation (MTG) InfraRed Fourier transform Spectrometer (IRS). The purpose of the level-1 processing is to derive geolocated, radiometrically and spectrally calibrated spectra from IRS raw measurements.

The IRS soundings transmitted to the ground (and which thus enter the level-1 processing) are interferograms that have been prepared for transmission by the on-board processing. Only a short description of the latter is provided as details are classified. The geolocation of the spectra is performed by the Image Navigation and Registration (INR) module, the interface of which is shortly described. Before dissemination, the radiances are compressed using the Principal Component (PC) technique, also addressed in the document.

The level 2 processing is not addressed in this document. The scenes analysis processing to provide the cloud information is shortly addressed.

1.2 Current IRS level-1 processing approach

The design of the L1 data processor can be driven either by the nature of the instrument data acquisition or by the requirements imposed on the generation of the output datasets i.e. timeliness, accuracy and completeness. Conversely to the IASI instrument, the design of IRS is such that it leaves a large flexibility on the architecture of the on-ground processing: indeed since interferograms are transmitted to the ground there are no constraints on the algorithm sequence[2]. The monitoring of the calibration process is also largely eased.

However, the baseline of the IRS ground processing described in this document follows the approach proposed by the industrial consortium responsible for providing both the instrument and the Instrument Quality Tool (IQT). The latter is intended to check that the performances of the instrument meet the requirements and is similar to the approach of the IASI processor: radiometric then spectral calibrations are performed in sequence and in this order. No significant changes or optimizations with respect to the IQT have been introduced except where it was needed to account for the environment of the L1 processor: indeed the IQT is an offline tool and is not meant to be run operationally. This impacts primarily the calibration target handling (i.e. the instrument background estimation). Moreover, the removal from the interferograms of the dependency on the instrument effects, hereafter referred to as uniformisation and considered as essential for the L1 products users, has been introduced.

In order to reach the required performance, the spectral calibration requires oversampled spectra. In order to limit the processing time, the number of operations and in particular the number of Fourier transforms is restrained. Spectra oversampling is thus taking place when

[1] Data are classified in terms of levels: The Level 0 (L0) products are raw measurements, Level 1 (L1) data are calibrated, time-referenced and geolocated spectral radiances, and Level 2 (L2) data are the geophysical products.
[2] Because the Fourier transform and the radiometric calibration of IASI measurements are taking place on board Metop, the spectral calibration has to be performed as a second step. Furthermore, only spectra are transmitted to the ground, thus reducing the degrees of freedom in the design of the on-ground algorithms.

the Fourier transform is applied, that is at the beginning of the processing. In consequence, all spectra involved in the radiometric calibration are oversampled by a factor of ~8. This adds processing and storage overheads, but:

- the radiometric algorithms are deemed simple enough that this is not a major issue;
- this prevents the apparition of artefacts ("Gibbs effect") that would otherwise appear especially on the band edges when the oversampling is performed after radiometric calibration.

1.3 Limitations of the document and current open issues

Table 1 lists the open issues or missing information in the present document. Some are linked to the L1 processing specification document. An estimate of the time when each issue should be solved is provided for information.

Id	Description	Timeliness for the resolution
1	**Industry information**: resolution of inconsistencies and omissions in the source industry documentation along with their expected evolution as part of the space segment milestones.	More information at CDR (2019)
	Metrology and on-board processing: the full description of the on-board processing is still classified by the instrument manufacturer. It is expected that more details such as the implementation of the decimation filter will be available in the next version.	Next version in 2020
2	**Metrology and on-board processing**: the validity of some assumptions made by the instrument manufacturer such as the non-dependence of the interferograms on the corner cube direction should be demonstrated and validated. If not, the processing would need to separate the two directions (one more dimension in the tables) and take into account in particular that more calibration views are needed.	CDR (2019)
3	**Radiometric calibration**: the calibration of the images is hampered by the fact that: • An image is a single sample of the interferogram baseline thus dependent on noise and spectral content • No processing is applied on the images on board and in particular no non-linearity correction. Investigations are needed to assess the impact of these limitations.	Next version in 2020
4	**Use of spectral or spatial smoothing** to reduce the noise and specifically outliers effects in the radiometric calibration. They both have impacts on the radiometric calibration performance which are still being assessed. This also relates to the handling of etalon effects.	Next version in 2020
5	**Scene heterogeneity:** the estimation of the scene heterogeneity depends on the accuracy of the radiometric calibration of the imager mode. This section will be then updated after the resolution of the open issue on the imager mode radiometric calibration	Next version in 2020
6	**Online monitoring:** The flags generated by the on-board processing to be used for the monitoring and/or to be made	Next version in 2020

	available in the L1 products will be listed in the next version.	

Table 1: List of open issues

1.4 Document structure

Chapter 1 gives the scope of the document and provides a rationale for the current IRS L1 processing approach as well as a list of the current open issues.

An overview of the MTG IRS mission, its context and its applications is presented in Chapter 2.

Defining the level-1 processing is not possible without an in-depth knowledge of the instrument. The latter is described in Chapter 3, highlighting the peculiarities that make IRS the first instrument of its kind: a large infrared detector made up of small pixels. This impacts the spectral response function of the instrument and thus the level-1 processing. For that reason, it is interesting to put IRS in perspective with IASI.

Chapter 4 is the logical continuation of the previous one as it provides a short overview of the processing taking place on board before transmission to the ground. Unfortunately, restrictions imposed by the instrument manufacturer have prevented a comprehensive description thus only the main functional blocks and their impact for the L1 processing are highlighted.

The following chapters form the core of the document. Chapter 5 describes the level-1 on-ground processing. Addressed here are both the routine processing performed on every Earth views as well as algorithms that are run on a different time scales. The latter includes the radiometric response estimation performed every 15 minutes or the spectral calibration and spectral response functions estimations, executed on a semi-hourly basis. The spectral uniformisation of the calibrated spectra is also addressed. The chapter ends with an explanation of the interface between the IRS processing and the Instrument Navigation and Registration (INR)

Chapter 6 and 7 give an overview of the IRS instrument and L1 processing monitoring. It has been split in two parts:

- The online monitoring for the assessment of the level-0 and level-1 products quality. It produces analysis data and flags inside the operational processing;
- The offline monitoring focusing on the assessment of the instrument, on-board and on-ground processing performances at short, medium and long terms as well as the tuning of the processing parameters if deemed necessary. It provides reports outside the operational processing (information not distributed by the products).

The final stage of the IRS level-1 processing includes two functions:

- principal component compression in order to reduce the volume of data disseminated to the users;

- scenes analysis to derive an estimate of each pixel cloud coverage, scene heterogeneity at sub-pixel level as well as an index indicating the contamination by dust.

These functions are the object of Chapter 8.

Finally, chapter 9 presents an overview of the modules decomposition and dataflows.

Applicable and reference documents are listed in the appendix, as well as the notations and the acronyms used in the document.

Assumptions, trade studies as well as alternative algorithms are given when possible to justify the choice of a given algorithm.

2 MTG IRS MISSION AND CONTEXT

2.1 Meteosat Third Generation

In order to build on the success of the Meteosat First and Second Generation missions, EUMETSAT is developing the Meteosat Third Generation (MTG) satellites. After an elaborated user-consultation, the following needs have been identified:

- Continuation of the current imagery missions:
  - Full Disk High Spectral Imagery (FDHSI);
  - Rapid Scan Service (RSS).
- Development of new services:
  - Lightning Imagery;
  - Infrared Sounding.

To cover these needs, the MTG space segment will consist in six satellites of two different types, namely four imaging satellites (MTG-I) and two sounding satellites (MTG-S). The MTG-I hosts the Flexible Combined Imager (FCI) and the Lightning Imager (LI) instruments, while the MTG-S hosts the Infra-Red Sounder (IRS) and the Copernicus Ultra-Violet and Near-infrared sounder (UVN) instruments. Conversely to the MSG and MFG series which were spin stabilised platforms, MTG will be a three axis stabilised platform. The development of the MTG space segment is in charge to Thales Alenia Space under ESA contract.

2.2 The IRS Mission

The MTG Infra-Red Sounder (IRS) has no direct MSG heritage but is related to the IASI mission on Metop (from the user point of view) and, from a more general point of view, to the GIFTS mission that has been considered in the USA but never been launched. The objectives of the IRS mission are to:

- Provide high spatial and temporal information of atmospheric temperature and moisture structures, in particular at small scale;
- Monitor atmospheric dynamic variables with improved height information;
- Monitor atmospheric instability / forecast of convection;
- Support emerging operational air chemistry and air quality applications.

To fulfil these objectives, IRS will acquire a number of spectral soundings simultaneously using a two dimensional detector array covering an area on Earth of 640x640 km (at NADIR). The full Earth disk (as seen from the geostationary orbit) will thus be covered by a succession of stares – called dwells, measuring the upwelling radiation at the top of atmosphere in two broad spectral intervals at moderate high spectral resolution (cf. Table 2) with a spatial sampling distance of 4 km at nadir in each band. These will allow deriving unprecedented four-dimensional information on structures of the atmosphere:

- horizontally;
- vertically (thanks to the relatively high spectral resolution);
- temporally (the scanning sequence guarantees a rather high time resolution i.e. 30 minutes over Europe).

Band	Wavenumber Range (cm^{-1})	Spectral sampling (cm^{-1})	Main Constituents	Application
Long Wave IR (LWIR)	700 – 1210	~0.6031*	CO2, O3, Surface	Temperature and Ozone profile, surface properties
Mid-Wave IR (MWIR)	1600 – 2175	~0.6037*	H2O	Humidity profile

Table 2: High level instrument characteristics (* the spectral sampling is defined as 1/(2*MaxOPD), MaxOPD = 0.829038 in LWIR, and = 0.8282447 in MWIR)

Operational meteorology is the primary target of the mission. Indeed, IRS data will meet the key needs of Global/Regional Numerical Weather Prediction (NWP) through the provision of:

- More frequent information on small scale features (horizontal and vertical) of water vapour;
- Atmospheric Motion Vectors (AMV) with higher vertical resolution in clear air, to be extracted from the tracking of three-dimensional water vapour patterns.

This will allow monitoring atmospheric instability, convective and down draught convective available potential energy, height assignment of atmospheric wind tracers and cloud microphysics.

IRS will benefit from the experience acquired with IASI as well as the expertise gained on CrIS and on the development of GIFTS; operation of the future similar Chinese instruments in space will certainly bring valuable information for the operation of IRS.

2.3 Background on infrared hyperspectral sounding from space

Hyperspectral measurement of the Earth infrared radiation from space is a powerful mean to remotely sense atmospheric parameters. Continuous spectral measurements in the infrared with high spectral resolution theoretically allow extraction of much valuable information on the state of the atmosphere and possibly the underlying surface without stringent a-priori hypotheses. This has thus triggered a long standing interest in the scientific community and the first attempts to launch infrared spectrometers date back to 1970 (namely the InfraRed Interferometer Spectrometer IRIS on-board the US satellites Nimbus 3 and 4 [RD-15] or the Fourier transform spectrometer SI-1 (Spektrometer Interferometer -1) which flew on-board the Soviet platforms Meteor [RD-16]. Routine infrared hyperspectral measurements are however only possible since the beginning of the 21st century so that several such sensors are operating today on polar-orbiting Earth observation satellites (Figure 1) in particular the Infrared Atmospheric Sounding Interferometer IASI on Metop [RD-22] and the Cross-track Infrared Sounder CrIS on Suomi-NPP [RD-23].

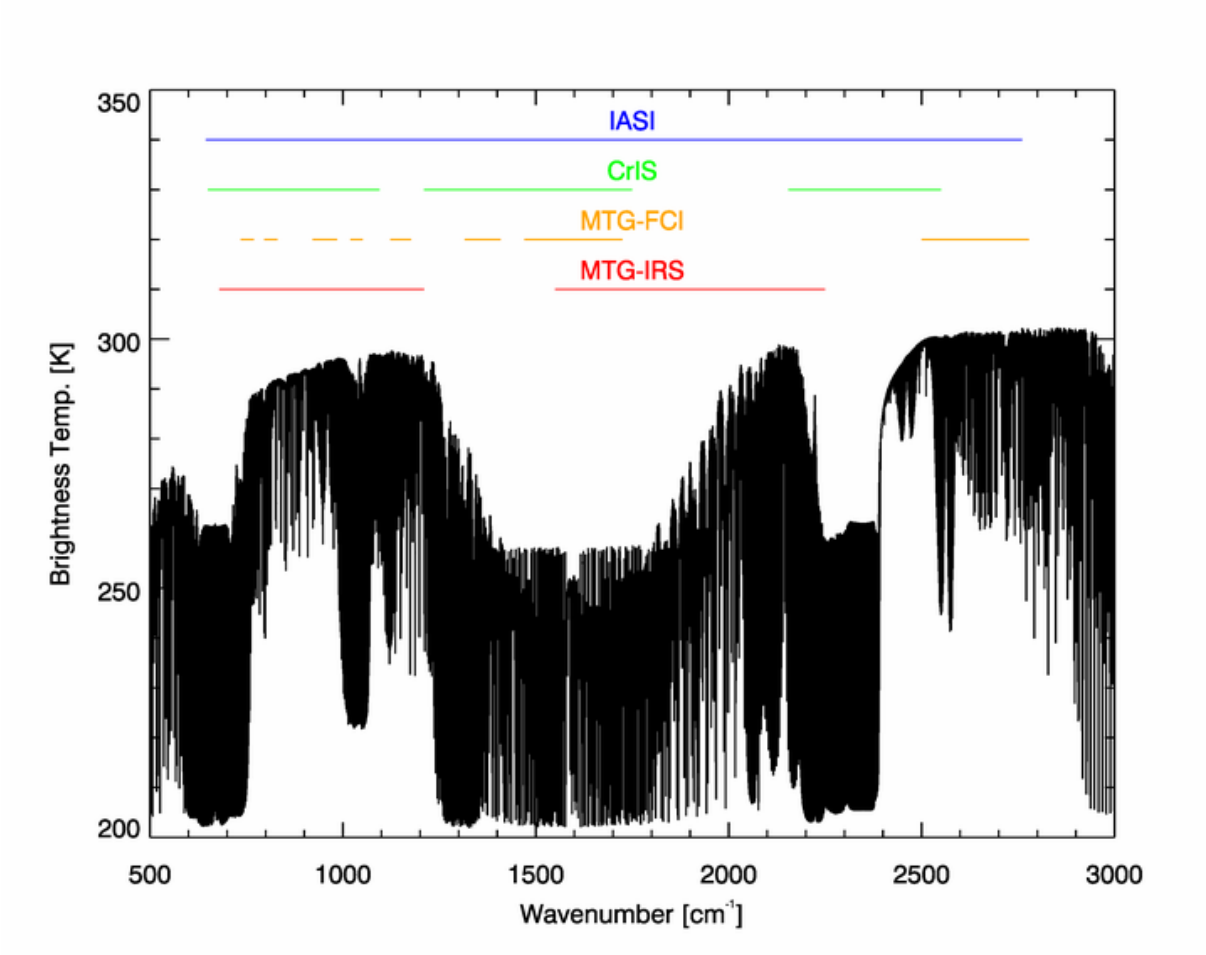

Figure 1: IR spectral regions used for sounding of the atmosphere by IASI and CrIS compared with the 2 bands used by MTG-IRS. The FCI bands, the imager on-board MTG, are also plotted for reference.

When launched in October 2006 on board Metop-A, IASI was the first fully operational polar-orbiting interferometer on a weather satellite. It is designed around a Michelson interferometer to provide measurements in 8461 spectral channels between 3.6 and 15.6 μm (645-2760 cm^{-1}). 120 spectra are acquired in the cross-track direction with a horizontal resolution of 12 km at nadir from the nominal 815 km high orbit. A second IASI instrument was subsequently launched aboard Metop-B in September 2012. Operation of these two twin instruments allowed Eumetsat to gain experience on hyperspectral algorithms and products.

The Cross-track Infrared Sounder (CrIS) was launched in October 2011 on board the Suomi-NPP platform. Like IASI, it is a Fourier transform spectrometer on a polar orbit scanning across track (30 steps of 9 pixels over 2200 km) with a spatial resolution of 14 km at nadir. There are 1305 spectral channels over 3 non-contiguous bands: LWIR (650 – 1095 cm^{-1}), MWIR (1210 – 1750 cm^{-1}) and SWIR (2155 – 2550 cm^{-1}) with originally a spectral resolution (unapodized) of 0.625, 1.25 and 2.5 cm^{-1} respectively; the processing has recently been adapted so that the spectral resolution is 0.625 cm^{-1} over the three bands.

The Geosynchronous Imaging Fourier Transform spectrometer (GIFTS) was part of the NASA New Millenium Program (NMP) [RD-24]. It was aimed at placing a 128x128 pixels imaging Fourier transform spectrometer on the geosynchronous orbit in order to gather high-spectral resolution (0.6 cm^{-1}) and high-spatial resolution (4 km) infrared spectra of the Earth

in two spectral bands: 685 to 1130 cm^{-1} and 1650 to 2250 cm^{-1}. An associated imager was foreseen to provide cloud imagery at a spatial resolution of 1 km. Full Earth disk coverage was ensured by step-scanning the instrument field of view. GIFTS was meant to be launched on board the "Earth Observing-3" mission of the NMP. The project however ended with the cancellation of the NMP in 2008.

Similar concepts have been studied and/or developed by several agencies. The Geostationary Interferometric InfraRed Sounder (GIIRS) on board the Chinese Meteorological Administration platform FY-4A has been launched in December 2016 and is, after the cancellation of the GIFTS, the first hyperspectral sounder on the geostationary orbit [RD-25]. It is however not an operational instrument: it is meant as a demonstrator for the subsequent GIIRS instruments that will be launched on board the members of the FY-4 family from 2018 on. Spectra are obtained in two bands: 700-1130 cm^{-1} with a spectral resolution of 0.8 cm^{-1} (later 0.625 cm^{-1}) and 1650-2250 cm^{-1} with a spectral resolution of 1.6 cm^{-1} (1.2 cm^{-1}). The spatial resolution of the first instrument is 16 km at nadir and 8 km on subsequent instruments. A visible imager with a spatial resolution of 1 km is associated to the spectrometer.

2.4 Science applications

Short science plan to be written.

3 MTG-IRS INSTRUMENT

The platform MTG-S, the sounding component of the MTG mission will embark both the IRS and the Ultraviolet Visible Near-infrared (UVN) spectrometers.

The satellite orbit is defined to be geostationary with a nominal altitude of 35786 km, an orbital period of 86164 seconds, an inclination of 0^o (+/- 1^o) and a Sub-Satellite Point (SSP) at 0°N 0°E. In order to protect the satellite from excessive Sun heating, the platform will perform a yaw flip manoeuvre at each equinox. Its lower face will point to the South from spring equinox to the autumn one (i.e. during northern hemisphere summer) i.e. the reference axis will be:

- +X: satellite anti-speed vector
- +Y: North direction;
- +Z: nadir toward the Earth.

From the autumn equinox to the spring one (i.e. during northern hemisphere winter) the lower face of the satellite will point to the North (Figure 2) so that the reference axis will be:

- +X: satellite speed vector;
- +Y: South direction;
- +Z: nadir toward the Earth.

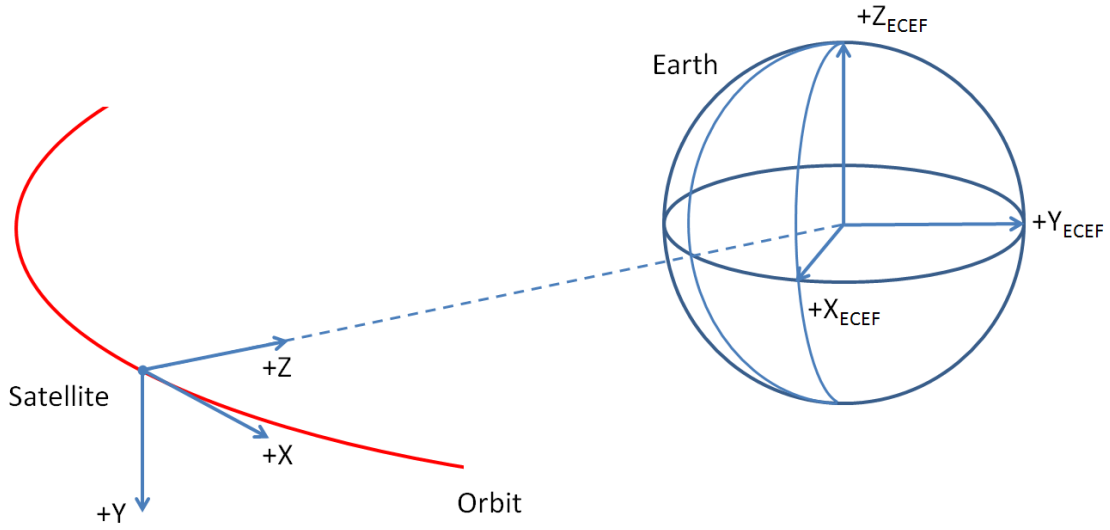

Figure 2: orientation of the satellite reference frame (X, Y, Z) and the Earth reference frame (X_{ECEF}, Y_{ECEF}, Z_{ECEF}) during northern winter. During northern summer the Y axis of the satellite is co-linear with the Z axis of the Earth reference frame.

3.1 Overall Design

The MTG IRS Instrument design is based on an infrared Michelson interferometer, which includes a detection chain composed of two types of imaging detectors (MWIR and LWIR) located in a cooled cryostat along with the processing electronics. Light from the observed area on Earth will be guided by an entrance- and inner baffle system, scan-mirror assembly for scanning the Earth and Front Telescope Assembly (FTA) to focus light into the

Interferometer Assembly (IA) and then via the Back Telescope Assembly (BTA) into the cooled Detection Assembly (DA) (Figure 3).

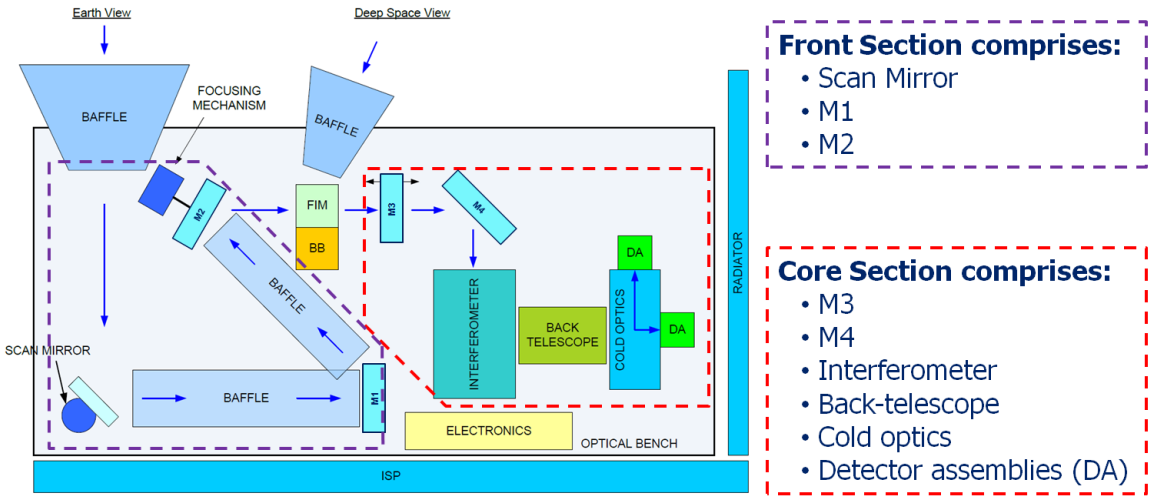

Figure 3: IRS instrument functional sketch. The flip-in mirror (FIM) separates the optical elements of the front section on the left (scan mirror, M1 and M2) with the core section of the instrument on the right (M3 and M4, interferometer, back-telescope and detector) (adapted from [RD-1]).

The part including the scan mirror (M0) and mirrors M1 and M2 is referred to as the "front section" (FS). On the other hand, the so-called "core section" (CS) comprises mirrors M3 and M4, the interferometer, the back-telescope and the detector.

The front telescope (FT), with an entrance pupil of 284 mm, an angular magnification of 4 and a field of view of 1.024 degrees, includes a 2-axis scan mirror (M0) and the four mirrors FT-M1 to FT-M4. The position of M2 is slightly adjustable in focus during the commissioning to account for possible misalignments following the launch. A moveable mirror, referred to as flip-in mirror (FIM), is located between M2 and M3 and feeds the interferometer with the radiance of either:

- the main optical path (that allows viewing the Earth, referred to as "EV", or the deep space referred to as "DS2"), in which case the FIM does not intercept the beam;
- the secondary path (used only for deep space referred to as "DS1");
- the blackbody ("BB").

Additionally, the FIM includes an obturation mode to prevent the Sun light entering the interferometer. Obturation mode will be commanded if the instrument enters safe or survival modes or if the Sun is present within the field of view.

The front telescope feeds a Michelson interferometer that includes a beam splitter, made of a separator and a compensator plate, and two corner cube reflectors. One of the corner cubes is fixed while the other can move along the optical axis with a range of +/-8.48 mm[3]; the recorded interferograms will thus be double-sided. It is worth noting that the interferometer assembly is basically the same as the one used on the IASI instrument in which the

[3] The actual course of the corner cube is +/-8.6 mm; however the speed of the corner cube is constant only on a part of this course. The interferograms are acquired only during this part when the speed does not vary (corresponding to ASE=1)

obsolescent parts have been updated. The position of the corner cube (and thus the actual on-axis optical path difference) is measured using a metrology system that uses three laser beams going through the interferometer along with the science beam with three different orientations. The optical phase difference between the three beams gives the 3D position of the moving corner cube. It is the first in-space 3D metrology system for a FTS (Spie2020/S.Abdon).

The back-telescope with an angular magnification of 2.56 is placed between the interferometer and the cold optics where the beam is separated into two in order to feed both the LWIR and the MWIR CCDs using a dichroic beam splitter.

The instrument acquires a number of interferograms simultaneously over a so-called "dwell" using a two-dimensional detector array for each band at the image focal plan. The 480 x 480 pixels of the detectors are read by groups of 3x3 (each sub-pixel being de-selectable), giving 160 x 160 interferograms per band and per dwell. A group of 3 sub-pixels spans 90 μm; knowing that the effective focal length of the instrument is 805.2 mm, the field of view of one dwell is 1.025° and the spatial sampling on the Earth surface thus 4 km at nadir increasing up to 10km and above near the limb (Figure 4).

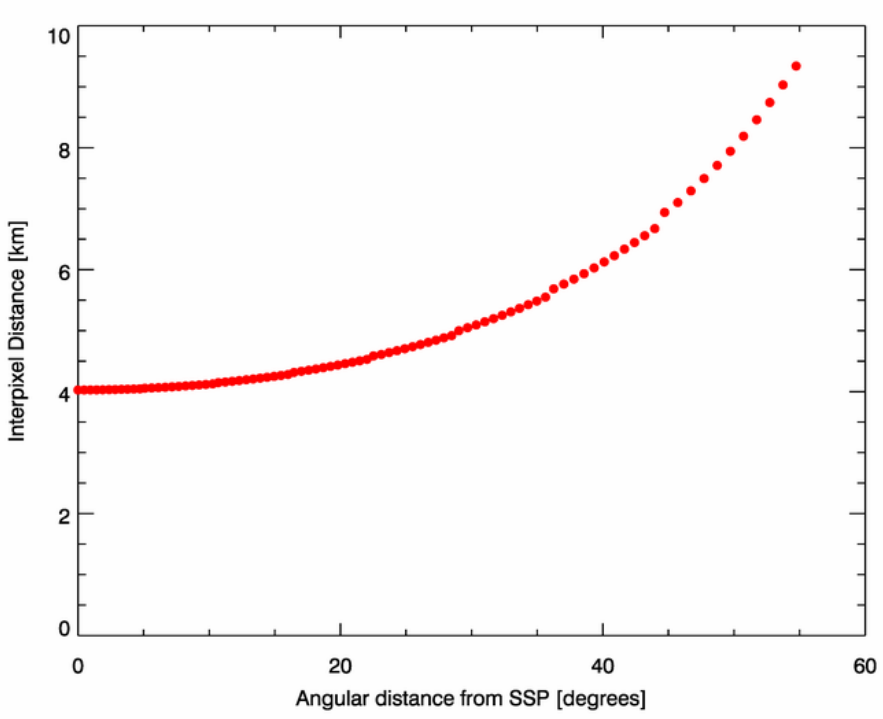

Figure 4: interpixel distance as a function of the angular distance to the sub-satellite point.

The nominal acquisition time of one dwell is a trade-off between the optimization of the number of dwells per LAC and the calibration needs. It has been set to 9.7 seconds. The latter are sampled at a nominal frequency of 2450 Hz yielding 23601 samples. The metrology is over-sampled by a factor 6 to adapt to any integration time of the interferograms. Moreover, there are 6 different metrology measurements: 3 lasers and their quadrature signals (needed to guess the MCC direction).

In addition to the interferograms data cube, one high spatial resolution broad images per band is produced from the detector sub-pixels readouts, consisting of 480x480 pixels.

There are thus two measurement modes, illustrated on Figure 5:

- The normal mode in which the interferograms are obtained binning the 9 elements of each sub-matrix;
- The imager mode in which high-resolution images are obtained by reading the detector over each band at sub-pixel level.

These two modes are rather two types of measurements systematically obtained in parallel and do not result from the operation of the instrument in different configurations: 4 broad-band images will be available each time a spectra datacube is acquired.

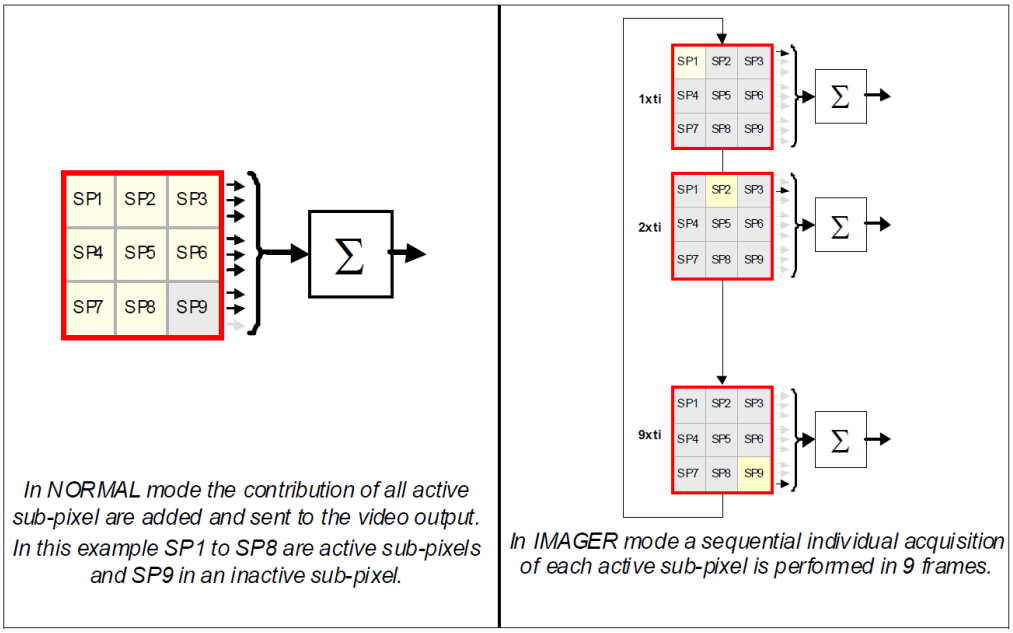

Figure 5: illustration of the sub-pixel readouts in normal and imager modes. On the left the "normal mode" consists in summing the readouts of the 480x480 sub-pixels of the detector by groups of 3x3, resulting in a 160x160 pixels image. In "imager mode", the 480x480 pixels are read individually and transmitted to the ground as 9 160x160 pixels frames.

The readout is only made for the size of the dwell, i.e. 160x160. So, the 480x480 pixels of the images will be transmitted to ground using 9 times the 160x160 frames, as illustrated on the Figure 5.

3.1.1 Measurements geometry and temporal sequencing

The field of view of IRS is 1.025 degrees i.e. much less than the apparent diameter of the Earth as viewed from the geostationary orbit (about 17 degrees). The instrument is thus scanning the Earth in a "stop and stare" mode: IRS will image an area of the Earth covered by the field of view of the instrument, collecting in 9.7 seconds 160x160 interferograms and 4 broad-band high-resolution images for each spectral band (2 at the beginning, 2 at the end), then will jump to the next adjacent area.

Furthermore, the Earth disk has been divided into 4 regions of interest called LACs (Local Area Coverage) numbered 1 to 4 from South to North. LAC 4, the northernmost LAC covering Europe, will be scanned every 30 minutes; LACs 1, 2 and 3 will be imaged in-between successively as defined in the EURD [AD-2] (Figure 6). The nominal coverage, illustrated on Figure 7, has been defined to optimize the coverage and the need for calibration views but it must be noted that the scanning law can be modified in flight, however keeping technical constraints such as the movement of the scan mirror and/or the data rate, in mind.

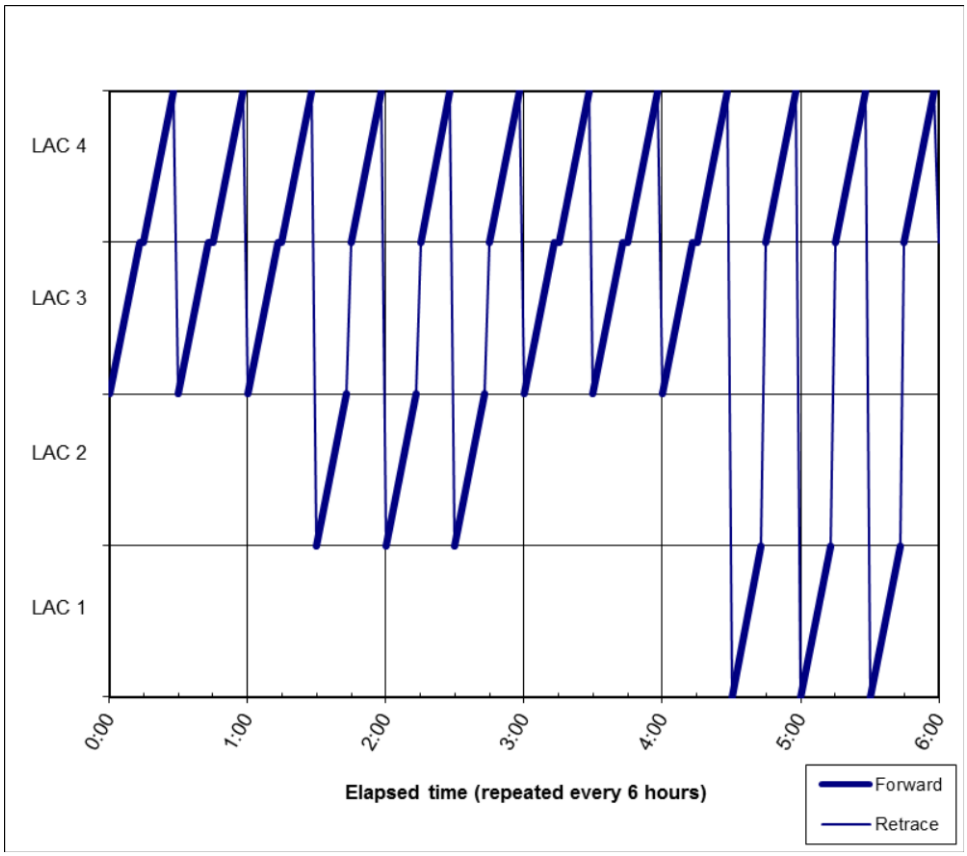

Figure 6: IRS operational scanning sequence

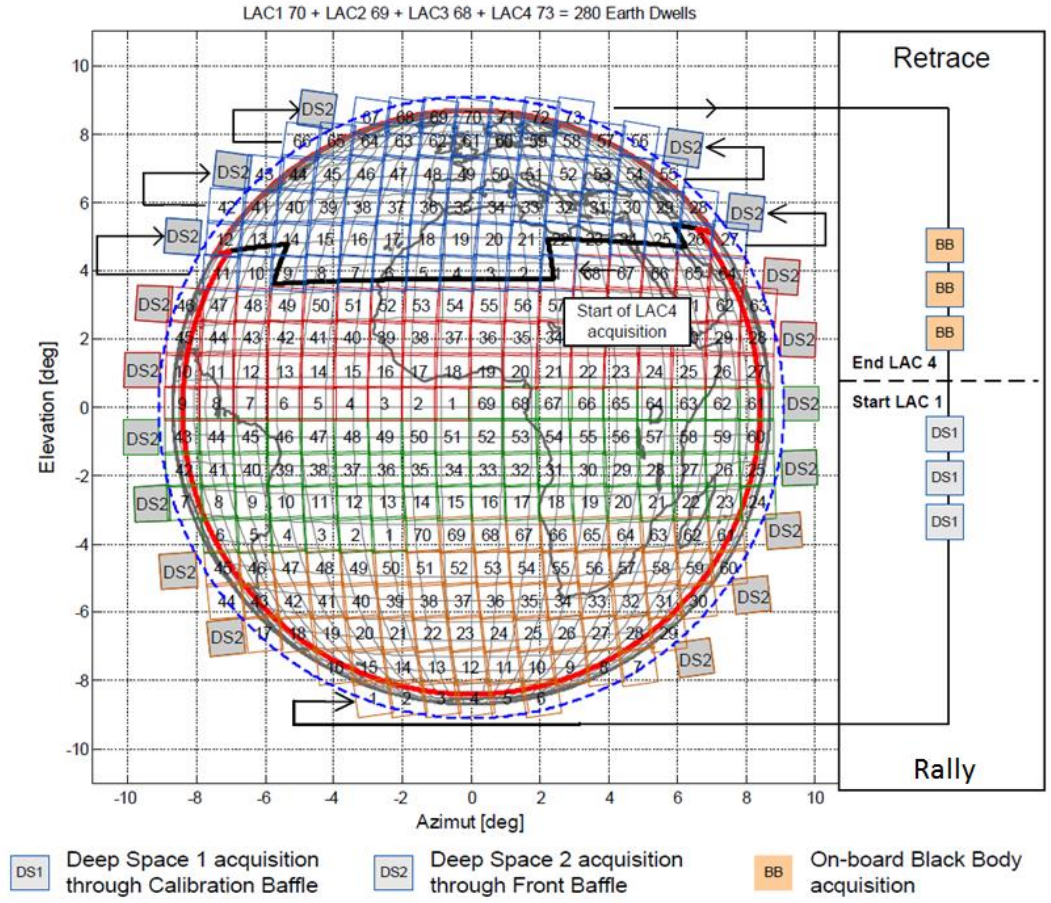

Figure 7: IRS scan pattern. The colours correspond to the four LACs. Deep space views used for the background determination appear as grey squares denoted DS2. Other calibration measurements (DS1 and BB) are performed during the transition between two LACs (here for example the transition between LAC4 and LAC1).

The data cube collected over the area covered by the field of view forms a dwell. Not only Earth views will be collected but also deep space views that will be used for the calibration. Deep space views are of two types:

- Deep-space views acquired through the front telescope (DS2), performed after a South-North transition of the scan mirror i.e. at the beginning of each line except the first one of each LAC;
- Deep-space views acquired through the secondary path (DS1), performed at the beginning of each LAC when the scan mirror moves from its neutral position then to the beginning of the first line of the next LAC (“rally phase’);

In addition to these deep space views, blackbody measurements (BB) are performed at the end of each LAC when the scan mirror moves from its position at the end of the last line of the considered dwell to its neutral position (“retrace phase”).

It is worth to note that:

- The acquisition duration of each single LAC is 15 minutes;

- The number of dwells is different for every single LAC. Moreover, the number of calibration dwells within a LAC was chosen in order to make optimal use of the acquisition duration of a LAC;
- The number of dwells (being Earth or calibration views) per LAC is an even number to ensure that the interferometer moves in a direction that is automatically synchronized to the platform performed compensation;
- The scan pattern can be changed in flight if needed.

Science data (i.e. interferograms as well as images) are acquired over each dwell during a stare of 9.7 seconds when the speed of the moving corner cube is constant ("linear phase"). At the end of this phase, the corner cube slows down and stops then accelerates in the other direction. During this period of at least 800 msec, the scan mirror moves to be in position for imaging the next dwell (Figure 8). This includes a settling time of 100 msec to damp any vibrations of the scan mirror after it has moved.

It can be noted that the science data acquired during dwell number s will be stored in a buffer and processed during dwell $s + 1$ (when the relative position of the corner cubes is estimated) and processed during dwell $s + 2$, as illustrated on Figure 9.

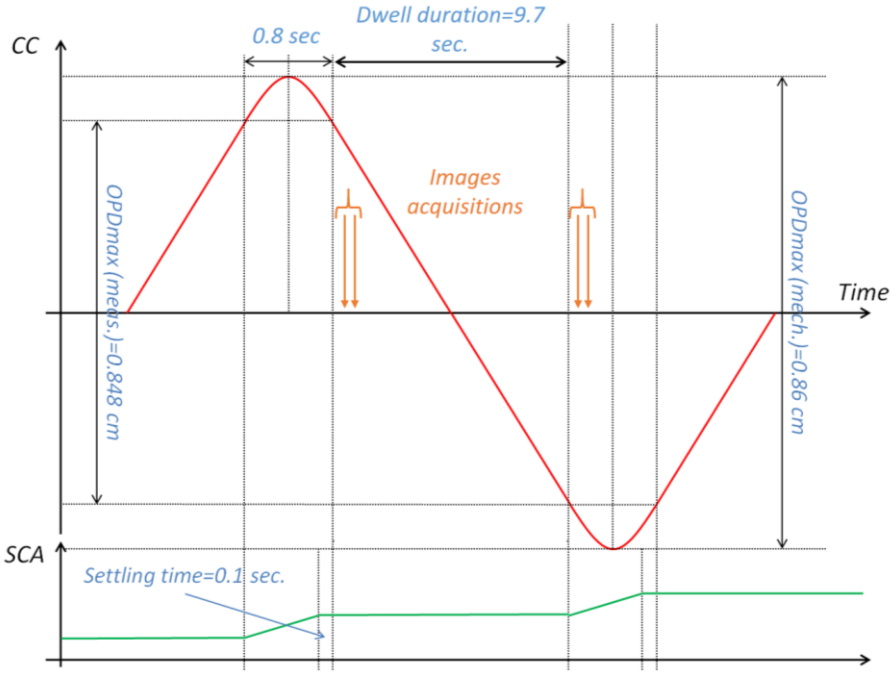

Figure 8: movement of the corner-cube (CC, in red) as a function of time. The duration of one dwell corresponds to the linear phase of the CC movement (constant speed) during which the interferograms are sampled; also on the plot is depicted the times when the full-resolution images are acquired. The position of the scan mirror (SCA) is also plotted in green. The time axis is not to scale.

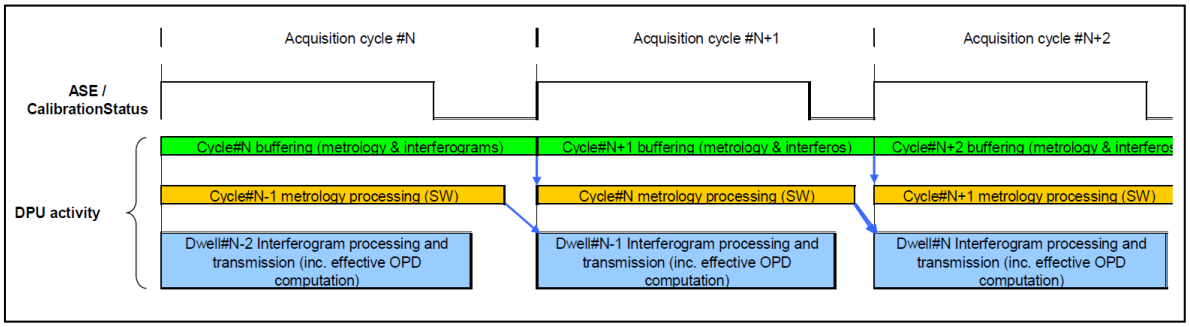

Figure 9: Data processing sequence

3.1.2 Particularities of the Front Section and the Instrument Background

While the temperature of the core section (i.e. elements located after the flip-in mirror) is expected to be stable, the first elements of the telescope (the so-called "front-section") are directly exposed to Sun heating and will thus exhibit large temperature variations. This is illustrated on Figure 10 that shows a simulation of the temperature of the mirrors of the telescope during day 56 of the year (one of the four "worst cases"): the temperature of the scan mirror (M0) exhibits a variation that reaches 15 K over one day.

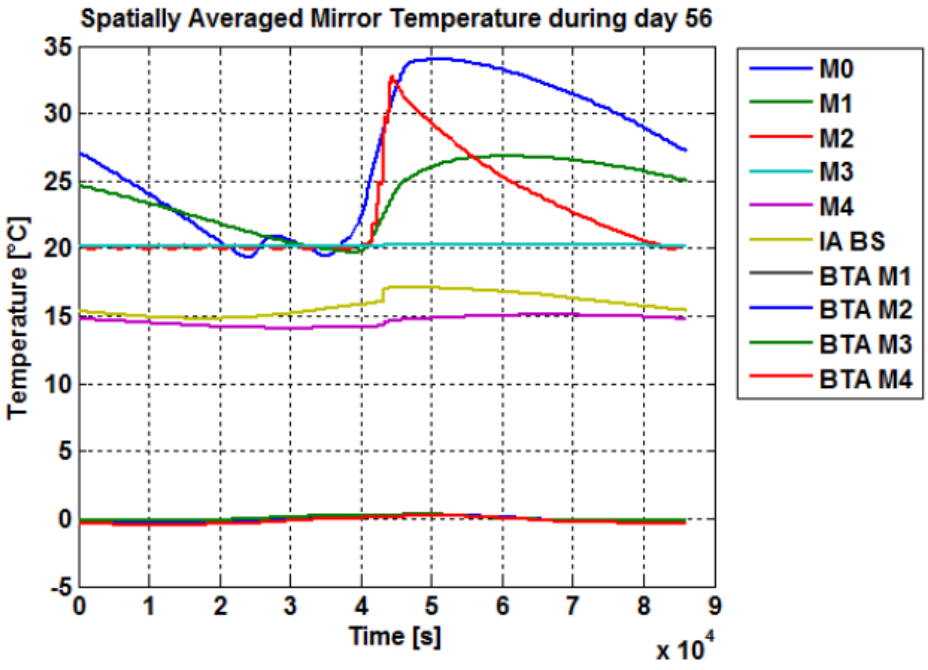

Figure 10: Diurnal variation of the temperature of the various mirrors of the optical chain. "IA" stands for "Interferometer Assembly" while "BTA" is the "Back Telescope Assembly" (from RD-2).

It can be noted that the amplitude of the variations is season-dependent. Figure 11 shows the value of the temperature daily peak of the various mirrors over a year: the amplitude is highest four days a year, 25 days before and after the equinoxes.

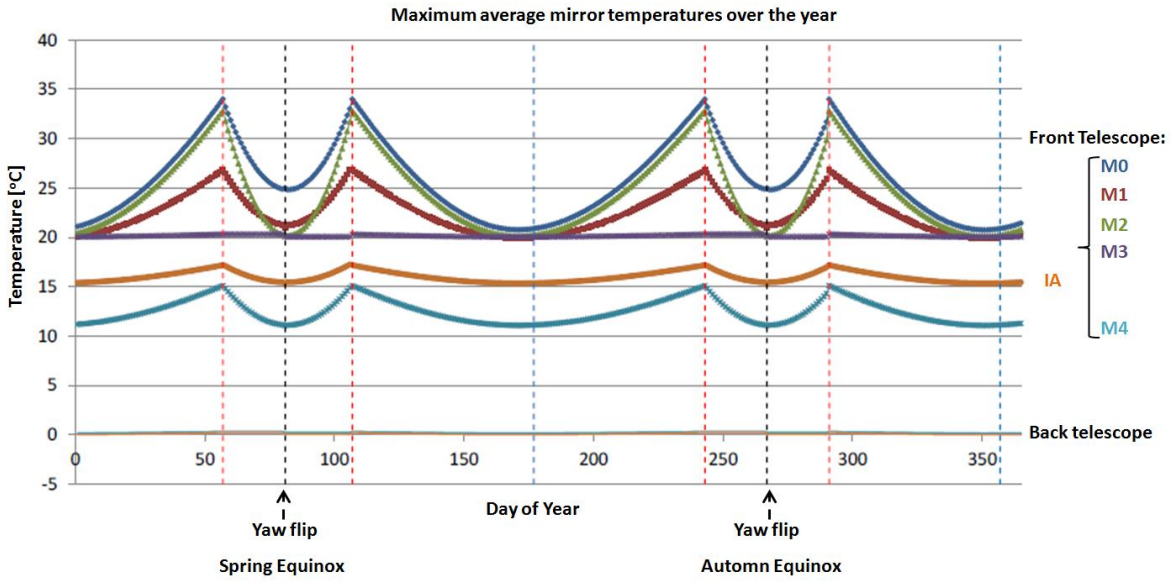

Figure 11: temperature variations of the various elements of the optical chain over one year.

The large amplitude and variability of the temperature variations translates into variations of the amplitude of the instrument background radiance and imposes regular measurements in order to capture its time evolution.

Measurements of the instrument background are performed through the so-called deep space views. They are of two kinds:

- Through the main telescope, i.e. following the same optical path than the Earth views, called DS2;
- Through a secondary baffle pointing at the deep-space that allows the measure of the background on the optical path of the black-body. These are referred to as DS1 in the IRS terminology.

While DS1 are measured between the retrace of the scan mirror at the beginning and at the end of each LAC, the DS2 measurements are performed at the beginning of each line (except the first one of each LAC, see Figure 7). The scan time of the longest lines (lines 2, 3 and 4 of LAC-2 and 3) being of the order of 200 seconds, it is expected to have a DS2 measurements every 3 minutes or less. Over LAC-4, that will be scanned most often, the duration of the lines, and so the time between two DS2, varies between 167 and 83 seconds.

It can be seen on Figure 10 that the temperature of mirrors M3 and M4 is quite stable over day 56 so that it can be expected that the instrument background radiance coming from the blackbody optical path is not subject to fluctuations as large as the ones seen on the DS2.

3.2 Concept of a Fourier Transform Spectrometer

The IRS design is based on a typical Fourier transform Michelson interferometer (Figure 12): the incident radiation of intensity A is divided into two beams along different optical arms of lengths $\delta 1$ and $\delta 2$. Recombination of the two beams will yield interferences, depending on

the optical path difference (OPD) *x= 2(δ1- δ2)* that is a function of the position of the mirrors (or corner cubes in the case of IRS) in the system.

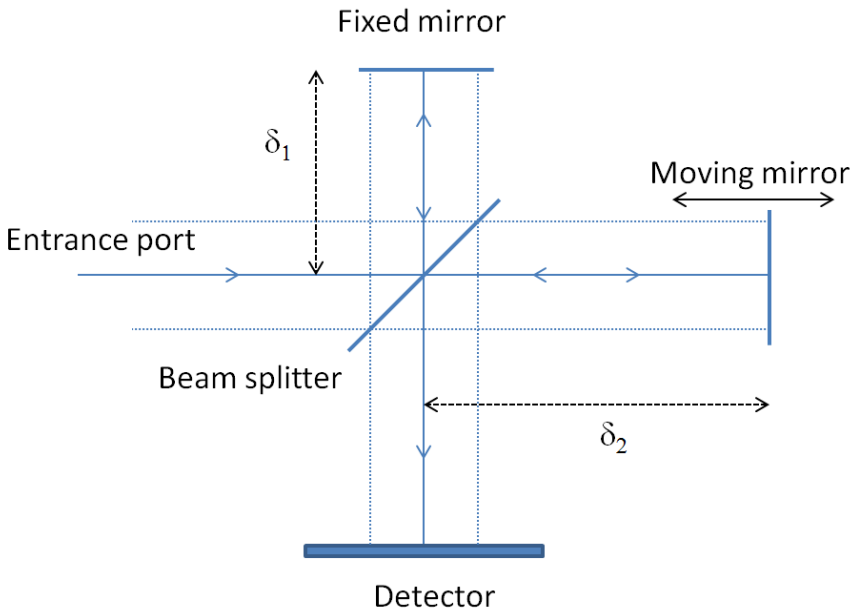

Figure 12: simplified layout of a Michelson interferometer for an on-axis pixel

Note that for IASI and IRS as opposed to CriS the two reflectors consist of corner cubes (CC) and not flat mirrors, the alignment properties then slightly diverges but the following basic equations remain valid.

For a monochromatic wave of amplitude A and wavelength λ so that its wavenumber is $\nu = 1/\lambda$, the detected intensity by an on-axis pixel is given by the expression [see for instance RD-26]:

$$I'(x) = A^2 \cos^2(\pi\nu x) = \frac{A^2}{2}[1 + \cos(2\pi\nu x)] \qquad \textbf{Eq. 1}$$

The constant part is called the baseline and the non-constant part of Eq. 1 is defined as the interferogram of a monochromatic source of amplitude:

$$I(x) = \frac{A^2}{2}\cos(2\pi\nu x) \qquad \textbf{Eq. 2}$$

If the source is a continuous spectrum *S(ν)* defined on the positive wavenumbers, the detected interferogram is the sum of the interferogram of each monochromatic wave:

$$I(x) = \int_0^\infty S(\nu)\cos(2\pi\nu x)d\nu = \int_{-\infty}^{\infty} \hat{S}(\nu)\exp(2i\pi\nu x)d\nu = FT^{-1}\left[\hat{S}(\nu)\right] \qquad \textbf{Eq. 3}$$

With $\hat{S}$s the symmetrized spectrum defined as: $\hat{S}(\nu > 0) = S(\nu)/2$ and $\hat{S}(\nu < 0) = S(-\nu)/2$. Hence the interferogram equals the inverse Fourier transform of the incident

symmetrized spectrum $\hat{S}(\nu)$, which is real. Since it is a reversible operation, the spectrum can be retrieved by taking the direct Fourier transform:

$$\hat{S}(\nu) = FT[I(x)] \qquad \textit{Eq. 4}$$

In an actual instrument, the optical path difference x is limited to a given value x_{max}; this is equivalent to multiplying the interferogram by a boxcar window $D(x)$:

$$D(x) = \begin{cases} 1 & \text{for } x \leq |x_{max}| \\ 0 & \text{for } x > |x_{max}| \end{cases}$$

Such that we have:

$$S(\nu) = FT[I(x) \times D(x)] \qquad \textit{Eq. 5}$$

The Fourier transform of the product of two functions being the convolution of the Fourier transform of each function, the limitation of the optical path difference to a value x_{max} yields the convolution of the infinite resolution spectrum by the Fourier transform of the boxcar function that is a cardinal sine function (Figure 13):

$$\mathrm{FT}\{D(x)\}(\nu) = \frac{\sin(2\pi\nu x_{max})}{2\pi\nu x_{max}} = \mathrm{sinc}(2\pi\nu x_{max}) \qquad \textit{Eq. 6}$$

The function $FT\{D(x)\}$ is the response of the spectrometer to a monochromatic input. It is called the Instrument Line Shape (ILS). The width of the base of the central peak (position of the first zeroes) is $1/x_{max}$, meaning that two spectral lines separated by this amount will be completely resolved. The theoretical resolution of the instrument is however better considering that the full width at half maximum (FWHM) criterion: indeed, two spectral lines will be visible if the spacing between them is greater than their FWHM that is:

$$\Delta\nu = \frac{1.207}{2x_{max}} \qquad \textit{Eq. 7}$$

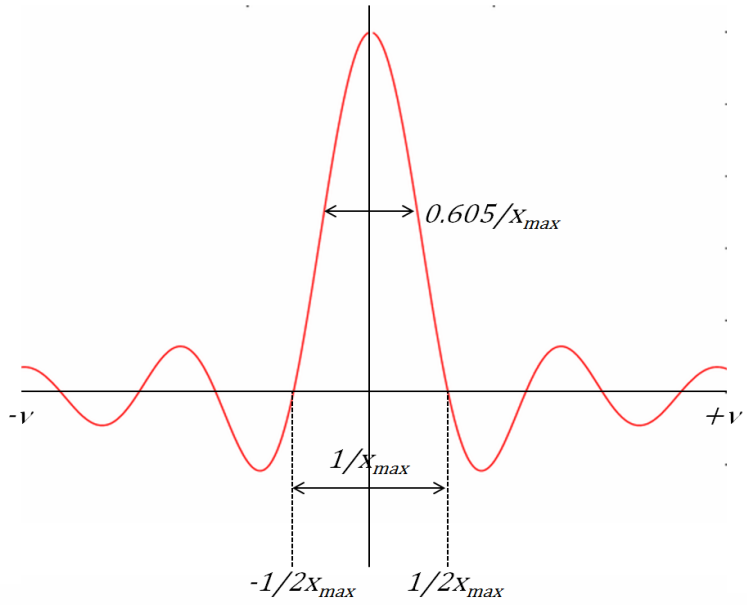

Figure 13: aspect of the cardinal sine function that is the Fourier transform of the boxcar window. The position of the first zeroes gives the theoretical resolution of the instrument.

In a real instrument, additional effects such as the finite and discrete acquisition, the radiometric response or the optical point spread functions has to be taken into account. They are exposed in the next sections.

3.3 Implication of an extended field of view

The Fourier transform spectroscopy principles have been presented in section 3.2, with the assumption that the measurements are done on the optical axis of the instrument without field dispersion. In reality, an interferometer has an extended field of view of up to a few degrees. This has important effects on the physics of the measurements.

In section 3.2, Eq. 1, we have seen that the detected intensity, i.e. the square of the amplitude is a function of $\cos(2\pi\nu x)$. It can be shown that, for a monochromatic wave ν entering the interferometer with an angle θ with the interferometric axis, the optical path difference x must be replaced by $x.\cos(\theta)$:

$$I(x) = A^2\cos^2(\pi\nu x\cos(\theta)) = \frac{A^2}{2}[1+\cos(2\pi\nu x\cos(\theta))] \qquad \textit{Eq. 8}$$

This causes a continuous change of the interferometric state over the field of view that induces the so-called fringes of equal inclination of the Michelson interferometer. These fringes form concentric circles in the focal plane. It can be shown that the centre of these circles is the direction defined by the apexes of the two corner cubes. Ideally the trajectory of the mobile cube corner is a straight line passing through the image of the fixed cube corner. Then the centre of the fringes is fixed in time. This direction is called the interferometric axis.

In a real (i.e. imperfect) instrument, the centre of the fringes will stay fixed only when the optical path difference is far from zero. This allows defining the interferometric axis in realistic conditions (errors coming from optical alignment or moving mirror guiding mechanism imperfections).

It is straightforward to see that the substitution of x by $x.\cos(\theta)$ in Eq. 8 implies that the interferogram of a monochromatic wave ν making an angle θ with the interferometric axis is exactly the same than the interferogram of a monochromatic wave $\nu.\cos(\theta)$ on the axis. One of the main effects is that the size (maximum OPD) of the interferograms decreases with the distance to the interferometric axis. That yields a spectral scaling that has to be corrected.

This spectral shift is compensated on-board by an interferogram resampling using the 3D metrology system (section 3.1).

3.4 Spectral response function

Extending the simple case of section 3.2 by taking into account all instrument defects, the measured spectrum $S_{meas}(\nu_0)$ for a given pixel and the spectral channel ν_0 can be expressed as a function of the true spectrum $L(\nu)$ as:

$$S_{meas}(\nu_0) = \int_0^{\infty} L(\nu).SRF_{\nu_0}(\nu)d\nu \qquad \textit{Eq. 9}$$

where $SRF_{\nu_0}(\nu)$ is the spectral response function (SRF) for spectral channel ν_0. It is worth to note that the SRF should be normalised in energy in order not to impact the radiometry:

$$\int_{-\infty}^{\infty} SRF_{\nu_0}(\nu)d\nu = 1 \qquad \textit{Eq. 10}$$

Eq. 9 shows that the knowledge of the SRF is critical for retrieving the true spectral radiance $L(\nu)$. The spectral response function depends on several instrument parameters which include the optical path difference acquisition range, the apodisation, the radiometric response and the optical path difference dependence on the field of view of the instrument. All those aspects are taken into account in the SRF estimation model, hereafter referred to as the SRF-EM, presented in section 5.4.

The spectral response function for the spectral channel ν_0 can be expressed as a combination of many elements:

- The maximum OPD cut-off at interferogram level will first shape the SRF as discussed in section 3.2.
- The SRF can also be shifted in wavenumber, for example, due to an optical misalignment not compensated by the on-board interferogram resampling like a focal plane drift.
- Since the light goes through an instrument with a non-uniform response, for each channel one should add the radiometric response $R_c(\nu)$ to the SRF:

$$SRF_{\nu_0}(\nu) = \frac{R_c(\nu_0 - \nu)}{R_c(\nu_0)}.ILS_{\nu_0}(\nu) \qquad \textit{Eq. 11}$$

This component is not always considered in the SRF definition of FTS and it is not the case for IRS, since at maximum one should consider one SRF per pixel (25600), per wavenumber (~1000) and band (2) which leads to non-realistic timeliness for most users. The residual noise is called the "calibration ringing", to cope with this effect, a dedicated mitigation, called RTF uniformisation, has been developed for IRS and is described in section 5.3.5.

- The spatial extension of a pixel (including the optical point spread function) causes a decrease of the interferogram contrast at high OPD, FOV and wavenumbers. The relatively short course of the corner cube (compared to IASI) and the small individual pixel size lead to a very weak self-apodisation (hereafter referred to as SAF). However, the straylight can add features with large field extensions, which could matter for IRS. For IASI, there is a cold plate at the focal plan that defines the pixel FOV and prevents such extended straylight effects. As for IASI, the IRS processing includes a SRF Uniformisation processing that cancels such effects and is described in section 5.3.5.

- The sample integration causes an interferogram loss of contrast of high wavenumbers in function of the MCC speed. This effect is compensated on-board at interferogram level after acquisition.

We now define the self-apodisation function (SAF) as the inverse Fourier transform of the SRF:

$$SAF_{\nu_0}(x) = FT^{-1}\left[SRF_{\nu_0}(\nu)\right] \qquad \textit{Eq. 12}$$

Note that, in the general case the SAF is complex. Ideally, the SAF filter is a box function. In reality, this box function is not perfect and its Fourier transform induces a deformation on the SRF. There are two aspects of the deformation:

- The shape of the SRF, which is related by Fourier transform to the modulus of the SAF (the SAF imaginary part is often considered low with respect to the real part),
- The shift of the SRF, which is related by Fourier transform to the phase gradients of the SAF.

In the end, IRS is only slightly self-apodized: the variations of the self-apodisation function over the detector array are weak. Indeed, the value of the self-apodisation function is at most 0.995 at 2250 cm^{-1} and is more than 0.9995 at 680 cm^{-1} for the corener pixel i.e. a variation of about 0.05%. Consequently, the ILS is very close to a cardinal sine function. Note that these figures do not include straylight and may evolve in the future.

Then, the SRF is also sensitive to the radiometric response, as expressed in Eq. 11. The spectral variability of the radiometric response has an influence on the shape of the SRF, within each band, and from one pixel to another:

- The shape of the radiometric response, an example of which is given on Figure 14, falls rapidly to zero at the beginning of band 1;
- On top of it, we expect RTF modulations induced by etalon effect: due to non-perfect coating, the light can loops in a low finesse cavity that produces modulation.

- Finally, the temporal variation of the radiometric response is not precisely known but according to the instrument manufacturer, could vary in time with a characteristic timescale of the order of one month. The SRF would thus vary with the same timescale.

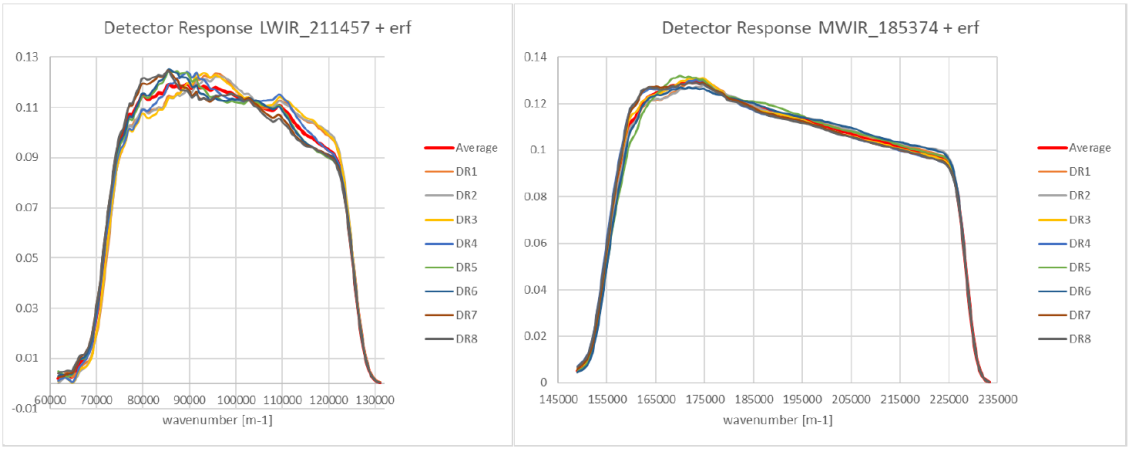

Figure 14: Example of radiometric response in band 1 (LWIR, left) and in band 2 (MWIR, right) for a series of pixels of the detector; the red thick line refers to the average response (based on the detector responsivity provided by ESA).

The knowledge of the SRF is required to analyse the measured spectrum. It is then important to accurately model it via the SRF Estimation Model (SRF-EM) presented in section 5.4. Furthermore, once the SRF is known, it becomes possible to perform the so-called uniformisation (except for the RTF component, see discussion in section 5.3.6) that aims at rendering the measurements independent from the instrumental effects. The users are then provided with products in which a single SRF for the whole detector array and independent of time is to be considered. The process to achieve this is presented in section 5.3.5.

3.5 Similarities and differences with IASI

IASI has a special importance for EUMETSAT. EUMETSAT has indeed a long-standing and profound experience in the processing of IASI data and many members of the future IRS user community have made first acquaintance with hyperspectral sounder data through IASI. Furthermore, the IRS interferometer assembly (IA) is based on heritage from the IASI instrument. The latter has been shown to be remarkably accurate, both radiometrically (absolute accuracy better than 0.35 K) and spectrally (relative accuracy better than 10^{-6}) so that IASI measurements are often used as a reference to calibrate other radiometers [RD-18]. It is thus worthwhile to highlight similarities and differences between the two instruments.

Obviously, the most striking difference is the platform: IASI is a Low-Earth Orbit (LEO) instrument, while MTG-IRS is on a geostationary (GEO) orbit. There are however other noticeable differences: IASI is a fast sensor with a small 2 x 2 detector array, while IRS is a slow sensor with a large 160 x 160 pixel array. The time for one measurement (interferogram) is 0.216 s for IASI and 9.7 s for IRS. The total field of view in the interferometer is 3.3° x 3.3° degrees for IASI and roughly 1° x 1° for IRS. The maximum optical path difference of 2 cm of IASI is much larger than the 0.8 cm of IRS.

The few pixels of IASI have a comparatively large individual FOV, generating a strong self-apodisation in the instrument. Conversely, the shorter optical path difference and smaller individual pixel size lead to a very small self-apodisation in IRS. As a consequence, the ILS function of IASI is spectrally narrow while the IRS ILS, being very close to an ideal cardinal sine function, will extend far away from the central peak in the spectral domain. This implies that IRS is much more sensitive than IASI to the shape of the radiometric response function especially on the band edges where the latter falls rapidly to zero; IASI is immune to this problem since the spectral bands are overlapping.

IRS is thus less sensitive to the detectors Point Spread Function (PSF) knowledge than IASI; on the other hand, it is more sensitive to the PSF chromatism and the detectors mean field angle. Moreover, straylight effects are expected for IRS since it has not a cold plate at focal plan level (not evaluated at the moment).

The Table 3 summarises the on-board and on ground characteristics for both instruments.

		IASI	**IRS**
Instrument	Corner cube mechanism	-	Same as IASI
	Metrology system	1 laser beam	3 laser beams
	Maximum OPD/spectral resolution requirement	2cm/0,5 cm^{-1}	0,8 cm/0,754 cm^{-1}
	Detector matrix	2x2 read in 0.216s	160x160 read in about 10 s (nominally 9.7s)
	Field angles	Small and similar spectral shifts over the matrix	Large range of spectral shifts over the matrix
	Field angles spread	Large self-apodisation ➔ Large SRF shape variation	Small self-apodisation ➔ Small SRF shape variation
	SRF domain width	SRF large self-apodisation + level 1c apodisation ➔ narrow spectral response function domain	SRF close to a cardinal sine ➔ large spectral response function domain
	Field compensation	None	Performed on board when the IFGs are resampled
On-board processing	Non-linearity correction	Done	Done
	Spike detection	Done + Flagging	Done + Flagging + correction
	ZPD estimation	done	Done using fringes counting
	Metrology processing	CCM 1D speed variation compensation (acquisition triggered on metrology)	CCM 3D position variation correction (resampling after acquisition)
	Interferogram resampling	None	Resampling on corrected OPD grid

	Interferogram compression	n/a	Decimation

Table 3: main similarities and differences between IASI and IRS.

4 MTG-IRS ON-BOARD PROCESSING

This section provides an overview of the on-board processing algorithms.

4.1 Objectives and design

The aim of the on-board processing is twofold:

- The first goal is to reduce the amount of data to be transmitted. As the raw data rate is about 2Gbit/s and the available board to ground transmission data rate is about 150Mbit/s, the data size reduction factor shall be about 13.5. For that purpose, two processing steps are performed:
    - Filtering and decimation, in order to isolate useful signal;
    - Bit-trimming, i.e. a purely numerical data-reduction.

- Furthermore, corrections need to be applied to the detected interferograms prior to any data reduction. These are (in processing order):
    1. Non-linearity correction and offset (i.e. constant component of the raw interferograms) removal;
    2. Spike detection and correction;
    3. Correction of the contrast variation caused by the speed variations of the cube corner;
    4. Resampling of the interferograms on a fixed common OPD grid.

An overview of these corrections is shown on Figure 15. The latter point, the sampling grid correction, requires the actual OPD sampling grid of the raw interferograms to be known for each super-pixel of the detector. This is achieved using the laser metrology signals as described in section 4.2. This metrology system and the associated interferograms resampling on a fixed OPD grid (section 4.6) will allow taking into account effects of the corner cube trajectory motion as described in [RD-17].

Note that some of the modules are only superficially described in this document due to restrictions from the instrument manufacturer. This is the case for the non-linearity, the spike and the contrast corrections.

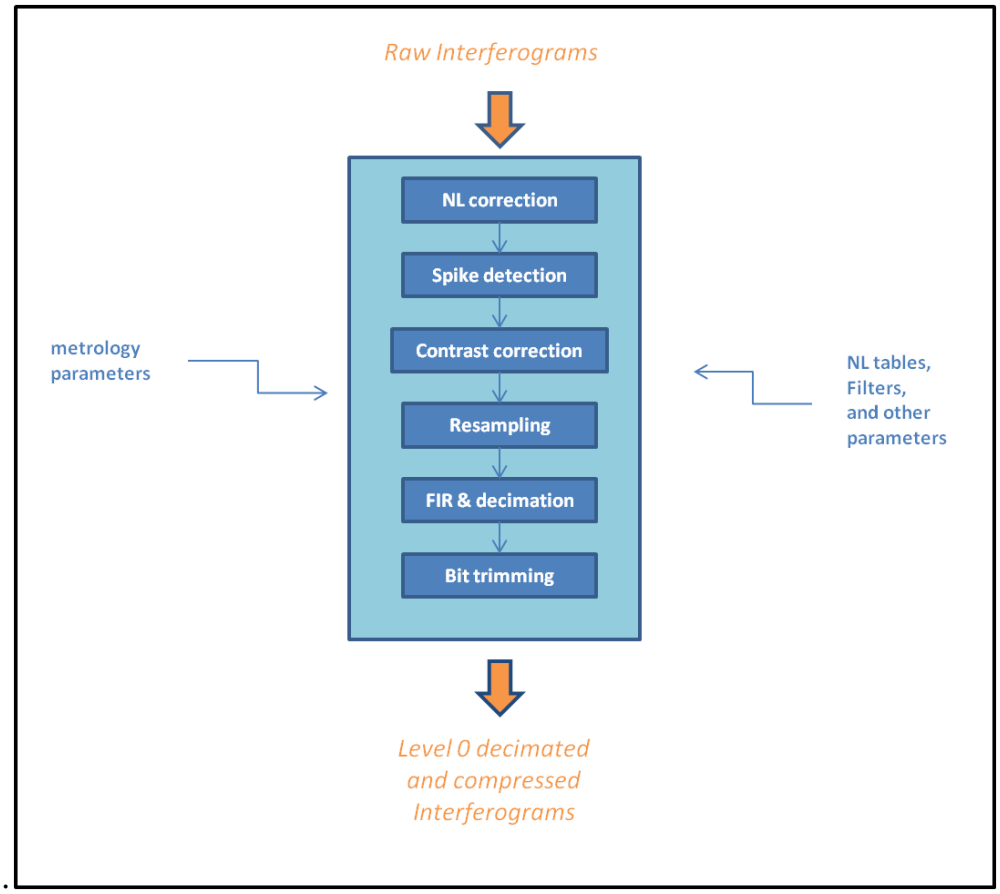

Figure 15: overview of the on-board processing

4.2 Metrology processing

The metrology processing aims at accurately measuring the optical path difference during the acquisition of the interferograms. To do so, the interferograms of three laser beams are recorded along with the science ones. One of the three lasers is injected into the center of the field of view of the interferometer. The two others lasers beams are in quadrature and are located at two different point in the field of view.

The metrology processing is divided into two parts:

- The first one uses the phases of the three laser beams to compute the OPD for three pixels of the detector array corresponding to the position of the three laser beams;
- The second part is extrapolating the three OPD computations to all pixels of the detector.

These will be described in the next two sections.

Note: it should be noticed that the metrology optical axis is independent from the science optical axis which is the position of the metrology axis on the detector matrix.

4.2.1 Laser phase measurement processing

Two interferograms are generated for each laser beam. These are sinusoids in quadrature, depending on the optical path difference x:

- The in-phase signal is ideally equal (after offset subtraction) to:
$$I_i^{\text{las}} = \cos(2\pi\nu_0 x)$$
- The in-quadrature signal is ideally equal (after offset subtraction) to:
$$I_q^{\text{las}} = \sin(2\pi\nu_0 x) = \cos\left(2\pi\nu_0 x - {}^{\pi}/_{2}\right)$$
ν_0 being the laser wavenumber.

Before any processing of the laser phase measurements, a regularization takes place, which corrects for amplitude distortions of the sine and cosine signals, the relative phase and for instabilities the metrology signal characteristics during the dwell.

The aim of the laser phase measurements is to get the phase variations (phase = $2\pi\nu_0 x$) for each laser. They are obtained by:

- Counting the fringes (i.e. counting the sine periods observed during the acquisition) to follow rough phase variations;
- Computing the angular position of the measurement in order to get an accurate phase estimation.

4.2.2 Pixel OPD computation

At the end of the laser measurement process, three laser phase measurements are available for each acquired interferogram sample m: $\varphi_{Las_1}(m)$, $\varphi_{Las_2}(m)$ and $\varphi_{Las_3}(m)$. Those three phases are giving an optical path difference measurement for three points of the interferometer field (i.e. for three pixels of the detector matrix) which are then extrapolated to get an OPD for each pixel (i.e. for each point of the interferometer field). The obtained effective OPD measurements is used to resample the interferograms (section 4.6).

In conclusion, the three lasers metrology system provides the optical path differences for each measurement point of the field of view. It is the first in-space 3D metrology system for a FTS (Spie2020/S.Abdon).

4.3 Nonlinearity correction

The compensation for the non-linear response of the detectors and the detectors electronics is split into three correction steps (first two steps are similar to the IASI ones, [RD-11]):

- High frequency (HF) nonlinearity due to the quantization effect of the analogue to digital converter, which can be characterised on ground;
- Low frequency (LF) nonlinearity due to electronics and detectors. This nonlinearity is pixel dependent;
- An offset correction of the super-pixels raw values.

4.4 Spike detection and correction

Interferograms measured by IRS can be contaminated by spikes caused by high-energy particles hitting the detectors. The large dimension of the detector arrays makes them vulnerable to such events that will translate to peaks at random independent locations in the interferograms. These spikes yield frequency perturbations in the spectrum and thus must be detected and corrected if possible.

The detection of spikes is performed using a filter which isolates the false signal from the useful one. The spike is detected when the signal exceeds a given threshold. The thresholds are determined on ground and are a function of the OPD (the threshold is not the same if the spike is in the central fringe or outside).

The data will then be flagged and possibly corrected. Details on the correction are currently restricted.

4.5 Integration contrast correction

The aim of this processing is to remove the variations of contrast on the OPD scale (i.e. after resampling) due to fluctuations of the speed of the corner cube which lead to fluctuations of the time integration during the detection of the interferogram.

The principle of the correction is to apply a 3 point filter on the interferogram before performing the resampling. The filter cancels the integration time filtering, which is constant in the temporal domain. Thereby, the contrast on the spectral domain does not vary with corner cube speed.

4.6 Interferogram resampling

In order to perform the filtering and decimation process, the interferograms have to be resampled on a regular OPD grid.

Details on the resampling process cannot be disclosed but it is possible to make the link with the metrology which provides the optical path differences at each measurement point of the field of view [RD-17].

It is important to note that:

- Since the effective OPD is pixel dependent (section 4.2), the resampling is implicitly accounting for the field effect: this thus performs a correction of the spectral shift due to the off-axis position of most of the pixels;
- The resampling is also taking into account the fact that the movement of the corner cube is imperfect. The interferograms will be corrected for every corner cube motion deviations such as the shear effect or the corner cube offset [RD-17];
- Furthermore, the interferograms measured along the two corner cube directions are resampled on board along one direction only.

As a consequence, the interferograms are all centred on the zero path difference and are independent from the corner cube direction.

In conclusion, the resampling will allow accounting for:

- The possible flaws of the corner cube trajectory (linear part of the vector apex, and possibly parabolic component and vibratory effect);
- The fixed corner cube position;
- The removal of the dependency of the corner cube direction.

4.7 Filtering and decimation

The module "filtering and decimation" aims at reducing the volume of the recorded signal for the transmission to the ground. Indeed, the observed bandwidth extends from -6500cm^{-1} to 6500cm^{-1} that is much more than the useful bands: [680cm^{-1}, 1210cm^{-1}] and [1600cm^{-1}, 2250cm^{-1}]. Using a filtering and decimation process allows transmitting only the interesting bandwidth. Furthermore, the filtering avoids the aliasing of useless frequencies (which contains noise) on the useful frequencies during the decimation process.

Finite Impulse Response (FIR) filters are applied to the entire interferograms after resampling; there are thus one complex filter per band (and the resulting decimated interferograms are thus complex). Only one over η samples is kept, η being the decimation factor. The value of the decimation factor is given by the ratio of observed and useful bandwidth; in the present case, it is 19 in LWIR and 18 in MWIR.

The decimation has an impact on the OPD range and thus on the instrument spectral sampling; characteristics of the decimated interferograms are summarized on Table 4. It is in particular important to note that, because the product of the decimation factor η with the size of the FFT *NdFFT* is not the same in both bands, the actual max OPD and thus the spectral sampling is not the exactly same in LWIR and MWIR.

	LWIR	**MWIR**
Decimation factor η	19	18
δOPD (nm)	721.216	
NdFFT	1211	1277
MaxOPD (mm)	0.8290380	0.8282447

Table 4: characteristics of the decimated interferograms

4.8 Bit-trimming

After the decimation, an additional data-reduction step is performed before the interferograms transmission through bit-trimming. This process takes advantage of the fact that the interferogram range is dependent on the sample number (i.e. on the optical path difference). As a consequence, for the spectral samples where the dynamic is low, a number of most significant bits (MSB) can be removed. Those MSB are necessarily equal to zeros.

The chosen technique is robust and simple. The data reduction rate is the same for all interferograms in the same band.

5 MTG-IRS ON-GROUND PROCESSING

5.1 Objectives and design

The objectives of the on-ground processing are to ensure that the spectra are radiometrically and spectrally calibrated and that the different calibrations and corrections are properly monitored.

As mentioned in the section 3.1, there are two types of measurements (named “modes”) that are handled separately: the normal mode illustrated on Figure 16and the imager mode on Figure 17.

5.1.1 Normal mode

The interferograms received from the satellite are decimated and compressed. The first step consists in decompressing the data. A light numerical apodisation is applied to reduce the extension of the SRF, followed by a Fourier transform on zero-padded interferograms to generate oversampled spectra, taking into account the aliasing induced by the on-board decimation. Oversampling the spectra is needed to ensure a proper spectral calibration. The choice to perform it at this stage has been made to minimise the number of Fourier transforms in the processing; furthermore, this prevents the introduction of any Gibbs effect that would be generated if the oversampling were performed after radiometric calibration.

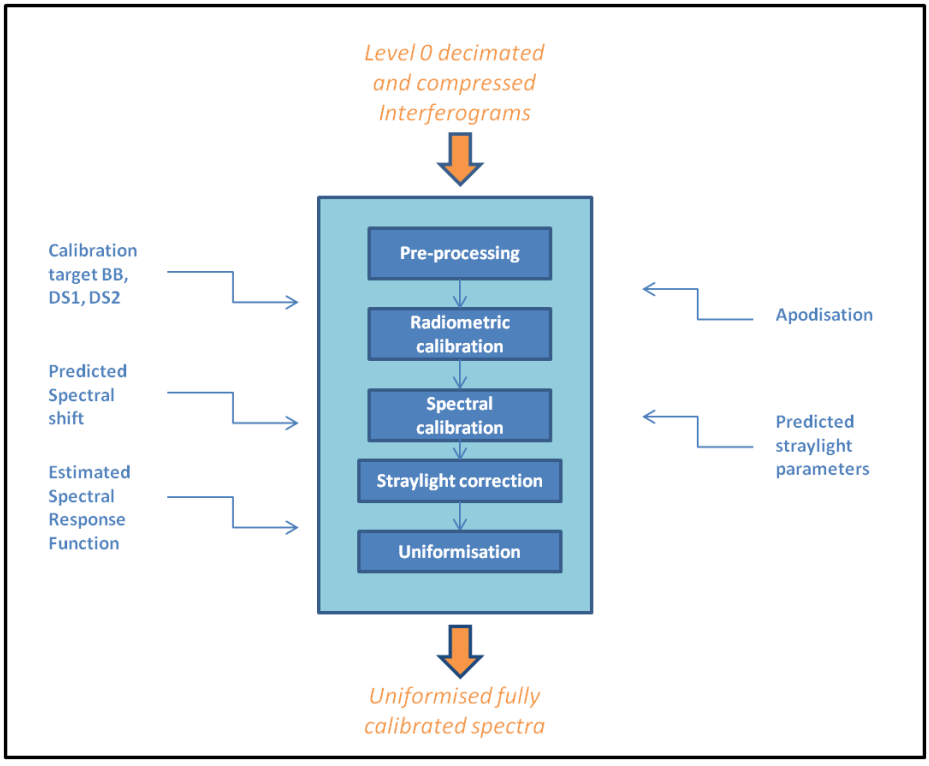

Figure 16: ground processing flow overview in normal mode (straylight correction and uniformisation are reversed)

The radiometric calibration cancels the instrument RTF and background signal to recover only the light entering the instrument. It is being performed before the spectral calibration and will thus act on oversampled spectra. This has an impact on the noise correlation: indeed, performing the oversampling before the radiometric calibration correlates the noise in a different way for each target involved in the radiometric calibration equation. On the other hand, oversampling after the radiometric calibration correlates the final noise.

The spectral calibration uses Earth spectra from a zone over the North-Atlantic in LAC4 to estimate the spectral scale error; this estimation is then used to spectrally correct the measured spectra in all dwells.

Then, we apply an uniformisation processing that will transform all pixels and channels spectral responses applying a single SRF that depends only on the numerical light apodisation.

Spectra are finally corrected from Sun straylight contamination if needed.

5.1.2 Imager mode

Bandwidth limitation imposes sending the high resolution broadband images from satellite to ground in 9 groups of 160x160 pixels, as presented on Figure 5, page 23. The first step of the processing is thus to reconstruct a single 480x480 pixels image. They are then radiometrically corrected using the gains and offsets computed from the BB, DS1 and DS2 images. An image of the detector uniformity is computed in parallel in order to check the health of the detector.

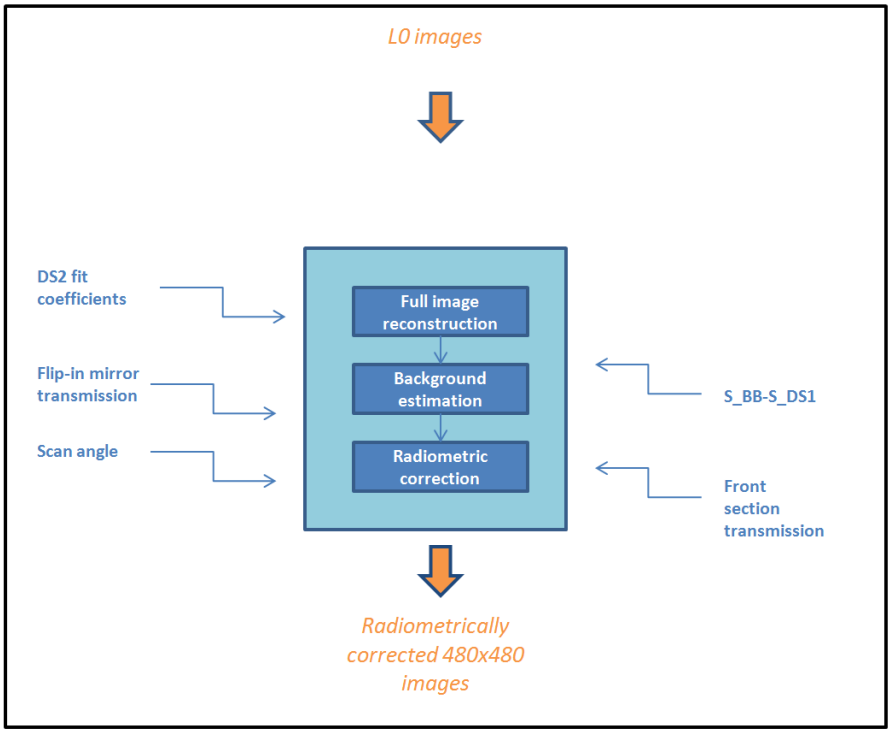

Figure 17: ground processing flow overview in imager mode

5.1.3 Wavenumber grids

The wavenumber grids evolves through the processing. At the radiometric calibration level (L1Ar), the grids are oversampled which is required for the spectral calibration. After the spectral calibration (L1Ars and L1B) we sample the spectra at exactly the Nyquist sampling given by the maximum OPD per band: $\delta\nu = \frac{1}{2\ OPD_{m,b}}$, it is the denser sampling achievable by a Fourier transform spectrometer.

Moreover, at each step, we gradually remove some spectral margins required for the processing. We finally reach the official output band limits at level 1B.

Parameters	Values	Comments
Maximum OPD MW: $\boldsymbol{OPD_{m,MW}}$	0.8282446861267 cm	
Maximum OPD LW: $\boldsymbol{OPD_{m,LW}}$	0.8290380239487 cm	

- **L1Ar**

The L1Ar grid on which is performed the radiometric calibration is defined as follow (LWIR, MWIR):

- Begin: 59200, 150000 m^{-1}
- End: 132167.2379295346, 227020.9733700643 m^{-1}
- Step: 8.908220965637232, 9.403122130394857 m^{-1}
- Length: 2^{13}, $2^{13} = 8192$

The wavenumber grid computations are described in section 5.3.1.3.

- **L1Ars**

The L1Ars grid on which the spectra are interpolated at the output of the spectral calibration is defined as follow (LWIR, MWIR):

- Begin: 63145.47522279918, 155147.3883895242 m^{-1}
- End: 125868.7743934770, 226865.3251236365 m^{-1}
- Step: 60.310864587190252, 60.368633614572616 m^{-1}
- Length: 1041, 1189

- **L1B**

The L1B grid is the final grid accessible to the users; it is output grid of the SRF and RTF uniformisation processing and we perform the straylight correction at this sampling (LWIR, MWIR),

- Begin: 67970.34438977440, 159976.8790786900 m^{-1}
- End: 121043.9052265018, 225054.2661151993 m^{-1}

- Step: 60.310864587190252, 60.368633614572616 m^{-1}
- Length: 881, 1079

NB: The L1B grid is a subset of the L1Ars grid, only some margins are removed.

To simplify the L1 data usage, the L1B grid can be computed using only multiples of the Nyquist wavenumber sampling, indeed:

- LW: $[1127:1:2087] \times \frac{1}{2\ OPD_{m,LW}}$
- MW: $[2650:1:3728] \times \frac{1}{2\ OPD_{m,MW}}$

We recommend to use at least 7 significate figures to define the wavenumbers.

5.2 Premises for the level 1 processing

This section lists the impacts of the on-board processing on the ground processing. It is thus assumed that:

- The on-board metrology system accurately estimates:
  - the optical path difference of each sample;
  - the position of the ZPD (Zero Path Difference).

  All interferograms are resampled on a common fixed OPD grid and are centred on the ZDP so that the phase error is minimized. This implies that:
  - The phase of all spectra is the same and the direction of movement of the interferometer plays no role. This simplifies the radiometric calibration estimation.
  - Spectral scaling is removed at first order. Only the residual spectral shift related to the interferometric axis displacements with respect to the sounding detector matrix and potential chromatism remains.

- The detector non-linearity has been corrected on board, so that the instrument can be considered linear in energy. It must be noted here that the non-linearity correction performed on board cannot be improved on ground for a lack of characterization elements.

- Spikes in the recorded interferograms have been detected and corrected on board. The affected interferograms will however be flagged.

5.3 Science processing for the normal mode

5.3.1 Pre-processing

Pre-processing is necessary to prepare the interferograms for the calibration. The core module of the pre-processing is a Fourier transform in order to transform interferograms into spectra.

However, before the Fourier transform, interferograms will be decompressed, apodized and zero-padded (Figure 18).

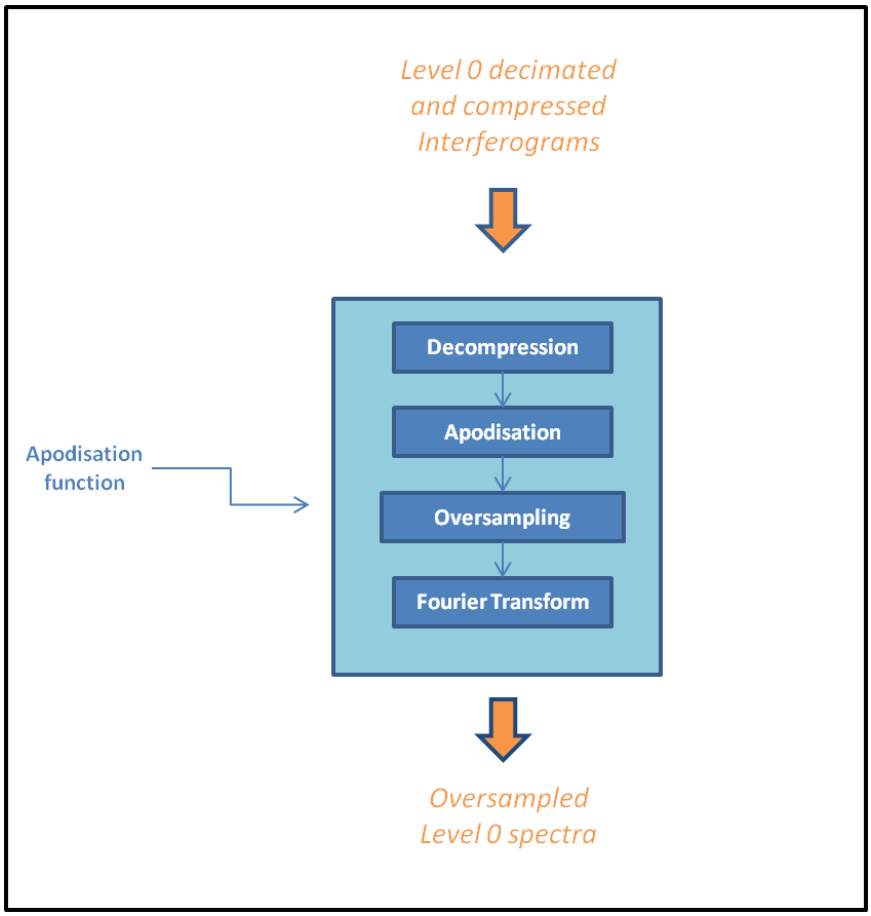

Figure 18: pre-processing in normal mode

5.3.1.1 Decompression

The decompression is classified by industry (TBC).

5.3.1.2 Apodisation

The aim of the numerical apodisation is to attenuate remote side lobes of the SRF. This operation is necessary because of the very low level of self-apodisation in MTG-IRS. If no numerical apodisation is applied, the SRF is close to a cardinal sine function with a very wide extension.

A wide SRF extension is problematic for several reasons:

- It implies computing and using the SRFs on a very wide range of wavenumbers, which considerably increases the computing power required to fully exploit IRS measurements. Typically, if there is no apodisation, the SRF has to be computed on a large spectral range covering the whole spectral bandwidth (MWIR or LWIR) plus a margin;
- It increases the sensitivity of the SRF to the radiometric response, with the following consequences:

- The radiometric response function has to be known on wide spectral range;
- It is required to know the radiometric response with a high accuracy. Indeed, without apodisation, all channels are affected by the radiometric response knowledge errors.
- It hinders the possibility of pixel grouping to reduce the number of radiometric response functions.

The numerical apodisation must be defined respecting several constraints:

- The spectral resolution requirement;
- The SRF shape error reduction;
- The impact on the radiometric noise;
- The limitation of the SRF extension.

Furthermore, the apodisation should be reversible.

Since most of the constraints depend on the maximum OPD, it is important to consider additional margins to account for the re-sampling and decimation processes. These margins prevent the degradation of the spectral resolution.

Several apodisations have been studied by industry taking all constraints into account but focusing on the spectral error due to the SRF truncation. The chosen apodisation is a gate function convolved with the Gaussian function, hereafter referred to as gauss-convolved window. It is defined as follows:

$$Apod(x) = \left[\mathrm{Gate}_{[-x_{gate}^{max},+x_{gate}^{max}]}(x) \otimes exp\left(-\frac{x^2}{2\sigma_x^2}\right)\right].\mathrm{Gate}_{[-x_a^{max},+x_a^{max}]}(x) \qquad \textit{Eq. 13}$$

where $x_{gate}^{max} = 0.8089\ \mathrm{cm}^{-1}$ is the width of the gate, $\sigma_x = 0.010666\ \mathrm{cm}^{-1}$ is the standard deviation of the Gaussian function and $x_a^{max}$is the width of the apodisation window (Figure 19) and corresponds to the maximum OPD after apodisation, namely 0.829 cm^{-1} in LWIR and 0.828 cm^{-1} in MWIR. This corresponds to a spectral sampling of 0.6031 cm^{-1} and 0.6039 cm^{-1} respectively in LWIR and MWIR respectively.

This light apodisation reduces the spectral bandwidth which lessens the effects of the radiometric response. On the other hand, it does not significantly attenuate the first lobes of the spectral response function, as shown on Figure 20 on which the functions are presented before normalisation. One can clearly see the impact on the spectral extension of the SRF, reducing the range from ± 40 cm^{-1} to ± 10 cm^{-1}. As expected, the spectral resolution is only slightly degraded.

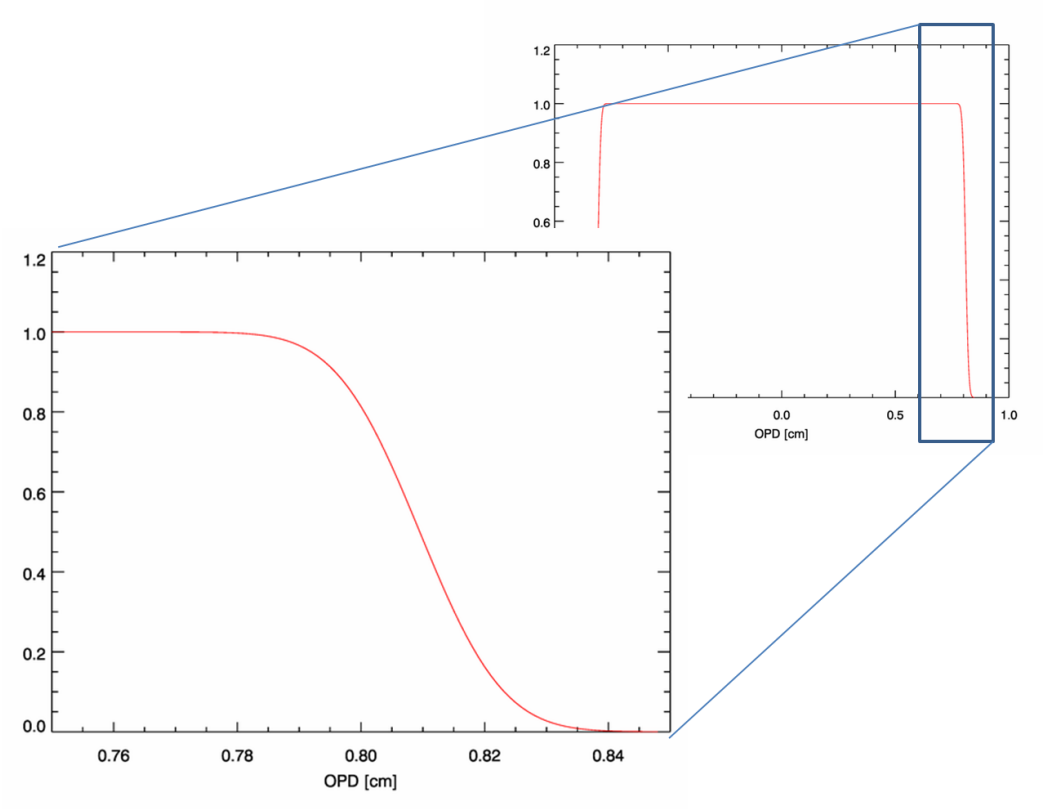

Figure 19: Aspect of the apodisation function

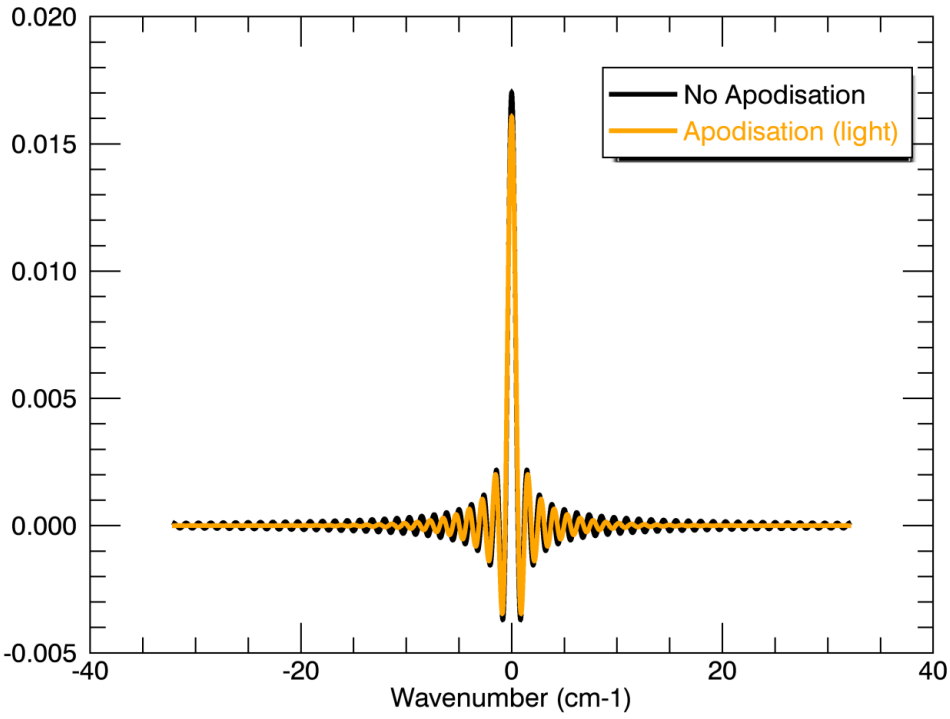

Figure 20: Effect of the apodisation on the spectral response function.

5.3.1.3 Oversampling

The oversampling is required by the spectral calibration process. It has been chosen to perform it along with the Fourier transform using the zero-padding approach, which consists in increasing artificially the definition domain of the interferogram by adding a number of zeros on each side. This yields a spectrum with a higher spectral sampling.

In the baseline algorithm, all interferograms are zero-padded with the same number of samples N_{L1} (namely 2^{13}). This value can be modified if necessary.

The expected wave-number steps becomes:

$$\delta\nu_b = \frac{1}{2\,(N_{L1}/2)\,\delta OPD\,D_b} = \frac{1}{N_{L1}\,\delta OPD\,D_b}$$

And the grid in the first Nyquist zone is:

$$\nu_b = \left(-\frac{N_{L1}}{2} : \frac{N_{L1}}{2} - 1\right) \times \delta\nu_b$$

NB: The number of samples before the zero-padding is odd and even after, therefore we have to add one more zero on the left than of the right of the vector. By chance, most of the fast FT routines does not interpret it as a ZPD shift in this case even if the vector symmetry is broken.

The zero-padding parameters are the following:

Parameters	Values	Comments
Length L1 : $\boldsymbol{N_{L1}}$	2^{13} =8192	
δOPD	721.216 nm	
Wave-number steps MWIR : $\boldsymbol{\delta\nu_{MW}}$	9.403122130394857 m^{-1}	
Wave-number steps LWIR : $\boldsymbol{\delta\nu_{LW}}$	8.908220965637232 m^{-1}	
Decimation: $\boldsymbol{D_b}$ (MW/LW)	18/19	

Table 5: Parameters zero-padding

5.3.1.4 Fourier transform

The Fourier transform is used to decompose a signal into the frequencies that make it up, a so-called spectrum. The latter is a complex function of the frequency, whose absolute value represents the amount of that frequency present in the original signal, and whose complex argument is the phase offset of the basic sinusoid in that frequency.

If the interferogram consists of *N* discrete equidistant points, one has to use the discrete version of the Fourier transform. Several implementations exist such as the one proposed by Cooley and Turkey [RD-7].

The FT processing is greatly sped-up if the number of samples have small prime decomposition factors, that is why we use a power of 2 for the sample numbers.

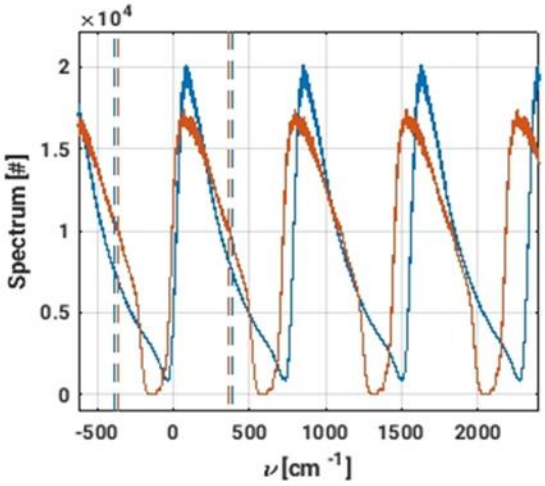

Figure 21: Representation of MWIR(blue) and LWIR(red) spectra, and first Nyquist zone (dotted lines).

5.3.1.5 Alias unfolding

In order to get an ordered spectrum, it is possible to either re-order the spectral sample after the FFT or to apply a phase gradient on the interferogram to slide its spectral components in the first Nyquist zone.

Indeed, applying a phase on the interferogram is equivalent to slide the spectrum:

$$FT\left[I(x) \times e^{-2i\pi\, \nu_{0,b}\, x_{dec}}\right](\nu) = FT[I(x)](\nu - \nu_0)$$

Caution: We apply a shift that places the first band channel on the Nyquisit zone centre therefore the right reordering is achieved only if the we do not apply the usual anf final *fftshit* reordering made in most coding languages (as matlab). Thus, we avoid the last usual step in the Fourier transform implementation.

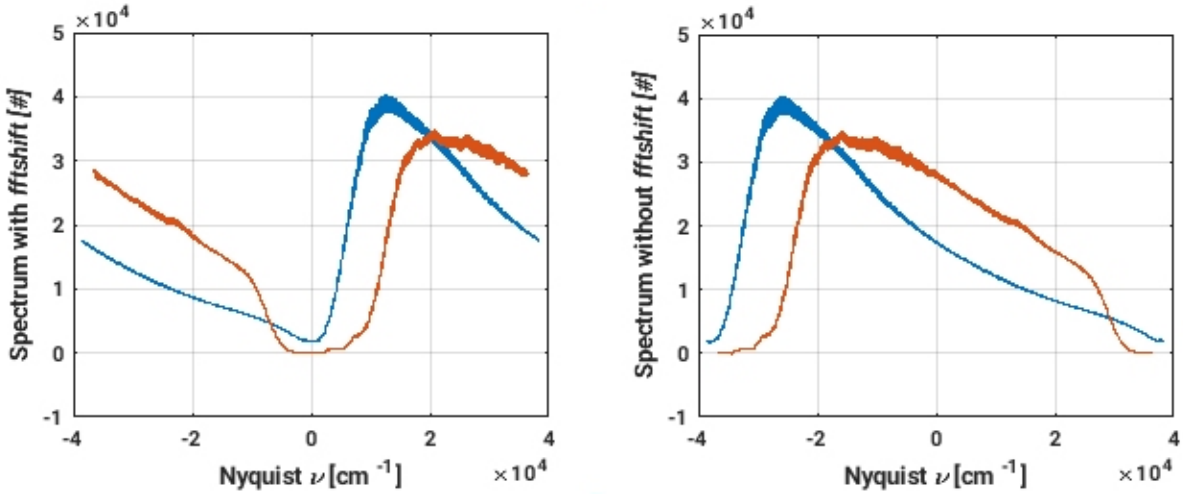

Figure 22: Spectra after phase gradient application with (left) and without (right) the usual ffthshift in the central Nyquist zone.

The slide amplitude ν_0 is chosen as the first channel of each bands:

Parameters	Values	Comments
Band centre MWIR : $\nu_{0,MW}$	150000 m^{-1}	
Band centre LWIR : $\nu_{0,LW}$	60000 m^{-1}	

Table 6: Parameters re-centring phase gradient

Finally, we redefine the wavenumber grids to reposition the Nyquist zone:

$$\nu = \nu_{0,b} + (0: N_{L1} - 1) \times \frac{1}{N_{L1} \times \delta_{OPD} \times D_b}$$

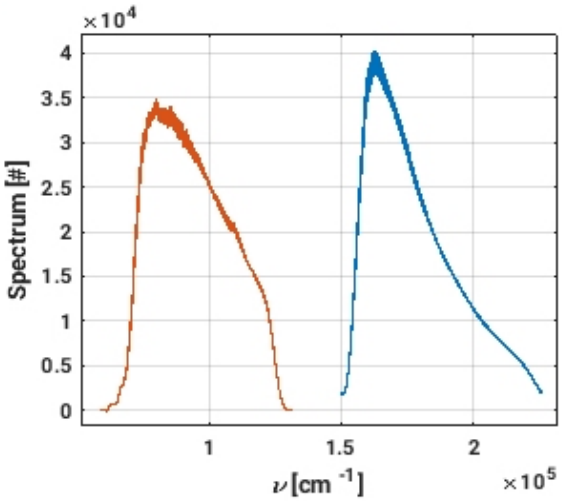

Figure 23: Spectra after phase gradient application without the usual ffthshift repositioned in wavenumbers

All the interferogram and related spectrum processing on-board and on-ground until the first spectrum generation is summed-up in the next figure:

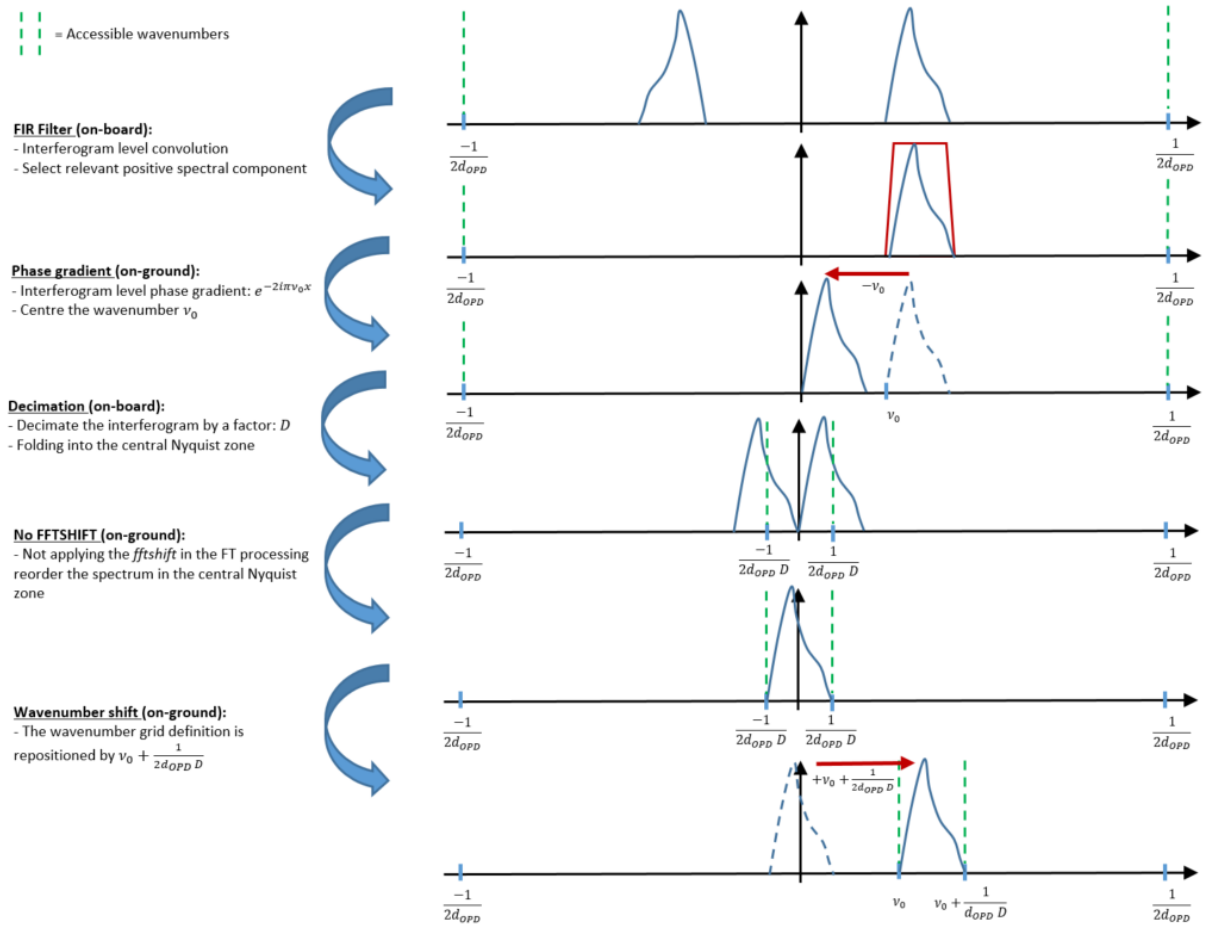

Figure 24: Spectrum evolution during the processing (the phase gradient is placed before the decimation for clarity)

5.3.2 Radiometric Calibration

The purpose of the radiometric calibration is to obtain the parameters of the calibration equation and to apply it for the conversion from raw data to a physically meaningful radiance. It is classically based on the measurement of both cold and hot blackbody (BB). The hot BB is an on-board unit at the ambient temperature of the instrument while the cold BB is a deep space view (DS).

IRS design is however such that the BB is located within the instrument, behind the front section of the telescope. The flip-in mirror (FIM) allows imaging either the BB or a dedicated DS that is hereafter referred to as DS1 (while the deep space view through the whole instrument is referred to as DS2). In order to radiometrically characterize the instrument, both the DS2 and the internal BB views are used, which slightly changes the radiometric calibration equation with respect to its classical form (as given for instance in RD-4).

The classical approach to the radiometric calibration consists in assuming that the instrument response is linear with respect to the incident radiance; a non-linearity correction is thus performed on board on the measured interferogram. If L_v^{EV} is the Earth radiance and $\widetilde{S_v^{EV}}$ the corresponding measured complex spectrum (in count), we can write:

$$L_v^{EV} = \widetilde{G(v)}\left[\widetilde{S_v^{EV}} - \widetilde{O(v)}\right] \qquad \textit{Eq. 14}$$

$\widetilde{G(v)}$ and $\widetilde{O(v)}$ are complex functions and are referred to as the gain, expressed in W/(m^2 sr m^{-1}) per count, and the offset, expressed in counts, respectively.

The first section will address the radiometric calibration correction that is performed for every science (Earth view) dwell (Figure 25). The following sections describe how the various parameters entering the radiometric equation are estimated with frequencies which range from 15 minutes to once a year. In the IRS terminology, this process is referred to as radiometric calibration estimation and is depicted on Figure 26.

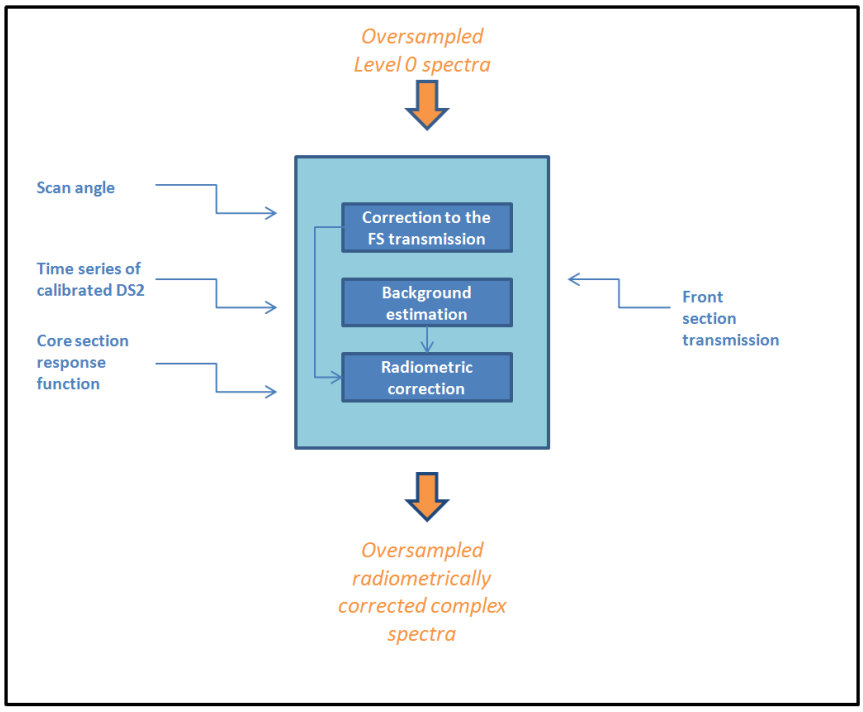

Figure 25: Overall flowchart of the radiometric calibration correction.

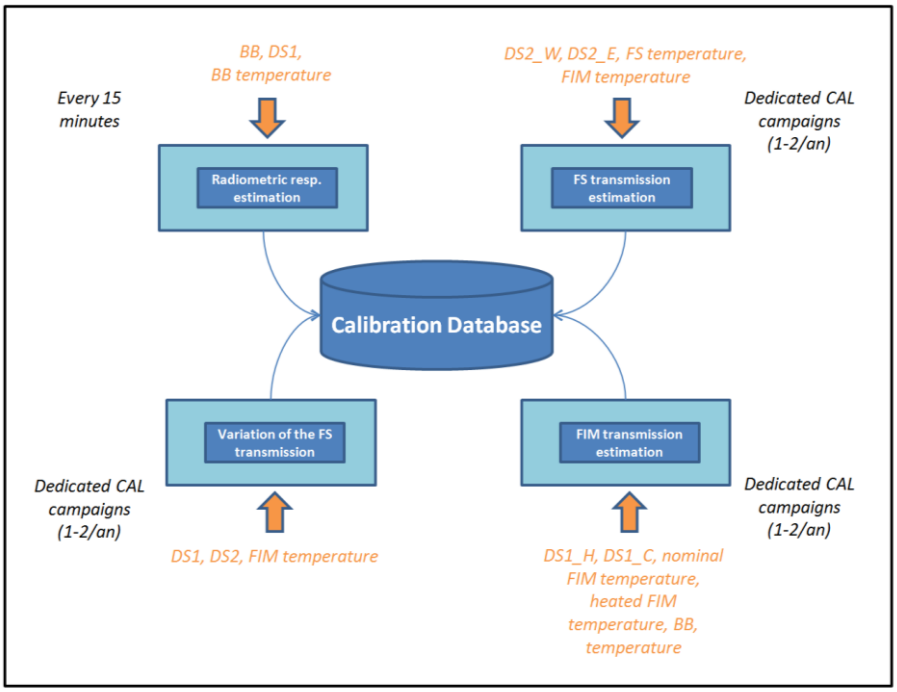

Figure 26: Overall flowchart of the radiometric calibration parameters estimation

Formally, interferograms and spectral radiances are Fourier transform pairs. Imperfections in the instrument will cause the measured interferograms to be asymmetric and consequently will cause the spectra used as input of the calibration process to be complex. Furthermore, emissions from the instrument (referred to as the "instrument background") will have an impact on the amplitude of the imaginary part of the measured spectrum. The observed phases of the Earth, deep space and blackbody views thus differ from each other; this effect is however taken into account thanks to the interferogram centring performed on board prior to the decimation.

5.3.2.1 Radiometric calibration equation

For each wavenumber, the deep space view spectrum acquired through the main telescope is, as a first approximation, written as:

$$\widetilde{S_\nu^{DS2}} = \widetilde{R_\nu}(\tau_\nu^{CS} L_\nu^{FS} + L_\nu^{CS}) + N_\nu^0 \qquad \textit{Eq. 15}$$

where $\widetilde{R_\nu}$ is the gain of the detection chain, N_ν^0 its offset, τ_ν^{CS} is the core section transmission, L_ν^{CS} is the radiance emitted by the core section and L_ν^{FS} is the radiance emitted by the front section.

Similarly, the deep space view spectrum is acquired at the level of the blackbody is:

$$\widetilde{S_\nu^{DS1}} = \widetilde{R_\nu}(\tau_\nu^{CS} L_\nu^{FIM} + L_\nu^{CS}) + N_\nu^0 \qquad \textit{Eq. 16}$$

And the blackbody spectrum is:

$$\widetilde{S_\nu^{BB}} = \widetilde{R_\nu}(\tau_\nu^{CS}(\rho_\nu^{FIM} L_\nu^{BB} + L_\nu^{FIM}) + L_\nu^{CS}) + N_\nu^0 = \widetilde{R_c(\nu)}\rho_\nu^{FIM} L_\nu^{BB} + \widetilde{S_\nu^{DS1}} \quad \textit{Eq. 17}$$

with L_ν^{FIM} is the radiance of the flip-in mirror, ρ_ν^{FIM} the reflectivity of the flip-in mirror, L_ν^{BB} the radiance of the blackbody and $\widetilde{R_c(\nu)} = \widetilde{R_\nu}\tau_\nu^{CS}$ is the core section response.

Then the measured spectrum can be written:

$$\widetilde{S_\nu^{EV}} = \widetilde{R_\nu}(\tau_\nu^{CS}(\tau_\nu^{FS} L_\nu^{EV} + L_\nu^{FS}) + L_\nu^{CS}) + N_\nu^0 = \widetilde{R_c(\nu)}\tau_\nu^{FS} L_\nu^{EV} + \widetilde{S_\nu^{DS2}} \quad \textit{Eq. 18}$$

The calibration equation can thus be written:

$$\widetilde{L_\nu^{EV}} = \frac{1}{\tau_\nu^{FS}} \frac{\widetilde{S_\nu^{EV}} - \widetilde{S_\nu^{DS2}}}{\widetilde{R_c(\nu)}} \quad \textit{Eq. 19}$$

with

$$\widetilde{R_c(\nu)} = \frac{\widetilde{S_\nu^{BB}} - \widetilde{S_\nu^{DS1}}}{\rho_\nu^{FIM} L_\nu^{BB}} \quad \textit{Eq. 20}$$

The polarization properties of the scan mirror impact the transmission of the front section (section 5.3.2.4); it has been shown by the instrument manufacturer that the impact on the transmission of these properties depends linearly on the scan mirror angle α. A correction term $\Delta\tau_\nu^{FS}(\alpha)$ is thus introduced such as:

$$\Delta\tau_\nu^{FS}(\alpha) = \frac{\alpha - \alpha^E}{\alpha^W - \alpha^E} \varrho_\nu^{FS} \quad \textit{Eq. 21}$$

The calibration equation is thus re-written:

$$\widetilde{L_\nu^{EV}} = \frac{1}{\tau_\nu^{FS} + \Delta\tau_\nu^{FS}(\alpha)} \frac{\widetilde{S_\nu^{EV}} - \widetilde{S_\nu^{DS2}}}{\widetilde{R_c(\nu)}} = \frac{1}{\tau_\nu^{FS} + \Delta\tau_\nu^{FS}(\alpha)} \left(\frac{\widetilde{S_\nu^{EV}}}{\widetilde{R_c(\nu)}} - \widetilde{L_\upsilon^{BG}} \right) \quad \textit{Eq. 22}$$

In which the background of the instrument is:

$$\widetilde{L_\upsilon^{BG}} = \frac{\widetilde{S_\nu^{DS2}}}{\widetilde{R_c(\nu)}}$$

By identification with Eq. 14, the gain $\widetilde{G(\nu)}$ is:

$$\widetilde{G(\nu)} = \frac{1}{\tau_\nu^{FS} + \Delta\tau_\nu^{FS}(\alpha)} \frac{1}{\widetilde{R_c(\nu)}} = \frac{\rho_\nu^{FIM}}{\tau_\nu^{FS} + \Delta\tau_\nu^{FS}(\alpha)} \frac{L_\nu^{BB}}{\widetilde{S_\nu^{BB}} - \widetilde{S_\nu^{DS1}}} \quad \textit{Eq. 23}$$

and the offset is:

$$\widetilde{O(\nu)} = \widetilde{S_{\nu}^{DS2}} \qquad \textit{Eq. 24}$$

It is worth to note that:

- $\widetilde{L_{\nu}^{EV}}$ is a complex quantity: its phase φ corresponds to the residual error due to instrumental noise and possible errors in the on-board, L0 to L1 and radiometric correction processing;
- The real part of $\widetilde{L_{\nu}^{EV}}$ is the radiometrically corrected spectrum that will then be used in further processing (i.e. spectral calibration).
- The imaginary part of $\widetilde{L_{\nu}^{EV}}$ is directly proportional to the residual phase: $\mathrm{Im}\left\{\widetilde{L_{\nu}^{EV}}\right\} \approx \left|\widetilde{L_{\nu}^{EV}}\right|\varphi$. The imaginary part of the radiometric equation output is thus a powerful indicator of any errors in the processing. For this reason, it will be used for monitoring purposes.

The above equation assumes that:

- **the instrument is linear in energy**. Therefore a non-linearity correction is performed on-board.
- **the phase of all spectra in the radiometric equation is the same** (or that the difference is negligible). The metrology system within the instrument allows to precisely estimate the optical path difference of each sample and thus to minimize the phase error when resampling the interferograms on a common fixed grid;
- **The interferograms do not depend on the cube-corner motion direction**. This is the case if the metrology processing allows an accurate estimation of apex position and if the departures with respect to an ideal instrument are corrected. Residuals are supposed negligible;

In order to perform the radiometric calibration of a IRS raw spectrum, it is thus necessary to know:

- The radiometric response of the core section $\widetilde{R_c(\nu)}$;
- The instrument background $\widetilde{L_{\upsilon}^{BG}} = \widetilde{S_{\nu}^{DS2}} \Big/ \widetilde{R_c(\nu)}$;
- The transmission of the front section τ_{FS} (characterized on ground, checked during the commissioning and regularly during the lifetime of the instrument using dedicated DS1 and DS2 measurements);
- The variation of the transmission of the front section with the scan angle $\Delta\tau_{FS}(\alpha)$ (characterized on ground, checked during the commissioning and regularly during the lifetime of the instrument using dedicated DS1 and DS2 measurements);
- The angle of the scan mirror for the considered dwell;
- The actual wavenumber scale if the spectral calibration has not been performed prior to the radiometric correction (will be used to compute the Planck function on the correct wavenumber grid). This comes from the previous spectral estimation step.

Only the determination of the instrument background is performed for each dwell from series of DS2 measurements (section 5.3.2.6); the other parameters are extracted from the radiometric calibration database where they have been stored after their computation that occurs:

- Between each LAC (i.e. every 15 minutes) for the determination of the radiometric response of the instrument (section 5.3.2.2);
- Every time the parameters of the spectral calibration are estimated (normally over a pre-defined region - over the Atlantic - of LAC4) i.e. every 30 minutes for the wavenumber grid (section 5.3.3);
- During dedicated calibration campaigns (with a frequency that is still to be determined when the instrument characterization will be known but that is estimated to be of the order of once a year) for the transmission of the front section and the transmission of the scan mirror (sections 5.3.2.3 and 5.3.2.5).

In some cases (for example for the offline radiometric noise characterization, see section 7.3.6), it is necessary to calibrate the blackbody measurements. From Eq. 17 we have then:

$$\widetilde{L_{meas}^{BB}} = \frac{1}{\rho_\nu^{FIM}} \frac{\widetilde{S_\nu^{BB}} - \widetilde{S_\nu^{DS1}}}{\widetilde{R_c(\nu)}} \qquad \textit{Eq. 25}$$

5.3.2.2 Characterization of the radiometric response of the core section

The estimation of the radiometric response of the core section of the instrument (i.e. the part between the Flip-in Mirror and the interferometer) is based on the observation of the internal blackbody and on DS1 views via the flip-in mirror. There is at the moment only little information available on the stability in time of the radiometric response and on the timescale of its variation. In theory the characterization can be performed between each LAC, when the BB and DS1 views are acquired, i.e. every 15 minutes. It is however improbable that the radiometric response varies over such a short time range and the radiometric response could thus be averaged in time over $n_{cal_{ev}}$calibration events (which value is to be defined) in order to reduce noise.

As seen in section 5.3.2.1, the complex radiometric response of the core section of the instrument $\widetilde{R_c(\nu)}$ is given by:

$$\widetilde{R_c(\nu)} = \frac{\widetilde{S_\nu^{BB}} - \widetilde{S_\nu^{DS1}}}{\rho_\nu^{FIM} L_\nu^{BB}}$$

where $\widetilde{S_\nu^{BB}}$ and $\widetilde{S_\nu^{DS1}}$ are the complex raw spectra of the on-board BB and DS1 respectively, L_ν^{BB} is the radiance of the blackbody and ρ_ν^{FIM} is the flip-in mirror (FIM) reflectivity. In order to remove noise and increase accuracy, an average can be performed over a pre-defined number of calibration events $n_{cal_{ev}}$. To do so, the radiometric response computed during each calibration event is archived in the calibration database as a rolling archive (only the $n_{cal_{ev}}$ most recent estimations of $\widetilde{R_c(\nu)}$ are kept).

The computation of L_ν^{BB} requires both the knowledge of the temperature of the blackbody (determined from the measurements of n_{BB_t} sensors) as well as a model of the effective radiance of the blackbody as a function of the temperature L_ν^{BB} given by:

$$L_\nu^{BB} = \varepsilon_\nu^{BB}\mathcal{P}(T_{BB},\nu) + (1-\varepsilon_\nu^{BB})L_\nu^{ext} \qquad \textit{Eq. 26}$$

where ε_ν^{BB} is the emissivity of the blackbody cavity and L_ν^{ext} is the radiance entering the cavity. The **baseline** is to assume that the blackbody is perfect i.e. $\varepsilon_\nu^{BB} = 1$. We have then:

$$L_\nu^{BB} = \mathcal{P}(T_{BB},\nu) \qquad \textit{Eq. 27}$$

This could possibly be replaced by a more accurate computation if provided by the supplier of the blackbody. Furthermore, L_ν^{BB} must be evaluated on the same spectral grid on which the measured spectra are (i.e. before spectral calibration) using the spectral shift determined in the previous spectral calibration estimation.

5.3.2.3 Characterization of the transmission of the front section

The transmission of front section is expected to be stable in time. It will be measured on-ground and will be stored in the calibration database as the default value. However, further characterizations will be performed in-flight during the commissioning and during the lifetime of the instrument with a frequency of about once a year (frequency that can be adapted as required). This characterization is thus not part of the routine operations.

The characterization will be performed at a given scan angle, knowing that the dependency of the transmission with the scan angle is taken into account in the radiometric calibration (Eq. 22).

The emission of the front section can be written:

$$L_\nu^{FS} = \varepsilon_\nu^{FS}\mathcal{P}(T_{FS},\nu) \qquad \textit{Eq. 28}$$

where ε_ν^{FS} is the emissivity and T_{FS} the temperature of the front section. Assuming that $\tau_\nu^{FS} = 1-\varepsilon_\nu^{FS}$, the transmission is then:

$$\tau_\nu^{FS} = 1 - \frac{L_\nu^{FS}}{\mathcal{P}(T_{FS},\nu)} \qquad \textit{Eq. 29}$$

From section 5.3.2.1, the radiance of the front section can be deduced from the two deep space views:

$$L_\nu^{FS} = \frac{\widetilde{S_\nu^{DS2}} - \widetilde{S_\nu^{DS1}}}{\widetilde{R_c(\nu)}} + L_\nu^{FIM} \qquad \textit{Eq. 30}$$

With $L_\nu^{FIM} = (1-\rho_\nu^{FIM})\mathcal{P}(T_{FIM},\nu)$ being the radiance emitted by the flip-in mirror. The transmission of the front section can thus be written:

$$\tau_\nu^{FS} = 1 - \frac{Re\left\{\frac{\widetilde{S_\nu^{DS2}} - \widetilde{S_\nu^{DS1}}}{\widetilde{R_c(\nu)}}\right\} + (1-\rho_\nu^{FIM})\mathcal{P}(T_{FIM},\nu)}{\mathcal{P}(T_{FS},\nu)} \qquad \textit{Eq. 31}$$

The front section including several mirrors (scanning mirror M0 and mirrors M1 and 2) of possibly significantly different temperatures (see Figure 11), the temperature of the front section T_{FS} is thus an average of the temperature of the various mirrors weighted by their relative contribution to the radiance of the front section i.e. their emissivity:

$$T_{FS} = \frac{(1-\tau_{M0})T_{M0}\tau_{M1}\tau_{M2} + (1-\tau_{M1})T_{M1}\tau_{M2} + (1-\tau_{M2})T_{M2}}{(1-\tau_{M0})\tau_{M1}\tau_{M2} + (1-\tau_{M1})\tau_{M2} + (1-\tau_{M2})} \qquad \textit{Eq. 32}$$

where T_{M0}, T_{M1} and T_{M2} are the temperatures and τ_{M0}, τ_{M1} and τ_{M2} are the reflectivities of the mirrors M0 (scan mirror), M1 and M2, respectively.

5.3.2.4 Characterization of the variation of the transmission of the front section

Polarization properties of the various elements in the IRS optical path impact the propagation of light within the instrument. Simulations have in particular shown that the transmission of the front section depends on the angle of the line-of-sight due to the properties of the coating of the scan mirror. A correction is thus to be applied to the value of the transmission of the front section $\tau_{FS}(\nu)$ that depends on the scan angle of the mirror M0.

The characterization of the scan reflectivity law of the scan mirror will be performed on-ground during in the instrument testing then in-flight during the commissioning and during the lifetime of the instrument with a frequency of about once a year (frequency that can be adapted as required). This characterization is thus not part of the routine operations.

It is based on measurements of DS2 taken at two opposite scan angles: indeed it has been verified by simulations that the variation of the transmission due to polarization effects occurs mainly between the far east and west dwells and is close to be linear (the difference between a linear variation of the transmission and the simulated one is at most 0.1% in LWIR and at most 0.001% in MWIR).

The reflectivity values for intermediate scan angles will be determined by linear interpolation:

$$\varrho_{\nu}^{FS} = \frac{\mathrm{Re}\left\{\frac{\widetilde{S_{\nu}^{DS2,W}} - \widetilde{S_{\nu}^{DS2,E}}}{\widetilde{R_c}}\right\}}{\mathcal{P}(T_{FS},\nu)} \qquad \textit{Eq. 33}$$

where $\widetilde{S_{\nu}^{DS2,E}}$ is a spectra recorded on the East side of the detector and $\widetilde{S_{\nu}^{DS2,W}}$ is recorded on the west side. Both spectra (or series of spectra) must be recorded within a short period of time so that the thermal background of the instrument can be assumed to be constant, and/or during a time of the year when the thermal background of the instrument is stable and does not exhibit large variations in time.

It can be noted that both $\widetilde{S_{\nu}^{DS2,E}}$ and $\widetilde{S_{\nu}^{DS2,W}}$ can be contaminated by Earth straylight. However, when recorded within a sufficiently short period of time, the magnitude of this contamination is the same on both sides of the Earth and thus cancels out in Eq. 33.

5.3.2.5 Characterization of the flip-in mirror

We have seen in section 5.3.2.2 that the radiance detected by the instrument when looking at the DS1 port is:

$$\widetilde{S_\nu^{DS1}} = \widetilde{R_\nu}(\tau_\nu^{CS} L_\nu^{FIM} + L_\nu^{CS}) + N_\nu^0$$

If the flip-in mirror is at temperature T_{FIM_H} we have $L_\nu^{FIM} = \varepsilon_\nu^{FIM}\mathcal{P}(T_{FIM\_H}, \nu)$ and

$$\widetilde{S_\nu^{DS1\_H}} = \widetilde{R_\nu}\left(\tau_\nu^{CS}\varepsilon_\nu^{FIM}\mathcal{P}(T_{FIM\_H}, \nu) + L_\nu^{CS}\right) + N_\nu^0 \qquad \textit{Eq. 34}$$

If we do another measurement when the flip-in mirror is at temperature T_{FIM_C} we have:

$$\widetilde{S_\nu^{DS1\_C}} = \widetilde{R_\nu}\left(\tau_\nu^{CS}\varepsilon_\nu^{FIM}\mathcal{P}(T_{FIM\_C}, \nu) + L_\nu^{CS}\right) + N_\nu^0 \qquad \textit{Eq. 35}$$

By taking the difference, we get:

$$\widetilde{S_\nu^{DS1_H}} - \widetilde{S_\nu^{DS1_C}} = \widetilde{R_\nu}\tau_\nu^{CS}\varepsilon_\nu^{FIM}\left(\mathcal{P}(T_{FIM_H}, \nu) - \mathcal{P}(T_{FIM_C}, \nu)\right) \qquad \textit{Eq. 36}$$

Or

$$\widetilde{S_\nu^{DS1_H}} - \widetilde{S_\nu^{DS1_C}} = \widetilde{R_c}\varepsilon_\nu^{FIM}\left(\mathcal{P}(T_{FIM_H}, \nu) - \mathcal{P}(T_{FIM_C}, \nu)\right) \qquad \textit{Eq. 37}$$

By substituting the expression for the core section radiometric response from section 5.3.2.2, we have then:

$$\frac{\widetilde{S_\nu^{DS1_H}} - \widetilde{S_\nu^{DS1_C}}}{\mathcal{P}(T_{FIM_H}, \nu) - \mathcal{P}(T_{FIM_C}, \nu)} = \frac{\widetilde{S_\nu^{BB}} - \widetilde{S_\nu^{DS1_C}}}{L_\nu^{BB}}\frac{\varepsilon_\nu^{FIM}}{\rho_\nu^{FIM}} \qquad \textit{Eq. 38}$$

Since $\varepsilon_\nu^{FIM} + \rho_\nu^{FIM} = 1$ we have finally:

$$\rho_\nu^{FIM} = \frac{1}{1 + \dfrac{\widetilde{S_\nu^{DS1_H}} - \widetilde{S_\nu^{DS1_C}}}{\mathcal{P}(T_{FIM_H}, \nu) - \mathcal{P}(T_{FIM_C}, \nu)}\dfrac{L_\nu^{BB}}{\widetilde{S_\nu^{BB}} - \widetilde{S_\nu^{DS1_C}}}} \qquad \textit{Eq. 39}$$

The characterization of the flip-in mirror will thus require a procedure in which DS1 views are measured both with the flip-in mirror at nominal temperature (T_{FIM_C}) and when it is heated (T_{FIM_H}). Measurements (or series of measurements) of the DS1 must be performed closely in time so that the emission of the core section (L_ν^{CS}) is not changing significantly. It is expected to perform this characterization once a year. This characterization is thus not part of the routine operations.

5.3.2.6 Estimation of the instrument background

An accurate knowledge of the so-called instrument background is a requisite for radiometrically correcting the measured raw spectra. Measurements of the instrument

background are performed regularly through deep space views (named DS2 in the IRS terminology) and stored in the calibration database. The background to be applied to each dwell is then determined from this series of DS2 measurements.

A straightforward approach consists in interpolating between two consecutive DS2 views to get the background of the considered dwell; this however implies to wait until a DS2 view is acquired to process a series of Earth views and thus to delay the processing. It is thus proposed to forecast of the instrumental background from past measurements as described in the following.

A simulation of time evolution of the instrument background over one day is shown on Figure 27. It is characterized by a sharp increase around midday followed by a slow decay during the second half of the day. The amplitude of the peak depends on the relative position of the Sun with respect to the satellite (i.e. on the day of the year) and is maximum 25 days before and after the equinoxes.

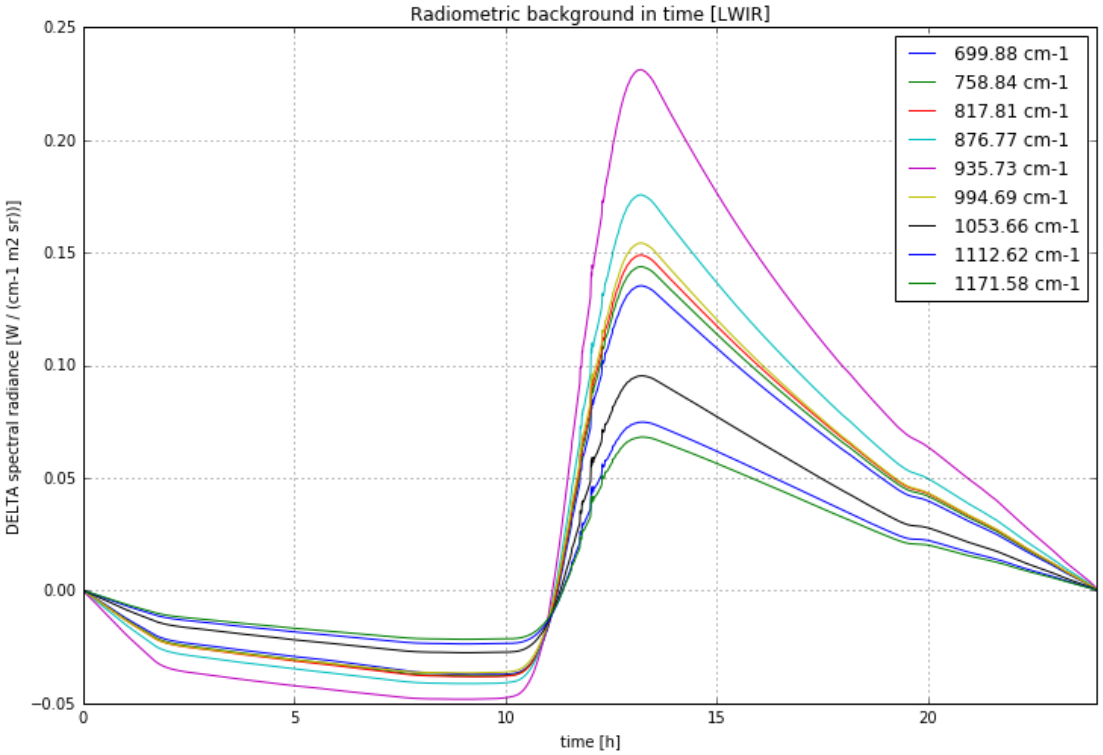

Figure 27: simulated time evolution of the instrument background for several wavenumbers of the LWIR band, over day 56 of the year (data from ESA). Negative values correspond to backmodulated radiance from the back of the interferometer.

It is worth recalling that the DS2 views are performed at the beginning of each line but the first one of each LAC that is at most every 3 minutes. The frequency of the sampling is thus much higher than the typical timescale of the signal variations. For this reason, it is thus possible to estimate the value of the DS2 at any time between two real DS2 measurements. The method presented here consists in a linear fit over the previous measurements; the use of a Kalman filter, which has been considered, has been discarded (see Appendix A).

Given the slow time variations of the signal with respect to the sampling frequency, the signal can be assumed to be linear over periods of the order of 10 minutes (the only exception being the vicinity of the daily peak). The most natural predictor consists thus in applying a linear regression over the past measurements of the DS2 to estimate the value at time *t*.

The problem consists thus in fitting a set of N_{DS2} noisy measurements $\widetilde{L_\nu^{DS2}}(t_i,\nu)$ with a standard deviation $\widetilde{\sigma_\nu}(t_i,\nu)=\widetilde{\sigma_\iota}$ to a straight line model such that:

$$\widetilde{L_\nu^{DS2}}(t,\nu)=\tilde{A}(\nu)+\tilde{B}(\nu)t \qquad \textbf{Eq. 40}$$

The merit function is the chi-square function:

$$\chi^2=\sum_{i=1}^{N_{DS2}}\left(\frac{\widetilde{L_\iota}-\tilde{A}-\tilde{B}t_i}{\widetilde{\sigma_\iota}}\right)^2 \qquad \textbf{Eq. 41}$$

Then, by defining

$$\tilde{\xi}=\sum_{i=1}^{N_{DS2}}\frac{1}{\widetilde{\sigma_\iota^2}} \qquad \widetilde{\xi_t}=\sum_{i=1}^{N_{DS2}}\frac{t_i}{\widetilde{\sigma_\iota^2}} \qquad \widetilde{\xi_L}=\sum_{i=1}^{N_{DS2}}\frac{\widetilde{L_\iota}}{\widetilde{\sigma_\iota^2}}$$

and

$$\widetilde{q_\iota}=\frac{1}{\widetilde{\sigma_\iota}}\left(t_i-\frac{\widetilde{\xi_t}}{\tilde{\xi}}\right)$$

as well as

$$\widetilde{\xi_{qq}}=\sum_{i=1}^{N_{DS2}}\widetilde{q_\iota^2}$$

the coefficients of the straight line are

$$\tilde{B}=\frac{1}{\widetilde{\xi_{qq}}}\sum_{i=1}^{N_{DS2}}\frac{\widetilde{q_\iota}\widetilde{L_\iota}}{\widetilde{\sigma_\iota}} \qquad \tilde{A}=\frac{\widetilde{\xi_L}-\widetilde{\xi_t}\tilde{B}}{\tilde{\xi}} \qquad \textbf{Eq. 42}$$

The number of DS2 views used to estimate the background is a tuneable parameter and should be chosen with care:

- If it's too small the estimation is sensitive to noise but is able to better capture small scale variations;
- If it's too large, the noise sensitivity is lessened but rapid time variations of the signal are missed.

Simulations have however shown that the noise on the DS2 measurements is of the order of 0.1%. N_{DS2} can thus be kept to a relatively small value. Note that DS2 measurements are continuous and not attached to any LAC so that there is no special conditions at the beginning of each LAC. On the other hand, DS2 measurements affected by straylight are excluded from the computation; straylight-contaminated measurements are defined by measurements for

which the Sun is less than 3 degrees from the line-of-sight (value to be confirmed during the commissioning).

5.3.3 Spectral calibration

The role of the spectral calibration process is to correct the spectral positions of the measured spectra to absolute calibrated values. Each pixel of the IRS detector is seen with a different spectral scale due to the off-axis as well as other instrument effects [RD-27]. Due to this scale variation, which is only nominal for a perfectly symmetric pixel centred on the interferometric axis, each spectral samples of the spectra will be measured at an apparent wavenumber different from the true wavenumber expected. The shift of each apparent spectral sample is linear with respect to the wavenumber, which is why the use of "spectral scale" or "spectral scaling factor" is preferred to the use of "offset".

As described in section 4.6, an implicit spectral calibration is performed on board when the interferograms are resampled on a common fixed OPD grid. This is however not sufficient to accurately complete the spectral calibration especially because the onboard metrology system gives no information about the position of the interferometric axis with respect to the detector arrays. In the case of IRS, the shift of the interferometric axis mostly affects the spectral scaling, more than in the case of IASI as discussed in section 3.5. Furthermore, the onboard metrology is not immune to mismatches and changes between the laser beam and the science beam, or to changes of rear-optics PSF[4] centroids due to opto-mechanical and thermal effects. Thus, in order to achieve the required absolute knowledge of the spectral scale, an onground spectral calibration is necessary [RD-28].

The optical effects, including lateral chromatic aberrations, coupled with thermal distortion of the system also introduce higher-order effects to the apparent spectral sampling of the measured spectra. These effects, which are in large part unpredictable and difficult – if not impossible – to model, introduce deviations from the first order spectral scaling effect. These spectrally-dependant deviations are defined as chromatism offsets. The effect on the spectral scaling factor and of the chromatism offsets is illustrated in Figure 28.

[4] Here, the PSF of the global optical system are not relevant. Only the PSF of the optical system between the detector arrays and the spectrometers, which have an impact on the relation between space in the detector domain and angles in the interferometer domain. This is defined here as rear-optics PSF.

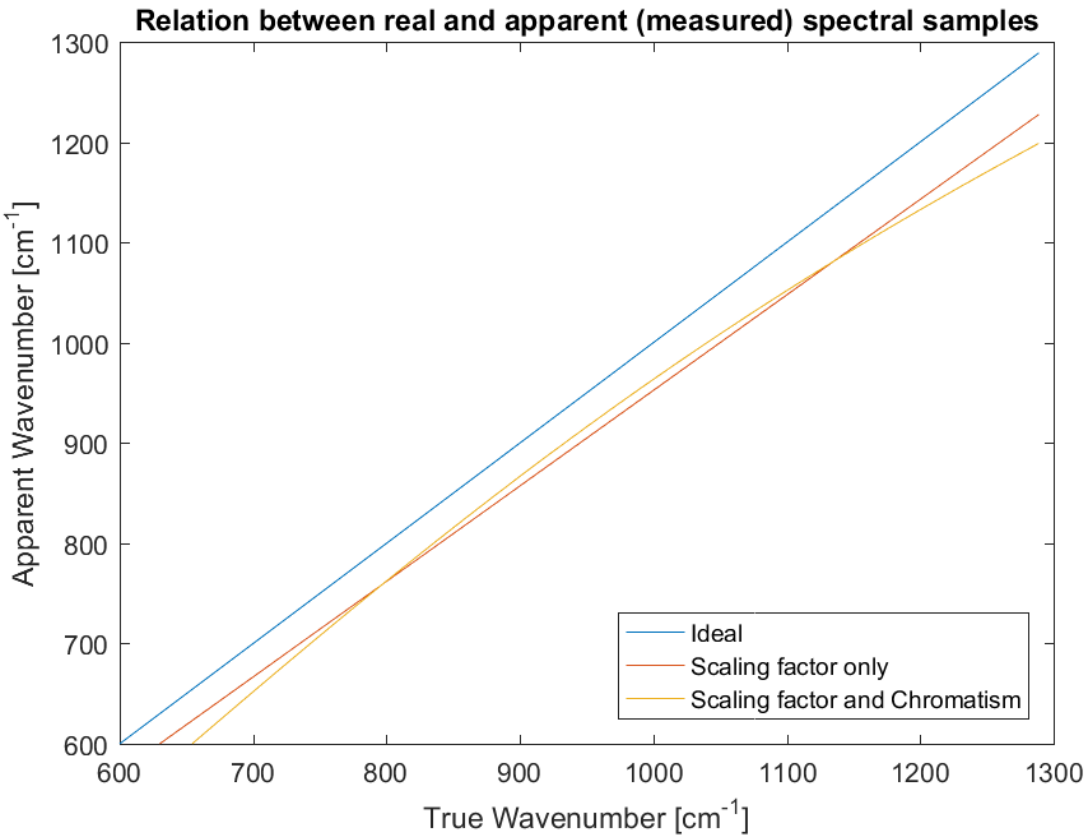

Figure 28: Illustration of the effect of the spectral scale factor and of chromatism offsets on the relation between the true wavenumber grid and the apparent (or measured) wavenumber grid. For illustration purposes, the scale factor and the chromatism offsets have been highly exaggerated. The apparent offset between the blue and the orange lines is in fact a change in the slope, with both lines intersecting at 0 cm-1.

Industrial analysis showed that the expected chromatism offsets could introduce errors to the spectral sample position knowledge, which exceed the overall budget for the spectral calibration. Hence, the chromatism must be corrected by the spectral calibration approach. Fortunately, the higher-order effects are expected to vary slowly and the correction will be based on extensive on-ground characterisation updated after launch during commissioning. Regular characterisation is nevertheless possible if the monitoring of chromatism shows a faster than expected variation.

The on-board spectral calibration, thereafter referred to as interferogram re-sampling, uses the *a-priori* knowledge of the relative position of every pixel combined with information from the metrology system to align the interferograms and bring them on a common OPD scale, correcting the off-axis effect on the focal plane array. This is made under the assumption that the relation between the detector arrays and the laser system or the spectrometer is stable and that the relations between the pixels within the arrays themselves are stable. The spectral content of the measurement itself is not used in this process; the re-sampling is only based on auxiliary measurement systems and model information of the instrument.

The on-ground spectral calibration, thereafter simply referred to as spectral calibration, uses spectral information from selected Earth view scenes to provide information about the

spectral scale shift and to correct all measured spectra for this shift. The spectral positions are estimated from the spectral content of dwells on a per-pixel basis. A simplified overview of the process path of a dwell from measurement to fully calibrated spectra with emphasis on the spectral calibration is shown in Figure 29.

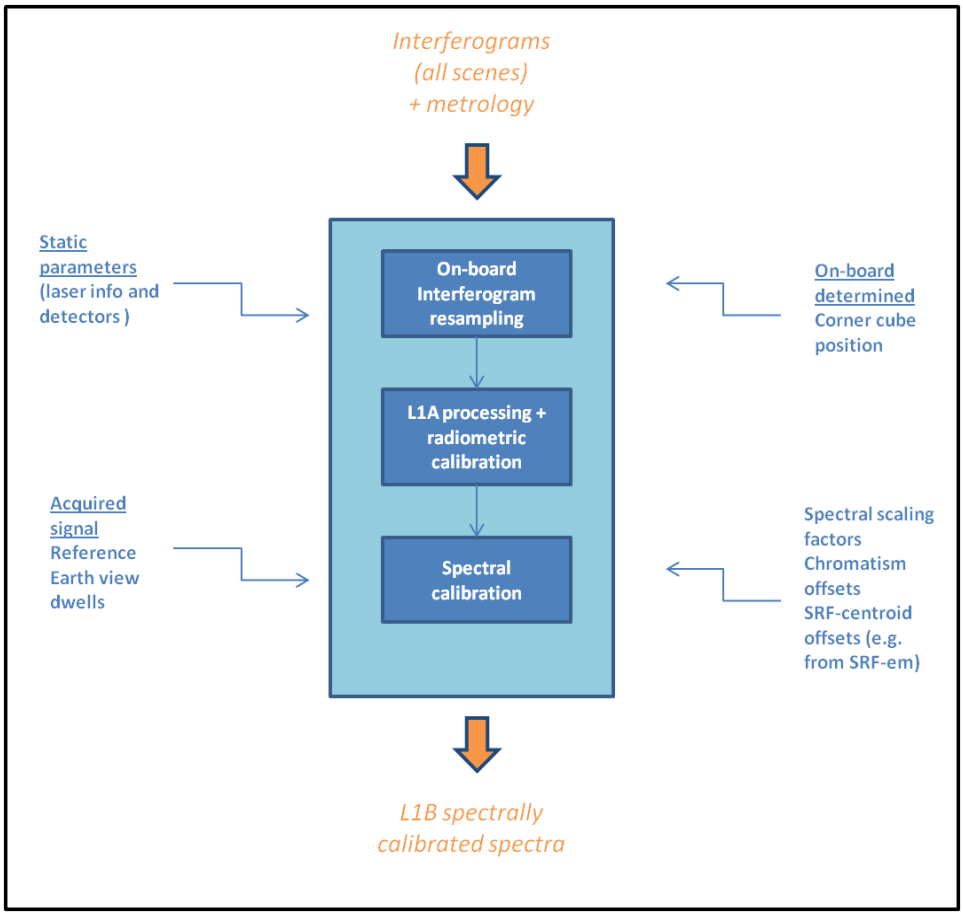

Figure 29: Illustration of the main processing flow of a Dwell through the level 1 processor with emphasis on the aspects regarding spectral calibration.

The spectral calibration process is performed in two steps:

1. Estimation of the actual spectral position of each sample (‘spectral determination’), shown on Figure 30;
2. Re-sampling of each spectrum on a common, uniform grid (‘spectral correction’), as shown on Figure 31

These two steps are done independently for each pixel of every dwell and for each spectral band.

The first step uses the spectral content of selected dwells to determine the residual spectral scaling factor left after the on-board correction (performed through resampling). Combined with prior knowledge about the chromatism of the optics, the true spectral position of each spectral sample is determined. This knowledge is given under the form of a spectral scaling factor, linearly scaling the spectral positions.

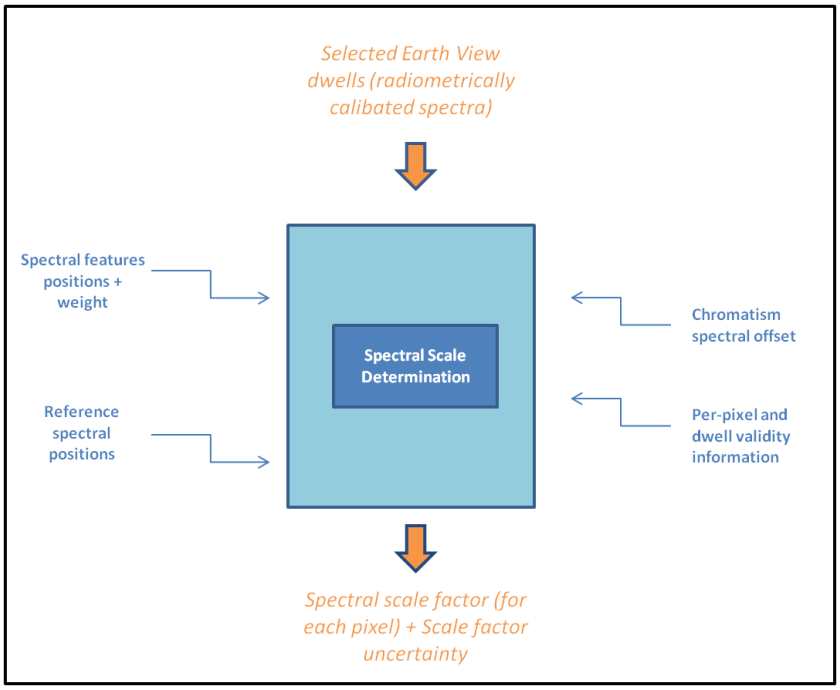

Figure 30: Spectral Scale Determination Parameters overview.

The information on the spectral positions is available only for the dwells where it has been computed. In order to correct spectra acquired in other dwells, an extrapolation is performed based on previously determined values.

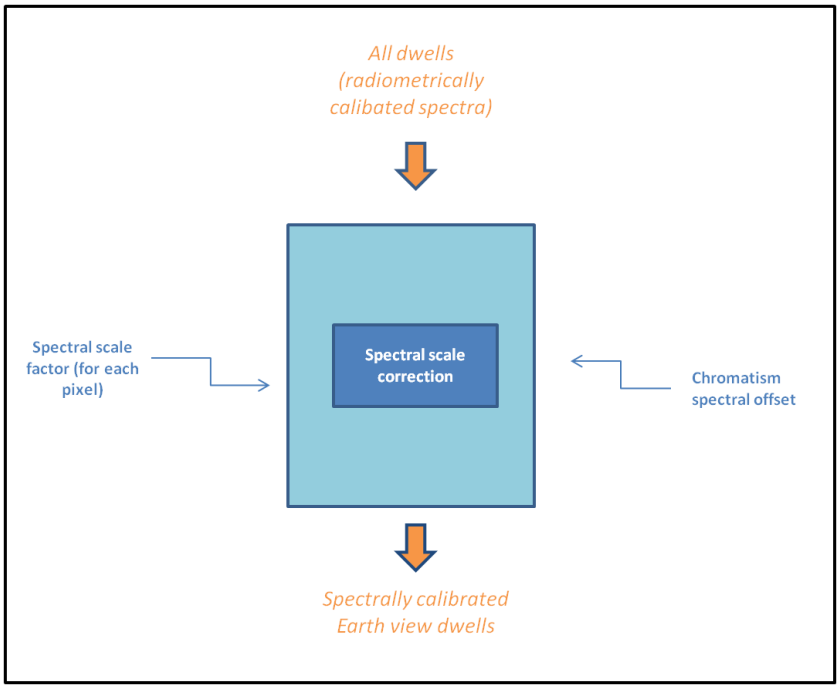

Figure 31: Spectral Scale Correction Parameters overview.

After the spectral calibration determination process, the spectra are on a known irregular spectral grid that is unique for each pixel in each band and each dwell. This grid may be distorted by effects that are not only pixel-dependant, but also time-dependant. The second step of the spectral calibration process resamples the spectra on a pre-defined regular uniform spectral grid common for all pixels and dwells using on the now known irregular grid for each spectra.

Parallel to the spectral scale identification process, the uncertainty of the process must be evaluated. This is necessary to keep out scales that are likely to be erroneous and ensure that the requirements on the spectral scale knowledge of the L1b product are met. More specifically, this quality information is used in the prediction process to ensure only spectral scaling factors determined with a good confidence are used. Current evaluation of the calibration process shows that erroneous scale factor determination should be a very scarce occurrence.

5.3.3.1 Residual from the On-Board Calibration

The spectral scale distortions in the spectra produced by an FTS instrument is driven by the angle at which the light propagates through the interferometer. The interferogram produced by a light beam that propagates along the interferometric axis will lead to a spectrum with exactly the correct spectral scale. On the other hand, a beam propagating off-axis will have its wavenumber axis (or sampling) scaled by a factor proportional to the cosine of the propagation angle of that beam. This apparent spectral scale is thus dependent on the nominal field of view angle. The wavelength dependency of the propagation angle causes the additional chromatism effects.

The imaging FTS is a special case of FTS instrument with multiple detectors, each having its own distinct field of view and thus with different angles through the interferometer. Knowing where the pixel is spatially located and knowing the properties of the optical system between the interferometer and the detector, one can deduce the angle at which the light observed by that pixel will propagate through the interferometer. Knowing this angle, the scaling factor can be determined and used for a spectral correction.

As described in section 4.6, the on-board correction (re-sampling) of the interferogram corrects the largest part of the spectral errors. This correction is also able to take into account the irregularities of the corner cube movements, thanks to the laser-based metrology system. To map this information onto each pixel of the detector, a model is needed hence leading to an imperfect correction. Effects such as variations of the laser wavelength or distortions of the detector spatial sensitivity on the array or optics due to thermal effects cannot be corrected on-board and lead either to absolute spectral errors affecting the whole array or to relative errors between the pixels.

The expected residual on the spectral scale after on-board processing is expected to be 10 ppm in both LWIR and MWIR bands.

The time-variation of the spectral scale distortions is difficult to assess as there is no heritage from similar instruments on geostationary orbit. The IASI instrument on LEO orbit nevertheless gives valuable insight on the variations which may be expected; both instruments are quite similar, with IRS sharing many design trades with IASI.

As the movement of the interferometric axis with respect to the detector due to changes in the aft-optics is not corrected in the on-board processing, its impact is of utmost interest in the conceptual design of the spectral calibration for IRS. The IASI instrument shows short-time variation of the interferometric axis roughly following the orbital period of ca. 100 minutes. The position of the interferometric axis varies in a range up to 90 µrad [RD-8], considering the highly different angular content of a pixel's FOV between IASI and IRS, which would translate in a spectral scale error exceeding 4 ppm for a corner pixel of IRS.

For IRS, with its geostationary orbit, the expected period for these short-term variations should be longer, but the amplitude may be higher. A diurnal trend can be expected. Looking at longer time spans, IASI also exhibits seasonal and long-term variations of the interferometric axis, albeit with much lower amplitude, in the order of 25 µrad [RD-9]. The stability of the IASI instrument is notable, but the IRS instrument is much more sensitive to such interferometric axis variations with regard to absolute spectral accuracy.

5.3.3.2 Requirements Related to the Spectral Calibration

The End-User Requirements Document (EURD) [AD-2] and the System Requirements Document (SRD) [AD-1] do not directly set any requirement on the knowledge or stability of the spectral scale. Those are rather indirectly given through the radiometric error related to the knowledge and stability of the spectral scale. The requirements are given in milli-Kelvin radiometric error for a given spectra.

The spectral scale knowledge is driven by requirement IRS-10600 of the SRD, giving a threshold of 50 mK on the radiometric error related to the determined knowledge of the spectral samples. The radiometric error due to the instability of the spectral samples shall not exceed 66 mK over a spectral calibration period as required by the SRD requirement IRS-10630.

These requirements can be roughly translate into an absolute spectral accuracy of 3 ppm in the LWIR band and 1 ppm in the MWIR band. The budget for the spectral scale determination is of 2 ppm in the LWIR band and 0.5 ppm in the MWIR band. Here it is important to note that this is a complete budget, including all bias in and end-to-end system. The budget for the algorithm used in the spectral calibration process may be considerably lower and as goal a factor two below those figures may be needed.

In comparison, the GIFTS mission aimed at an absolute spectral accuracy of 5 ppm with a stability of 1 ppm over a period of one hour [RD-10]. Both instrument designs and mission environments are similar, with both MTG-IRS and GIFTS being hyperspectral imaging FTS on geostationary orbits. The GIFTS instrument and engineering model also had a two-band approach, with one band in the LWIR and one in the MWIR covering similar region than those to be covered by MTG-IRS.

The spectral calibration concept for the GIFTS instrument also aimed at using atmospheric measurements. Case studies based on data from S-HIS and AERI show that a spectral accuracy between 1.1 ppm and 1.5 ppm could be expected in the LWIR [RD-11]. The same studies showed that in the MWIR band the achived spectral accuracy is worse by a factor of 2 to 10 than in the LWIR band.

Another instrument with a larger heritage is the IASI instrument, which has a spectral accuracy requirement of 2 ppm. The spectral calibration approach of IASI is also based on atmospheric measurement, using periodic structures of CO_2 bands, which are not available to IRS. The goal of 2 ppm is met with difficulty, with few small spectral windows remaining non-compliant due to spectrally local outliners after the calibration process at the end of IASI-A commissioning [RD-12]. The IASI instrument is more difficult to compare with IRS, having only four pixels with large angular field of view and a higher spectral resolution than IRS. The instrumental variations will influence the product through different mechanisms, with spectral scaling effects dominating IRS measurements while line shape effects will play a more important role in IASI measurements.

The CrIS instrument, laying somewhere in between the IASI design and the GIFTS design, uses a completely different approach to the spectral calibration. This instrument relies on an on-board spectral reference rather than on atmospheric measurements. While this approach is much simpler (from the processing point of view), it comes at the cost of additional flight hardware and lower accuracy with an expected spectral determination accuracy of 5 ppm. The overall spectral calibration accuracy requirement is 10 ppm [RD-13].

5.3.3.3 Spectral Scaling Factor Determination Approach Overview

The approach presented here has been developed by Dr. Philippe Giaccari (Micos / Zurich (Dübendorf), CH) in the frame of the industry Instrument Quality Toolbox (IQT) for IRS.

The spectral scale determination is made on a per-pixel basis, without any model taking into account a possible spatial correlation of the spectral scale between pixels. This is needed as it has been demonstrated during the industrial Phase B through thermo-optical simulations, that the expected variations, which cannot be modelled, will induce spectral errors over budget. No *a-priori* information about the geometry and its effect on the spectral scale is needed for the determination process.

For the spectral scale determination, so-called spectral features distributed over the spectra are used. The spectral features are not observed directly in the spectrum directly or in a derivate of any order of the spectrum, but rather in a spectrum, which has been processed with a special kind of apodisation function. This very strong apodisation function suppresses both the area around ZPD and at the end of the interferogram. This transform the spectral signature of the spectrum in spectral features while make them more stable and immune to SRF variations. This double apodisation also enhances the first side-lobes while strongly suppressing higher order lobes; these side-lobes are also used as spectral features. The spectral resolution of the IRS instrument the spectral features are in most cases related to spectral structures from unresolved lines or line groups, such as the CO_2 structures in the region of 700 cm^{-1}.

The determination process follows these steps, which are described more in detail later:

1. Selection of spectra suitable for spectral scale determination;
2. Averaging of the spectra for spectral determination over multiple Local Area Coverage (LAC) revisits;
3. Filtering with a special apodisation function to stabilize spectral features and remove any sensitivity to either the spectral baseline or the SRF;

4. Determination of the spectral position of specific spectral features;
5. Combination of the spectral position information of the spectral features to determine the spectral scaling factor.
6. Extrapolation of the scale factors based on short-term knowledge to predict the scale factor to be used for the correction.

The position information of the spectral features is combined using a weighted average, where each spectral feature has its own weight (a static parameter). The outcome of this averaging operation is then compared to a reference position to compute a scaling factor. Which spectral features are to be used for the determination, their weighting factors and the reference position are all part of a Solution. The determination may use multiple Solutions for the complete spectral range or a small spectral window.

This approach, with the combination of special apodisation of the spectra and of the weight averages of the position of selected spectral features lead to a spectral invariant. This spectral invariant is independent of the input spectral scene, given the scene respects the selection criteria, and provided a fixe spectral reference frame.

The determination process using the Solution is not designed to work with every Earth-View (EV) spectra, but rather with a set of selected spectra. The basis criterion is that the dwells are in a selected zone of interest, in this case over the ocean. In principle, other regions of interest, having different atmospheric and radiometric characteristics could be chosen and used, in which case new Solutions specific for these regions of interest must be crafted.

The determined scale factors are not used directly for the spectral correction. A predicted scale factor is used based on historical values of scale factors over a given period. For the prediction, only scale factors determined with good confidence and not showing any statistical anomaly (both spatially and temporally) are used. For this selection process, the uncertainty of the determination process is estimated and tracked along the determination process itself.

5.3.3.4 Spectral Scale Determination Solutions

The spectral scale determination process uses information of multiple spectral features. Some spectral features may be more adequate than other for the determination process. This is partly due to factors such as normal variability in the atmospheric composition or to the properties of the spectral lines themselves.

To cope with this reality, the so-called Solutions have been introduced to effectively use and combine the spectral information of multiple spectral features while providing immunity to scene variability, scene mixing, viewing geometry and instrument radiometric performance. Each solution is based on a unique spectral invariant for the selected spectral calibration zone.

The name “Solution” originates their creation processes, searching optimal solutions through a genetic algorithm. This section further discusses these solutions and their generation.

5.3.3.4.1 Concept of Solutions

The spectral scale determination uses the spectral positions of a set of pre-selected spectral features, each having a different weight in the determination. The information of the different spectral features is combined though the weighted average of their positions. By doing this on the position of the selected spectral features for a known reference spectrum, a reference position, ν_{ref}, is obtained. When doing the same process on a measured spectrum, a determined position, ν_{sol}, is obtained. The spectral scaling factor is deduced from those two values as shown later in Section 5.3.3.5.

This process is illustrated in a simplified principle diagram in Figure 32. The measured spectrum is represented in red and their spectral position is determined with their position identified by the red circles. The size of the circles represents the weight of each spectral feature for the position average leading to ν_{sol}. The black part on top shows the same positions of the spectral features and the corresponding weights (represented by the circles), but this time for the true (or reference) spectrum. That leads to the reference position ν_{ref}. The set of information used in this process is called a Solution. Each Solution contains:

- A list of spectral feature nominal central positions and range;
- An averaging weight for the position of each spectral feature;
- A reference position for the solution;
- The type (positive or negative) of each spectral feature;

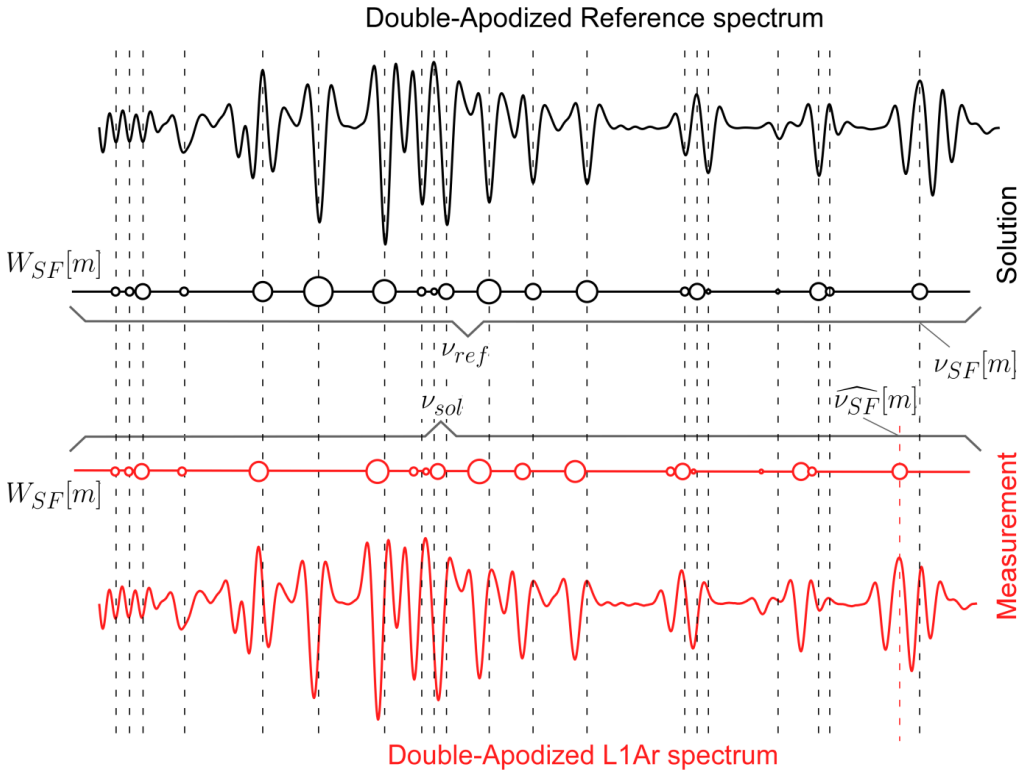

Figure 32: Simplified illustration of the approach to the use of solutions to determine the spectral scaling factor using a reference spectrum (black) and a measured spectrum (red). The position of each spectral feature is marked by the circles. The size of whichrepresent the averaging weight for the spectral feature positions (larger circle for a larger weight).

Along the solution, additional information is required to determine the validity of a spectrum for the spectral calibration. This information may be shared between multiple solutions or be used for all solutions, as it is the case for MTG-IRS:

- A representative spectral feature (see §5.3.3.4.2);
- A representative spectral feature amplitude threshold.

In Figure 32, features with lower averaging weight (smaller circles) contributed less to the determined spectral position. For example, a spectral shift of the first spectral feature to the left will have a higher impact on ν_{sol} than an equivalent shift on the last spectral feature to the right because of the difference in the averaging weight.

The selection of the spectral features and their respective weight must be tuned to ensure immunity to the normal variation of the atmosphere within the spectral calibration zone. To achieve this immunity, the solutions are not based on a single reference spectrum, but rather on a set of spectra representative of the atmosphere in the region used for the spectral calibration. For the Solutions presented in this document, a set of 1900 spectra were used as later presented in 5.3.3.4.3.

5.3.3.4.2 Representative Spectral Feature

From the spectral features used for the determination process described above, one feature is used as a Representative Spectral Feature (RSF). This RSF is common to all solutions (if multiple solutions are used) for the calibration process and is used to determine if a spectrum is suitable for the spectral scale determination process.

The main characteristic of the RSF is that its amplitude (usually negative as isolated absorption lines are better suited) is strongly correlated to the error in the determination of the spectral scale factor. In other words, its amplitude (or intensity) is representative of the quality of the spectral scale determination for a given spectrum. A spectrum with a strong RSF will lead to a determination of the spectral scale with a lower uncertainty as a spectrum with a weak RSF. A threshold can thus be put on the RSF amplitude to decide if a spectrum is suitable for the spectral determination process.

The selection of the RSF and of the amplitude threshold for the selection of spectra is part of the solution creation process. The RSF for the solutions are presented in the Appendix F of the document.

5.3.3.4.3 Representative Atmosphere and Spectra

The representative spectra set (not to be confused with the representative spectral feature described previously) is a number of simulated spectra used to tune the solutions, leading to the best possible performance in determining the scale factor. The spectra must cover a wide number of possible scenarios, taking into account atmospheric variation (mostly temperature, ozone profile and water profile), cloudiness and viewing geometry. The simulated spectra are all “real” cases based on historical atmospheric conditions and are not based on averaged conditions. The historical conditions have been grouped in families sharing similarities and random spectra have been chosen in each family to ensure representativeness.

The solutions for the spectral scale determination of IRS have been generated using a set of 1900 spectra. These spectra have been produced using a line-by-line radiative transfer model

with input from ECMWF-ERA data for the spectral calibration zone over the North Atlantic. The ECMWF-ERA data for the selected region over a period of a year has been compiled and analysed statistically to determine statistically representative profiles of temperature, water vapour and ozone. These profiles have been combined along with a set of skin temperatures following the distribution observed over the period of one year to generate cases of 600 atmospheric conditions. These conditions are statistically representative of the atmosphere over a full year in the spectral calibration zone (SCZ) for the spectral calibration determination. From these 600 atmospheric conditions, the set of 1800 spectra have been calculated for a viewing angle in the centre of the SCZ:

- 600 clear-sky spectra for each of the representative atmospheric conditions;
- The 600 spectra with a cloud layer at 1 km;
- The 600 spectra with a cloud layer at 4 km;

Furthermore, to include the effect of the viewing geometry, 100 additional spectra have been generated based on 100 selected cases of the 600 atmospheric conditions with a cloud layer at 1 km, but with a nadir viewing geometry. In other words, for those 100 selected atmospheric conditions, spectra have been generated assuming the scene is directly below the satellite rather than in the SCZ. This leads to a set of 1900 spectra in total to be used for the generation of solutions.

For those forward calculations, the Sub-Satellite Point (SSP) is assumed to be at 0°N 0°E. The simulation of cloud layers is highly simplified, assuming a perfect thin and opaque blackbody (emissivity of 1.000) at the altitude of the cloud, with the temperature of the atmosphere at that altitude. The forward calculation has been done taking into account the most common species and isotopes.

5.3.3.4.4 Solution Generation

[Placeholder for future releases]

This is placeholder section for the presentation of the generation of the solutions for the spectral calibration approach. Until completed, interested readers may refer to §5 of MTG-MCS-IR-RP-0005 “Analysis Reports (PL-8)” from the industrial Phase B or MTG-IRS spectral calibration activities.

5.3.3.5 Spectral scaling factor determination based on Earth-view scenes

This determination process uses as input the spectra after radiometric calibration with 2^{13} samples. In those spectra, the position of selected spectral features is determined. This operation is done on spectra after being pre-processed with a double apodisation in the interferogram domain (see §5.3.3.6), attenuating both the end of the interferogram to reduce SRF spread and sensibility as well as the central part of the interferogram to remove the spectral baseline. In other words, the spectra are being band-pass filtered to retain only the features of interest. This way, the determination of the position is more reproducible and less sensitive to noise, to variation of scene temperature or emissivity.

The weighted mean of the positions of the pre-determined spectral features are compared to a reference position to deduce the spectral scaling factor. The information needed for this

process is defined as a Solution (see more details in §5.3.3.3). The spectral determination may use multiple solutions; For the IRS instrument, 4 solutions are given for each band:

- One general solution for the determination of the scale factor for the spectral correction;
- Three local solutions for the determination of the scale factor in a smaller window of the spectral range to be used for the evaluation and monitoring of chromatism changes in flight (see §7.1.4 for more details on the use).

The eight identified solutions are described in full in Appendix F. These solutions have been optimized and verified through a genetic approach, without guarantee that there are no better, more performant solutions existing. The general solutions for the LWIR band and for the MWIR band respectively contain 30 and 40 spectral features spread over the whole spectral range.

The determination is made using dwells from LAC 4 located (completely or only partly) over the North Atlantic (Figure 33). These dwells together form the spectral calibration zone (SCZ).

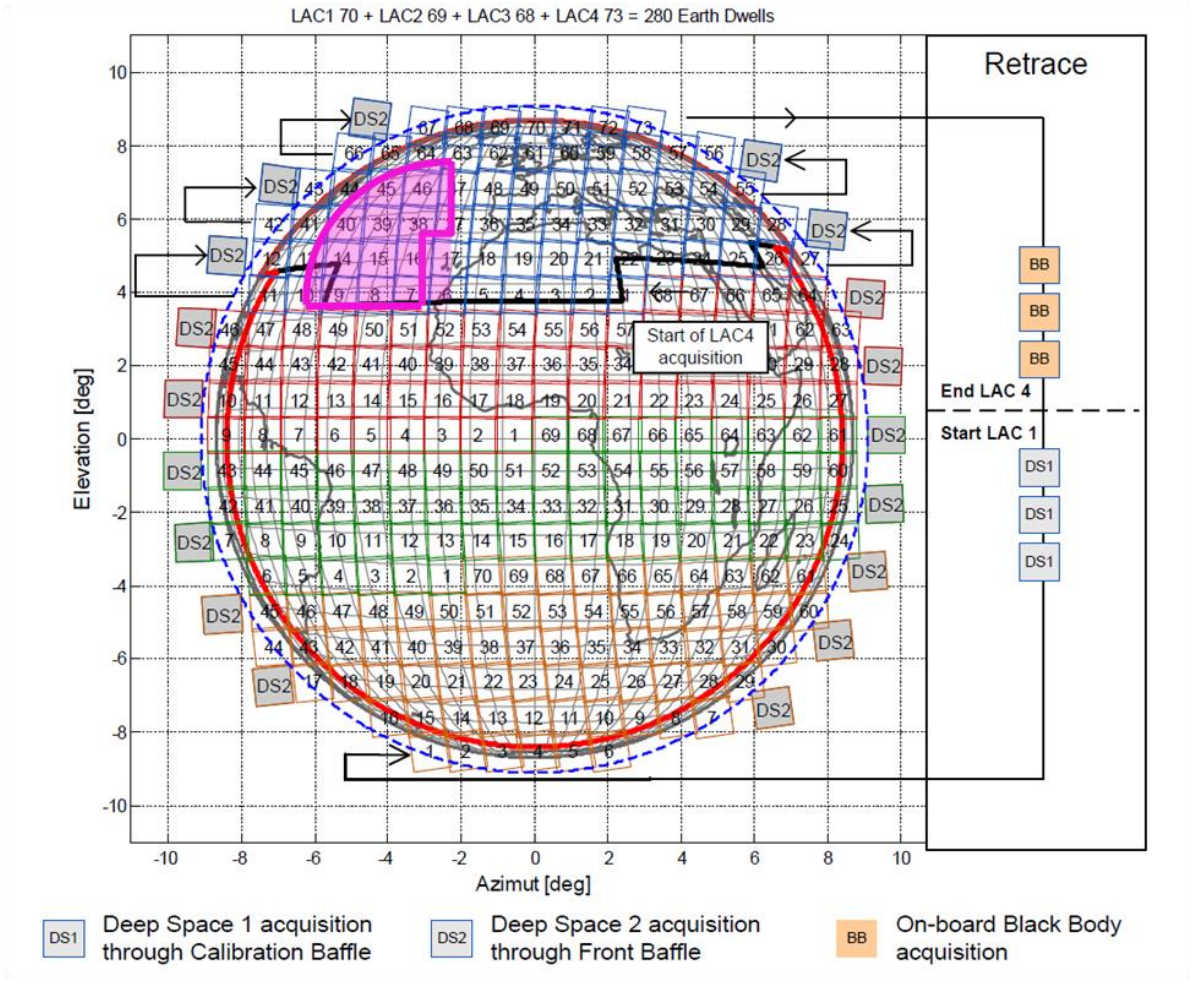

Figure 33: Potential spectral calibration zone (in pink) coming from the LAC 4 used for the spectral scale determination. Depending on the position of the satellite or of the actual extent of the desired coverage, the SCZ may actually differ from the above illustration.

The rationale for the use of these dwells for the spectral scale determination is based on:

- The frequent revisit (every 30 minutes);
- Limited emissivity variation over water;
- Limited skin temperature variation, both in space and time;
- Very few cases of where lines which are normally absorption lines over the SCZ are seen as emission lines or vice versa, for example due to strong temperature or emissivity variations.

The cases showing radiometric inversions are filtered out by putting a threshold on the amplitude of the representative spectral feature. This must be done both for the generation of the solution as for the determination process using those solutions.

For the selected dwells, only the pixels valid for the spectral calibration determination are retained. The pixel validity criteria are:

- No error raised by the instrument or processing chain up to that point;
- Pixel only over water;
- Observation angle smaller than 8°.

In coastal areas, enough margins must be foreseen to avoid accidental land contamination, this taking into account any uncertainty on the pointing determination. The observation angle is defined as the angle between nadir and the line of sight. This is computed from both the elevation angle and azimuth angle of the observation line of sight in the NED reference frame of the satellite:

$$\psi_{view}[i,j] = \sqrt{\theta_{view}[i,j]^2 + \phi_{view}[i,j]^2}\ . \qquad \textit{Eq. 43}$$

A ψ_{view} of zero would correspond to downward-looking (nadir).

A further validity criterion is used to reject spectra with unusual features such as those caused by temperature inversions where lines expected to be seen as absorption lines are seen as emission lines or vice versa or spectra with features to weak, which may occur under specific cloud conditions.

To identify such special cases, the spectral amplitude of the representative spectral feature (RSF) is determined and compared to a pre-defined amplitude threshold value $A_{RSF,\min}$.

The amplitude of the RSF is evaluated on the apodized spectra using a special double apodisation (see 5.3.3.6). The determination of the RSF amplitude can be done simply by finding the position of the minimum value, assuming a sufficient number of samples. Analysis have shown that a 2^{13} samples are sufficient, which the number of samples required for the spectral correction (see 5.3.3.11).

Any spectrum with a minimum value above this threshold is rejected – The RSF amplitude is expected to be negative (absorption feature), as is the amplitude threshold value.

The baseline amplitude threshold value for each spectral band is given in Appendix G. The representative spectral feature is part of the solutions. All solutions for one band (the general solution and the local solutions for spectral windows) share the same RSF.

All the valid spectra of the selected dwells from a LAC 4 revisit are averaged temporally on per-pixel basis. This step, while being inexpensive in resources, considerably reduces the sensitivity to radiometric noise, which is a dominant source of error in the spectral calibration approach. Furthermore, these valid spectra are also averaged with the valid spectra from the last N_{ma_rev} LAC 4 revisits (baseline $N_{ma\_rev} = 3$). This process can be understood as making a time-based moving average with a time window of t_{av_spec} hours over all valid spectra for each pixel, causing a smoothing of the spectral scale variations. In practice, the number of valid spectra for each pixel must also be tracked to allow proper averaging. For each pixel, a different number of spectra may be used for the moving average.

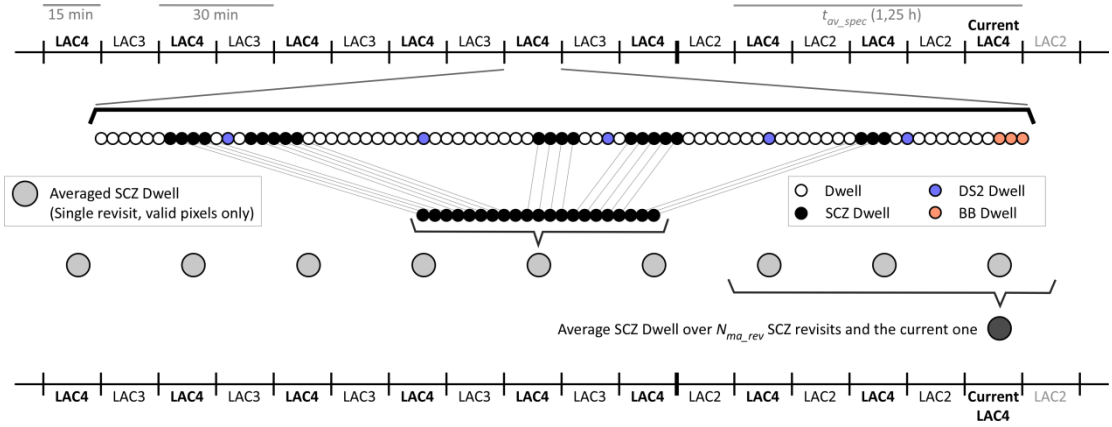

Figure 34 Diagram illustrating the averaging ranges for the spectral scale determination.

The average spectra are brought on a sufficiently dense spectral sampling grid (baseline $N_{LFi} = 2^{17}$ samples) for a feature position determination based on quadratic fit and filtering with the Double Apodisation. The quadratic fit is done on two point and using the a-priori knowledge of orientation (minima or maxima) of the spectral feature. The power of two is not required, but was optimal for the implementation used for the analysis. The determined position of each spectral feature, $\widehat{\nu_{SF}}[i,j,b,m]$, where m represents the index identifying the spectral feature, is determined on a line-by-line approach with a quadratic/parabolic fit. The extrema determination through a fitting approach allows the determination for spectral features closely surrounded by other features – usually of opposite sign – without having to reduce considerably the search range. The spectral feature database may also include information whether the line is an emission line or an absorption line, facilitating the fit process.

Once determined, the positions of the spectral features are corrected with the known chromatism offsets, which are, as introduced in 5.3.3, deviations from the linear scaling factor define as additional spectral offset for each spectral sample. These offset may be given for any spectral grid, including the grid defined by the nominal position of the spectral features themselves. In case the chromatism offsets are given in a generic spectral grid (L1Ar, L1Ars or LFi), their corresponding chromatism offsets are defined as:

$$\Delta\nu_{chrom\_SF}[i,j,m,b] \triangleq \Delta\nu_{chrom}[i,j,k,b]\big|_{k\to k_{SF}[m]} \qquad \textit{Eq. 44}$$

The chromatism correction for the spectral features can thus be done on the spectral grid with N_{LFi} points or using a pre-determined lookup table of chromatism offsets of each spectral features (The spectral features are static and the chromatism-offsets are quasi-static).

The chromatism offsets, which are pixel and band dependant, are determined on ground and re-evaluated during commissioning to take into account any changes due to, for example, the change of gravity after launch. These offset may be updated as needed during the lifetime of the instrument. If a lookup table is used to store the offsets for the spectral features instead of a spectral grid with 2^{17} samples, the lookup table must also be updated with an update of the chromatism offsets.

Once the positions are known and corrected for chromatism, they are not directly compared to their nominal positions $\nu_{SF}[m]$. The positions are averaged with their corresponding weights $W_{SF}[m]$ and the relative spectral scale is determined using the reference position ν_{ref}.

For each solution of each band, for each pixel, the spectral scale factor is thus given by:

$$\zeta[i,j,b] = \frac{\frac{\sum_{N_{SF}} W_{SF}[m]\ \nu_{SF\_CR}[m]}{\sum_{N_{SF}} W_{SF}[m]} - \nu_{ref}}{\nu_{ref}} \times 10^6\,, \qquad \textit{Eq. 45}$$

where N_{SF} is the number of spectral feature in the solution and ν_{SF_CR} is the Spectral Feature position after correction of chromatism offsets. The result is in parts per million (ppm).

5.3.3.6 Double apodisation

The double apodisation is a special apodisation designed specifically for the spectral calibration process of IRS to stabilize spectrally the spectral features for the spectral scale determination process. This apodisation both strongly reduces the spectral line side lobes and the SRF-dependency of the features while increasing the immunity to background temperatures, continuums, clouds, background emissivity and radiometric correction errors. This is achieved by windowing not only the end of the interferogram, but also the centre part of the interferogram (the ZPD). The name "double apodisation" is used here to highlight this double windowing. This apodisation is also referred to as "strong apodisation" in some MTG-related documents; this name was originally chosen by the authors who derived the algorithm. The use of "strong" may cause confusion with the commonly used Norton-Beer Strong apodisation and is therefore not used in this document.

The double apodisation is based on the Kaiser apodisation window, which defined as:

$$I_K[l] = \begin{cases} \dfrac{I_0\left(\pi\alpha\sqrt{1-\left(\frac{2l}{M}-1\right)^2}\right)}{I_0(\pi\alpha)} & ,0 \le l \le M \\ 0 & ,\text{otherwise} \end{cases} \qquad \textit{Eq. 46}$$

where I_0 is the modified Bessel of the first kind (0^{th} order) and the parameter M is constant with the value 100 and the parameter $\pi\alpha$ is also constant with value 8, which was demonstrated to be the optimal value during the industrial Phase B studies. Here l is the index position in the interferogram domain and the double apodisation is applied in this domain.

The double apodisation is given by the normalized product of a Kaiser Windows and an inverted Kaiser Window:

$$I_{DA}[l] = \frac{I_K[l] \cdot (1 - I_K[l])}{Maximum\{I_K[l] \cdot (1 - I_K[l])\}} \qquad \textit{Eq. 47}$$

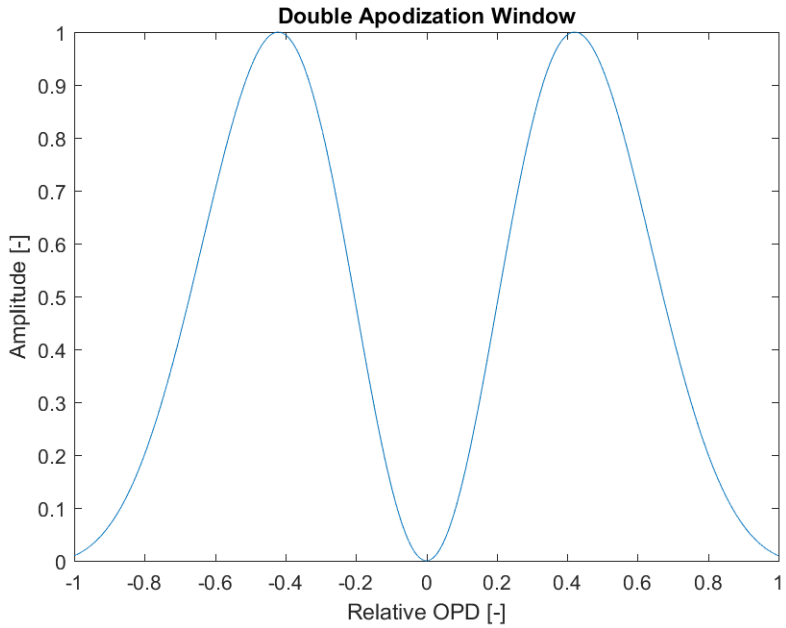

Figure 35: Double Apodisation window in the interferogram domain

Figure 32 shows actual atmospheric spectra filtered with the double-apodisation function.

5.3.3.7 Spectral scaling factor determination uncertainty evaluation

Along with the spectral scale factor determination process using the invariant given by the Solutions, a method has been developed to estimate the uncertainty of the process. The uncertainty is given in ppm and is the absolute uncertainty of the spectral scale factor, also given in ppm (not to be mistaken for a relative uncertainty, regardless of the ppm units).

In section 5.3.3.4.2 the concept of Representative Spectral Feature, RSF, was introduced and used in 5.3.3.4.2to filter out spectra not expected to work well for the spectral calibration process; any spectrum where the amplitude of the RSF is over a pre-determined threshold are rejected. The RSF has uses beyond that of simple filtering: There is a systematic relation between the amplitude of the RSF and the determination uncertainty.

The relation between the RSF amplitude and the determination uncertainty is a by-product of the Solution determination process. This relation has a quasi-linear part, followed by a strong non-linear increase. The second region is used to set the rejection threshold used in 5.3.3.5 and is thus of no interest. Only the quasi-linear region is of use. Along the determination process, the relation has been modelled by a polynomial, which can be used to estimate the uncertainty. This is illustrated on Figure 36.

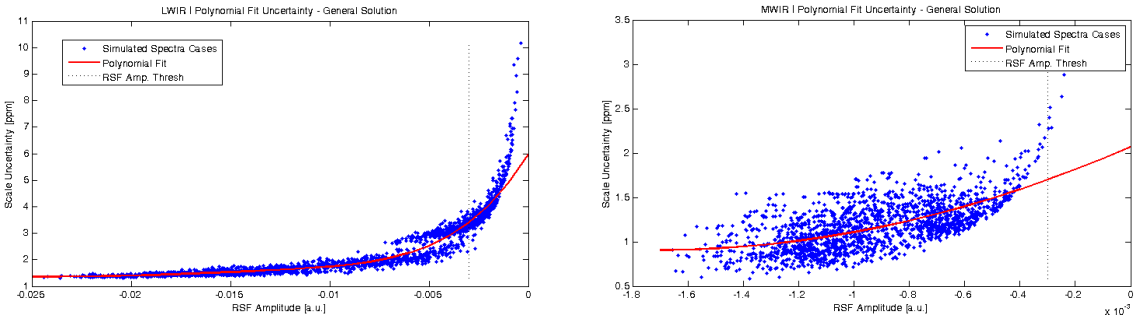

Figure 36: Relation between the scale factor determination uncertainty and the RSF amplitude for the LWIR (Left) and for the MWIR (right). The blue points represent the results from the 1900 training spectra and the red line the result of the fitting process. The thin vertical dotted line is the amplitude threshold used to reject spectra. Illustration from MTG-MCS-IR-RP-0005, Giaccari et al.

The uncertainty $U[i,j,b]$ in the LWIR is given by:

$$U = 2808267651.30\,A^5 + 244942476.52\,A^4 + 8355397.59\,A^3 + 140728.71\,A^2 + 1210.89\,A + 5.97 \qquad \textit{Eq. 48}$$

and in the MWIR is given by:

$$U = 394684.38\,A^2 + 1355.59\,A + 2.07 \qquad \textit{Eq. 49}$$

where $A[i,j,b]$ is the amplitude of the RSF.

The uncertainty of the single scale factors is of little use for the determination as the process uses averaging. The overall uncertainty of the determined scale factor is given by:

$$U_{est}[i,j,b] = \frac{1}{N_{avg}[i,j,b]}\sqrt{\sum U[i,j,b][t]^2} \qquad \textit{Eq. 50}$$

where N_{avg} is the number of average spectra, each leading an uncertainty $U[i,j,b][t]$.

5.3.3.8 Spectral scaling factor prediction

The correction of the spectral scale is not directly based on the spectral scale determined in Eq. 45, rather with a predicted value. The predicted value is found by fitting historical scale factors values from the last LAC 4 revisit within a period of t_{LAC4} (corresponding to 4 revisits) and extrapolating to a time t_{ex_pred} into the future. The time t_{ex_pred} represents the half time between the end of the last SCZ revisit and the expected end of the next SCZ revisit, a duration of 30 minutes. This is illustrated in Figure 37.

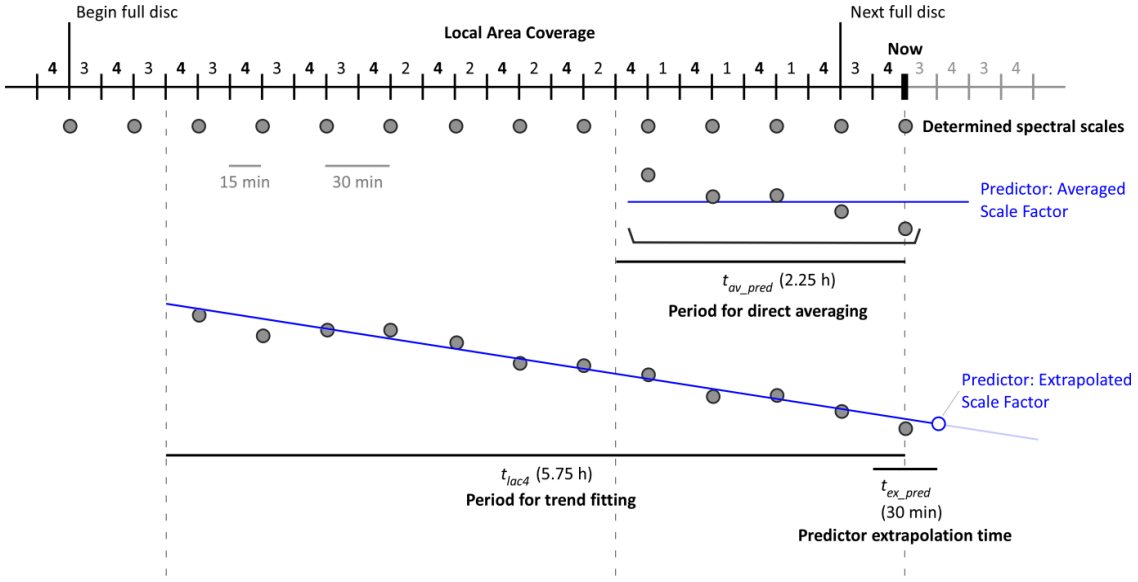

Figure 37 Diagram illustrating the timing for the scale factor prediction process.

The assumption for the extrapolation process is that there are enough valid spectral scale factors available to do a proper fit. In case an extrapolation is not possible because the number of past valid scale factors is not sufficient for an accurate polynomial fit, two alternatives are possible:

- If any valid spectral scaling factor are available for the period t_{av_pred} before the end of the last SCZ revisit, the mean of the available spectral scaling factors in that timeframe is used as predicted spectral scale factor for the correction:

$$\zeta_{pred}[i,j,b] = \frac{\sum_{N_{av\_pred}} \zeta[i,j,b][t]}{N_{av\_pred}[i,j,b]} \qquad \textit{Eq. 51}$$

where N_{av_pred} is the number of spectral scaling factor available in the duration t_{av_pred}.

As shown in Eq. 51, there is a predicted value for each pixel (i,j) in each band b. The averaging may include a different number of scale factors for each pixel.

- If no spectral scaling factors are available or valid, the predicted spectral scale factor for the correction ζ_{pred} is set to zero (hence no correction will be undertaken).

On the other hand, if there are enough valid scale factors available (the baseline being 10), a fit and an extrapolation can be made to find the predicted scale factor. Before performing an extrapolation, additional filtering steps have to be done on the available spectral scale values to eliminate possible anomalies and ensure best possible prediction. The elimination of anomalies is done on a per-pixel basis with the following steps:

1. Smooth all the available scaling factors values with a special temporal moving average. This special moving average consists in taking the average of the N_{sma_avg} median values of N_{sma_win} values around each scale factor value. Baseline is 3

median values of 5 values around each point. Here, the borders need to be handled separately.
2. The difference between each scaling factor values and the smoothed scale factor values is determined for each pixel and band. This gives a deviation from a local trend.
3. From all the scale factor determination uncertainty (see 5.3.3.3) for a pixel, find the minimum value. This minimum uncertainty is multiplied with a static margin factor (250%) to serve as a rejection threshold.
4. This deviation from the local trend is compared to the previously determined threshold. Any scale factor values showing difference from the local behaviour which is above the threshold are rejected as anomalous.

The presence of anomalies is possible, but very unlikely. Only very few spectral scales are expected to be rejected by this filtering step.

With the remaining scale factors, a polynomial of order Ω_{fit_pred} (baseline is to use a linear fit) is fitted to the available values. The resulting polynomial is evaluated at $t_{LAC4} + t_{ex\_pred}$ and the result of the extrapolation is then used as scaling factor for the correction, ζ_{pred}. This whole process is done independently for each pixel and nowhere in the process is any kind of spatial smoothing or averaging used.

In the event that following the anomalous values rejection process there is not enough scaling factors remaining for the extrapolation based-prediction, the prediction reverts to the above-described simple averaging.

5.3.3.8.1 Predictor re-initialization

The predictor may need to be re-initialized, setting all the counters to zero and discarding all spectra preceding the re-initialization time. After this operation, it will not be possible to compute the predictor until enough SCZ revisits are in storage to do either an averaging or an extrapolation.

Re-initialization has to be done after major events affecting the evolution of the spectral calibration, such as the failure of a sub-pixel of a detector super-pixel. Other events, which could require a reset of the predictor, are decontamination and yaw-flip of the platform. Without any in-flight experience with the instrument, it is difficult to foresee all the possible causes for a reset of the predictor.

5.3.3.8.2 Uncertainty estimation of the predictor

The uncertainty estimation propagation to the predicted spectral scaling factor depends on the method the predictor uses, that is either averaging or extrapolating. In case no prediction can be made and the predicted spectral scaling factor is set to zero, the uncertainty makes no sense in this context; it can be set to a pre-defined “missing value” or “invalid value”.

In case temporal averaging is used, the predicted spectral scale factor determination uncertainty is given by:

$$U_{pred}[i,j,b] = \frac{1}{N_{av\_pred}[i,j,b]}\sqrt{\sum U_{est}[i,j,b][t]^2} \times \sqrt{\frac{t_{av\_pred}}{t_{av\_spec}}} \qquad \textit{Eq. 52}$$

where t_{av_spec} is the time window used for the averaging of spectra during the determination of the spectral scale in §.

If the predictor is giving by fitting and extrapolating from historical values of spectral scaling factor, the uncertainty is given by:

$$U_{pred}[i,j,b] = \frac{\sqrt{\sum U_{est}[i,j,b][t]^2}}{N_{av\_pred}[i,j,b]} \times \sqrt{\frac{t_{av\_pred}}{t_{av\_spec}}} \times \sqrt{t_{ext\_pred} \times \Omega_{fit\_pred} + 1} \qquad \textit{Eq. 53}$$

5.3.3.9 Medium-Term Spectral Scaling Factor Prediction

Medium-Term Prediction, based on a period of several days, with a baseline of 16 days, was considered during the industrial Phase-B for MTG-IRS, but later dropped and not included in the IQT. Considerations are made to include this as part of the IDPF-S, regardless of the status in the IQT. Verifications are still pending whether the approach was dropped because the requirements were met otherwise or because the assumptions required for it to work were not met. In the latter case, an implementation in the IDFP-S would be of little use.

The Medium-Term Prediction is very similar to the predictor previously described in §5.3.3.8, but with different time and dwell number constrains as well as adapted filtering constrains to reject anomalous scale factors. The approach nevertheless remains similar. A key feature of the Medium-Term Prediction, is that the Predictor runs over several days, but always at the same time of day. This approach was considered in the IQT to identify fine variations over larger daily, quasi-periodic, variations and was later rejected as such a variation pattern could not be guaranteed. Furthermore, it was shown that short term prediction was sufficient to reach the goals of the spectral calibration determination. This may be reassessed in flight.

5.3.3.10 Spectral Scales involved in the Correction Process

In the spectral calibration process, different spectral grids are involved. These grids have different number of points, different use and signification. Three grids have a fundamental significance in the spectral calibration process:

- The grid giving the assumed position of the measured spectral samples. The samples in this grid are equidistant and this grid is static. The 0-order assumption is that the on-board interpolation correctly interpolated the samples on this grid;
- The grid giving the true position of the measured samples. The sampling in this grid is non-equidistant and is the outcome of the spectral calibration determinations. This grid is unique for each single spectrum – that is for each pixel, band and dwell;
- The correct grid with equidistant samples giving the true position of the spectral samples. This is the grid used for the product and can be different from the initial assumed grid. The spectral samples are on this grid after the spectral calibration correction.

Here one should observe that the first two grid describe the same spectral samples, whereas the last grid describes different spectral samples, determined through an interpolation process.

The true spectral grid can be, as described above, determined with the use of the spectral invariant provided by the Solutions. This spectral invariant is insensitive to line deformation due to line shape deformation related to the SRF. The consequence of this is that, whereas any line displaced due to spectral scale errors are corrected in the process, SRF-centroid displacements are not determined or corrected. This third order effect (after the linear scaling factor and the chromatism) has been shown to be especially important spectral regions where the instrument gain function shows large gradients.

The consequence of these SRF-centroid displacements is very similar to that of chromatism, albeit significantly weaker. The centroid offsets are wavelength and pixel dependent. Within a single Dwell, even if perfectly spectrally calibrated, the centroids of the spectral lines will be slightly different between the pixels and different from what would be expected with an ideal cardinal sine line shape.

The deformation of the line shape and slight displacement of the SRF-centroid induced by this deformation can also be corrected under the following assumptions:

- The line shape or shape of the SRF varies slowly. As the distortion of the line shape is driven by instrument gain gradients that vary slowly, this assumption is expected to me met by IRS;
- The SRF-EM can provided an accurate SRF centroid position. The SRF centroid position must be significantly better than the determination accuracy of the spectral calibration process, which is 0.6 ppm in the LWIR and 0.3 ppm in the MWIR;
- The information needed to model the SRF within the required accuracy is available to the SRF-EM;
- The monitoring and operation concept allows to track events leading to expected changes in the SRF.

Such events may be, for example, the loss of a sub-pixel or decontamination. Other major events such as yaw-flips may also be considered.

If all the above considerations are met, the correction may be undertaken in the spectral calibration correction process without additional complexity. The pixel and spectral dependent offsets provided by the SRF-EM can be handled the same way the chromatism offsets are handled and are quasi-static

After the introduction of offsets to compensate the displacement of SRF-centroids, the spectral samples will be on a uniform spectral grid, which does not represent the true position of the spectral samples anymore. The grid will rather align all SRF-centroids for measurements on an erroneous spectral grid, placing those SRF-centroids at their expected location in case the SRF would be ideal.

5.3.3.11 Spectral Scale Correction

The spectral scale correction is done for every Earth-View L1Ar spectra after radiometric calibration. The input spectra have to be on a spectral sampling grid with

N_{L1Ar} points sufficient for the process. A spectral sampling size of 2^{13} points has been shown to be sufficient to for the interpolation process in the spectral domain using spline interpolants. Another combination of sampling and interpolation technique may lead to equivalent performances. The power of two is not required, but was optimal in the development environment used to evaluate the performances.

The direct and natural way to proceed with the interpolation process would be to assume that the N_{L1Ar} are located on an erroneous grid and interpolate them on the real grid. This requires the interpolation of a much higher number of points than the end-product requires. This can be optimised by determining the position of the real grid in the reference frame of the erroneous grid. In other words, the real grid, which has a much lower number of points, is distorted with the known errors of the erroneous grid. The interpolation is done between the erroneous grid and the distorted grid in the reference frame of the erroneous grid. The result of the interpolation process are the points on the real grid. This allows to make the interpolation directly for the end-product number of points and reduce the number of operations considerably.

The correction is made for each dwell and each band independently on a per-pixel basis.

In a first step, a distorted spectral scale $\widehat{\nu_{L1Ars}}$generated based on the predicted spectral scaling factor ζ_{pred} and on the known chromatism offsets for each spectral point $\Delta\nu_{chrom}$.

$$\widehat{\nu_{L1Ars}}[i,j,k,b] = \frac{\nu_{L1Ars}[k,b] + \Delta\nu_{chrom}[i,j,k,b]}{1 + \zeta_{pred}[i,j,b] \cdot 10^{-6}} \qquad \textit{Eq. 54}$$

The spectral scale correction is done by interpolating the L1Ar spectra after radiometric correction from ν_{L1Ar} to the distorted spectral scale $\widehat{\nu_{L1Ars}}$ using spline interpolant. The resulting spectra will be uniformly sampled on the ν_{L1Ars} grid (or ν_{L1B}). Both ν_{L1Ars} and $\widehat{\nu_{L1Ars}}$ grids have $N_{L1\boldsymbol{B}}$ samples.

This process, using the predicted scale factor, is done for every EV dwells, regardless if they are also used for the spectral scale determination or not. In practice, the new predicted scale factor value using an EV dwell from a LAC revisit may not be available in time to correct that dwell while ensuring the timeliness constrains.

5.3.4 Straylight correction

The straylight is the unintended light reaching the detector and contaminating the measurements, which possibly impacts the radiometric accuracy. Countermeasures have been taken at instrument level to limit the propagation of such a parasitic light (baffles, field stops, low contamination level...) but it is impossible to eliminate it completely. A straylight correction algorithm is thus foreseen after spectral/radiometric calibration.

In the case of IRS, the most stringent straylight is caused by the Sun shining within the field of view of the instrument (Figure 38). That can happen at most 30 minutes per day, 15 minutes on each side of the Earth disk or 60 minutes per day in the extreme case where the Sun is just above the poles as seen from the satellite. Only those dwells need to be corrected

for Sun straylight i.e. no correction is applied on the measurements if the Sun is far away enough from the observed scene.

In the instrument quality tool (IQT), the straylight correction is performed after radiometric and spectral calibration. This is thus also the baseline of the IRS L1 processing described in this document. It is however worth to note that this correction could very well be performed before the calibration, in the pre-processing after the Fourier transform.

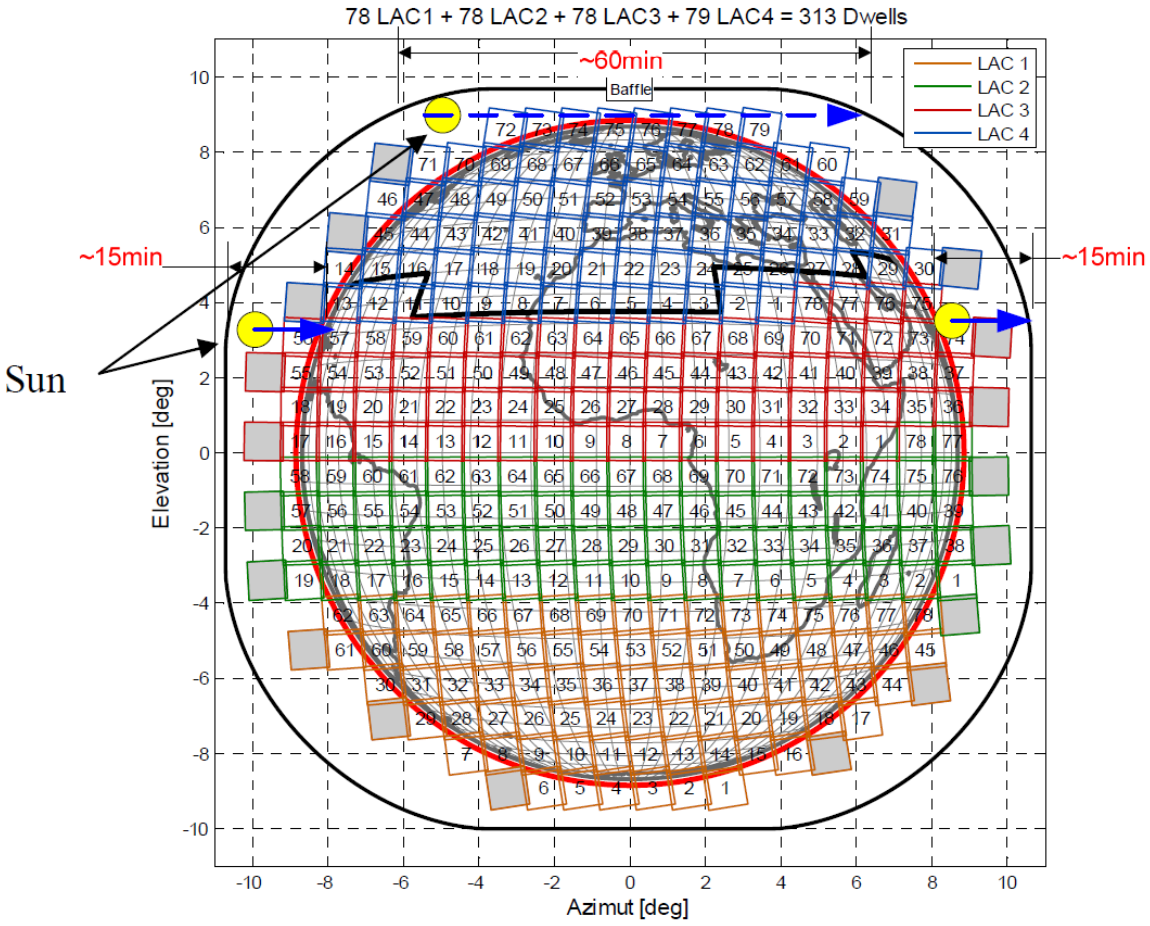

Figure 38: Cases of Sun viewing in the IRS field of view.

Simulation of the Sun straylight requires an accurate knowledge of the state of all surfaces in the optical path as well as the level of contamination of the environment. If the acquisition of this knowledge is possible on-ground during the characterisation of the instrument, it is inaccessible in-flight. Furthermore, modelling the interactions of light with the various surfaces using ray-tracing is expensive in terms of computing time and is not possible in an operational environment. For this reason, the correction is based on a model built both from an on-ground characterization performed before launch as well as another performed in-flight during the commissioning. The latter could be repeated during the lifetime of the instrument to account for its aging.

The Sun straylight model is based on radiometrically and spectrally corrected characterisation data obtained both:

- On-ground, by characterization of the elements contributing to straylight simulation: surfaces roughness, BRDF of the mirrors and contamination of the optical elements, level of ghosting. The mathematical model of the Sun straylight propagation will be adjusted so that the results match these measurements.
- In-flight during the commissioning, where the full characterization of the Sun straylight will be performed.

The latter will be achieved by pointing the instrument to deep-space for a set of pre-defined Sun angles in North-South (Relative Sun elevation angle θ_{sun} equal to zero and varying relative Sun azimuth angle ϕ_{sun}) and East-West (Relative Sun azimuth angle ϕ_{sun} equal to zero and varying relative Sun elevation angle θ_{sun}) directions (Figure 39). Characterisation data are thus obtained along two orthogonal axes and are interpolated with one polynomial fit function per axis:

$$L_\nu^{stray,\phi}(\phi_{sun},\nu) = \frac{1}{\phi_{sun}^2}\sum_{i=1}^{7} a_i(\nu)\phi_{sun}^{8-i}$$
$$L_\nu^{stray,\theta}(\theta_{sun},\nu) = \frac{1}{\theta_{sun}^2}\sum_{i=1}^{7} b_i(\nu)\theta_{sun}^{8-i} \qquad \textit{Eq. 55}$$

This can be done once and for all, and the obtained polynomial coefficients are a static input parameter to the algorithm.

For each operational measurement obtained with a specific combination of angles ϕ_{sun} and θ_{sun}, the Sun straylight distribution is approximated by a combination of those polynomials:

$$L_\nu^{stray}{}_0(\theta_{sun},\phi_{sun},\nu) = \frac{2}{\pi}\arctan\left(\frac{\phi_{sun}}{\theta_{sun}}\right)L_\nu^{stray,\phi}(\phi_{sun},\nu) + \frac{2}{\pi}\arctan\left(\frac{\theta_{sun}}{\phi_{sun}}\right)L_\nu^{stray,\theta}(\theta_{sun},\nu) \qquad \textit{Eq. 56}$$

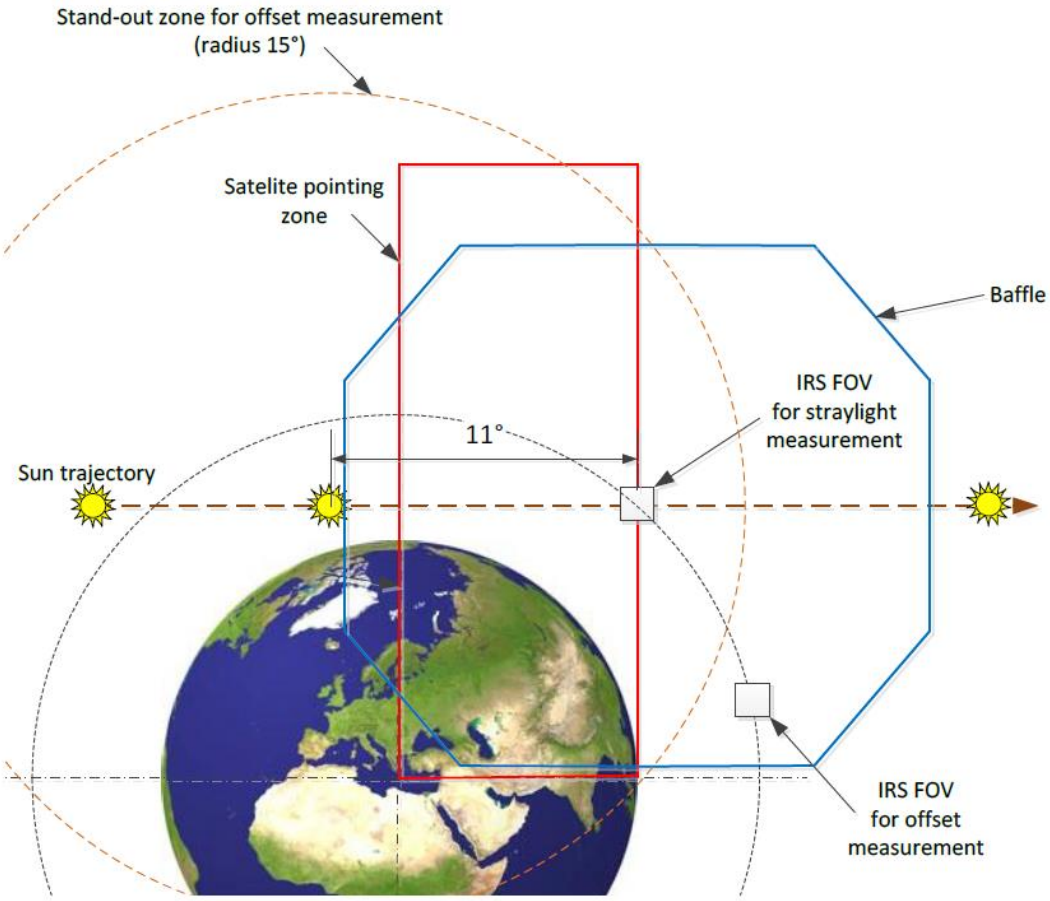

Figure 39: IRS field of view in the case of straylight characterization for a Sun azimuth angle of -11 degrees

Eq. 56 generates a "nominal" Sun straylight distribution corresponding to the Earth-Sun distance on the day at which the characterization was performed and without shadowing from the baffle or eclipse of the Sun disk by the Earth. The actual Sun straylight distribution will be a scaled value of the nomiunal distribution:

$$L_v^{stray} = \gamma_s \gamma_b \gamma_e L_v^{stray}{}_0 \qquad \textit{Eq. 57}$$

where γ_s, γ_b and γ_e are the scaling factors relative to the seasonal variations, baffle shadowing and Sun eclipse, respectively. They are described below.

5.3.4.1 Seasonal variations

Sun straylight characterisation will be performed on day of year DOY_0 of the commissioning phase. The Sun straylight computed with the model for day of year DOY has thus to be scaled with the squared reciprocal of the Earth-Sun distance d_{E-S}:

$$\gamma_s = \frac{1}{d_{E-S}^2} \qquad \textit{Eq. 58}$$

with the distance Earth-Sun being expressed in astronomical units as:

$$d_{E-S} = 1 + 0.01673 * \sin\left(\frac{2\pi * (DOY - 93.5)}{365}\right) \quad \textit{Eq. 59}$$

5.3.4.2 Baffle shadowing

In some cases, the IRS baffle shadows the pupil of the instrument, yielding a decrease of the Sun straylight. This is accounted for by scaling the computed straylight. We define:

- α_{sun}, the Sun angle at which baffle shadowing starts;
- β_{sun}, the Sun angle at which M0 is completely in the shadow;
- θ_{E-S}, the absolute elevation angle between the Earth centre and the Sun centre;
- ϕ_{E-S}, the absolute azimuth angle between the Earth centre and the Sun centre.

A correction is needed as soon as the absolute Sun angle is above α_{sun} that is if:

$$\sqrt{{\theta_{E-S}}^2 + {\phi_{E-S}}^2} \geq \alpha_{sun} \quad \textit{Eq. 60}$$

Then the height of segment circle in the shadow is:

$$h = 2 * \left(1 - \frac{\sqrt{{\theta_{E-S}}^2 + {\phi_{E-S}}^2} - \alpha_{sun}}{\beta_{sun} - \alpha_{sun}}\right) \quad \textit{Eq. 61}$$

and the correction to be applied to the Sun straylight distribution is:

$$\gamma_b = \begin{cases} 1 & \text{if } \sqrt{{\theta_{E-S}}^2 + {\phi_{E-S}}^2} > \alpha_{sun} \\ \frac{1}{\pi^2}\left[\arccos\left((1-h) * \frac{\pi}{180}\right) - \sqrt{2*h-h^2} * (1-h)\right]^2 & \text{if } \sqrt{{\theta_{E-S}}^2 + {\phi_{E-S}}^2} \leq \alpha_{sun} \end{cases}$$

5.3.4.3 Sun eclipse

The Sun can partially be hidden by the Earth disk. As in the case of baffle shadowing, this leads to a decrease of Sun straylight and, similarly, a scaling factor γ_e is applied to the theoretical value of the straylight to take this effect into account.

The apparent area of the Sun is given by:

$$A_S = \pi\, {r_S}^2 \quad \textit{Eq. 62}$$

with the apparent radius of the Sun r_S given by:

$$r_S = \frac{d_{IRS-E}}{(d_{E-S} + d_{IRS-E})} R_S \quad \textit{Eq. 63}$$

where d_{IRS-E} is the distance between IRS and the Earth centre, d_{E-S} is the Earth-Sun distance (see Eq. 59) and R_S is the Sun radius.

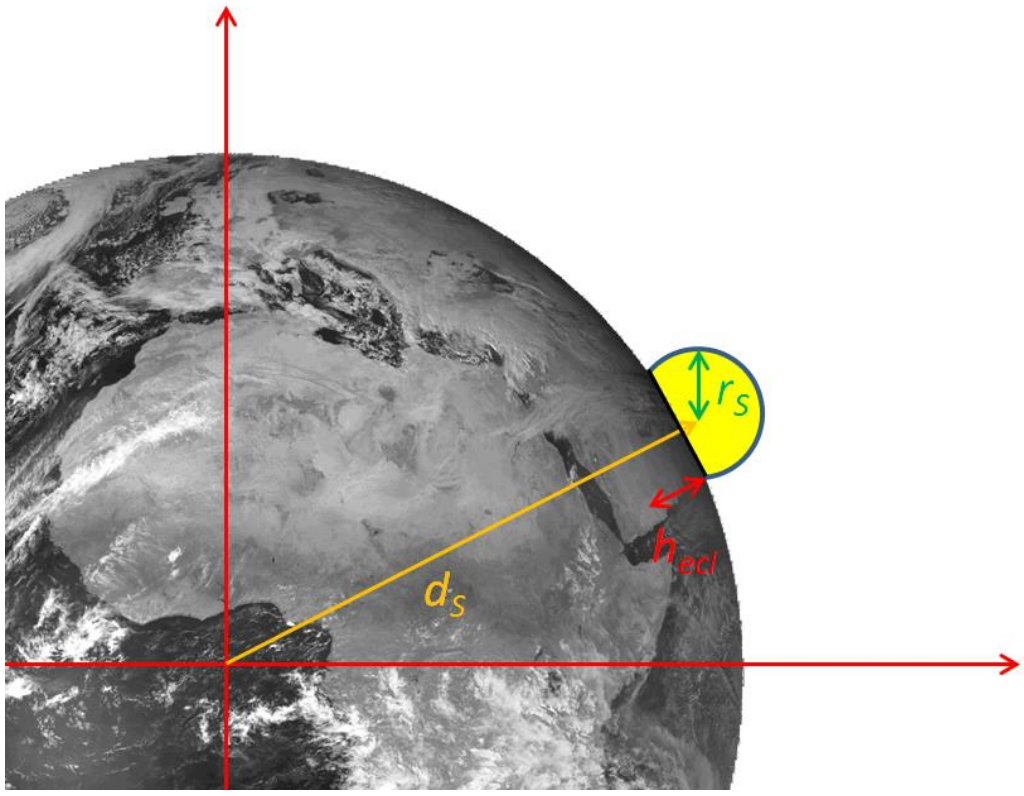

Figure 40: geometry of a Sun eclipse as seen from IRS (Sun disk not to scale).

In order to compute the area of the Sun intercepted by the Earth, it is necessary to calculate d_s the apparent distance between the Earth and the Sun:

$$d_s = \sqrt{[\tan(\phi_{Earth})\ d_{IRS-E}]^2 + [\tan(\theta_{Earth})\ d_{IRS-E}]^2} \qquad \textbf{Eq. 64}$$

The Sun disk will be intercepted by the Earth if $d_s < r_E$. Then the height of the segment circle intercepted by the Earth is:

$$h_{ecl} = r_S + (r_E - d_s) \qquad \textbf{Eq. 65}$$

So that its area is given by:

$$A_{CS} = {r_S}^2 acos\left(1 - \frac{h_{ecl}}{r_S}\right) - \sqrt{2\, r_S\, h_{ecl} - {h_{ecl}}^2}\ (r_S - h_{ecl}) \qquad \textbf{Eq. 66}$$

The correction to be applied to the Sun straylight distribution is given by the ratio of the area hidden by the Earth disk A_{CS} divided by the apparent area of the Sun A_S:

$$\gamma_e = \begin{cases} 1 & \text{if } d_s \geq r_E \\ \dfrac{A_{CS}}{A_S} & \text{if } d_s < r_E \end{cases} \qquad \textit{Eq. 67}$$

5.3.5 SRF and RTF Uniformisation

The uniformisation aims at removing the distortions of the spectral response function from the measurements, so that all pixels contain the same spectral information for all spectral channels. This process ensures that users benefit from the most accurate knowledge of the SRF, capturing any of the possible time-evolution of the instrument, without having to care about it.

The uniformisation is split in two parts:

- **SRF Uniformisation:** The processing cancels the self-apodisations (SAF) at interferogram levels. Indeed, the measured interferograms are not punctual measurements: the signal is integrated over the area covered by each pixel and includes non-optimal optical performances such as straylight and diffraction. That generally leads to a drop in the contrast of the interferogram at high OPD, wavenumber and field of view, see section 3.4.

- **RTF Uniformisation:** The processing cancels the distortions of the SRF produced by the radiometric transfer function (RTF) using a high-resolution guess of the spectrum. The IRS optical transmission varies at large but also at very short spatial scale (the so-called "*etalon effect*"), these fluctuations will create a residual noise, called calibration *ringing*", in the spectra, see section 3.4 and [RD-29].

Removing instrumental effects thus amounts to having a single time-independent SRF for all pixel positions and all wavenumbers. This is essential for the users of the level-1 products who do not have to cope with the possible spatial and temporal fluctuations of the SRF.

The SRF and RTF uniformisation is thus a very versatile processing that allows reaching selectively any defects in wavenumber and anywhere in the pixel matrix. It will be also an entry of choice to correct any unexpected instrumental defects during the mission.

5.3.5.1 Approach

SRF Uniformisation:

The SRF uniformisation allows targeting and correcting (linear) instrumental defects for any pixels and wavenumber. The key is to go back at interferogram level by Fourier transform for small ranges of wavenumber of the input spectrum and correct there the instrumental imperfections. Finally, we compute the corrected spectra pieces by inverse Fourier transform and recombine them by interpolation to retrieve the output spectrum.

The SRF uniformisation processing steps are the following:

- Extract a piece of the L1Ars spectrum (output of the radiometric and spectral calibrations) around a chosen wavenumber ν_0

$$L_{L1Ars,\nu_0}(\nu) = L_{L1Ars}(\nu \in [\nu_0 \pm \delta\nu])$$

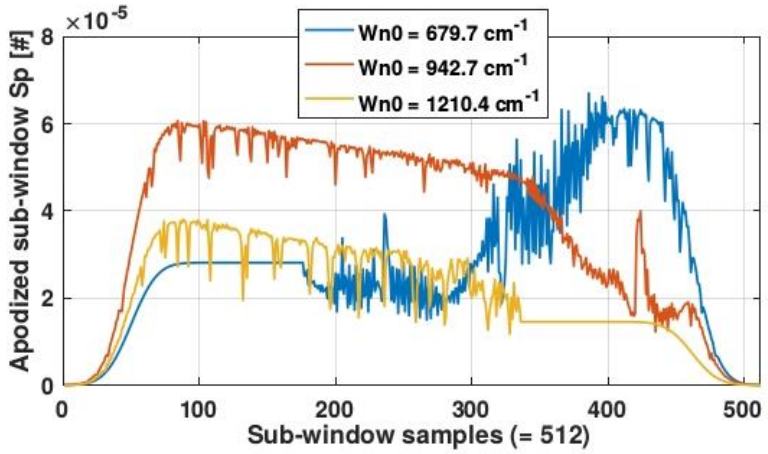

- Divide the interferogram the instrumental the self-apodisation:

$$\hat{I}_{\nu_0}(x) = \frac{I_{\nu_0}(x)}{SAF_{\nu_0}(x)}$$

- Apply an inverse Fourier transform to retrieve the corrected spectrum piece,

$$\hat{L}_{L1Ars,\nu_0}(\nu) = FT^{-1}\left[\hat{I}_{\nu_0}(x)\right]$$

- Re-perform the previous steps for other wavenumbers ν_0. This operation is conducted on the whole spectral domain including spectral margins that are important to minimize edge effects; a study has shown that margin of the order of 50 cm-1 are adequate.
- Reconstruct the spectrum from the two closest corrected sub-windows ($\nu \in [\nu_{0-}, \nu_{0+}]$) by linear interpolation:

$$L_{L1B,SRF}(\nu \in [\nu_{0-}, \nu_{0+}]) = C1(\nu) \times \hat{L}_{L1Ars,\nu_{0-}}(\nu) + C2(\nu) \times \hat{L}_{L1Ars,\nu_{0+}}(\nu)$$

$$C1(\nu) = \frac{\nu_{0+} - \nu}{\nu_{0+} - \nu_{0-}}, \qquad C2(\nu) = \frac{\nu - \nu_{0-}}{\nu_{0+} - \nu_{0-}}$$

RTF Uniformisation:

In addition to the SRF uniformisation, we apply an RTF uniformisation that cancels the SRF distortions produced by the RTF variations and in particular, the effect of etalon (RTF fast modulations). The idea is to cancel the signal distortion at spectrum level using a high spectral resolution guess of the measurement Sp_{ref}.

The issue is that we measure a product, which is not rigorously independent of the instrument transmission $T(\nu)$:

$$L_{L1Ar}(\nu) \cong \frac{[Sp.T \otimes SRF](\nu)}{[T \otimes SRF](\nu)} \neq [Sp \otimes SRF](\nu)$$

The factor $[T \otimes SRF](\nu)$ at the denominator is actually equal to the calibration factor computed with the radiometric calibration views noted $R_c(\nu)$.

Then, we use a high-resolution guess Sp_{ref} of Sp to compute the following correction factor:

$$L_{L1B,RTF}(\nu) = L_{L1B,SRF}(\nu) \times f_{corr}(\nu) \cong [Sp \otimes SRF](\nu)$$

With:

$$f_{corr}(\nu) = \frac{R_c(\nu) \times \left[Sp_{ref} \otimes SRF\right](\nu)}{\left[Sp_{ref}.T \otimes SRF\right](\nu)} \cong \frac{R_c(\nu) \times \left[Sp_{ref} \otimes SRF\right](\nu)}{\left[Sp_{ref}.R_c \otimes SRF\right](\nu)}$$

The RTF uniformisation processing steps are the following:

- Perform the guess computing the PC scores using a reference basis at IRS resolution $\hat{L}_{ref,n}(\nu)$:

$$PC(n) = \sum_{\nu} L_{L1B,SRF}(\nu) \times \hat{L}_{ref,n}(\nu)$$

- Compute the related high-resolution reference spectrum using the high-resolution basis:

$$Sp_{ref}(\nu) = \sum_{n} PC(n) \times L_{ref,n}(\nu), \quad \hat{L}_{ref,n}(\nu) = \left[L_{ref,n} \otimes SRF\right](\nu)$$

- Correct the spectra using the reference and the instrument total transmission $T(\nu)$ computed from the calibration views:

$$L_{L1B,RTF}(\nu) = L_{L1B,SRF}(\nu) \times \frac{R_c(\nu) \times \left[Sp_{ref} \otimes SRF\right](\nu)}{\left[Sp_{ref}.R_c \otimes SRF\right](\nu)}$$

After these two operations, the resulting spectra are independent of the instrument spectral response function: the information content is the same for all spectral samples and for all pixels. As a result, the only function to be considered by the users of the level-1 products is the numerical apodisation function applied at the beginning of the on-ground processing (section 5.3.1.2).

5.3.5.2 Computation issues and optimisation

SRF Uniformisation:

The SRF uniformisation versatility comes at a cost: memory access and heavy computation issues. We want to correct all 160x160 pixels in the matrix and target N_{wn0} wavenumbers, therefore, we need to perform N_{wn0}x160x160 fast Fourier transforms to compute the interferograms. Then each interferogram is divided by a SAF depending on the pixel number and the wavenumber. Finally, we perform again N_{wn0}x160x160 inverse fast Fourier transforms to retrieve the corrected spectra.

The total number of fast Fourier transforms is:

$$N_{FFTs} = 2 \times N_{wn0} \times 160 \times 160$$

Considering potential spatial interpolations, the SAF table size is (complex numbers):

$$Size_{SAF} = N_c \times N_r \times N_{opd} \times N_{wn0}$$

In order to reduce the computational cost of the SRF uniformisation, it is possible to act on:

- The pixel number $N_c \times N_r$:
  - Adjusting the pixel number do not affect the number of Fourier transforms but can decrease the size of the SAF table. Since we expect low SAF spatial variation, we could gather the SAFs in pixel sub-groups and re-compute them by spatial interpolation.

  To avoid the interpolation step and to be able to selectively correct unexpected defects at pixel level, we chose to set $N_c \times N_r = 160 \times 160$.

- The OPD length N_{opd}:
  - The SAF functions can fluctuate at high frequency, especially close to maximum OPD in the presence of RTF variations. However, we chose to include the RTF uniformisation processing after the SRF uniformisation to cope with the RTF variations.

  Therefore, the SAFs length could be reduced to only $N_{opd} = 2^9 = 512$ samples (using a power of two for the interferogram length greatly decreases the processing time).

- The wavenumber correction samples N_{wn0}:
  - Since we expect low SAF spectral variations, we can perform the SRF uniformisation for only a few wavenumbers and then recover the corrected spectrum by spectral interpolation (see 5.3.5.1).

  Taking N_{wn0} =100 samples per bands allows keeping a quite good liberty to tackle any unexpected defects. It is the same order of magnitude for the uniformisation processing of IASI.

In conclusion, to limit the data size and the processing power, the defaults parameters per band are the following:

$$N_{wn0} = 100, \qquad N_{opd} = 2^9 = 512$$
$$\rightarrow \quad N_{FFTs} = 2.621.440, \qquad Size_{SAF} = 1.3\ 10^9$$

RTF Uniformisation:

In the general case, the RTF uniformisation depends dynamically on the instrument transmission, to simplify the processing the transmission is considered a static data that can be updated on demand after the analysis of long series of calibration data. Since the correction vector is insensitive to RTF scaling, long-term optics deterioration without strong

wavenumber dependencies (such as icing) would not harm the processing efficiency. With the current knowledge of the instrument stability, we expect to update the transmission only between once a month and a year.

Then, to speed-up the processing, we pre-compute the two following matrix $V_{ref,n}(\nu) = T(\nu) \times \left[L_{ref,n} \otimes SRF\right](\nu)$ and $W_{ref,n}(\nu) = \left[L_{ref,n}\,.T \otimes SRF\right](\nu)$ and the correction writes simply:

$$L_{L1B,RTF}(\nu) = L_{L1B,SRF}(\nu) \times \frac{\sum_n PC(n) \times V_{ref,n}(\nu)}{\sum_n PC(n) \times W_{ref,n}(\nu)}$$

Then, the processing can also only target a particular wavenumber range, for IRS we plan focusing the correction at the beginning of the LWIR band between 680 and 800cm^{-1}.

The $L_{ref,n}$ basis is currently computed from high-resolution simulations, we expect to be able to use IASI-NG real data in the future. The correction is not expected to depend much on the basis computation hypothesis since the correction vector is insensitive to reference bias without any strong wavenumber dependencies.

We have shown that 10 PCs are enough to efficiently decrease the SRF distortions below 100mK equivalent temperature error.

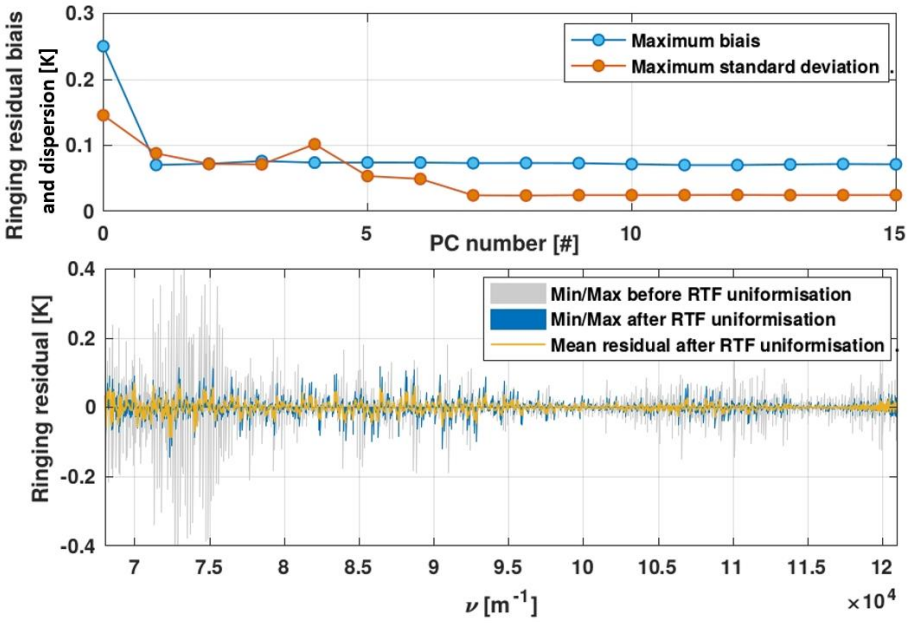

Figure 41: The maximum calibration ringing bias and standard deviation on the band is plotted in function of the number of PCs used in the RTF uniformisation (up). The minimum and maximum ringing errors are represented before and after RTF uniformisation using 10PCs, as well as the average residual (down)

5.4 SRF/SAF estimation model

The instrument state estimation is based on the on ground characterisation and in-flight

observables is the most representative of the actual state of the instrument. The table of SRFs, pre-calculated with the spectral model of IRS (section 5.4.1), must span the whole instrument state space i.e. the number of dimensions of the table must equal to the number of different types of observables.

A typical observable is the spectral shift of the measured spectrum. The spectral shift may be the consequence, for example, of a focal plane misalignment or of residual perturbations (i.e. uncorrected by the metrology system) of the cube corner motion. The observable "spectral shift", if available from various detector positions, can then provide information on the instrument state by separating the impact from different contributors (listed in 5.4.1) if they are adequately resolved in the simulated look-up tables. In other words, the SRF-EM exploits the differential effect of instrument state parameter variations on the spectral shift, as explained in **Error! Reference source not found.**

The number of dimensions of the look-up tables can be increased during the mission lifetime if perturbation sources contributing to the observables, unknown before launch, are detected during the calibration/validation phase or by the routine monitoring. An hypothetical example of such an effect is the impact of the instrument temperature variations on the chromatism.

The SAF table is generated fully offline. Hence the SRF simulation model (section 5.4.1) is not part of the IRS L1 processing specification that addresses solely the online processing.

5.4.1 IRS spectral model

As presented in section 3.4, the spectral response function SRF of the spectral channel ν, of a pixel (i,j), of a band b, is the function that links the real spectrum $S(\nu)$ of a spatially uniform scene observed by the instrument with the measured spectrum $S_{meas}(\nu_0)$:

$$S_{meas}(\nu_0) = \int_0^{\infty} S(\nu).SRF_{\nu_0}(\nu)d\nu \qquad \textit{Eq. 68}$$

As such, the SRF is thus tightly linked to the instrument parameters as well as the characteristics of processing performed on board. Its estimation takes into account:

- The instrument PSF (IPSF) which is the result of the convolution between the optical PSF of the instrument with the detector response. It depends on the focal of the back telescope, on the size and position of the considered pixel, on the sampling step and varies spectrally;
- The corner cube motion law, described by:
  - the speed and speed variations of the corner cube,
  - the frequency of the oscillations: phase and amplitude,
  - the trajectory (characterized for example by a polynomial offset, linear, parabolic and cubic).

  In the case of IRS, these effects are estimated and corrected on-board by the metrology system;
- The focal plane alignment with respect to the interferometer axis;
- Zero path distance positions of the interferometer (including for example the fixed corner cube misalignment)
- The wavenumber = chromatism;
- The interferogram OPD sampling;

- The numerical apodisation as defined in the section 5.3.1.2.

Among all these, the PSF and the ZPD map play a major role.

The Fourier transform of the spectral response function (SRF) gives the self-apodisation function (SAF) times the numerical apodisation:

$$\boxed{SRF_{L1A}(\nu) = FT[SAF(x) \times Apod(x)]}$$

As mentioned in the previous section, the SAF represents the monochromatic interferometer spectral transfer function. This function is applied in the SRF uniformisation processing in order to harmonize the spectral response function over the matrix detectors.

After SRF and RTF uniformisation, the SRF is computed exclusively from the numerical apodisation:

$$\boxed{SRF_{L1B}(\nu) = FT[Apod(x)]}$$

5.4.2 Main steps and parameters involved in the SRF/SAF computation

5.4.2.1 Interferogram sampling

We consider that the resampling processing performed on-board corrects perfectly the anomalies of the corner cube trajectory. This assumption accuracy has been verified by industry on ground.

Moreover, we assume that the interferogram filtering performed on-board is not influencing the SRF shape, since the L1B wavenumbers are far from the FIR response edges it is a safe hypothesis.

Therefore, the only factor affecting the SRF is the maximum OPD that defines the SAF definition range.

5.4.2.2 Self-Apodisation computation

In the following subsections, we describe the calculation of the self-apodisation function $SAF(x)$.

- **<u>Complex interferogram</u>**

We write the complex interferogram at field of view $\boldsymbol{\theta_0}$ in function of the OPD for a laser at wavenumber ν and an instrument free of any defects:

$$I(\boldsymbol{\theta_0}, x) = e^{2i\pi\nu x\cos(\boldsymbol{\theta_0})}$$

Then, we introduce the fixed corner cube misalignment and the beam splitter defects; they are accounted with a ZPD function of $\boldsymbol{\theta_0}$ and ν, $ZPD(\boldsymbol{\theta_0}, \nu)$:

$$I(\boldsymbol{\theta_0}, x) = e^{2i\pi\nu[x\cos(\boldsymbol{\theta_0}) + ZPD(\boldsymbol{\theta_0},\nu)]}$$

Now, we consider the chromatic angular PSF of the pixel at $\boldsymbol{\theta_0}$, $PSF_{\boldsymbol{\theta_0}}(\boldsymbol{\theta}, \nu)$:

$$I(\boldsymbol{\theta_0}, x) = \int d\boldsymbol{\theta}\, PSF_{\boldsymbol{\theta_0}}(\boldsymbol{\theta}, \nu) \times e^{2i\pi\nu[x\cos(\boldsymbol{\theta}) + ZPD(\theta,\nu)]}$$

- **Metrology**

We now introduce the metrology resampling at field of view $\boldsymbol{\theta_0}$. The related metrology field of view at which the resampling occurs is noted $\boldsymbol{\theta_{metro}(\theta_0)}$, the on ground tests of the interferometer allows characterizing the metrology alignment so that $\boldsymbol{\theta_{metro}(\theta_0) \cong \theta_0}$.

$$I(\boldsymbol{\theta_0}, x) = \int d\boldsymbol{\theta}\, PSF_{\boldsymbol{\theta_0}}(\boldsymbol{\theta}, \nu) \times e^{2i\pi\nu[x\cos(\boldsymbol{\theta}) + ZPD(\boldsymbol{\theta},\nu)]} \times e^{2i\pi\nu[x\{1-\cos(\boldsymbol{\theta_{metro}})\} - ZPD(\boldsymbol{\theta_{metro}},\nu)]}$$
$$= e^{2i\pi\nu x} \times \int d\boldsymbol{\theta}\, PSF_{\boldsymbol{\theta_0}}(\boldsymbol{\theta}, \nu) \times e^{2i\pi\nu[x\{\cos(\boldsymbol{\theta}) - \cos(\boldsymbol{\theta_{metro}})\} + ZPD(\boldsymbol{\theta}) - ZPD(\boldsymbol{\theta_{metro}},\nu)]}$$

For IRS, in the general case, we can safely take $\boldsymbol{\theta_{metro}(\theta_0) = \theta_0}$ without degrading the performances since the spectral calibration cancels the related spectral scale factor and the self-apodisation is too weak to be affected; the second point was not fulfilled for IASI.

Therefore, the interferogram writes as a perfect laser interferogram $e^{2i\pi\nu x}$ times a self-apodisation function:

$$\boxed{SAF_0(\boldsymbol{\theta_0}, x, \nu) = \int d\boldsymbol{\theta}\, PSF_{\boldsymbol{\theta_0}}(\boldsymbol{\theta}, \nu) \times e^{2i\pi\nu[x\{\cos(\boldsymbol{\theta}) - \cos(\boldsymbol{\theta_{metro}})\} + ZPD(\boldsymbol{\theta},\nu) - ZPD(\boldsymbol{\theta_{metro}},\nu)]}}$$

- **Radiometric calibration**

Then, we model approximately the radiometric calibration as a low spectral frequency correction, the SAF becomes:

$$\boxed{SAF_R(\boldsymbol{\theta_0}, x, \nu) = \frac{SAF_0(\boldsymbol{\theta_0}, x, \nu)}{SAF_0(\boldsymbol{\theta_0}, 0, \nu)}, \qquad SAF_R(\boldsymbol{\theta_0}, 0, \nu) = 1}$$

At the end of the radiometric calibration, we keep only the real part of the spectra:

$$Re[Sp(\nu)] = \frac{Sp(\nu) + Sp(\nu)^*}{2} = \frac{FT[I(x) \times SAF_R(\boldsymbol{\theta_0}, x, \nu)] + FT[I(x) \times SAF_R(\boldsymbol{\theta_0}, x, \nu)]^*}{2}$$
$$= FT\left[I(x) \times \frac{SAF_R(\boldsymbol{\theta_0}, x, \nu) + SAF_R(\boldsymbol{\theta_0}, -x, \nu)^*}{2}\right]$$

Therefore, the SAF applied to the real product becomes:

$$\boxed{SAF_{RR}(\boldsymbol{\theta_0}, x, \nu) = \frac{SAF_R(\boldsymbol{\theta_0}, x, \nu) + SAF_R(\boldsymbol{\theta_0}, -x, \nu)^*}{2}}$$

5.4.2.3 Radiometric Transfer Function

The SRF model implicitly assumes a constant radiometric response over the relevant spectral domain. The radiometric transfer function $R_c(\nu)$, also called the radiometric response, plays a key role in the SRF estimation in the case of MTG-IRS. It has been shown that the local fluctuations of the response around the considered spectral channel have a significant impact on the SRF. For IRS we have designed a dedicated processing called the RTF uniformisation to cope with these effects, therefore the SAF computation does not include the RTF variations.

5.4.2.4 Input stability

For IRS, all inputs of the SRF-EM are considered quasi-static. Following the industry reports, we expect to update the inputs less than once a month.

5.4.2.5 Numerical Apodisation

In the IRS processing, numerical apodisation is used to damp the SRF lobes far away from the central peak. It is described in the pre-processing, section 5.3.1.2. The numerical apodisation is not part of the SAF definition.

5.5 Science processing for the imager mode

In total, four high-resolution broadband images are generated in each band: two at the beginning and two at the end of each dwell. The primary use of these images is the geo-location of the corresponding dwell, a usage that does not impose stringent requirements on the radiometric performances (there is no such requirement in the EURD). But the imager mode can also be used for monitoring the detector and estimating the scene heterogeneity at sub-pixel level. The main advantages of doing so are the co-registration and the simultaneity with the sounder data by design. The drawback with respect to classical radiometers is the broad spectral response implying a reduced sensitivity to cloud contamination.

It is worth recalling that image mode data are extracted as single samples from the sub-pixel interferograms. Their integration time corresponds to a single sample of the interferogram i.e. just below 400 microseconds; since they are acquired when the cube corner is moving, each image is actually an instantaneous view of the base line of the interferogram and will be contaminated by noise and spectral content. Even if read at the same time, a pixel in the vicinity of the interferometric axis and a pixel on the edge of the detector will not sample the same position of the interferogram (they will see a different OPD). Furthermore, since the detector is read in 9 successive frames, a single image will be made up of samples corresponding to a large range of OPD values i.e. spectral content. Finally, the individual images do not undergo any processing on board; they are in particular not corrected for the detector and electronic non-linearity.

5.5.1 Imager mode performances

5.5.1.1 Non-linearity correction

The documentation provided by the instrument manufacturer does not give any information on linearity characterisation at sub-pixel level; indeed, all efforts (characterisation and correction) apply to the sounding pixel level, i.e. to binned interferograms over 3x3 sub-pixels. Furthermore, the non-linearity characterization does not access to any sub-pixel information: the correction polynomials are directly derived at the scale of the sounding pixel.

In practice, there are the following alternatives for imager mode non-linearity correction:

1) It is simply ignored. However, uncorrected non-linearity can lead to calibration errors at the percent level, which is significant in terms of absolute calibration.
2) It is ignored, but the error is mitigated by an absolute calibration of imager mode radiances with the corresponding integrated sounder radiances at the scale of a sounder pixel. The (sub-pixel independent) non-linearity correction applied at pixel level is thus implicitly propagated to the imager mode radiances. Residual non-linearity errors will be due to variable sub-pixel non-linearity (if any) and to the non-linearity in the sub-pixel radiance distribution.
3) Non-linearity correction is explicitly applied with correction parameters derived from non-linearity correction polynomials at the sounder pixel scale (under the hypothesis of homogeneous sub-detector non-linearity). However, the feasibility is not guaranteed due to potentially different detection and video chains (and associated non-linearity) involved in imaging and sounding mode acquisition.
4) Non-linearity correction is explicitly applied at sub-pixel scale if correction polynomials are available. The latter is yet not ensured during commissioning but this has to be confirmed. Alternative (4) is the only one accounting for potential sub-pixel variations of non-linearity, but there is no capacity for stability monitoring, thus it supposes lifetime stability of sub-pixel non-linearity.

Considering the available information, we have chosen to follow the approach 2) that is both easy to implement and expected to be efficient in removing most of the non-linearity error without explicit knowledge at sub-pixel level.

5.5.1.2 Radiometric noise

The radiometric noise of the individual images has been estimated from simulations and is summarized in Table 7 for different temperatures. It is recalled that in nominal operations, four images are acquired per dwell so there is potential for a further noise reduction by a factor of 2 when they are averaged.

	SNR	NEdT@260K [K]	NEdT@280K [K]	NEdT@300K [K]
LWIR	1300	0.085	0.067	0.055
MWIR-AT	200	0.144	0.079	0.047
MWIR-EB	800	0.198	0.108	0.059

Table 7: Estimated noise of calibrated single-sample imaging mode data in SNR and in NEdT at 260K, 280K, 300K

This estimate however does not take into account the baseline deviations. It has been assumed that typical imaging mode raw data are characterized by the baseline (BL) value and a random variability corresponding to the reported BL standard deviation of the EV target. Without noise, this random variability represents the source of the radiometric calibration error due to the inequality between IFG baseline and extracted IFG sample. For the LWIR channel, errors due to BL variation dominate the effect of instrument noise in the equivalent total SNR. The estimated equivalent radiometric calibration SNR corresponds to calibration errors of about 0.15K in NEdT at 280K. The radiometric noise on the other hand will be below 0.10K. These performances suggest equivalence with performances of classical atmospheric window imager channels, even when taking account the slightly reduced sensitivity to surface or cloud variability due to the increased sensitivity to atmospheric composition.

The noise in MWIR is of the order of 0.1 K and the impact of the baseline variations is lower. However, due to the low sensitivity of this channel to surface features, the benefit for users from calibrated images is, independently of the radiometric performance, less obvious. This channel will thus not be considered for user dissemination (but MWIR images will be calibrated).

5.5.2 Imager mode calibration concept

The explicit radiometric calibration of imaging mode radiances using imaging mode calibration target acquisitions is replaced by a relative calibration. The absolute calibration is obtained by adjusting the image mode data of each (by design perfectly co-registered) sounder pixel to the spectrally integrated radiance derived from the normal (sounding) mode processing chain.

5.5.2.1 Processing of BB and DS1 acquisitions

The images $\mathbf{Z^{BB}}$, $\mathbf{Z^{DS1}}$ and $\mathbf{Z^{DS2}}$ are obtained along with the interferogram data cubes when the BB, DS1 and DS2 views are acquired, respectively. The quantity $\mathbf{Z^{BB} - Z^{DS1}}$ is computed at each LAC transition phase i.e. every 15 minutes by averaging the images taken at that time:

$$\mathbf{Z^{BB}} = \frac{1}{N_{BB}} \sum_{t=1}^{N_{BB}} \mathbf{Z_t^{BB}}$$

$$\mathbf{Z^{DS1}} = \frac{1}{N_{DS1}} \sum_{t=1}^{N_{DS1}} \mathbf{Z_t^{DS1}}$$

Eq. 95/A

The value $\mathbf{Z^{BB} - Z^{DS1}}$ is used in the radiometric equation until a new set of BB and DS1 become available.

No filtering including the recent measurement history of BB and DS1 acquisitions is applied, opposite to the processing (in sounder mode) of the complex radiometric response of the core section (section 5.3.2.2 of ATBD). This is because $\mathbf{Z^{BB}}$ variations include temperature variations of the calibration blackbody, moreover the assumption is made that this temperature is constant over the period of N_{BB} dwells (nominally about 30 seconds during a

LAC transition).

Instrument noise contributing to $\mathbf{Z^{BB} - Z^{DS1}}$ is certainly not fully negligible, which is a shortcoming of the former explicit calibration concept. In the proposed concept, such filtering is introduced, but postponed to the next step (avoiding any dependence on the current BB temperature), which consists of the evaluation of the sub-pixel detector uniformity.

5.5.2.2 Detector uniformity

The uniformity of the detector, called **K,** also known as the photo-response non-uniformity (PRNU), is the variation of the output signal from pixel to pixel. It is calculated from the blackbody views acquired for each band between the LACs (which have the property to be spatially uniform) from which the dark current estimated from the DS1 views is removed and normalized by the mean value of the signal:

$$\mathbf{K} = \frac{\mathbf{Z^{BB} - Z^{DS1}}}{\frac{1}{N_{cc}N_{rr}}\sum_{ii}^{N_{cc}}\sum_{jj}^{N_{rr}}\left(Z^{BB}[ii,jj] - Z^{DS1}[ii,jj]\right)} \qquad \textit{Eq. 92/B}$$

where $\mathbf{Z^{BB}}$, $\mathbf{Z^{DS1}}$ and **K** are 480x480 pixels arrays. **K** is used for monitoring the health of the detector.

The approach is indeed to use **K** for monitoring of the detector health and, via thresholds (which necessarily should take a certain history into account), for sub-pixel deselection. Details of such monitoring appear currently still undefined.

In terms of radiometric calibration, **K** can also be used for a relative calibration of imaging mode radiances ("flat-field correction", see section 5.5.2.4).

The noise in **K** is reduced by implementation of a time filtering process over several LAC transitions. The filtering process should be identical to that of the core section radiometric response at sounder pixel scale (described in ATBD section 5.3.2.2):

In order to remove noise and increase accuracy, an average can be performed over a pre-defined number of calibration events $n_{cal_{ev}}$. To do so, the radiometric response computed during each calibration event is archived in the calibration database as a rolling archive (only the $n_{cal_{ev}}$ most recent estimations of $\widetilde{R_c(v)}$ are kept).

5.5.2.3 Processing of DS2 acquisitions (instrument background)

DS2 images are acquired once at the beginning/end of each E-W and W-E scan, i.e. typically four or five times per LAC.

The first step is to apply the straylight rejection test, indeed straylight contaminated DS2 images should not be processed for calibration purpose. The rejection criterion is currently undefined, even in normal (sounding) mode. It is expected that the imaging mode rejection criterion will be linked in some way to the criterion in nominal mode.

DS2 views are acquired at different scan mirror incidence angles. The impact of the angular dependence of the scan mirror reflectivity (and residual emission) had been neglected in

former ATBD versions of the radiometric calibration equation, not only in imaging mode.

Each DS2 image should therefore be normalised to a reference scan mirror incidence angle (most practically α_E, for which the front section transmission is characterised).

As a reminder, for complex raw spectra:

$$\widetilde{S_\nu^{DS2}(\alpha_E)} = \widetilde{S_\nu^{DS2}(\alpha_{DS2})} + \widetilde{R_c(\nu)} \cdot \left(\mathcal{P}(T_{SM}) \cdot \frac{\alpha_{DS2} - \alpha_E}{\alpha_W - \alpha_E} \Delta\tau_\nu^{FS} \right) \qquad \textbf{Eq. C}$$

The same equation in imaging mode writes

$$Z^{DS2}(\alpha_E) = Z^{DS2}(\alpha_{DS2}) + \frac{\alpha_{DS2} - \alpha_E}{\alpha_W - \alpha_E} \int R_c\ (\nu) \cdot \Delta\tau_\nu^{FS} \cdot \mathcal{P}(T_{SM})\, d\nu \qquad \textbf{Eq. D}$$

The adjustment consists in the addition (or subtraction) of the scan mirror emission difference at the actual and reference scan mirror incidence angles. It depends on the scan mirror reflectivity difference, characterised at two reference incidence angles for each sounder pixel, and in addition on the scan mirror temperature T_{SM}.

However, the core section transmission $R_c\ (\nu)$ is not accessible in Eq. D. It is unlikely that the module of the complex core section transmission in sounding mode $\widetilde{R_c(\nu)}$ can be used, since it is evaluated after decimation and Fourier transform. On the other hand, it can be derived as a quasi-static function from an external Radiometric Transfer Function (RTF) Model $RTF^{ref}(\nu)$. It is currently unknown if such model should be dependent on the sounder pixel $[i,j]$. In the most favourable case, the same model can be used for the entire detector array. The RTF model shall take account of the detector efficiency and all transmission effects of the core section, i.e. excluding front section and FIM reflectivity.

The second part of the approach is to characterise once in a while the integrated average detection response for a given BB/DS1 acquisition event with known BB temperature T_{BB}.

We define the average detection response R_D^{av}:

$$R_D^{av} = \frac{\frac{1}{N_{cc}N_{rr}} \sum_{ii}^{N_{cc}} \sum_{jj}^{N_{rr}} \left(Z^{BB}[ii,jj] - Z^{DS1}[ii,jj] \right)}{\int RTF^{ref}(\nu) \cdot \rho^{FIM}(\nu) \cdot \mathcal{P}(T_{BB},\nu)\, d\nu} \qquad \textbf{Eq. F}$$

In Eq.F, the FIM reflectivity $\rho^{FIM}(\nu)$ appears explicitly in the denominator. The FIM reflectivity $\rho_\nu^{FIM}[i,j]$ is characterised at low frequency for each sounding pixel and stored in PAD. As for the static or quasi-static RTF model $RTF^{ref}(\nu)$, it is expected that the array average of the FIM reflectivity as function of wavenumber is sufficiently accurate. Both terms are meant to provide a realistic "windowing" shape for the blackbody emission $\mathcal{P}(T_{BB},\nu)$ under the integral of the denominator in Eq.F. The knowledge accuracy requirements are not very demanding.

Deviations of the individual sub-pixel core section response $R_c\ [ii,jj]$ are due to detector uniformity. Thus:

$$R_c\ [ii,jj] = R_D^{av} \cdot K[ii,jj] \qquad \textbf{Eq. G}$$

This approach is separating the (in imager mode unknown) spectrally integrated detection gain from the effects relevant to the sub-pixel core section response (included in the detector uniformity matrix, which in addition takes benefit from noise reduction).

The knowledge of the detection gains is required for the only purpose of implementing the scan mirror incidence angle normalisation of the instrument background DS2 raw images.

In Eq.D, we can substitute the sub-pixel dependent spectral core section response:

$$R_c\ (\nu)[ii,jj] = R_c\ [ii,jj] \cdot RTF^{ref}(\nu) \qquad \textbf{Eq. H}$$

Note: The normalisation condition for RTF is unity of its integral.

Eq.D simplifies to:

$$Z_{ii,jj}^{DS2}(\alpha_E) = Z_{ii,jj}^{DS2}(\alpha_{DS2}) + \frac{\alpha_{DS2} - \alpha_E}{\alpha_W - \alpha_E} \cdot R_c\ [ii,jj] \int RTF^{ref}(\nu) \cdot \Delta\tau^{FS}(\nu)[i,j] \cdot \mathcal{P}(T_{SM})\, d\nu \qquad \textbf{Eq. I}$$

The expression under the integral contains the static RTF model, the E-W front section transmission variation characterised at low frequency for each sounding pixel, and depends on the scan mirror temperature T_{SM}.

We refer this expression to as the scan mirror angle correction sensitivity S_{SM}.

$$S_{SM}(i,j,T_{SM}) = \int RTF^{ref}(\nu) \cdot \Delta\tau^{FS}(\nu)[i,j] \cdot \mathcal{P}(T_{SM})\, d\nu \qquad \textbf{Eq. J}$$

This quantity must be provided as Processing Analysis Data (PAD) to the L1 processor for each sounding pixel *[i,j]* (considered constant for the nine associated sub-pixels *[ii,jj]*) with a sampling of various scan temperatures in the expected range of variability, from which the scan mirror angle correction sensitivity is interpolated to the actual scan mirror temperature.

The final formulation of the instrument background normalisation to the reference angle $\square_E$ is then:

$$Z_{ii,jj}^{DS2}(\alpha_E) = Z_{ii,jj}^{DS2}(\alpha_{DS2}) + \frac{\alpha_{DS2} - \alpha_E}{\alpha_W - \alpha_E} \cdot R_c\ [ii,jj] \cdot S_{SM}(i,j,T_{SM}) \qquad \textbf{Eq. K}$$

with $Z_{ii,jj}^{DS2}(\alpha_{DS2})$ the measured background.

Only after this normalisation, the linear regression coefficients for the extrapolation in time of the instrument background up to the next DS2 acquisition can be evaluated, as originally described in the ATBD.

The instrument background, noted $\mathbf{Z^{DS2}}$ is extrapolated from the series of previous DS2 images as it is done for the interferograms data cubes: each time a new DS2 image is acquired, a linear fit is performed for each pixel over the previous valid DS2 to compute the offset A and the slope B of the fit:

$$(A,B) = LINFIT(Z_t^{DS2}[ii,jj]) \qquad \textbf{Eq. 96/L}$$

5.5.2.4 Processing of EV acquisitions (radiometric calibration)

It is proposed to abstain from an explicit absolute calibration of EV images not only to simplify the imaging mode processing chain, but also to take benefit of the radiometric calibration already accomplished in normal (sounding mode), which do not need to be repeated and which is approximate with regard to some spectrally integrated properties.

The first step is to extrapolate the instrument background (normalised to scan mirror incidence angle α_E).

Then $\mathbf{Z^{DS2}}$ at time t is estimated using:

$$Z^{DS2}(\alpha_E)[ii,jj] = A + Bt \qquad \textit{Eq. 97/N}$$

The latter equation is used as function of acquisition time of the current EV dwell with coefficients (*A*, *B*) from Eq.96/L in section 5.5.2.3.

The resulting background values must be adjusted to the current scan mirror incidence angle α_{EV}. After interpolation of the scan mirror angle correction sensitivity to the current scan mirror temperature:

$$Z^{DS2}(\alpha_{EV})[ii,jj] = Z^{DS2}(\alpha_E)[ii,jj] - \frac{\alpha_{EV} - \alpha_E}{\alpha_W - \alpha_E} \cdot R_c\ [ii,jj] \cdot S_{SM}(i,j,T_{SM}) \qquad \textit{Eq. O}$$

Notation: $Z^{DS2}(\alpha_{EV})[ii,jj]$ are the elements of the matrix $\mathbf{Z^{DS2}}$ in the following. This matrix describes the instrument background at the time of the current EV dwell and for the same scan mirror incidence angle for which the current EV image $\mathbf{Z^{EV}}$ is taken.

A flat-field correction is applied after background subtraction.

5.5.2.5 Image calibration

The Earth views can then be flat-field corrected using matrix **K**; we have then:

$$\mathbf{S^{EV}_{Flat}} = \frac{(\mathbf{Z^{EV}} - \mathbf{Z^{DS2}})}{\mathbf{K}} \qquad \textit{Eq. 93/P}$$

where $\mathbf{Z^{EV}}$ and $\mathbf{Z^{DS2}}$ are 480x480 pixels images (note that the division is here done elements by elements). ……

$\mathbf{S^{EV}_{Flat}}$ corresponds to an EV raw radiance matrix (per band), normalised to a uniform photo response across the detector array.

Main perturbation sources are noise (in particular on $\mathbf{Z^{EV}}$, based on a single dwell) and the physical deviation of the extracted sample constituting $\mathbf{Z^{EV}}$ from the actual IFG baseline (effects assessed in section 5.5.1). Neglecting, these effects, the image is nevertheless not fully proportional to the received energy because of the variation of the FIM mirror reflectance/FS transmission ratio across the detector array.

However, this ratio is constant over the nine sub-pixels of any sounder pixel. The variation across the array can therefore be introduced by integration of the calibrated spectral radiances derived from the sounding mode, where the FIM/FS transmission correction has been achieved.

Thus, for any sounder pixel *[i,j]*, the integrated calibrated radiance $L_{int}[i,j]$ corresponds to the average of the flat-field corrected imaging mode raw radiances $\mathrm{S}^{\mathrm{EV}}_{\mathrm{Flat}}[ii,jj]$ and the distribution of $\mathrm{S}^{\mathrm{EV}}_{\mathrm{Flat}}[ii,jj]$ describes, in relative terms, the sub-pixel variability of the EV target some users ask for having access to.

For consistency in terms of information available to the user, the radiance is considered only

in the useful band, composed of *NL1B* spectral channels (with sampling distance *dWn*) associated with calibrated spectral radiances $L_{EV}[i,j,k]$ (in $Wm^{-2}sr^{-1}cm$). Although the actual raw radiances contain (limited) information from outside the useful band, the convention to refer the signal to information in the useful band appears most practicable.

The integrated radiance $L_{int}[i,j]$ (in $Wm^{-2}sr^{-1}$) is thus derived from the L1B spectral radiance $L_{EV}[i,j,k]$ as output of the nominal (sounding) mode processing:

$$L_{int}[i,j] = dWn \cdot \sum_{k=1}^{NL1B} L_{EV}[i,j,k] \qquad \textbf{Eq. Q}$$

The condition for each sounder pixel $[i,j]$ with its associated $N_{ii,jj}$ (≤9) non-deselected sub-pixels $[ii,jj]$ is:

$$L_{int}[i,j] = G[i,j] \cdot \frac{1}{N_{ii,jj}} \cdot \sum_{n=1}^{Nii,jj} S_{Flat}^{EV}[ii,jj] \qquad \textbf{Eq. R}$$

The sounder pixel dependent gain factor between flat-field corrected raw images and absolute radiances is thus:

$$G[i,j] = L_{int}[i,j] / \left(\frac{1}{N_{ii,jj}} \cdot \sum_{n=1}^{Nii,jj} S_{Flat}^{EV}[ii,jj] \right) \qquad \textbf{Eq. S}$$

It accounts for the gain of the detection chain and the "array localised" integrated ratio of the FIM/FS transmission ratio.

The calibrated imaging mode sub-pixel radiances are:

$$L_{IM}[ii,jj] = G[i,j] \cdot S_{Flat}^{EV}[ii,jj] \qquad \textbf{Eq. T}$$

The unit of the image $\mathbf{L_{IM}}$ is ($Wm^{-2}sr^{-1}$).

However, for most applications a conversion in brightness temperature might be preferable, even if brightness temperature conversion for broadband channels inevitably involves further approximations (the problem is well known for any classical imager channel, it is just enhanced by the unusual bandwidth).

Explicit brightness temperature conversion involves two steps: (i) conversion into spectral radiance by means of an effective bandwidth, (ii) conversion into brightness temperature by means of a central wavenumber. However, the effective central wavenumber of broad bands depends on the measured spectrum itself.

We pursue a simpler while not less accurate approach, which is to use an analytical conversion equation derived from brightness temperature conversion look-up tables at suitable sampling m of the blackbody temperature T^{BB}.

For each L1B channel $k \in \{1, NL1B\}$ and all sampled blackbody temperatures (index m), the spectral radiances are:

$$N_k^m = \mathcal{P}(T_m^{BB}, Wn_k) \qquad \textbf{Eq. U1}$$

The integrated radiances are:

$$L_{int}^{m} = dWn \cdot \sum_{k=1}^{NL1B} N_k^m \qquad \textit{Eq. U2}$$

The brightness temperature conversion is obtained by polynomial regression of the samples $T_m^{BB}(L_{int}^m)$, leading to the global, static conversion formula:

$$Tb(L_{int}) = a_0 + a_1 \cdot L_{int} + a_2 \cdot L_{int}^2 + \ \ldots \qquad \textit{Eq. U3}$$

Note: $Tb(L_{int})$ is a static function, available from PAD.

The resulting images in brightness temperature $\mathbf{BT_{IM}}$ are given by:

$$\mathbf{BT_{IM}} = Tb(\mathbf{L_{IM}}) \qquad \textit{Eq. V}$$

IRS imaging mode data constitute the only reliable NRT data source providing heterogeneity information at the IRS sounder pixel scale. Inclusion of this information to the L1B product is requested by users, even if outside of any cloud flag retrieval, but as an indicator of the radiative sub-pixel heterogeneity. It is still open if full images are included in the L1B product or if the images are condensed to a heterogeneity index (HI), which is potentially the information most adequate to user needs.

An obvious candidate for such heterogeneity index (HI_V) (per spectral band, independently of the question whether an MWIR heterogeneity is beneficial for any user application), is the standard deviation of calibrated radiances $L_{IM}[ii,jj]$ over the $N_{ii,jj}$ valid sub-pixels of each IRS sounder pixel *[i,j]*.

$$HI_V[i,j] = \sqrt{\frac{1}{N_{ii,jj}} \cdot \left(\sum_{ii,jj=1}^{Nii,jj} \left(L_{IM}[ii,jj]\right)^2 \right) - \left(\frac{1}{N_{ii,jj}} \cdot \sum_{ii,jj=1}^{Nii,jj} L_{IM}[ii,jj] \right)^2} \qquad \textit{Eq W.}$$

The second term, by construction has been used for absolute calibration and is already available from Eq. Q.

$$HI_V[i,j] = \sqrt{\frac{1}{N_{ii,jj}} \cdot \left(\sum_{ii,jj=1}^{Nii,jj} \left(L_{IM}[ii,jj]\right)^2 \right) - (L_{int}[i,j])^2} \qquad \textit{Eq. X}$$

It appears recommendable to include the average radiance (HI_M) per band and sounder pixel as second index, unless it is left to the interested user to compute this radiance via Eq. Q.

$$HI_M[i,j] = L_{int}[i,j] \qquad \textit{Eq. Y}$$

This enables

- a first-glance discrimination of hot and cold scenes;
- the *a posteriori* evaluation of the heterogeneity index over an area extended to several IRS sounder pixels.

The proposed heterogeneity indices are in radiance units. Most likely, users prefer brightness temperature units.

The conversion (no matter if included in the L1 processing or left to the users) is applied as

follows.

The conversion of the sounder pixel average radiance in brightness temperature:

$$BT\_HI_M[i,j] = Tb(HI_M[i,j]) \quad \textit{Eq. Z1}$$

The conversion of sub-pixel standard deviation from radiance to brightness temperature:

$$BT\_HI_V[i,j] = \frac{Tb(HI_M[i,j] + HI_V[i,j]) - Tb(HI_M[i,j] - HI_V[i,j])}{2} \quad \textit{Eq. Z2}$$

Or, alternatively, the conversion of sub-pixel standard deviation from radiance to NEdT at reference temperature T_0 (usually 280K) and with L_{int}^0 the integrated BB radiance at T_0 after Eqs. U1 and U2:

$$NEdT\_HI_V[i,j] = \frac{Tb(L_{int}^0 + HI_V[i,j]) - Tb(L_{int}^0 - HI_V[i,j])}{2} \quad \textit{Eq. Z3}$$

The above proposal of two heterogeneity indices corresponds to a compression factor 4.5 with respect to the hypothetical scenario of full inclusion of images in the IRS L1B product. In case that lower compression is acceptable, next candidates for an extended heterogeneity index are the peak-to-peak radiance/brightness temperature difference or the maximum/minimum values over the sub-detectors.

5.5.3 Summary of the imager mode science processing

Long-term monitoring (PAD interface)

- RTF model (static or quasi-static if proved obsolete during lifetime). One model per spectral band (TBC) – No equation, section 5.5.2.3
- Computation of the global, static, analytical radiance-brightness temperature conversion function (per spectral band) – Eq.U(1-3), section 5.5.2.4
- Array average of the FIM reflectivity (per spectral band) as function of wavenumber (update at each FIM reflectivity characterisation) – No equation, section 5.5.2.3
- Update of the array averaged detector response upon a nominal BB/DS1 acquisition triplet with known BB temperature – Eq.F (frequency TBD)
- Computation of the scan mirror angle correction sensitivity for an adequate sampling (M) of scan mirror temperatures (160 X 160 X M)– Eq.J (update depending on low-frequency front section transmission characterisation and – if any – on RTF model update)

Every LAC transition (BB and DS1 acquisitions, 480 X 480))

- Averaging of BB and DS1 triple-acquisitions – Eq.95/A
- Computation of the instantaneous PRNU – Eq.92/B
- Filtering of the instantaneous PRNU with recent history – No equation, section **Error! Reference source not found.**
- Computation of the sub-pixel (spectral) core section response – Eq.G (required for DS2 scan mirror incidence angle normalisation, section 5.5.2.3)

Every DS2 acquisition (4 or 5 times per LAC, 480 X 480)

- Straylight rejection test – Yet undefined.
- Interpolation of the scan mirror angle correction sensitivity to the actual scan mirror temperature (160 X 160) – Interpolation of Eq.J
- DS2 normalisation to the reference scan mirror incidence angle – Eq.K
- Determination of linear regression coefficients (for time extrapolation) from the recent DS2 acquisition history – Eq.96/L

Every EV acquisition (480x480)

- Time extrapolation of the instrument background to the acquisition time of the current dwell – Eq.97/N
- Interpolation of the scan mirror angle correction sensitivity to the actual scan mirror temperature (160 X 160) – Interpolation of Eq.J
- Adjustment of the extrapolated instrument background to the scan mirror incidence angle of the current dwell – Eq.O
- Computation of the flat field corrected EV raw images (subtraction of instrument background, division by PRNU) – Eq.93/P
- Extraction of the (calibrated) spectral radiance of each sounding pixel (160 X 160) and spectral integration – Eq.Q
- Computation of the sub-pixel dependent absolute calibration gain factor – Eq.S
- Absolute calibration of the (up to) nine sub-pixel radiances of each sounding pixel – Eq.T
- Image brightness temperature conversion – Eq.V
- Computation of a heterogeneity index (radiance units, 160 X 160) – Eq.X
- Brightness temperature/NEdT conversion of the heterogeneity index in radiance units (160 X 160) – Eq.Z(1-3)

5.5.4 Options for merging individual images extracted from a common dwell

So far, the radiometric calibration process for the IRS imaging mode is described as if there would be a single image per dwell. In standard operational conditions, four images are acquired: two at the beginning and two at the end of the interferogram acquisition (normal mode) period within each dwell.

There is a strong interest to merge all available images into one average image/heterogeneity index in the operational L1B product:

- For operational use of the product, it appears undesirable to provide several, potentially inconsistent estimations supposed to represent the same quantity.
- Averaging reduces the instrument noise (mainly the dominating contribution from $\mathbf{Z}^{\mathbf{EV}}$).

The merging can be envisaged at various stages of the imaging mode processing chain. It is partly due to the absence of user requirements for imaging mode product performances that the question how to merge the individual images cannot be addressed conclusively at this stage of the specification phase. On the other hand, consolidated performance assessments are difficult to obtain due to incomplete knowledge of specific imaging mode acquisition parameters, which the instrument prime is not supposed to release, not even to investigate, in

absence of requirements.

At this stage, we can only mention and briefly discuss the options for such merging options.

A brute-force approach is to merge the four extracted raw images per dwell from the beginning, whatever the target. The subsequent processing is limited to a single, averaged image. The underlying hypotheses are stability of the instrument during a dwell as well as stability of the target. It is not excluded that this approach is compliant with actual user needs of the L1 product, because the processing of a single image is (except for instrument background processing) "linear", i.e. the final calibrated image is (in theory) expected to be identical, no matter if the merge of individual images is performed on raw images at the beginning or on calibrated images at the end.

However, processing of separate images is certainly useful for INR applications concerning extra-terrestrial targets as well as for NRT and offline monitoring of the IRS LOS stability. Therefore, at the minimum, it should remain possible to process the four images separately for these applications.

If images are processed separately within the operational L1 processor, there are nevertheless some quantities that should be processed in common.

The detector uniformity matrix **K** is meant to be unique. A separate, instantaneous computation from the four BB/DS1 images at each LAC transition period is recommendable, but the subsequent filtering with the recent history should be performed for the four images in common, i.e. the same matrix **K** should be used in the further processing of the four images.

Similarly, the average detection response R_D^{av} (Eq.F) and the scan mirror angle correction sensitivity $S_{SM}(i,j,T_{SM})$ (Eq.J), both used in the DS2 scan mirror incidence angle normalisation, should be identical for the processing of the four images.

5.6 Instrument Navigation and Registration (INR)

The Instrument Navigation and Registration (INR) module performs the navigation and registration processing for the IRS instrument. It determines the geolocation of each spatial sample and provides the geometric inputs as required by the IDPF-S for the radiometric and spectral processing and for the level 1b dataset aggregation and formatting.

Most of the INR processing is done by the IDPF-S INR module that is a Customer Furnished Item (CFI); its main functional blocs are:

- navigation of the spatial samples in the instrument reference frame; this is done for the two IRS bands in normal mode and imager mode;
- intersection of the line of sight with the Earth ellipsoid and computation of the geodetic coordinates for the spatial samples;
- feature extraction and observables filtering; stars are extracted from the imager mode data over the deep space region; landmarks are extracted from the locally rectified imager mode data (radiometrically calibrated) and normal mode data (radiometrically calibrated and spectrally binned) over the coastlines;
- state vector estimation including co-registration (launched at the end of a repeat cycle);
- geometric calibration performed typically every 24h.

They are described in section 5.6.1.

Additional geometric processing, described in section 5.6.2, is not part of the main IDPF-S INR module, should be implemented in the IRS Level-1 geolocation module. It should contain:

- computation of the relative angles between the Sun centre and the line of sight for each spatial sample;
- computation of the angle between the Sun and Earth centres as a function of time;
- computation of the Sun and satellite angles for each spatial sample, as seen from the point of Earth designated by the intersection of the line of sight with the Earth ellipsoid;
- flagging of the spatial samples: deep space and limb flags;
- geometric quality assessment.

The scope of this section is to give an overview of the INR processing and to describe the interfaces with the INR module and additional processing needed for the IRS L1 processing.

5.6.1 INR module overview

The geolocation processing aims at navigating the level 1b spatial samples in the reference coordinate system and, as a result, providing their geodetic coordinates along with time stamps. The main INR processes are the geolocation process, the features extraction process and the state vector estimation, including the geometrical calibration (Figure 42).

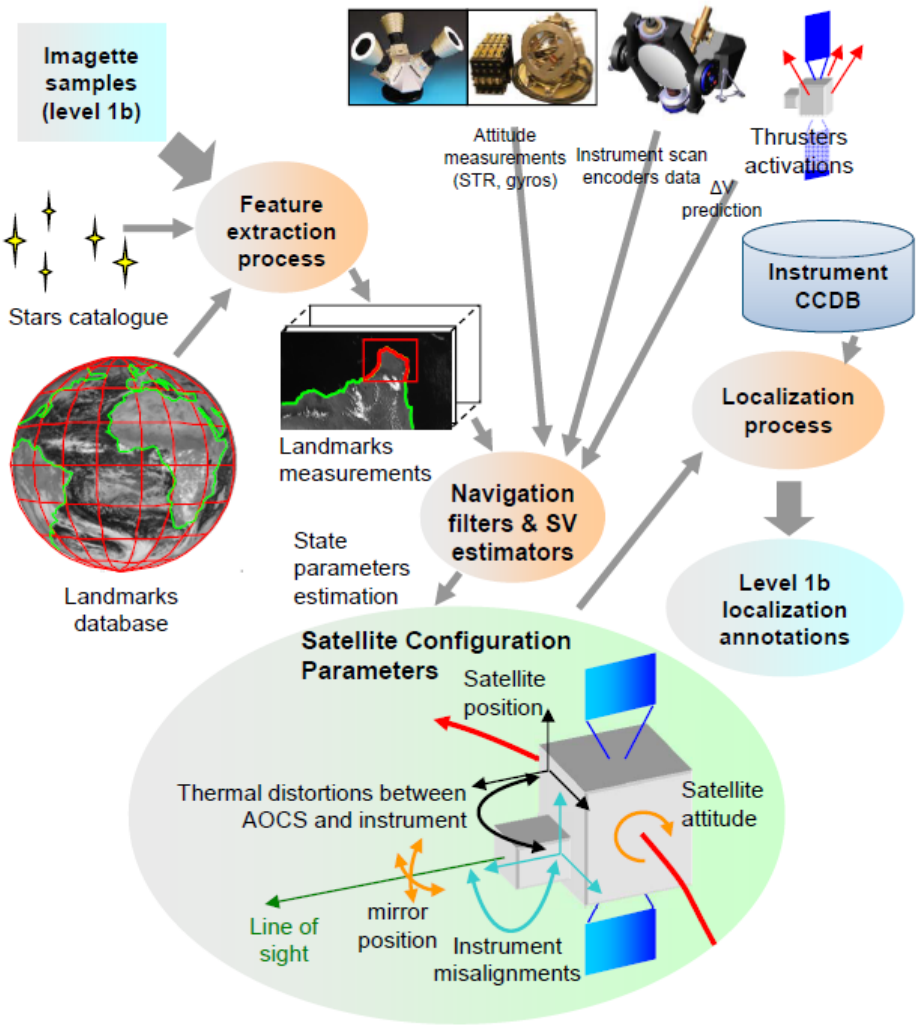

Figure 42: INR Processing Overview (Credit: Airbus)

5.6.1.1 Geolocation processing

The geolocation is the position on Earth of the line of sight intersection with the Earth ellipsoid. This line of sight corresponds to the barycentre of the Point Spread Function of a given spatial sample and is computed at the average acquisition time. The geolocation is assumed to be stable during over a dwell but a different geolocation is computed for the normal mode data and for the imager mode data.

The geolocation processing needs the following inputs:

- Instrument auxiliary data such as time stamps and scan angles (from telemetry);
- Platform auxiliary data such as estimated attitude angles estimated by the Attitude and Orbit Control System (AOCS) (from telemetry);
- Characterisation parameters such as alignments and focal plane cartography (from the Satellite Characterisation and Calibration Data Base - SCCDB);
- State Vector parameters (from the Data Processing Parameters File (DPPF) updated at the end of the previous repeat cycle);
- Geometrical calibration model parameters (from the DPPF updated at the end of the previous 24h cycle).

Note that the auxiliary data from telemetry (attitude, scan angles) would theoretically be sufficient to compute the geolocation however with insufficient accuracy to meet the geometric requirement. For this reason, the geolocation processing needs the State Vector and geometrical calibration model parameters.

The samples geolocation is based on the following equation:

$$\vec{T}(t,i) = \vec{S}(t) + dist(t,i) \cdot \vec{U}(t,i)$$

where:

- $\vec{T}(t,i)$ is the point on Earth corresponding to the sample *i* at time *t;*
- $\vec{S}(t)$ is the position of the satellite at time *t;*
- $dist(t,i)$ is the distance between the satellite and the point on Earth corresponding to the sample *i* at time *t;*
- $\vec{U}(t,i)$ is a unitary vector aligned with the line of sight of the sample *i* at time *t* (Figure 43).

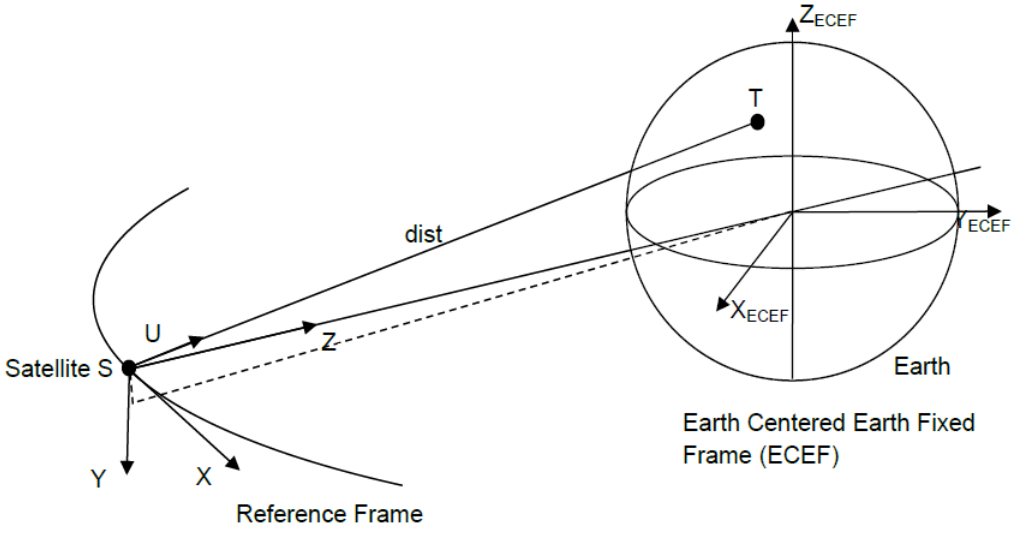

Figure 43: reference frames used in a sample geolocation

The output of the geolocation processing, as stored in the estimated acquisition grid, is the following:

- (azimuth, elevation) angles in instrument reference frame; this grid is used for the Sun straylight correction and also for the star processing;
- (longitude, latitude) coordinates for Earth samples (space samples are only flagged); these geodetic coordinates are derived from the (azimuth, elevation) angles;
- time stamps.

The processing applies to an elementary chunk of data defined by a dwell. It is composed of two main steps:

1) Propagation of the satellite orbit state to generate the satellite position (polynomial model) over the chunk period;
2) Estimation of the acquisition grids.

The outputs, for each dwell, are:

- In imager Mode (IM): one 480x480 grid per band (2 bands) and per acquisition (2 acquisitions per dwell);
- In normal Mode (NM): one 160x160 grid per band (2 bands).

5.6.1.2 Feature Extraction and State Vector Estimation

The basic INR principle is to fit a set of observations with a physical model describing the acquisition process which is represented in a state vector. The INR filter (a Kalman type filter) allows re-estimating the state vector which is then propagated over space and time in order to compute the geolocation of the spatial samples of the next repeat cycle.

The observations used by the INR filter are:

- stars detected in the vicinity of the Earth limb of the level 1b data;
- landmarks (land/sea interfaces);
- processed ranges computed by the Ground Segment[5].

The extraction of star is performed only with radiometrically calibrated level 1b images (from IRS imager mode data). A star catalogue is used to provide the reference location of the stars and their magnitude.

The extraction of landmark is made on radiometrically calibrated level 1b spectra (from IRS normal mode data) and images (from IRS imager mode data). This implies a pre-processing step which aims at generating rectified vignette around the landmark position by applying a spectral binning (only for the normal mode data) and a resampling onto the reference grid. A landmark database contains the landmark position in the reference grid and the associated shoreline vectors.

The INR cycle is illustrated in Figure 44. The INR processing (filter) is launched at the end of a repeat cycle (i.e. one LAC), ingest all observables extracted over the geo-located image (i.e. binned spectra and imager mode data of the IRS) plus the ranging data, and produces an updated state vector to be used for the processing of the next repeat cycle.

[5] Ground segment determined orbit is used only in case of cold start of the processing chain.

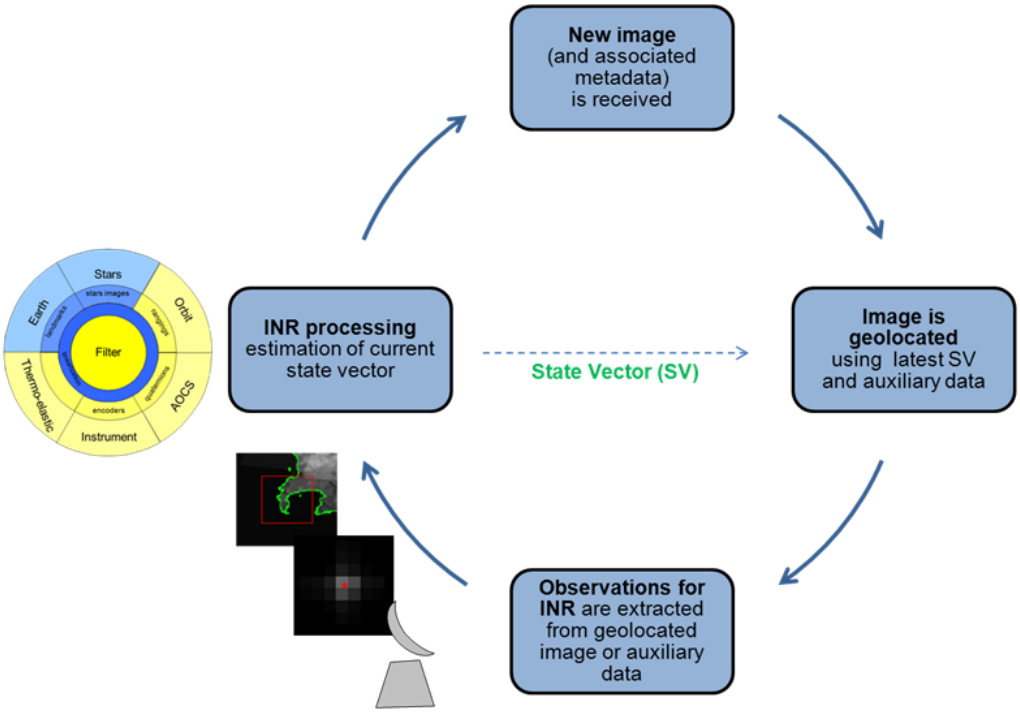

Figure 44: INR Cycle Overview (credit: TAS)

5.6.2 IRS level-1 geolocation processing

Additional geometric processing must be implemented in the IDPF-S as an IRS Level-1 geolocation module in order to compute the Sun and satellite angles. This requires a first module acting as an interface with the INR (referred to as the “INR-S Geometric APEs” at the top of Figure 45). Both modules are described in the next sections.

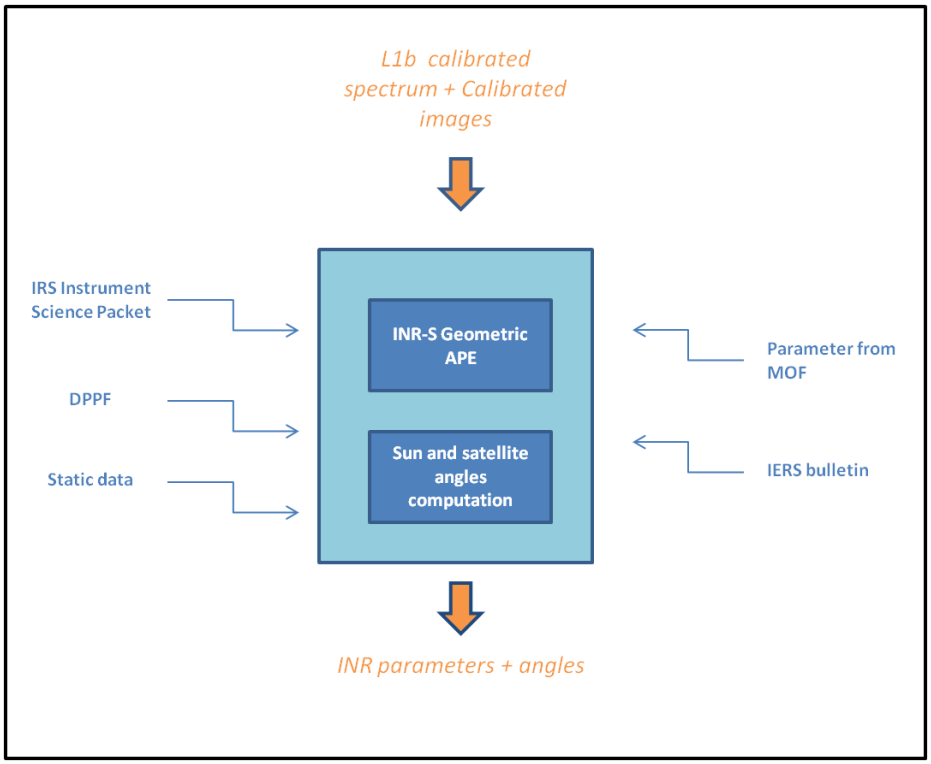

Figure 45: Overall flowchart showing the INR Module External Interfaces

5.6.2.1 Interfaces with the INR module

The dataflow between the INR and the IDPF-S is illustrated on Figure 46. The parameters are listed in Table 8.

APE Name	Data Size / Periodicity	Description
IRS_Geolocation	chunk (dwell)	Combines INR state vector from previous cycle with latest satellite AOCS information for the current Earth view dwell to provide geolocation and associated parameters required for the generation of IRS datasets. TBC: provision for deep space 2 (DS2) parameters?
IRS_LMK	chunk (dwell)	Process any landmark observables from the latest chunk (dwell).
IRS_STAR	chunk (dwell)	Process any star observables from the latest chunk (dwell).
IRS_INR	repeat cycle (LAC)	Process the processed landmark and star observables from all chunks (dwells) in this repeat cycle, and update the INR state vector and associated parameters required for the generation of IRS datasets.
IRS_GeoCalibration	[TBC 24hr?]	Assess diurnal updates to INR process to improve performance if needed.

Table 8: parameters exchanged between the INR and the IDPF-S

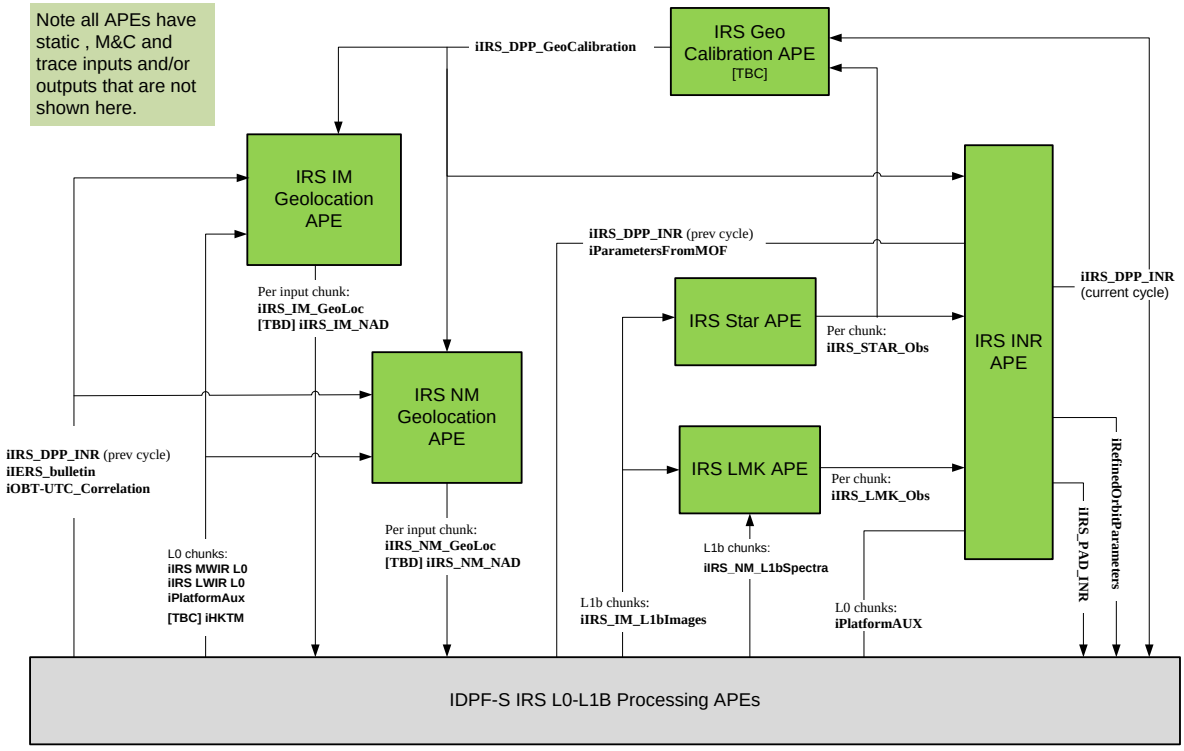

Figure 46: Dataflow between the IDPF-S and the IRS INR data processing units

5.6.2.2 Sun and satellite angle computation

The computation of the Sun and satellite angles as seen from the location on Earth given by the intersection of the line of sight with the Earth ellipsoid, for each spatial sample

These angles are obtained from the following output of the IDPF-S INR module (CFI):

- the geodetic coordinates (λ = longitude, φ = latitude) as given by the estimated acquisition grid (the one corresponding to the interferometry in a given band) for the Earth samples only (space looking samples are flagged);
- the satellite position and Sun position Cartesian coordinates (x, y, z) with respect to an Earth fixed reference frame, as given by the Navigation Auxiliary Data.

The Sun and satellite angles are computed in the topocentric frame, as shown on Figure 47. The topocentric frame z-axis coincides with the normal vector to the Earth's reference ellipsoid and is positive towards the zenith. The x-y plane is the plane orthogonal to the z-axis, and the x-axis and y-axis point positive, respectively, towards east and north.

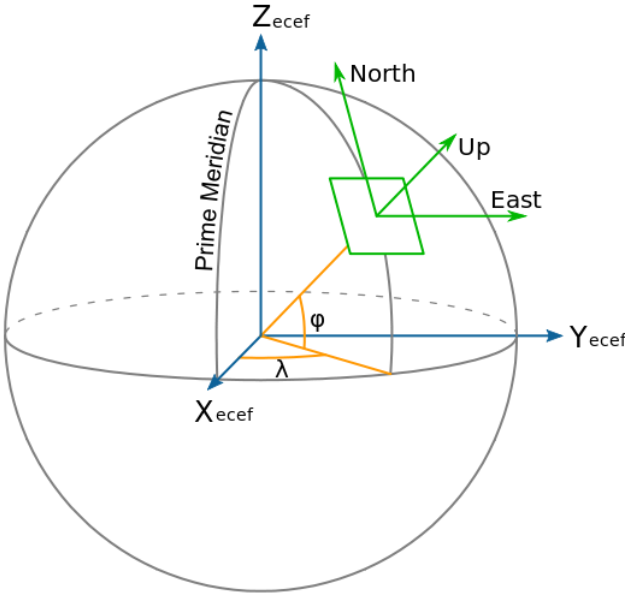

Figure 47: Topocentric Frame

The sample geodetic coordinates (λ, φ), where they are defined, are converted to Cartesian coordinates (x_0, y_0, z_0) in the ECEF. The Cartesian coordinates (x, y, z) of the Sun and satellite are expressed in the topocentric frame: e = easting, n = northing, u = upwardness, as follows:

$$\begin{bmatrix} e \\ n \\ u \end{bmatrix} = \begin{bmatrix} -\sin\lambda & \cos\lambda & 0 \\ -\cos\lambda\sin\varphi & -\sin\lambda\sin\varphi & \cos\varphi \\ \cos\lambda\cos\varphi & \sin\lambda\cos\varphi & \sin\varphi \end{bmatrix} \begin{bmatrix} x - x_0 \\ y - y_0 \\ z - z_0 \end{bmatrix} \qquad \textit{Eq. 69}$$

Finally, the Cartesian coordinates (e, n, u) are converted to zenith angle (θ) and azimuth angle (ϕ) using:

$$r = \sqrt{e^2 + n^2 + u^2}$$

$$\begin{bmatrix} \theta \\ \phi \end{bmatrix} = \begin{bmatrix} \arccos\dfrac{u}{r} \\ \arctan\dfrac{n}{e} \end{bmatrix}$$

Each spatial sample is flagged as being deep space, limb or Earth. This flagging makes use of the following output of the IDPF-S INR module:

- the geodetic coordinates (λ = longitude, φ = latitude) as given by the estimated acquisition grid for the Earth samples only (space looking samples are flagged);
- the line of sight angles in the instrument frame (λ = azimuth, φ = elevation), as given by the estimated acquisition grid for all samples;
- the satellite position and attitude with respect to an Earth fixed reference frame, as given by the Navigation Auxiliary Data.

First of all, the Earth centre is projected in the instrument frame using the satellite position and attitude. If the line of sight intersects the solid Earth, then the sample geodetic coordinates are defined and the space view flag is set to 0 (“Earth”), else if there is at least

one sample with defined geodetic coordinates in a circle of a given radius with respect to the Earth centre then the flag is set to 1 (“Limb”), otherwise the flag is set to 2 (“deep space”).

In addition, additional geometric parameters are needed for the radiometric and spectral calibration, in particular for the straylight correction. These are:

- the relative angles between the line of sight and the Sun centre for a given spatial sample;
- the angle between the Earth centre and the Sun centre as a function of time.

These angles are obtained from the following outputs of the IDPF-S INR module:

- the line of sight angles in the instrument frame (λ = azimuth, φ = elevation), as given by the estimated acquisition grid for all samples;
- the Sun position and the satellite position and attitude with respect to an Earth fixed reference frame as given by the navigation auxiliary data.

Furthermore a land/sea flag for each spatial sample is generated from the line of sight angles and using a land sea mask.

6 ONLINE MONITORING

The online quality monitoring algorithms are meant to continuously check, as far as possible, that the science measurements (spectra and images) quality match the IRS mission performances, as specified by the System Requirements Document (SRD) [AD-1] and the End User Requirement Document (EURD) [AD-2]. These routines are integrated inside the processor (IDPF-S); their main objectives are to produce relevant flags as output for the users. The main functions are listed in Table 9.

On-board processing and instrument	- Initial data flagging - On-board processing replica
Radiometric performances	- Monitoring of the imaginary part - Medium term stability - LoS Monitoring - RTF uniformisation monitoring
Spectral Performances	- Spectral Scale Correction accuracy - Spectral Scale Correction stability
Geometric monitoring	- Pointing - Coverage
Others	- ZPD - Metrology laser
Top-level flags	- On-board and instrument - Radiometry - Spectral - Geometry

Table 9: main elements of the online monitoring.

6.1 On-board Processing Monitoring

6.1.1 Initial data flagging

The on-board processing reports the interferograms quality: $FLG_{L0Hdr,b}[i,j,h]$

The initial data decompression also provides an error flag: $FLG_{comp,err}[i,j,b]$

Then, we perform basic statistical analysis during the pre-processing to mask the anomalous pixels from the processing:

- Pixel saturation: $FLG_{dpm,sat}[i,j,b]$, $FLG_{EV,sat}[i,j,b]$
- Noisy pixels: $FLG_{dpm,noise}[i,j,b]$
- Non-responsive pixels: $FLG_{dpm,bln}[i,j,b]$, $FLG_{EV,bln}[i,j,b]$

6.1.2 On-board processing replica

This algorithm takes from each dwell, the handful of raw (undecimated) interferograms and the raw metrology signals. These are processed using a replica of the on-board processing (IRS-OBR algorithm). The outputs are compared to the L0 interferograms and a flag is raised if it exceeds a certain threshold: $FLG_{replica}(b)$.

6.2 Radiometric calibration monitoring

6.2.1 Monitoring of the Imaginary Part of the L1Ar Spectra

The imaginary part of the radiometrically calibrated spectra $\widetilde{L_v^{EV}}$ is directly proportional to the residual phase: $\mathrm{Im}\{L_r^{EV}\} \approx |L_r^{EV}|\delta\varphi$. The remaining imaginary part of the radiometric equation output is thus a powerful indicator of any error in the processing.

The phase error writes:

$$\delta\varphi(\nu) = Arg[\mathrm{Re}\{L_r^{EV}\} + \mathrm{i}\ \mathrm{Im}\{L_r^{EV}\}]$$

The monitoring of this imaginary part consists in computing both the average and standard deviation of the phase on the two bands, if they exceed the given thresholds we raise a flag: $FLG_{AvgPhi}[i,j,b]$, $FLG_{StdPhi}[i,j,b]$.

6.2.2 Medium Term Radiometric Stability

This routine checks the compliance of the instrument measurements against the medium term radiometric stability. The algorithm looks at the difference between the last background measurement and the estimated background and the difference between the last LAC core section transmission computation and the estimated core section transmission, to guess the radiometric stability. This is ran for every DS2 views, just after the spectra background modelling algorithm.

The difference between the last background measurement and the estimated background at the time of the DS2 measurement writes:

$$\widetilde{\Delta L}_{BG}(\nu) = \tilde{L}_{BG}(\nu) - \left[\tilde{\alpha}_{BG}(\nu) + \tilde{\beta}_{BG}(\nu) \cdot t_{DS2}\right]$$

The difference between the last LAC core section transmission computation and the estimated core section transmission writes:

$$\widetilde{\Delta R}_c\ (\nu) = \tilde{R}_{C,LAC}(\nu) - \tilde{R}_C(\nu)$$

The radiometric calibration writes:

$$L_{L1Ar}(\nu) = \frac{L_{ref}(\nu) - \tilde{L}_{BG}(\nu)}{\tilde{R}_C(\nu)}$$

Considering the differences, we find the product should be impacted as follow at first order:

$$L_{L1Ar,d}(\nu) = \frac{L_{ref,L1A}(\nu) - \left(\left[\tilde{\alpha}_{BG}(\nu) + \tilde{\beta}_{BG}(\nu) \cdot t_{DS2}\right] + \widetilde{\Delta L}_{BG}(\nu)\right)}{\tilde{R}_C(\nu) + \widetilde{\Delta R}_c\ (\nu)}$$
$$\cong L_{ref}(\nu) - L_{ref}(\nu)\frac{\widetilde{\Delta R}_c\ (\nu)}{\tilde{R}_C(\nu)} - \frac{\widetilde{\Delta L}_{BG}(\nu)}{\tilde{R}_C(\nu)}$$

The radiance drift writes:

$$\boxed{\Delta L_{L1Ar}(\nu) = L_{ref}(\nu)\frac{\widetilde{\Delta R}_c\ (\nu)}{\tilde{R}_C(\nu)} + \frac{\widetilde{\Delta L}_{BG}(\nu)}{\tilde{R}_C(\nu)}}$$

Finally, we take the reference $L_{ref}(\nu)$ as a typical clear view spectrum and then convert the radiance drift in equivalent temperature.

We compute the temperature average on each band and raise a flag if it exceeds a threshold: $FLG_{MTS}[i,j,b]$. We also store the temperature drift in function of the wavenumber after averaging all pixels: $\Delta T_{\nu,avg}[\nu,b]$.

6.2.3 LoS stability monitoring

The LOS stability can be monitored on-line by using the images acquired before and after the interferogram acquisition, if the difference between the two images exceed a certain threshold, it is a hint at LOS instability during the cube corner displacement.

We raise a flag if the difference between the aggregated DC images at super-pixel level exceeds a threshold: $FLG_{LoS}[i,j,b]$. If the number of LoS flags raised exceeds a threshold we flag the dwell as instable: $FLG_{LoS,dwell}[b]$.

We also take the opportunity to flag the non-uniform scenes; we raise a flag if the relative signal standard deviation over the subpixels exceeds a threshold: $FLG_{SubNUnif}[i,j,b]$.

We expect a radiometric impact on the product only if both the non-uniformity and LoS at dwell level flags are raised. Indeed, if the scene is uniform, a LoS drift has no radiometric impact, only a geometric one.

6.2.4 RTF uniformisation monitoring

The algorithm uses the radiometric response function generated by the radiometric calibration averaged over 24 hours to assess the RTF Uniformisation accuracy. The radiance difference of a reference scene when viewed with the reference RTF and the current RTF are compared to derive an expected error in equivalent delta temperature. This error is compared to a threshold to decide if the reference radiometric response function for the RTF uniformisation needs to be updated.

The radiance difference between the current correction using the reference transmission and the one using the new transmission is the following:

$$\Delta L_{L1B}(\nu) = L_{L1B,SRF}(\nu) - L_{L1B,SRF,new}(\nu)$$

We define $L_{L1B,SRF}(\nu)$ using a reference clear sky high-resolution spectrum Sp_{ref}:

$$L_{L1B,SRF}(\nu) = \left[Sp_{ref} \otimes SRF\right](\nu)$$

The SRF is considered here after the SRF uniformisation, which means that it depends only on the numerical apodisation.

To compute $L_{L1B,SRF,new}(\nu)$ we cancel the current RTF uniformisation applied to $L_{L1B,SRF}(\nu)$ and apply the new one:

$$L_{L1B,SRF,new}(\nu) = L_{L1B,SRF}(\nu) \times \frac{T_{new}(\nu) \times \left[Sp_{ref} \otimes SRF\right](\nu)}{\left[Sp_{ref}.T_{new} \otimes SRF\right](\nu)} \Big/ \frac{T_{ref}(\nu) \times \left[Sp_{ref} \otimes SRF\right](\nu)}{\left[Sp_{ref}.T_{ref} \otimes SRF\right](\nu)}$$

$$= \frac{T_{new}(\nu)}{T_{ref}(\nu)} \times \frac{\left[Sp_{ref}.T_{ref} \otimes SRF\right](\nu)}{\left[Sp_{ref}.T_{new} \otimes SRF\right](\nu)}$$

Finally:

$$\boxed{\Delta L_{L1B}(\nu) = \left[Sp_{ref} \otimes SRF\right](\nu) \times \left\{1 - \frac{T_{new}(\nu)}{T_{ref}(\nu)} \times \frac{\left[Sp_{ref}.T_{ref} \otimes SRF\right](\nu)}{\left[Sp_{ref}.T_{new} \otimes SRF\right](\nu)}\right\}}$$

Then we convert the radiance error in equivalent temperature a reference temperature of 280K.

We compute the temperature average on each band and raise a flag if it exceeds a threshold: $FLG_{RTF}[i,j,b]$. We also store the temperature error in function of the wavenumber after averaging all pixels: $\Delta T_{\nu,avg}[\nu,b]$.

6.3 Spectral Performances

6.3.1 Spectral calibration accuracy

We use directly the uncertainty estimation of the predictor $U_{pred}[i,j,b]$ described in the section 5.3.3.8.2, to raise a flag on the quality of the prediction. If the uncertainty prediction exceeds a threshold, we raise the flag: $M_{spec-acc}[i,j,b]$

6.3.2 Spectral calibration stability

This algorithm does compares the Spectral Scale Factors before and just after a calibration. Their difference is a measure of spectral stability. If this difference overcomes a fixed threshold, then a flag is raised: $\mathrm{M}_{sp-stb}[i,j,b]$

6.4 Geometric Performances

The geometric performances are characterised by several different parameters, which relate to absolute knowledge errors at both dwell and LAC level, and a series of relative errors (dwell to dwell, band to band, pixel to pixel, etc.). Most of these requirements can be checked.

6.4.1 Monitored performances

The main IRS geometric performance parameters can roughly be classified in two categories, coverage and pointing. To each category, a number of SRD requirements [AD-1] can be associated, namely:

- Coverage performances:
  - LAC coverage (IRS-10060, IRS-10120, IRS-10240);
  - Overlap (IRS-10270, IRS-10300);
- Pointing performances:
  - Sample position (IRS-11200, 11230);
  - Line of sight (LoS) stability (IRS-11260);
  - Integrated Energy (IRS-11290);
  - Absolute sample position knowledge error (APKE) (LAC and dwell) (IRS-11500,11530);
  - Relative sample position knowledge error (RSPKE) (IRS-11590);
  - relative sample position error (RSPE) (IRS-11320);
  - inter-dwell navigation error (IDNE) (IRS-11560).

6.4.2 Available inputs

The available data for carrying out a verification of the geometrical performance are the outputs of the INR algorithms, in particular:

- The L1b grids, i.e. the estimated positions of every spatial sample, in both azimuth & elevation (azimuth/elevation) and (where possible, i.e. inside the Earth disk), latitude & longitude; this information is refreshed at every dwell;
- The estimated errors for the landmarks; at the end of every LAC the estimated errors (in km) for all the nominal landmarks are provided, together with validity flags, indicating whether a given landmark has been used or not (for example because covered by clouds).

6.4.3 Coverage performances

The LAC coverage requirements aim at ensuring that each LAC is properly covered. These requirements can be verified in flight by estimating the position of each spatial sample, in terms of latitude/longitude and azimuth/elevation and verifying that the estimated positions fall within the LAC without any clipping. It is worth observing that every LAC has two kinds of borders:

- The natural borders associated with the Earth limb;
- Artificial borders, from one LAC to the neighbouring one.

The Earth limb is identified as the circle placed at a distance of 8.7° from the centre. Since a circle is convex, a simple verification that the Earth limb is fully covered consists of the following steps:

- Check whether the current dwell nominally contains the limb;
- If so, identify the dwell corners that nominally look at deep space (1 to 3);
- For every corner take the azimuth/elevation coordinates and derive the angle ψ with respect to the sub-satellite point;
- Compare all angles with the limb angle ψ_{limb}; if it is $\psi < \psi_{limb}$ for at least one corner, then the coverage requirement is not met and a flag is raised.

Note that the first two steps can be verified using a dwell coverage table. Also note that the above steps do not ensure that all limb points are covered; some points could be missing if two adjacent dwells do not overlap. However the overlap check covers this problem

The LAC-to-LAC borders are defined in the SRD [AD-1] in terms of latitude and longitude, hence the check must use these parameters. An algorithm similar to that used for limb can be applied; it again requires identifying dwells belonging to a LAC-to-LAC border and the corners that are supposed to fall within the neighbouring LAC. The position of the corners of each of such dwells is checked to determine in which LAC it falls. If the corner falls in the current LAC then the coverage requirement is not met and a flag is raised. It should be observed that, since the algorithm is exactly valid only for convex figures, there is a zone between LAC3 and LAC4 where it loses validity (see Figure 48). Dwells around that area deserve therefore additional care.

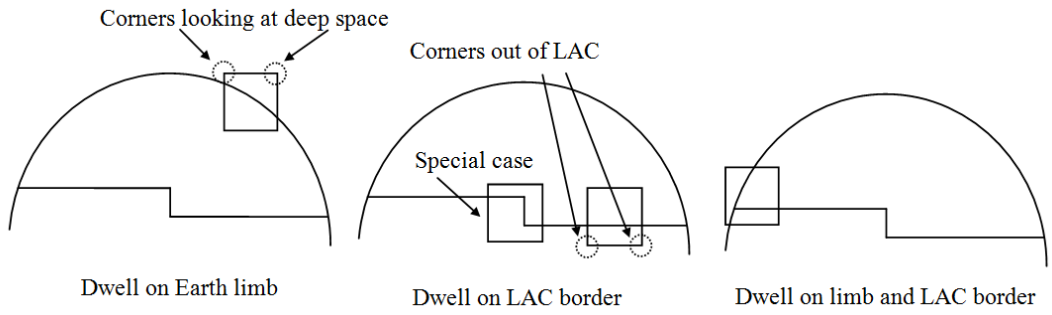

Figure 48: Dwells on limb and LAC border.

The LAC coverage table simply consists in the list of all dwells, where for each dwell:

- A field identifies the corners out of the limb;
- A field identifies the corners inside the limb but out of the LAC.

The corners are numbered from 1 to 4. If the first field is empty it means the dwell is inside the limb; if it contains the numbers 2 and 3 it means that the corners 2 and 3 are expected to look at deep space, whereas the corners 1 and 4 are expected to be inside the Earth disk. The same concept is applicable to the second field. If both fields are empty that means the dwell is not on the LAC border.

The LAC overlap can be estimated using a LAC overlap table (that could be merged with the dwell coverage table) that contains, for every dwell:

- The list of all dwells (at most two) adjacent to it, whose ID is lower (that is only those dwells that have been already covered);
- For each adjacent dwell, the pair of corners that nominally overlap (one for the current and one for the adjacent dwell, see Figure 49).

Then, for each dwell:

- looking at the LAC overlap table, check if an already covered dwell is adjacent to the current one; if not the procedure is ended;
- for every pair of adjacent dwells, retrieve the azimuth/elevation coordinates of the overlapping corners (by exploiting the information from the table);
- for each corner, the pixel in the adjacent dwell, whose centre is closest to the corner coordinates are identified;
- if the centre is at a distance larger than half pixel (TBC), then there is no dwell overlap and a flag is raised;
- if the centre is at a distance below 4 pixels from the border, then the overlapping requirement is not met and a flag is raised.

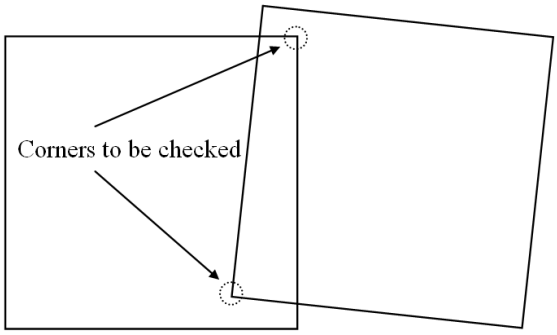

Figure 49: Overlapping adjacent dwells

A similar approach can be applied for verifying the common coverage between two subsequent dwells (IRS-10300). Details are TBD.

6.4.4 Pointing performances

The requirements on sample position (IRS-11200, 11230), LOS stability (IRS-11260), ASPKE over a dwell (IRS-11530), RSPE (IRS-11320), cannot be monitored in flight and their compliance is verified at design level and/or during the on-ground testing. A possible check of the integrated energy requirement (IRS-11290) consists in looking at stars. Note that this could give an indirect verification of the LOS stability, since the latter is assumed to be main contributor to IE. This needs to be further analysed.

The ASPKE at LAC level (IRS-11500) can be monitored by looking at landmark errors. The statistics is hampered by the relatively low number of landmarks per LAC (about 100). An alternative is to compare the error of all valid landmarks value with the upper limit (specifically 2.37km), plus an uncertainty margin. The requirement is considered met if and only if all landmark errors are below this limit. If not a flag is to be be raised.

The uncertainty margin is currently assumed as a static parameter. In a possible evolution of the INR module it could be that this value is an additional output from it.

The following additional information can easily be evaluated:

- Maximum error;
- Minimum error;
- Mean error;
- Rms error (or, alternatively, standard deviation).

The requirement on RSPKE (IRS-11590) is similar to the one on ASPKE but apply to error differences instead of absolute errors. It is assumed that information on error difference at landmark level is directly available from INR. Therefore, considering that the confidence level is the same as the one of ASPKE (99.73%), the same procedure is applied with the same kind of outputs.

Finally, the requirement on IDNE (IRS-11560) nominally asks to compare mean values on row or columns from two adjacent dwells. Since information at this level of detail is not available, a simplified approach is needed. A possibility consists in looking at landmark pairs that are known to belong to adjacent dwells. A list of landmark pairs can easily be produced *a priori* and recorded within a table, by just looking at the nominal dwell positions and excluding landmarks too close to the dwell border (a margin of a few pixels is sufficient). The error difference is estimated for each valid pair.

The table of landmark pairs can be built by associating to each landmark the index of all other landmarks belonging to the nearby dwells.

6.5 Others

The following processing computes data and flags that are not used in the top-level flags for the users, it means that they extract information which is not directly related to the performance. Nonetheless, they provide useful information about the instrument good health.

6.5.1 ZPD Monitoring

If the interferogram is not centred in OPD, we say that it acquires a ZPD (zero path distance).

$$I \rightarrow I(x + ZPD)$$

After Fourier transform, the spectrum acquires a phase proportional to the ZPD and the wavenumber:

$$L(\nu) = FT^{-1}[I(x + ZPD)] = FT^{-1}[I(x)\,] \times e^{2i\pi\nu ZPD} = L_0(\nu) \times\ e^{2i\pi\nu ZPD}$$

In the general case, the ZPD is chromatic and depends on the pixel position $ZPD(i, j, \nu)$.

We extract the spectrum phase and compute the ZPDs performing a linear fit of the phase as follow:

$$[ZPD, Off_{ZPD}] = linearfit\left[\nu\,, \frac{ARG[L_{L1A}(\nu)]}{2\pi}\right]$$

We also extract the chromatism as follow:

$$ZPD_{chrom} = \frac{ARG[L_{L1A}(\nu)] - 2\pi[ZPD \times \nu + Off_{ZPD}]}{2\pi \times \nu}$$

We compute and store the ZPD average on each band: $ZPD(i,j,b)$. We raise a flag if the average ZPD exceeds a threshold: $FLG_{ZPD}[b]$. We also store the average chromatism in function of the wavenumber for each detector.

6.5.2 Metrology Laser Monitoring

The scale factors computed by the spectral calibration processing can be used to approximately extract the metrology alignment and the metrology laser wavenumber drift.

We note pixel field of view position at interferometer level $\boldsymbol{\theta_0}$ and the metrology field of view position used for the resampling of the pixel $\boldsymbol{\theta_{metro}}$. The on ground tests of the interferometer allows characterizing the metrology alignment so that $\boldsymbol{\theta_{metro}}(\boldsymbol{\theta_0}) \cong \boldsymbol{\theta_0}$, but then this alignment can vary during the instrument lifetime.

The spectra are affected as follow:

$$L(\nu) = FT^{-1}\left[I(x)\, e^{2i\pi\nu[\cos(\boldsymbol{\theta_0})+\{1-\cos(\boldsymbol{\theta_{metro}})\}]x}\right] = L(\nu \times [\cos(\boldsymbol{\theta_0}) + 1 - \cos(\boldsymbol{\theta_{metro}})])$$

Taking the following small misalignments:

$$\boldsymbol{\theta_{metro}} = \boldsymbol{\theta_0} + \delta\theta y\, \boldsymbol{y} + \, +\delta\theta z\, \boldsymbol{z}$$

The spectrum acquires a scaling factor:

$$L(\nu) \cong L\left(\nu \times \left[1 - [\boldsymbol{\theta_0}.\boldsymbol{y}\, \delta\theta y - \boldsymbol{\theta_0}.\boldsymbol{z}\, \delta\theta z]\right]\right)$$

Then, we choose three pixels whose angular positions match the metrology lasers angles:

- 1: $\boldsymbol{\theta_0}.\boldsymbol{y} = 0, \boldsymbol{\theta_0}.\boldsymbol{z} = 0$
- 2: $\boldsymbol{\theta_0}.\boldsymbol{y} = sin[\theta_r], \boldsymbol{\theta_0}.\boldsymbol{z} = 0$
- 3: $\boldsymbol{\theta_0}.\boldsymbol{z} = sin[\theta_r], \boldsymbol{\theta_0}.\boldsymbol{y} = 0$

The measured scale factor at the detector centre SF_1 gives simply the scale factor shift of the metrology wavenumber with respect to the one used in the resampling:

$$SF_1 = \frac{\delta\nu_{metro}}{\nu_{metro,0}}$$

Finally, taking the three pixels scale factors following differences we extract the metrology alignment:

$$\frac{SF_1 - SF_2}{sin[\theta_r]} = \delta\theta y, \quad \frac{SF_1 - SF_3}{sin[\theta_r]} = \delta\theta z$$

6.6 Top level flags aggregation

This processing computes top-level flags directly useful for the users.

1) On-board and instrument flag

We gather the L0, pre-processing and replica flags into a top-level instrument flag, see section 6.1:

- On-board interferogram quality: $FLG_{L0Hdr,b}[i,j,h]$
- Decompression error: $FLG_{comp,err}[i,j,b]$
- Pixel saturation: $FLG_{dpm,sat}[i,j,b]$, $FLG_{EV,sat}[i,j,b]$
- Noisy pixels: $FLG_{dpm,noise}[i,j,b]$
- Blind pixels: $FLG_{dpm,bln}[i,j,b]$, $FLG_{EV,bln}[i,j,b]$
- On-board processing replica: $FLG_{replica}(b)$

$$FLG_{Ins}[i,j,b] = \left\{ \begin{array}{c} FLG_{L0Hdr,b}[i,j,1]\ OR\ FLG_{L0Hdr,b}[i,j,2] \\ OR\ FLG_{comp,err}[i,j,b]\ \ OR\ FLG_{dpm,sat}[i,j,b]\ \text{OR}\ FLG_{dpm,bln}[i,j,b] \\ \text{OR}\ FLG_{dpm,noise}[i,j,b]\ OR\ FLG_{replica}(b) \\ OR\ FLG_{L1b,sat}[i,j,b]\ \ OR\ FLG_{L1b,bln}[i,j,b] \end{array} \right\}$$

2) Radiometry flag

The radiometry flag gathers all flags related to the radiometry accuracy and noise, see section 6.2:

- Medium term stability: $FLG_{MTS}[\mathrm{i,j,b}]$
- Average spectrum phase: $FLG_{AvgPhi}[i,j,b]$
- Spectrum phase standard deviation: $FLG_{StdPhi}[i,j,b]$
- RTF uniformisation accuracy: $FLG_{RTF}[i,j,b]$
- Dwell LoS: $FLG_{LoS,dwell}[b]$
- Sub-pixel non-uniformity: $LG_{SubNUnif}[i,j,b]$

$$FLG_{Rad}[i,j,b] = FLG_{MTS}[\mathrm{i,j,b}]\ OR\ FLG_{AvgPhi}[i,j,b]\ Or\ FLG_{StdPhi}[i,j,b]\ OR\ FLG_{RTF}[i,j,b]\ OR\ \left(FLG_{LoS,dwell}[b]\ \&\ FLG_{SubNUnif}[i,j,b]\right)$$

Note that we expect a radiometric impact if we have simultaneously a LoS anomaly at dwell level and a non-uniform sub-scene: $FLG_{LoS,dwell}[b]$ & $FLG_{SubNUnif}[i,j,b]$.

3) Spectral flag

The spectral flag gathers the accuracy and stability flags of the spectral calibration methods, see section 6.3:

- Spectral calibration accuracy: $M_{spec-acc}[i,j,b]$
- Spectral calibration stability: $\mathrm{M}_{sp-stb}[i,j,b]$

$$FLG_{Spe}[i,j,b] = M_{spec-acc}[i,j,b]\ OR\ \mathrm{M}_{sp-stb}[i,j,b]$$

4) Geometry flag

The definition of this flag is not decided yet.

7 OFFLINE CHARACTERIZATION AND PERFORMANCES ASSESSEMENT

The offline monitoring is focused on the performance analysis and characterization of the processing (both on-board and on-ground). This characterization requires in general a dedicated set of measurements acquired during special scanning sequences that resemble the external calibrations of IASI; furthermore, conversely to the online monitoring that is completely automated, offline characterization may require human intervention to decide updating certain parameters of the processing. Finally, the partition between online and offline monitoring entails a distinction between the frequency with which these assessments are performed: while online monitoring is performed on every dwell (or at least every given type of dwell), the offline monitoring is performed at a lower frequency, from once a day to once a year. The main elements of the offline monitoring are listed in Table 10.

	Algorithm	Freq.	Ext Cal
Parameters characterization	FIM characterization	Year	No (but requires FIM heating)
	FS transmission characterization	Year	DS2
	Scan mirror reflectivity law	Year	DS2 on both sides East/West (could be done along with the FS characterization)
	Determination of chromatism offsets	Low	No
Instrument and on-board monitoring	Non-linearity characterization and monitoring	Low	BB in EXP mod
	OPD stability check	Continuous	No
	ZPD monitoring	Continuous	No
	Metrology laser wavelength monitoring	Continuous	No
	Spike filter threshold monitoring	Continuous	No
	Bit trimming table monitoring	Continuous	No
	On-board processing monitoring	Continuous	No
	IFG baseline characterization	Continuous	No
Radiometric monitoring	In-field straylight	Low	DS2/EV transition
	Sun straylight level check	Low	DS2 straylight scan
	Background monitoring (diurnal and annual cycle)	Continuous	No
	Out of band signal monitoring	Low	No
	Complex radiometric calibration monitoring	Continuous	No
	Radiometric noise characterization and correlated noise	Month	No

		Low	BB only if a pixel-dependent analysis is done
Spectral monitoring	Absolute spectral calibration monitoring	month	EV
	Inter-pixel spectral calibration assessment	Month	EV
	Spectral performance evaluation over overlapping zones	Month	EV
End-to-end check	Verification IF End-to-End processing chain	Continuous	No
Inter-calibration	Inter-calibration with IASI (and possibly with CrIS and IASI-NG)	Continuous	No

Table 10: Main elements of the offline monitoring with example of external calibration needed.

7.1 Parameters characterization

The following parameters are characterized in-flight at low frequency, partly in external calibration modes. The results may lead to updates of the corresponding parameters in the NRT L1 processing. Thus, they are described in detail in section 5.

7.1.1 FIM characterization

The FIM characterisation is detailed in the section 5.3.2.5.

7.1.2 FS Transmission Characterization

The FS transmission is detailed in the section 5.3.2.3.

7.1.3 Scan Mirror Reflectivity Law

The FS transmission is detailed in the section 5.3.2.4.

7.1.4 Determination of Chromatism Offsets

The chromatism offsets give for each spectral sample the deviation from the linear scaling factor. Whereas the linear scaling factor is expected to vary from measurement to measurement, the chromatism offsets are expected to vary slowly in the lifetime of the instrument, of at all. The only event, which is expected to have a considerable impact on chromatism, is the launch of the satellite.

The chromatism offsets are fully characterised on ground and delivered with the instrument. Once in orbit, these offsets will be updated during commissioning to provide a final set to use for the spectral calibration processes. This in-flight update is described in this section.

Once the chromatism offsets are determined in-flight, the routine may be used to produce monitoring output or update once again the offsets in case they changed.

For the determination of the uncorrected chromatism offsets, the determined scale factor from the general solution and from all three local solutions are used (see §5.3.3.5) and is made for each pixel and each band separately. The scale factors determined over N_{av_chrom} SCZ revisits are average together:

$$\langle \zeta[i,j,b] \rangle = \frac{\sum_{N_{av\_chrom}} \zeta[i,j,b][t]}{N_{av\_chrom}} \qquad \textbf{Eq. 70}$$

and

$$\langle \zeta_{LOC\_X}[i,j,b] \rangle = \frac{\sum_{N_{av\_chrom}} \zeta_{LOC\_X}[i,j,b][t]}{N_{av\_chrom}} \qquad \textbf{Eq. 71}$$

where ζ_{LOC_X} is either ζ_{LOC_1}, ζ_{LOC_2} or ζ_{LOC_3} for the scale factors from the 3 local solutions.

As the general and local scale factors are determined taking into account the known scale factors, they should ideally lead to the same scale factor. Any changes in chromatism will be depicted in a difference between the general solution and the local solutions. The chromatism residual are given by:

$$\Delta\zeta_{LOC\_X}[i,j,b] = \langle \zeta_{LOC\_X}[i,j,b] \rangle - \langle \zeta[i,j,b] \rangle \qquad \textbf{Eq. 72}$$

At this point, the previously known chromatism offsets may be directly updated using these residuals. Additional preliminary steps were nevertheless foreseen during Phase B developments:

- Spatial filtering (smoothing) of the residual;
- Bias removal.

The first step is an effort to improve noise suppression and is possible as the variation of chromatism offsets over the detectors is expected to be slow and smooth. The second step is more of precautionary nature: the central pixels have been shown to have negligible chromatism, thus any residual for the central pixels can be seen as a bias from the method.

Many methods may be used for spatial filtering; one that proved efficient and compatible with expected spatial chromatism variations is a 4th order 2D polynomial fitting process. This filtering, done for each chromatism residuals pixel maps, leads to a smoothed chromatism residues $\overline{\Delta\zeta_{LOC\_X}}$ and is done with the following steps:

1. For each row i, fit a 4th order polynomial;
2. Evaluate the resulting polynomial at the position of each pixel and replace the value with the result of the evaluations;
3. Repeat steps 1 and 2 for every column j.

The bias is given by the average chromatism residual for the 10 by 10 central pixels and is removed from the overall residual map to give the final chromatism residual map.

$$\widehat{\Delta\zeta_{LOC\_X}}[i,j,b] = \overline{\Delta\zeta_{LOC\_X}}[i,j,b] - \frac{\sum_{i,j=[85,95]} \overline{\Delta\zeta_{LOC\_X}}[i,j,b]}{100} \qquad \textbf{Eq. 73}$$

The chromatism residuals are the residual at the spectral location corresponding to the reference position of each local Solution, ν_{LOC_X}. To determine the residuals for all spectral

samples, a 2nd order polynomial fit is done on $\Delta\widehat{\zeta_{LOC\_X}}[i,j,b]$ over ν_{LOC_X}. The resulting polynomial is then pixel and band wise evaluated for every spectral samples, leading to $\delta_{chrom}[i,j,k,b]$.

From these offsets, corrected chromatism offsets may be determined:

$$\Delta\widehat{\nu_{chrom}}[i,j,k,b] = \Delta\nu_{chrom}[i,j,k,b] + \nu[k] \times \delta_{chrom}[i,j,k,b] \times 10^6 \qquad \textbf{\textit{Eq. 74}}$$

The new chromatism offset can be used either for monitoring and diagnostic purposes or to replace the old chromatism offsets for the spectral calibration processing.

If the chromatism offsets are defined as quasi-static parameters on different spectral grids, the polynomial and correction process must be done independently for each grid.

7.2 Instrument health check and on-board monitoring

The most critical units as well as the most susceptible of variations during the lifetime of the instrument are the detector and the interferometer. A continuous check of their behaviour is therefore important for monitoring the health status of the instrument.

Two different levels of checks are possible:

- a less accurate, real time continuous monitoring, carried out in parallel with the processing of the science data;
- a deeper check, aimed at verifying the status of a larger set of instrument parameters. This latter check, however, requires a special configuration of the instrument, which is not compatible with the nominal flow of operations. Its execution represents an operational outage and must be programmed in such a way not to interfere with the routine working conditions.

7.2.1 Non-linearity characterisation and monitoring

Using series of BB raw IFGs (the same as used for non-linearity monitoring, the useful band limits and the out-of-band signals corresponding to artefacts other than residual non-linearity. The method would be based on the iterative removal of the out-of-band signal that is introduced by the quadratic non-linearity of the raw interferograms. The quadratic term of the interferograms appears in the spectrum space as a convolution of the spectrum with itself, which, for the IRS band limits, has a signal only out of the band.

This monitoring would be needed at low frequency and would require a special external calibration providing a collection of raw BB interferograms, sufficiently large that all detectors are covered several (typically 20) times (to minimise the noise impact), transmitted in EXPERTISE mode (interruption of the operational service in favour of a significantly increased number of transmitted raw IFGs).

7.2.2 Interferometer Check

7.2.2.1 OPD stability check

The general objective is to monitor the on-board metrology processing (laser phase measurement including fringe counting and regularization; pixel OPD computation).

Raw metrology samples and, optionally, the computed laser phases are transmitted to the ground via the L0 engineering products METRO and LASER. The offline monitoring is aiming at estimating the stability and long-term performance of the on-board metrology processing.

The method itself is still under consolidation and will be detailed in a future version.

7.2.2.2 ZPD monitoring

There is not enough information regarding the ZPD determination. This algorithm will be described in a future version.

7.2.2.3 Metrology laser wavelength monitoring

The stability of the apparent laser wavelength is a measure of the actual laser wavelength stability under the following hypotheses:

- Instability or drift of the sampling clock is negligible. In other words, the Maximum OPD is dependent only on the laser wavelength.
- The laser alignment relative to the interferometer axis is perfectly known. Residual knowledge errors are not discernible from the absolute wavelength estimation. However, the estimation is less sensitive to alignment knowledge error of the on-axis laser.

Stability of the metrology laser wavelength is monitored through analysis of the LASER engineering product containing the on-board phase estimation of the three metrology lasers.

For a given dwell, the first step is to recover the on-axis OPD law *opd(t)*.

The second step is to recover the times where the phase of the on-axis laser (θ=0) is a multiple of 2π, such that:

$$\varphi(t_k) = k \cdot 2\pi \qquad \textit{Eq. 75}$$

Then the "instantaneous" apparent laser wavelength λ is given by:

$$\lambda(t_k) = (opd(t_{k+1}) - opd(t_k))/\cos\theta \qquad \textit{Eq. 76}$$

The instantaneous wavelength is analysed statistically over configurable collections of dwells, where the average is associated to estimation of the apparent wavelength. Standard deviation and histogram distribution are used as quality indicators of the monitoring.

7.2.3 Spike filter threshold monitoring

The spike filter thresholds are only functions of the spike filter design and the gain of the detection chains. It is assumed that the spike filter design is correct and do not need to be monitored during the instrument life. If not, the instrument manufacturer has to set it right during the CalVal period.

The thresholds have to be initialized during CalVal, once for all, for each detection chain and redefined only if the detection chain gains are modified.
Components of the monitoring process are:

- Compute the spike filter response as a function of the spike amplitude.
- Set up a spike model: typical amplitude, typical width (for IRS instrument, the width will be a Dirac at the raw interferogram sampling scale).
- Set up a spike amplitude scale factor vector of size N as: 1, 0.5, 0.2, 0.1, 0.005, etc.
- Select M Blackbody Verification Interferograms without spike detected (typically M=100) together with all the parameters needed for processing up to level 1: on-board/ground parameters, NZpd, Opd law, Radiometric Calibration Coefficients (Gain and Offset), Spectral calibration functions (shift and shape).
- Process the interferogram set using the End to End processing chain (refer to §7.5). This will produce the reference set of Black Body spectra.
- Process N (spike amplitude scale factors vector size) times the same set but with scaled spikes. The spikes are introduced at a random OPD for each of the M interferograms.
- Compare to the reference Black Body spectra set, compute the noise introduced by the spikes and select the spike amplitude scale factor which introduces a noise X times lower than the radiometric noise (typically X=4).
- The spike threshold would be the spike filter response of the typical spike amplitude weighted by the selected spike amplitude scale factor.

Note: the spike correction flag has to be set to disable in the End to End processing chain.

7.2.4 Bit trimming table monitoring

This algorithm ensures the continuous monitoring of interferogram coding table adequacy with respect to the OPD dependent coding limits of the decimated interferograms, in view of a possible in-flight update.

NRT flags on individual interferograms are raised in case of overflows (section **Error! Reference source not found.**) The objective here is to analyse the occurrence of overflows over a configurable period and target selection in support the decision if on-board bit-trimming parameters need to be updated, if yes how. Main input to this analysis is the L0 engineering product BITTR, which contains a bit trimming report (i.e., the required information on underflows/overflows).

7.2.5 On-board Processing Monitoring

The on-board processor converts the raw interferograms at the direct detector output into decimated interferograms ready for the level 1 processing. Some raw interferograms are

however also available as inputs to this processor and can be exploited to replicate on-ground the entire on-board processing chain. This parallel processing chain can be used for identifying potential flaws in the processing itself and for diagnostic reasons in general.

The on-board processor converts the raw interferograms as the direct detector output into decimated interferograms ready for the level 1 processing. Some raw interferograms (baseline six per dwell) are however also transmitted available as inputs (together with metrology) to this processor and can be exploited to replicate on-ground the entire on-board processing chain. This parallel processing chain can be used for identifying potential flaws in the processing itself and for diagnostic reasons in general.

The raw interferograms are not processed continuously, but offline "as necessary" according to the monitoring objective. Therefore, the processor includes a tool to select a configurable collection from the archive of raw interferograms.

In order to cover all monitoring objectives, the processor is modular with respect to on-board processing parameters: Spike filter, non-linearity correction coefficients, resampling parameters, decimation filter, bit trimming.

Outputs are either decimated or undecimated IFGs obtained from raw IFGs. Monitoring objectives are manifold, some of them require further processing in the raw IFG end-to-end verification chain (section 7.5):

- Check of identity between on-board and on-ground processed raw IFGs.
- Check of the status of on-board processing quality indices and flags.
- Check of tuneable on-board parameters prior to inflight update (see above).
- Performance assessment of the FIR decimation.

7.2.6 Interferogram baseline characterization

During the CalVal phase, the baseline sensitivity with respect to the detector position in the focal plane and with respect to the scene temperature will be assessed. A set of $VarBaseLine$ functions of spectral band, detector position and scene energy will be defined. These will be inputs to the on-line monitoring of the LOS stability (section 6.2.3).

The interferogram baseline characterisation is done using verification interferograms, without spikes, corrected from the non-linearity, integration contrast corrected and resampled using the OPD law from metrology module:

- Polynomial fitting in the least square sense of the interferogram, $IFG(1:L)$ weighted in order to remove the central fringe domain.
    - Set the central fringe domain
    - $Wgt(l) = 0\ if\ Opd(l) \in Central\ Fringe\ Domain, else\ Wgt(l) = 1$
    - $P(A0, A1, A2, \dots) = LeastSquareFit[IFG(1:L), Wgt(1:L)]$
    - $BaseLine(1:L) = A0 + A1\ Opd(1:L) + A2\ Opd(1:L)^2 + \cdots$
    - $VarBaseLine = ABS[IFG(1) - IFG(L)]$

7.3 Radiometric monitoring

7.3.1 In-field stray light check

The in-field stray light is made up of ghost images due to possibly multiple reflections on the lens surfaces as well as scattered light due to contamination of the optical path. It translates into a loss of contrast of the beam focused on the detector in particular at the edge between a dark and a bright area. The Figure 50 shows how the dark area is contaminated by the in-field stray light. Note that the in-field stray light varies mostly along an axis perpendicular to the dark/bright edge.

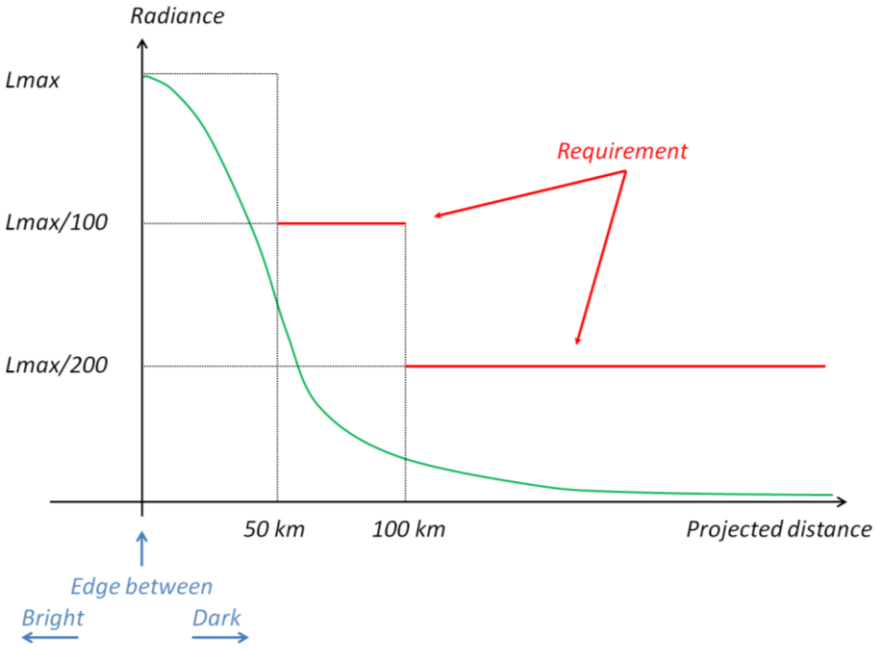

Figure 50: Distribution of in-field stray light radiance for a wavenumber ν as a function of the projected distance to the edge between a bright and a dark area (green). The red lines mark the requirement.

In order to monitor (expectedly at low frequency) the in-field straylight, a limb/earth disk transition sequence is acquired during less than one LAC period in fixed-stare external calibration, such that the scene is characterised by an almost exact 50% Earth coverage and a possibly uniform Earth scene. The preferred dwell position is close to the equator where array columns are parallel to the Earth disk edge. These views are radiometrically calibrated and averaged in time in order to reduce the noise on the estimation.

For each wavenumber, the maximum value of the in-field radiance $L_\nu^{IFSTRAY\_MAX}$ is determined by averaging the radiance of all pixels in the bright area:

$$L_\nu^{IFSTRAY\_MAX}(\nu) = \frac{1}{160.N^{EDGE}} \sum_{i=1}^{N^{EDGE}} \sum_{j=1}^{160} Re\left(\widetilde{G(i,J,\nu)}\left[\widetilde{S_\nu^{DS2}(i,J,\nu)} - \widetilde{O(i,J,\nu)}\right]\right)$$

where N^{EDGE} is the column corresponding to the dark/bright transition. The residual radiance in the dark area will be computed for all the columns *i* on the limb edge.

The radiance varying mostly in the East-West direction (i.e. along the x-axis), the residual radiance in the dark area is thus averaged along all rows in order to reduce the noise:

$$L_{\nu}^{IFSTRAY\_RES}(\nu,i)=\frac{1}{160}\sum_{\mathrm{j}=1}^{160}Re\left(G\widetilde{(\imath,J,\nu)}\left[S_{\nu}^{DS2}\widetilde{(\imath,J,\nu)}-O\widetilde{(\imath,J,\nu)}\right]\right)\ ;\ i>N^{EDGE}$$

This leads to the one-dimensional distribution of the average limb radiance (including in-field straylight) as function of the column i, thus of the limb tangent height $d(i)$ (green curve in (Figure 46). For N^{EDGE}close to 80 (i.e. a 50% Earth/limb coverage), the maximum tangent height is close to 400 km.

The values, $L_{\nu}^{IFSTRAY\_RES50}(\nu)=L_{\nu}^{IFSTRAY\_RES}(\nu,d=50km)$ and $L_{\nu}^{IFSTRAY\_RES100}(\nu)=L_{\nu}^{IFSTRAY\_RES}(\nu,d=100km)$, at tangent heights 50 km and 100 km, respectively, are interpolated from $L_{\nu}^{IFSTRAY\_RES}(\nu,i)$ with $d(i)$ known.

A flag is raised whenever incompliance with requirements of Figure 50 is stated.

$$\mathrm{FLG}_{IFSTRAY\_MOD50}(\nu)=\begin{cases}0 & L_{\nu}^{IFSTRAY\_RES50}(\nu)\le L_{\nu}^{IFSTRAY\_MAX}(\nu)/100\\ 1 & L_{\nu}^{IFSTRAY\_RES50}(\nu)>L_{\nu}^{IFSTRAY\_MAX}(\nu)/100\end{cases}\qquad \textbf{\textit{Eq. 77}}$$

$$\mathrm{FLG}_{IFSTRAY\_MOD100}(\nu)=\begin{cases}0 & L_{\nu}^{IFSTRAY\_RES100}(\nu)\le L_{\nu}^{IFSTRAY\_MAX}(\nu)/200\\ 1 & L_{\nu}^{IFSTRAY\_RES100}(\nu)>L_{\nu}^{IFSTRAY\_MAX}(\nu)/200\end{cases}\qquad \textbf{\textit{Eq. 78}}$$

7.3.2 Sun straylight level check

The Sun straylight check (sometimes referred to as out-of-field straylight check) consists in checking the quantity of Sun light reaching the detector when the Sun is in the field of view. To do so, the test relies on DS2 views affected by Sun straylight, i.e. acquired when the Sun is within 3 degrees of the line of sight. These are radiometrically calibrated to remove the contribution of the thermal background and the spatially averaged radiance is compared to a model of the straylight distribution.

Although this test could theoretically be performed during routine operations on a single DS2 view, it is advisable to carry it out during dedicated periods where several DS2 are acquired successively and averaged to reduce the noise. In that case, the instrument background is estimated using DS2 views acquired on the Earth side opposite to the Sun. The comparison is performed between the model L_{ν}^{stray} and the measurement $L_{\nu}^{DS2}(i,j,\nu)$. In case the difference $\Delta L_{\nu}^{SSTRAY}(\nu)=\left|L_{\nu}^{DS2}(i,j,\nu)-L_{\nu}^{stray}\right|$ exceeds a threshold, it means that the model is not valid and that the straylight correction cannot be properly performed. In that case, a new characterization campaign is needed.

7.3.3 Background monitoring (diurnal and annual cycle)

The instrument thermal background is expected to experience large variations over the day and the year that impact the radiometric calibration. Monitoring these variations is thus important to assess the accuracy and the stability of the process.

Background online monitoring is covered in the frame of calibration offset stability assessment (section **Error! Reference source not found.**). The present algorithm aims at analysing the diurnal variations and its annual cycle. It is applied once per day.

All DS2 views S_{DS2} (normalized by the radiometric gain R_c) measured within 24 hours will be fitted by a cubic spline to yield a model of the background radiance at any given time t:

$$\widetilde{L_{DS2}}(i,j,k,t) = \text{SPLINT}\left(\frac{\widetilde{S_{DS2}}(i,j,k,t_{DS2})}{\widetilde{R_c}(i,j,k,t_{DS2})}, t\right)$$

where t_{DS2} are the times at which the DS2 are acquired and SPLINT is a spline interpolator. The fit (representing the "truth") will be compared to the estimations of instrument background $\widetilde{L_{BG}}$ generated by linear extrapolation within the radiometric calibration over the same period. The spatially average background error in radiance is then given by:

$$\Delta L_v^{BG}(k,t_{BG}) = \langle \left| \widetilde{L_{BG}}(i,j,k,t_{BG}) - \widetilde{L_{DS2}}(i,j,k,t_{BG}) \right| \rangle_{i,j} \qquad \textit{Eq. 79}$$

where t_{BG} are the times at which the instrument backgrounds are evaluated.

This evaluation can only be carried out once per day so it is not possible to flag the L1b products if the value $\max(\Delta L_v^{BG}(k,t_{BG}))$ exceeds a given threshold. However, this value can be used for the mid-term monitoring of the stability of the process, and eventually to a refinement of the operational background signal extrapolation (section 5.3.2.6)

7.3.4 Out of band signal monitoring

The objective is to monitor the non-linearity coefficients and to raise an alert if these deviate beyond a certain threshold for the coefficients applied on-board, initiating the full non-linearity characterization (see section 7.2.1). Using single blackbody raw interferograms (obtained in nominal operations), the out-of-band radiometric noise is evaluated (in arbitrary units), mainly in view of monitoring the evolution of non-linearity, radiometric noise and potentially of signals corresponding to artefacts other than residual non-linearity.

The out-of-band signal is evaluated on the blackbody raw interferograms after non-linearity correction and resampling to the nominal OPD grid using the OPD law from the metrology module and without decimation. Ideally, there is no signal after non-linearity correction in the domain out-of-band as determined during commissioning for the non-linearity characterisation algorithm.

The algorithms steps are:

- Fourier Transform of the resampled interferogram,
- Compute, separately for real and imaginary parts, the average and the standard deviation over the spectral range:

$$\nu \geq 0 \; and \; \nu \leq \frac{1}{2dOPD} \; and \; \nu \in out \; of \; band \; spectral \; domain$$

- Compute the modulus of the averaged signal: $AVG = complex[AVG_{Real}, AVG_{Imag}]$

The departure of the average signal from zero is a sign for residual non-linearity. The standard deviation of the real and imaginary parts, representative for the noise, are expected to be similar.

The time evolution of the average and the standard deviation are representative respectively to the non-linearity and the noise evolution and have to be controlled by two threshold values established during the commissioning phase.

7.3.5 Complex radiometric calibration monitoring

The complex radiometric calibration ideally removes systematic contributions to the imaginary spectrum and the remaining imaginary part contains only the radiometric noise equal to the radiometric noise of the real part.

The quality of this operation can by monitored through the analysis of the complex spectrum. The phase correction error is:

$$\delta\varphi(\nu) = Arctang[Imag(L(\nu), Real(L(\nu)]$$

Online monitoring, described in section **Error! Reference source not found.**, raises a pixel-independent flag available to users in case of phase correction errors exceeding a threshold. This threshold is determined offline, as described in the present section.

The input data set would be at least a dwell of blackbody calibrated spectra. The phase correction error acts as a cosine on the real part where $\widetilde{L^{BB}_{meas}}$ is the complex calibrated spectrum:

$$Real\left[\widetilde{L^{BB}_{meas}}(\nu)\right] = \left|\widetilde{L^{BB}_{meas}}(\nu)\right| \cos\left(\delta\varphi(\nu)\right) \cong \left|\widetilde{L^{BB}_{meas}}(\nu)\right| \left(1 - \frac{\delta\varphi(\nu)^2}{2}\right)$$

and as a sine on the imaginary part:

$$Imag\left[\widetilde{L^{BB}_{meas}}(\nu)\right] = |\widetilde{L^{BB}_{meas}}(\nu)| \sin\left(\delta\varphi(\nu)\right) \cong |\widetilde{L^{BB}_{meas}}(\nu)| \delta\varphi(\nu)$$

This means that the imaginary part of the (complex) calibrated spectrum is much more sensitive to the phase correction error than its real part. For example, if the phase error is 1 mrad, the imaginary part is 2000 times more sensitive than the real part.

The main contributor to the phase correction error is the stability of the ZPD during the radiometric calibration period (affecting all pixels in a similar manner), its signature will be a linear variation with respect to the wave numbers.

The phase correction error is fitted in the least square sense weight by the real part of the spectrum:

$$P(A0, A1, A2, \dots) = LeastSquareFit[\delta\varphi(\nu), Real[\widetilde{L^{BB}_{meas}}(\nu)]]$$
$$Fitted\delta\varphi(\nu) = A0 + A1\,\nu + A2\,\nu^2 + \cdots$$

It is expected that only the linear coefficient A1 will be significant.

The corrected spectrum is:

$$Real[(L_c(\nu)] = |L(\nu)|\cos[\delta\varphi(\nu) - Fitted\delta\varphi(\nu)]$$
$$Imag[(L_c(\nu)] = |L(\nu)|\sin[\delta\varphi(\nu) - Fitted\delta\varphi(\nu)]$$
$$L_c(\nu) = complex[Real[(L_c(\nu)], Imag[(L_c(\nu)]]$$

If the observation targets are blackbody the radiometric noise characterisation, described in section 7.3.6, is applied to the data sets L and L_c. The real and imaginary noise figures should be identical for L_c (corrected) data set and the imaginary part noise figure biased with respect to real part noise figure for L (uncorrected) data set.
The results should be used to consolidate the thresholds for raising the phase correction error flag in the online monitoring for the atmospheric targets. As the quantity phase correction error is independent of the amplitude of the spectrum (dynamic of the scene), it is easier to use it for controlling the quality of the radiometric calibration for atmospheric targets.

7.3.6 Radiometric noise characterization and correlated noise

The characterization of the radiometric noise is estimated using blackbody observations; indeed:

- BB views are spatially uniform so that it is possible to define the mean level of the radiance and to compute how much the measured radiance differs from it (i.e. characterization of the precision);
- The temperature of the blackbody is known and so is then its theoretical radiance. The difference with the measured mean level yields a characterization of the accuracy.

The blackbody observations must be spectrally and radiometrically calibrated. The radiometric calibration equation is however slightly different from Eq. 22: the blackbody is not seen through the main telescope so that only the DS1 views have to be considered. From Eq. 17 we have then:

$$\widetilde{L_{meas}^{BB}} = \frac{1}{\rho_\nu^{FIM}} \frac{\widetilde{S_\nu^{BB}} - \widetilde{S_\nu^{DS1}}}{\widetilde{R_c(\nu)}}$$

The radiometric noise spectrum is, for each pixel of the detector array:

$$\Delta\widetilde{L_{meas}^{BB}(\imath,\jmath,\nu_k)} = \widetilde{L_{meas}^{BB}(\imath,\jmath,\nu_k)} - \langle\widetilde{L_{meas}^{BB}(\imath,\jmath,\nu_k)}\rangle_{i,j} \qquad \textbf{\textit{Eq. 80}}$$

The noise covariance between spectral channels k1 and k2 is given by:

$$CoVar(Re\{\Delta\widetilde{L_{meas}^{BB}(\imath,\jmath,\nu_{k1})}\}, Re\{\Delta\widetilde{L_{meas}^{BB}(\imath,\jmath,\nu_{k2})}\})$$

and the noise equivalent delta radiance in channel k as the square root of the variance is:

$$NEdL_R(\nu_k) = \frac{1}{N_c N_r}\sqrt{\sum_i\sum_j \left(Re\{\Delta\widetilde{L_{meas}^{BB}(\imath,\jmath,\nu_k)}\}\right)^2} \qquad \textbf{\textit{Eq. 81}}$$

that can be converted in NedT using:

$$NEdT_R(\nu_k) = {NEdL_R(\nu_k)} \Big/ \left(\frac{\partial \mathcal{P}(\nu_k)}{\partial T}\right)_{280K}$$

Noise covariance and NedT are made available to the users independently of the NRT dissemination of the IRS L1 product.

According to Eq. 81, the noise is evaluated from the imaginary part as a check of consistency. In case of inconsistency, the further analysis is covered by the monitoring described in section 7.3.5.

The baseline algorithm is applied approximately once per month and exploits a selected triple of consecutive BB dwells acquired in nominal operation, after averaging. It is assumed that the blackbody temperature can be considered as constant over the three consecutive acquisitions.

This baseline algorithm does not enable a detector dependent analysis, the output of which (25600 covariance matrices) is not desired by the user. Nevertheless, one must ensure that the long-term monitoring must is representative of the communicated 'average' noise covariance at detector level. Therefore, a variant of the above algorithm is required for a detector-specific evaluation of the noise covariance where the selection of detectors is configurable. Objectives include a general estimation of the variability of noise covariance over the detector array up to a specific analysis upon suspicious detectors (e.g. identified elsewhere as affected by dead sub-detectors).

The prerequisite to do so is an external calibration sequence over one LAC period in fixed BB acquisition mode, including a few DS1 acquisitions at the beginning and at the end of this period.

During this external calibration, the blackbody temperature cannot be considered as constant and must be corrected. The pixel and time dependent noise spectrum has to be scaled to a reference blackbody temperature and is then given by:

$$\Delta L^{BB}_{meas\ IJ}\widetilde{(t,\nu_k)} = L^{BB}_{meas\ IJ}(t,\nu_k)\cdot\widetilde{\frac{\mathcal{P}\left(\nu_k,T^{BB}_{ref}\right)}{\mathcal{P}(\nu_k,T^{BB}(t))}} - \langle L^{BB}_{meas\ IJ}(t,\nu_k)\cdot\widetilde{\frac{\mathcal{P}\left(\nu_k,T^{BB}_{ref}\right)}{\mathcal{P}(\nu_k,T^{BB}(t))}}\rangle_t \qquad \textbf{Eq. 82}$$

All following steps are carried out according to the baseline algorithm.

7.4 Spectral calibration performance monitoring

Spectral performance assessment distinguishes between the monitoring of instrument state observables affecting directly the performance of the SRF estimation (thus, the spectral calibration) process, and a direct analysis of the spectral calibration performance independently of any parameters of the IRS spectral model. The spectral calibration performance monitoring is described in the present section.

The IASI concept can be adopted for IRS: it is primarily based on the acquisition of a sequence of a fixed Earth scene in external calibration to obtain a low-noise spectrum per super-detector corresponding to a quasi-stable terrestrial scene, which is compared to a radiative transfer simulation based on collocated NWP data.

The frequency of this dedicated external calibration, the length of each external calibration event in fixed Earth View stare, the selection of the stare and the selection of the detectors to be analysed shall be configurable in lack of any in-flight experience with the IRS system. Qualitatively:

1) The frequency of fixed Earth View external calibrations will be eventually adjusted to the observed stability of the spectral calibration performance. As a thumb number, the corresponding frequency for IASI routine external calibration is once per month. A much higher frequency is expected during the IRS commissioning, a reliable statement upon the required frequency of IRS external calibration in fixed Earth View mode should be derived from IRS commissioning.
2) The length of the external calibration event is driven by noise reduction on the one hand, and scene stability on the other hand (with the length of operational service outage as additional constraint). During one LAC, the noise reduction is close to a factor 8, while cloudy scenes cannot be considered as stable at the scale of an IRS spatial sample (opposite to clear-sky ocean scenes). Fixed stare external calibration will therefore typically not last more than one LAC period (15 minutes).
3) The fixed stare position in a given LAC, should maximise the probability of observations of clear-sky areas with elevated surface temperature. This is to enhance spectral signatures in the measured and theoretical reference spectra. Details depend on the configurability of the fixed stare position (which may be optimised at the climatological or at the more or less short-term forecast time scale.
4) The analysis should be feasible for any of the 25600 detectors per spectral band. However, the routine monitoring of the spectral calibration performance can certainly be limited to a strongly subsampled set of detectors (e.g. a 5x5 matrix selecting one line out of 40 and one column out of 40).

7.4.1 Absolute spectral calibration assessment

The spectral shift between the measured average spectrum and the simulated reference spectrum is determined by maximizing their correlation in various spectral windows (see section 7.4.4). Limitations of this method regarding the algorithm performance are related to spectroscopic uncertainties and knowledge errors of geophysical conditions (including residual cloudiness) in the radiative transfer simulation, to residual noise in the measurements, and to the hypothesis of instrument stability during the acquisition period. The hypothesis is made that chromatic effects do not vary significantly over the width of the spectral windows. Furthermore, the suitability of spectral windows is variable. Therefore, the monitoring is applied to a variety of spectral windows (order 20), and the overall interpretation of the results requires knowledge (pre-established based on simulations) on the expected performance deficiencies due to the mentioned limitations.

A scale factor between the average of fully processed measured spectra and the reference spectrum is derived for each selected detector and each considered spectral window. These scale factors, potentially after spectral smoothing, provide the absolute accuracy of the spectral calibration.

Details concerning the reference spectrum simulation with regard to the required NWP interface and the radiative transfer model to be run will be described in a future update of this document.

7.4.2 Inter-pixel spectral calibration assessment

Monitoring of the inter-pixel consistency of the IRS L1 radiances is a mean to assess the performance of spectral uniformisation. Residual inter-pixel inconsistency translates unavoidably into constraints and/or errors the user has to deal with.

Scene homogeneity over an entire IRS stare cannot be reasonably assumed, thus fully processed spectra from different detectors cannot be reliably compared.

Analysis of absolute scale factors derived in section 7.4.1 at the inter-detector level removes this limitation to a large extent, because the scale factor determination takes scene variations into account via variations of the reference spectra. The scale factor estimation is therefore supposed to be insensitive to moderate scene variations across the stare.

7.4.3 Spectral Performance evaluation over overlapping zones

Initially, the spectral calibration performance assessment was exclusively based on the analysis of overlapping scenes. This approach is based, as the absolute assessment (section 7.4.1), on the availability of a stable Earth scene measured several times.

Exploitation of stare-to-stare overlapping pixel pairs or zones is potentially useful for monitoring purposes other than spectral performance. It can also provide an indication of the relative spectral calibration performance of spectra corresponding to the overlapping parts of the array. However, by its limitation to a few detectors close to the array borders, the approach is insufficient for absolute spectral calibration assessment.

The algorithm runs on nominally processed L1 spectra, it can be activated whenever necessary in nominal operational mode, independently of scheduling external calibration sequences.

The initial specification was to compare coincident spectra from overlapping pixels in adjacent stares, exclusively acquired in the Spectral Calibration Zone (SCZ), and after elimination of locally heterogeneous scene conditions. Furthermore, a minimum “overlapping ratio” was required to qualify a pixel pair as coincident.

A modified version of this algorithm is maintained in this document:

- In order to ensure scene stability, the selection of overlaps is restricted to successive dwells, i.e. in E-W direction.
- Spectra are averaged over the entire overlapping zone. This ensures a considerable reduction of radiometric noise and increases the overlapping ratio.
- The filtering of heterogeneous scenes is abandoned since the sensitivity of the algorithm performance is removed at the scale of the size of the overlapping zone.
- The restriction of the analysis to scenes within the Spectral Calibration Zone is abandoned, since spectral accuracy requirements apply anytime and everywhere.

The algorithm aims at assessing the spectral accuracy. The evaluated accuracy covers all sources of errors including the instrument itself as well as the spectral calibration and correction routines.

It exploits the fact that overlapping regions are present in adjacent dwells. By directly comparing the spectra from overlapping pixels of adjacent dwells many conclusions on the instrument and processing performances can be drawn. By iteratively correlating two spectra assumed identical, it is possible to determine a residual spectral scaling factor error. This approach provides an assessment and monitoring approach completely independent of the approach used for the spectral calibration and correction.

7.4.3.1 Inputs and assomptions

Inputs to the analysis are:

- Selection of an E-W adjacent pair of stares N/N+1.
- Corresponding L1 products.
- List of pixels to be averaged for stares N and N+1 (if not static to be determined from L1 geolocation).
- List of spectral windows to be analysed.

An important assumption in this approach is that both spectra being compared are similar. Quasi-simultaneity of the measurements in overlapping zones is ensured only for adjacent stares in E-W direction where the delay corresponds to one dwell period of about 10 seconds. The delay of measurements in N-S overlapping zones is variable and can reach up to 300 seconds. In this context, only overlaps in E-W direction are considered.

This monitoring routine processes the radiometrically and spectrally corrected spectra (L1B).

The analysis is performed independently for a selection of suitable spectral windows.

Spectra are averaged over all pixels in the overlapping areas, consisting of (roughly) 3(E-W) by 154 (N-S) sounding samples.
It is currently not known if the list of overlapping pixel pairs can be considered as static for any stare position, static for a given stare position, or if it must be considered as variable.

The overlapping region of two adjacent E-W stares is illustrated on Figure 51.

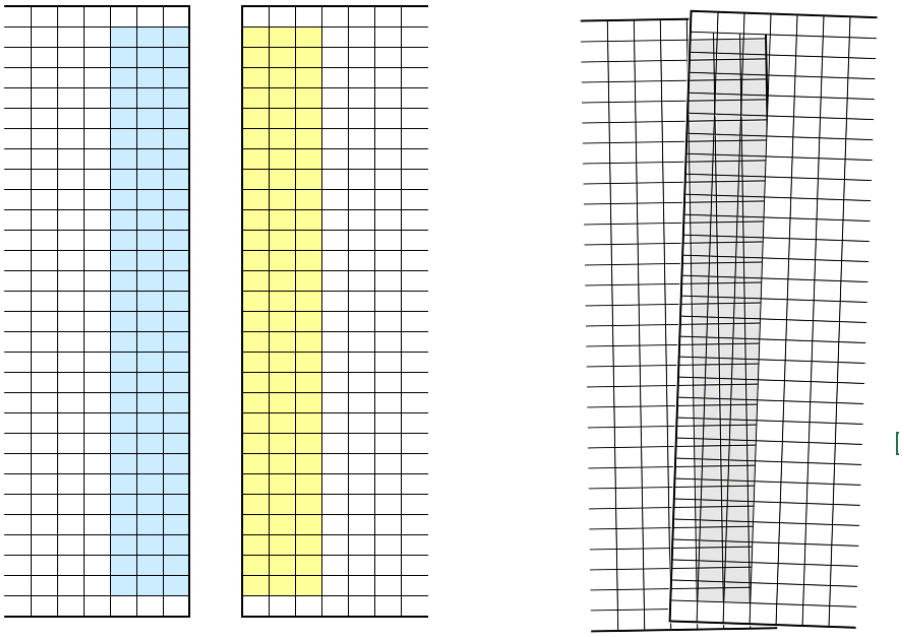

Figure 51: Illustration of pixels considered as overlapping for adjacent E-W stares (yellow and blue). The resulting overlapping area is illustrated in grey for non-ideal stare positions.

With the surface of the pixel A_{px} and the surface of the overlapping region A_{ol}, the overlapping ratio is given with the number of pixels constituting the overlapping zone N_{px} by:

$$\rho_{ol} = \frac{A_{ol}}{N_{px} \cdot A_{px}} . \qquad \textit{Eq. 83}$$

If the overlapping ratio is considered unstable in time and over stares, the geometric information about overlapping areas has to be provided by the INR. It is probably sufficient to derive the overlapping ratio and the list of overlapping pixels from the geolocalisation of the corner detectors. These routines are not covered here and the information is assumed available.

7.4.3.2 Characterization of the overlapping zone

Conceived as an offline monitoring, the analysis of spectra in overlapping zones can be activated “whenever necessary” (in the extreme case continuously) on a configurable selection of L1 spectra as a post-processing. In this context, a filtering of unfavourable conditions is not required, but overlapping conditions should be characterized in view of a potential impact on the algorithm performance.

Equivalence of the average spectra in the overlapping zone is characterized by a constant and negligible time delay of 10 seconds and by the overlapping ratio. The theoretical worst-case overlapping ratio is roughly 2.5*153.5/(3*154) ≈ 5/6 where the actual ratio is much more sensitive to the E/W overlapping conditions. This means that an overlapping ratio of > 0.8 is guaranteed (assuming insignificant inter-dwell geolocation errors) for any overlap.

The geophysical scene content can be characterized by the L1 radiances averaged over all individual spatial samples and, as a heterogeneity index, their standard deviation over detectors. The computation can be restricted to one or a few reference spectral channels in the atmospheric window, independently of the considered spectral window.

In summary, the following characterization parameters are available:

- The overlapping ratio.
- The average radiance of a reference window channel in the overlapping zone (stares N and N+1);
- The standard deviation of a reference window channel over pixels contributing to the overlapping zone (stares N and N+1).

Differences of average radiances and their standard deviations between stares N and N+1 are expected to be small. They characterise the scene equivalence.
The spectral scale estimation performance between average spectra is expected to decrease with decreasing average radiance due to lower amplitudes of spectral signatures. However, due to the low noise level of the average spectra, the algorithm performance may still be high enough even in case of cold scenes.
Scene heterogeneity and overlapping ratio (as long as remaining in the expected range) are not expected to affect the algorithm performance.

7.4.3.3 Correlation analysis and relative scale factor

The relative scale factor between the two average spectra of the overlapping zone is determined according to the absolute shift determination method (section 7.4.4) based on correlation maximisation between a measured and a reference spectrum.

In the present case, two “measured spectra” are investigated, and no matter which of the two is considered as reference (i.e. on the nominal L1B spectral scale), the resulting scale factor must be considered as relative.

This relative scaling factor should ideally be 0, meaning that both average spectra have the same scaling factor. Any other value is a direct indicator of the spectral accuracy performance.

7.4.4 Absolute spectral shift determination

This classical method, is based on the maximisation of the spectral correlation between observed and theoretical reference spectra in predefined calibration windows. The specification of the calibration windows remains to be consolidated. It is expected that residual chromatic distortion of the reference spectral grid (including its not well-known variability) favours the specification of narrow windows, which contain only one or a few spectral absorption features.

Spectral shifts are determined between processed input EV spectra and consistently processed reference spectra (oversampling, apodisation)

- per spectral band $b = LWIR, MWIR$

- per spectral calibration window in each band $SW_b = [1, NSW_b]$
- per selected detector (i, j)

Spectrum samples are $S_{ij}(k)$ and $S_{ref,ij}(k)$ with $k = [k_1(SW_b) - L_0, k_2(SW_b) + L_0]$ where L_0 applies as a margin only to the measured spectrum.

The reference spectrum is associated to a known, regular (identical to the oversampled L1B spectral grid) wave number grid $\nu_{ref,ij}(k)$. This wavenumber grid is independent of the detector position (i, j).

In a loop over l_0, the correlation coefficient $C(l_0)$ between $S_{ij}(l)$ and $S_{ref,ij}(k)$ is computed over the domain $k_1 \leq k \leq k_2$ with $l = k + l_0$ and $-L_0 \leq l_0 \leq L_0$.

$$C(l_0) = \frac{\sum_{k=k1}^{k2} \left(S\left(l(k)\right) - \bar{S}\right) \cdot \left(S_{ref}(k) - \overline{S_{ref}}\right)}{\sqrt{\sum_{k=k1}^{k2} \left(S\left(l(k)\right) - \bar{S}\right)^2 \cdot \left(S_{ref}(k) - \overline{S_{ref}}\right)^2}} \qquad \textit{Eq. 84}$$

L_0 has to be defined consistently with the spectral sampling step grid $\delta\nu_{ref,ij}$ and the expected maximum shift.

The maximum of $C(l_0)$ is determined by a parabolic fit, leading to the fractional sample position s_0. In practice, the sampling loop over l_0 may be optimised through iterative sampling, in a first round at massively reduced spectral sampling for rough determination of correlation maximum position, in a second round at full sampling over a reduced spectral range for precise estimation of s_0.

The window dependent, individual instantaneous scale factor estimation is given by:

$$\frac{1}{1 + SF_{SWb}} = \left(\frac{\nu}{\nu_{ref}}\right)_{SWb} = 1 + \frac{s_0}{(k_1 + k_2)/2} \qquad \textit{Eq. 85}$$

7.5 Verification Interferogram End-to-End processing chain

The objective is to run the whole processing chain (on-board, on-ground) with the verification raw interferograms to test the quality of each module in the processing and to perform some characterisation and monitoring.

The processing chain will be a concatenation of on-board operators excluding the metrology module (see section 7.2.5) and on-ground operators excluding the radiometric and spectral calibration coefficients computation.

The inputs are Verification Interferograms, NZpd, Opd law from metrology module, L0 parameters, L1 parameters, Radiometric Gain and Offset, Spectral Calibration functions (shift, shape) according to IF acquisition date.

It is necessary to introduce some options in the processing chain: spike correction enable/disable, low frequency non linearity correction enable/disable, decimation enable/disable, apodisation enable/disable, spectral calibration enable/disable…

7.6 Inter-calibration with IASI (and possibly with CrIS and IASI-NG)

Inter-calibration between two systems providing comparable L1 products is usually not addressed in the L1 ATBD of any of the two systems due to the absence of coordinated intersystem requirements and the incapacity to state compliance with such requirements if they were existent.

Nevertheless, inter-calibration is a key approach to the verification and monitoring of the L1 product of both systems, in particular to assess radiometric and spectral uncertainties as far as hyperspectral sounding instruments are concerned.

The perspective for IRS is particularly promising in this context, capitalizing on the increasing experience gained with the Global Space-based Inter-Calibration System (GSICS):

- Inter-calibration is being performed operationally between LEO hyperspectral IR atmospheric sounders, namely the three IASI flight models, the two CrIS flight models and still with AIRS. Continuity is ensured during the MTG operational period, in particular with the IASI-NG flight models on the MetOp-SG platforms.
- Accuracy of the reference system and several other backup systems as well as the knowledge of uncertainty of this accuracy is well established.
- The inter-comparison processing level (level 1 products from both systems degraded spatially and spectrally to the lower performance of the two instruments to be compared) is well established and fully adoptable for IRS.
- Inter-calibration of the IASI flight models is constrained by the absence of strictly simultaneous observations, inter-calibration of IASI with CrIS (and AIRS) by relatively rare “Simultaneous Nadir Overpasses” (SNO), which happen exclusively in high latitudes, i.e., in relatively unfavourable atmospheric conditions. These constraints are significantly less stringent for IRS inter-calibration with one of these LEO systems (and their successors). Simultaneous overpasses will happen regularly and at higher frequency all over the Meteosat disk, those happening in the vicinity of the MTG sub-satellite point will provide SNOs with the LEO system. Associated to lower latitudes, they will generally represent more favourable atmospheric conditions. Furthermore, inter-calibration processing facilities concerning GEO-LEO SNO handling do already exist (SEVIRI, FCI in the near future) and need little adaptations in view of an exploitation with IRS.
- IRS provides spatial coverage without gaps at relatively high spatial sampling. Spatial coincidence with a given LEO sounder sample can be ensured more accurately than between LEO samples.
- Beyond a continuous inter-calibration monitoring during nominal operations, inter-calibration in nearly perfect conditions of simultaneity and coincidence can be obtained punctually through external calibration events in fixed Earth View stare mode, specifically coordinated with a predicted overpass period of the reference system, and potentially optimised with respect to geophysical conditions through mid-term weather forecast.

IRS inter-calibration requirements exceed the scope of the IRS system alone, except those for the feasibility of the external calibration mode. The potential of inter-calibration for assessing the radiometric and spectral quality of IRS L1 product is unquestionable; the implementation of requirements across systems and readiness of IRS inter-calibration is desirable already at the start of IRS operations.

8 POST-PROCESSING

8.1 Principal Components compression

8.1.1 Principle

MTG-IRS measurements consist of signal and noise. The MTG-IRS L1b measurements are represented as radiances at about 1700 wavenumbers, which are spectrally highly correlated. This correlation comes from the signal itself as the noise is expected to be spectrally uncorrelated; except within a few neighbour channels apart in case of apodisation. This information redundancy means that the effective rank of the subspace spanned by the signal within the measurements is much lower than the number of channels – or in other words, the number of independent pieces of information within the MTG-IRS measurements is much smaller than 1700. These are the principal components scores (PCS) computed with the leading eigenvectors representing the natural variance and covariance of the noise-normalised measurements.

Reconstructed radiances can be computed from the PCS, by projecting the measurements onto this signal subspace with the objective of preserving the signal while suppressing a major part of the noise. The difference between the original and the reconstructed radiances is called the reconstruction residuals and mainly consist of random instrument noise. The residuals are used to compute reconstruction scores, which is an indicator of the fidelity of the reconstructed information *versus* the original spectra.

If the reconstruction score for a given spectrum is too high (i.e. exceeds a configurable threshold), there is suspicion that some atmospheric signal could not be represented by the selected leading principal components. An outlier flag can be raised for the corresponding pixel. The threshold for the identification of the outliers is different for each detector and depends linearly on the sum of the radiances, to account for the photonic noise.

The compression of the spectra is performed for each band separately.

8.1.2 Off-line configuration

This section describes how to compute the static coefficients (i.e. the eigenvectors, E, and the radiance mean vector, $\bar{y}$) which are required for the on-line compression as well as the subsequent decompression. The description applies to either of the two spectral bands, which will be compressed similarly but independently, using a single set of eigenvectors to compress spectra from any of the 160x160 MTG-IRS detectors.

We assume that an estimate of the instrument noise covariance matrix, $N^2 \in R^{mxm}$ (where m is the number of channels being compressed), is available. This matrix is used for noise normalisation in order to distribute the amount of noise carried by (i.e. projected onto the direction of) each eigenvector evenly and thereby to achieve a better separation of signal and noise. It should therefore encompass all inter-channel correlations of the instrument noise.

The (principal) matrix square root, $N \in R^{mxm}$, of the instrument noise covariance matrix, N^2, is referred to as the noise normalisation matrix (and is unique since N^2 is positive semi-definite).

In practice it is very likely that the instrument noise covariance will be different for each detector and that it will have a component of photonic noise which increases with the strength of the signal. However, experience from IASI shows that the use of a single noise normalisation matrix is fully acceptable, even though the noise normalisation will be less than perfect.

As an initial baseline we propose to use any official estimate of the instrument noise covariance matrix as it becomes available (probably derived from blackbody measurements). However, the noise covariance matrix should also be estimated from the Earth scene measurements and if there turns out to be a large difference, the latter may be adopted.

Given the noise normalisation matrix, we need to select two further items before we can compute the eigenvectors and the radiance mean vector: a) a training set, $Y \in R^{mxn}$, of n L1B spectra and b) the number, s, of eigenvectors to retain. We will discuss the choice of Y and s in some detail later – once they have been selected we proceed as follows:

Compute the mean, $\bar{Y} \in R^m$, and covariance, $Y_{COV} \in R^{mxm}$, of the training set using an update formula. (Example code to compute the sample mean and covariance with an update formula can be found in Appendix H)

We now have two options for computing the coefficients:

1) Set $\bar{y} = \bar{Y}$ and let $E \in R^{mxs}$ be the matrix composed of the s first eigenvectors of the noise normalised covariance matrix $N^{-1}Y_{COV}N^{-1}$
2) Set $\bar{y} = 0$ and let $E \in R^{mxs}$ be the matrix composed of the s first eigenvectors of the matrix $N^{-1}(\bar{y}\bar{y}^T + Y_{COV})N^{-1}$

Where, in both cases, 'first eigenvectors' refer to the ordering by decreasing eigenvalue. The second option ensures that the reconstructed radiances will be contained in a linear subspace of R^m (whereas with the first option, in general, they will be contained in an affine subspace only). This might have some practical advantages. However, the initial baseline is to use the first option similarly to what is currently done for IASI, but this choice might be reconsidered. The choice does not impact the on-line compression.

When N is not diagonal (which will not be the case when the instrument noise covariance matrix N^2 isn't) it is convenient for the users to have access to the pre-computed reconstruction operator $R = NE \in R^{mxs}$ in the eigenvector files.

8.1.2.1 Choice of training set

Although the use of a training set consisting of simulated spectra would be helpful in suppressing instrument artefacts, it is not recommended for dissemination purposes, since the suppression of some atmospheric signal which has not been properly modelled by the radiative transfer model is almost inevitable. The training set should therefore be composed of real measurements, which should be large in number and include rare features such as fires

and volcanic eruptions. The large number of spectra is important to ensure an evenly distribution of the noise among all eigenvectors and the inclusion of rare features is needed in order to represent spectra with similar features properly as a small number of PC scores.

An obvious choice would be to use a training set consisting of all spectra measured so far, as it would be the best way to ensure that all rare features ever observed would be included. For this purpose it is recommended to keep a series of daily covariance matrices (together with the mean vector and sample count), which allows the covariance matrices over a period to be merged. Such a series of daily covariance matrices would also be useful for offline investigations of possible trends, which might not be easily observed directly from the spectra. The occurrence of a hitherto unobserved spectral feature (for example the first major volcanic eruption after launch) would be a natural occasion to update the training set. Such events are easily detected by monitoring the reconstruction scores. However it is clear that in this way the ability to properly compress the newly seen feature would only be added with some delay.

We therefore supplement to global PC scores with a small number of local PCs and corresponding scores based on the noise normalised residuals of the current dwell after reconstruction with the global PCs. It is up to the end user to decide whether to include the additional local PC scores in the radiance reconstruction. Including the additional local PC scores results in reconstructed radiances which are closer to the original, but for the vast majority of dwells this is achieved only by including a little more of the original noise.

For many applications, including NWC and NWP, the rare events with unusual spectral features are not important and should preferably be filtered out, which can be done based on the reconstruction score as long as the features have not been included in the training set.

8.1.2.2 Number of eigenvectors to retain

The number of eigenvectors to retain, s, should be chosen to be sufficiently large such that the amount of atmospheric loss is negligible and the residuals (original minus reconstructed spectra) consist almost exclusively of transformed noise $(I-A)N^2(I-A)^T$, where A = RP is the reconstruction projection. A practical approach would be to choose s to be the eigenvector rank where the rate of decrease of the eigenvalues starts to get constant (second derivative equal to zero). Any detectable atmospheric loss would be seen when comparing the covariance of the residuals, $(I-A)Y_{COV}(I-A)^T$, with the transformed noise, $(I-A)N^2(I-A)^T$.

8.1.2.3 Detector harmonisation

IRS spectra will be measured by 25600 different pixels that will have different responses and will possibly generate various artefacts. It is not unusual that a large portion of the eigenvectors carries instrument artefacts rather than atmospheric signal (as is for example the case with IASI). Typically, instrument artefacts from different detectors will manifest themselves along the same directions, but possibly with different strengths. In the case that instrument artefacts from different detectors go in different directions of the radiance space, all these directions will be included in the eigenvectors, which are common for all detectors. When building eigenvectors for PC compression using a training set consisting of spectra from several detectors with different characteristics, features which are only seen for some of the detectors will be captured in the eigenvectors – if enough of them are retained. This is fine if the purpose is to be able to reconstruct noise filtered spectra retaining the individual

flavour of each pixel. But, unless there is a clear deficiency in one or more of the pixels, true features originating from the observed scenes will be common to all pixels and by retaining only a common subspace we can homogenise the spectra from different detectors while partly suppressing the instrument artefacts. Canonical angles between subspaces can be used to determine the directions of a subspace common to all detectors as detailed in RD-6. Admittedly this method carries the danger that a single bad detector could compromise (i.e. exclude important directions of) the common subspace, if not properly detected. However, as the common subspace is a subspace of the overall signal subspace, it is possible to partition the directions of the overall signal space into those which are common to all detectors and those which are not. In this way, the suppression of instrument artefacts (not common to all detectors) could be optionally applied by the user by restricting the reconstruction to use only PC scores corresponding to the common directions[6]. The on-line compression remains unchanged whether detector harmonisation is applied or not.

8.1.2.4 Offset and slope for outlier thresholds

The slope, b, and the detector dependent offset, a_j, used to set the dynamic threshold for outlier detection are based on statistics from a large number of sample spectra, say the training set, Y, used for the computation of the eigenvectors above. For each spectrum, $Y_{:,i}$ we compute the reconstruction score, r_i^{score} (see on-line compression), and the sum of the radiances, $y_i^{sum} = \sum_{k=1}^{m} Y_{k,i}$, which we need to compute the slope, b, as

$$b = \frac{\sum_{i=1}^{n}(y_i^{sum} - \overline{y^{sum}})r_i^{score}}{\sum_{i=1}^{n}(y_i^{sum} - \overline{y^{sum}})(y_i^{sum} - \overline{y^{sum}})} \qquad \textit{Eq. 86}$$

where, $\overline{y^{sum}} = \frac{1}{n}\sum_{i=1}^{n}\sum_{k=1}^{m} Y_{k,i}$. The rationale behind this is that the instrument noise, and therefore also the reconstruction score, increases with the signal (due to photonic noise), and we model this as a linear relationship between the reconstruction score and the radiance sum. To compute the offsets we consider the statistics (mean and standard deviation) of the normalised reconstruction scores, $r_i^{score} - by_i^{sum}$, computed individually for each of the detectors, j, and set the offset a_j to the mean plus four times the standard deviation.

8.1.3 On-line compression

The following subsections explain how PC compression is achieved and how to compute reconstruction scores in each of the spectral bands. These algorithms shall be applied to the LWIR and MWIR separately.

8.1.3.1 Computation of PC scores

The transformation of the L1B radiances, *y*, into principal component scores, $p \in R^s$, is a linear transformation which can be performed in two steps

[6] It should be noted that this optional filtering also has the potential to suppress rare spectral features which have only been observed by some of the detectors and should therefore be applied with care for applications where such features are important. Since this method for detector homogenisation requires manual tuning and the potential benefit depends on the detailed characteristics of the detectors, which will only be known post-launch, it is not included in the initial baseline, but should be studied once real observations become available.

$$y_N = N^{-1}(y - \bar{y}) \qquad \textit{Eq. 87}$$

$$p = E^T y_N = E^T N^{-1}(y - \bar{y}) \qquad \textit{Eq. 88}$$

where y_N – the noise normalised radiances – are kept as they are needed for subsequent computations . For computational efficiency it is recommended to compute the PC scores for more than one spectrum at a time, such that the matrix-vector multiplication of equation (73) is replaced with a matrix-matrix multiplication, which permits better exploitation of the cache.

8.1.3.2 Quantisation of the PC scores

The computed floating point PC scores must be quantised and stored as integers, i.e. divided by the quantisation factor, *qf*, and rounded to the nearest integer before they are written to the product. This ensures that the product size is not unnecessarily increased by storing unimportant less significant bits of the floating point representation of the PC scores. It can be shown that a quantisation factor of 0.5 corresponds to an increase of the random noise of one percent. The quantisation factor should be configurable, although we recommend to use the value *qf* = 0.5, and must be written to the product, since it is needed for the reconstruction of the radiances.

If a quantised PC score overflows, i.e. falls outside the range, which can be represented using a 4-byte signed integer, it shall be set to 'UNDEFINED' value and a flag shall be raised to indicate the failure of the compression. It is expected that this will never happen in practice.

We note that the dynamic range of the quantised PC scores decrease with the rank and that most of them could fit in a small number of bits. They are therefore compressed considerably by using standard compression tools such as gzip and bzip2.

8.1.3.3 Noise normalised reconstruction residuals and reconstruction scores

The noise normalised residuals, r_N, are computed as the difference between the noise normalised L1B radiances y_N and the noise normalised reconstructed radiances, Ep,

$$r_N = y_N - Ep \qquad \textit{Eq. 89}$$

The reconstruction score, r^{score}, is the root mean square of the noise-normalised residuals computed as follows:

$$r^{score} = \sqrt{\frac{1}{m}\sum_{k=1}^{m}(r_{N_k})^2} \qquad \textit{Eq. 90}$$

Although the difference is very small, the computation of the reconstruction score shall, strictly speaking, be based on the quantised PC scores, i.e. using $qf * Round(p_j/qf)$ instead

of p_j for j=1,...,s in the computation, as this corresponds to the information which will be delivered to the Users.

If the compression failed due to overflow (see section 8.1.3.2), no attempt to compute the reconstruction score shall be made and it shall be set to "UNDEFINED" value.

8.1.3.4 Detection of outlier spectra

The spectra for which the residuals are larger than expected due to instrument noise are called 'outliers' and are detected by comparing the reconstruction score to a dynamic threshold, τ, computed as

$$\tau = a_i + b \sum_{k=1}^{m} y_k \qquad \textit{Eq. 91}$$

where i is the index of the detector and a and b are the offsets and slope taken from the static configuration, determined as described in section 8.1.2.4. An unusual high reconstruction score might be an indication of atmospheric loss from the compression, which could happen for spectra with rare features which have not been properly represented in the training set used to build the eigenvectors. Or it could be an indication of an instrument or processing problem resulting in a noise, which is higher than normally. A spectrum shall be flagged as outlier, if the dynamic threshold on the reconstruction score (Eq. 90) is exceed in either or both of the bands, with an indication of the bands for which this happened.

8.1.3.5 Computation of supplementary local eigenvectors and corresponding PC scores

Let $X = \overline{r_N r_N}^T + r_{N_{COV}}$ where $\overline{r_N}$ and $r_{N_{COV}}$ are the mean and the covariance computed over the full dwell of the noise normalised residuals r_N. Compute the s_L first eigenvectors of X and gather them to form a matrix $E_L \in R^{m*s_L}$. The local PC scores for each pixel is computed as

$$p_L = E_L^T r_N \qquad \textit{Eq. 92}$$

The local PC scores p_L are provided in the product together with the corresponding reconstruction operator NE_L (rather than the local eigenvectors E_L themselves). The trace (sum of diagonal elements) of X and the eigenvalues corresponding to the s_L first eigenvectors shall also be provided in the product.

Furthermore the reconstruction scores after application of the local eigenvectors shall also be computed and provided in the product. For this we compute the updated noise normalised residuals

$$r_{NL} = r_N - E_L p_L \qquad \textit{Eq. 93}$$

for which we compute the root mean square as in equation 137.

8.2 Scenes analysis

The Scene Analysis processing module aims at providing an estimate of the cloud amount in each IRS pixel and an estimation of the aerosol optical depth (AOD). If clouds or elevated amounts of AOD have been detected, then the scene analysis will set the corresponding quality flag. Furthermore, the IRS imaging mode is used to derive an heterogeneity index; this mode indeed constitutes the sole near-real-time data source providing heterogeneity information at sub-pixel scale.

8.2.1 Cloud Determination Method

8.2.1.1 Introduction

The cloud analysis processing module will provide estimates of the cloud fraction within the MTG-IRS footprints as well as the radiative impact of the clouds on the observations (which we will refer to as the cloud signal). The cloud signal is measured in Kelvin and is defined as the difference between the observed window channel brightness temperature and the clear sky predicted window channel brightness temperature of the scene. Obviously, the cloud signal for clear scenes is expected to be (close to) zero, but the cloud signal can also be close to zero for some cloudy scenes if the cloud top temperature is similar to the surface temperature. For this reason, the cloud signal is supplemented with the cloud fraction.

8.2.1.2 Cloud Analysis

The estimates of the cloud fraction and the cloud signal are obtained by a statistical retrieval aapproach which we call PWLR^3 (PieceWiseLinearRegression-cube). The two main principles of PWLR^3 are: a) to apply different linear regressions in different classes determined by the measurements and auxiliary information such as satellite and solar zenith angles and the surface altitude b) use measurements from neighbouring pixels as additioanal predictors in the regression. Many variations are possible within these principles. For the retrieval of the cloud information we use a two step approach, where a first estimate of the cloud parameters is obtained by linear regression in a number of classes which are determined by K-means clustering of leading PC scores of the observations. The first estimate of each retrieved parameter is then compared to threshold values to obtain a further subdivision of the initial classes. For further background on the general PWLR^3 algorithm, the reaser is invited to refer to the IRS L2 ATBD [RD-19]

8.2.1.2.1 Training set

The training set is composed of real measurements paired with collocated reference data for the two parameters to be retrieved:

- Cloud signal (OmC, *stands for Observed minus Calculated*)
- Cloud fraction (CF).

Using a very large number of training pairs helps to avoid overtraining and sensitivity to random errors found in the reference data. Nevertheless, the choice of the reference data to be paired with the measurements is important, since any systematic biases present in the reference data are inherited by the PWLR^3. While the PWLR^3 method is sensitive to systematic errors in the reference data it is largely insensitive to random errors, provided that the training set is big enough. It is perfectly normal to achieve a retrieval precision which is better than the precision found in the training data.

To explain the cloud signal OmC to be retrieved by the PWLR^3, we start by looking at a common cloud screening method in NWP and Level 2 data processing. It consists in comparing the observed window channel brightness temperature with the corresponding brightness temperature computed by a forward model with clear-sky assumption. If the absolute value of the difference between the two is high, exceeding a configurable threshold, then the scene can be considered likely cloudy.

For the forward model computation the best available profiles shall be used and often profiles from a short range forecast are used. However, even if fine scale vertical structures of the profiles are present in the forecasts but cannot be retrieved (because they do not affect the upwelling radiance), the broader vertical structures of the profiles are usually better captured by the retrievals (with less representation error), which do therefore exhibit superior OBS minus CALC statistics in clear sky. Retrieved profiles are hence better suited for the detection of clouds.

In order to save online computation time and possibly reduce random errors, the OBS minus CALC values described above are computed offline for measurements in the training set. The OBS minus CALC can be computed for any channel, but is most sensitive to clouds in window channels. We will use the average value of the two windows channels at about 819.5 and 831.75 cm^{-1} for the training.

The reference cloud fraction to be trained against could come from many different sources, including ECMWF analysis. Another natural choice would be to use the cloud fraction coming from the variational cloud parameter retrieval within the Level 2 processing [RD-19], which would be applied offline to generate the reference cloud fraction of the training set.

8.2.1.2.2 Detailed description of the retrieval algorithm

The first step of the PLWR^3 retrieval algorithm is to compute the PC scores which represents the measurements in a group of 4 by 4 pixels.

It is a central concept of the PWLR^3 approach that the retrieved parameters of each individual pixel is predicted from the measurement of this pixel as well as the measurements of a group of adjacent pixels. In a conservative MTG-IRS Day-1 approach consistent with the IASI and IASI-NG schemas we choose groups of 4 by 4 pixels as the basic unit of the retrievals. This means that each vector of predictors carries information about the IRS spectra in 16 (4 by 4) pixels and that the corresponding output vector carries information about the retrieved parameters for the same group of 16 pixels.

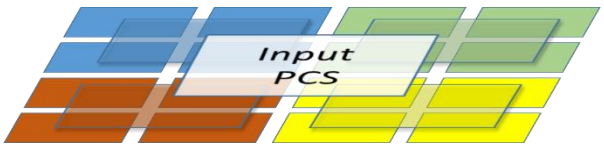

Figure 52: PWLR^3 adjacent pixels grouping. Principal components of PCs in each individual IRS pixel are computed first in the 2x2-pixel quadrants (blue, green, red, yellow) and then combined again to form the inputs to the PWLR^3 retrieval (white box).,.

The full vector of input IRS PC scores for the 16 pixels would contain a big portion of co-linearity coming both from the spectral correlation (between the two bands) and the spatial correlation (between the 16 adjacent pixels). It is therefore necessary to compute PC scores of the input PC scores. This is done in two hierarchical steps as follows for improved computational efficiency and simpler handling of missing pixels (for example off disc pixels or pixels with bad quality spectra). First the PC scores in both band 1 and band 2 of each group of 4 adjacent (2 by 2) pixels are combined to a single set of PC scores, then the final set of PC scores for the 4 by 4 pixels is obtained by combining the 4 sets of the PC scores for 2 by 2 pixels computed in the first step. These final PC scores are supplemented in the input vector, X, by the secant of the satellite zenith angle, the surface elevation in meters and optionally a measure of the inhomogeneity within the pixel .

The second step is to apply the actual piecewise linear regression. The algorithm is the same for all four LACs, but each of the four LACs is served by a different set of PWLR[3] coefficients. In a given particular LAC we furthermore distinguish between four types of scenes each served by its own set of coefficients: Day-Land, Day-Sea, Night-Land and Night-Sea. If the average sun zenith angle of the 16 pixels is below 90 degrees Day coefficients are to be used (the Night coefficients are used when the average sun zenith angle is higher or equal to 90 degrees). The Sea coefficients are only to be used if all 16 pixels are over sea; if one or more of the 16 pixels are over land, the Land coefficients must be used.

Once the scene type has been determined, a number of independent retrieval instances are applied and the final retrieval vector, $\boldsymbol{Y}$, is obtained as the average of the individual instances of retrievals. The algorithm is the same for all instances, but different sets of coefficients are used for each of them. Each instance follows the following retrieval sequence:

i. Regression class determination for first regression
ii. Application of the first regression coefficients
iii. Regression class refinement
iv. Application of the regression coefficients

Besides the PC scores a group of 4 by 4 pixels, the predictors, $\boldsymbol{X}$, consists of 3 parameters which are particular to each individual pixel: the secant of the satellite zenith angle, the surface altitude and a measure of the inhomogeneity of the pixel.

i. <u>First regression class identification:</u> The regression class is determined by choosing the class where the centre is closest (in terms of Euclidian distance) to the scaled input vector. Only a subset of the predictors in the input vector $\boldsymbol{X}$ are used for the computation of these distances and the scale factors to be multiplied with each predictor are configuration coefficients (a scale factor equal to zero indicates that the corresponding predictor is not used for the classification and should not be used for the computation of the distances to the class centres).

$$k_x = argmin\,(\sum_i (c_{k,i} - w_i . x_i)^2) \qquad \textit{Eq. 94}$$

where

k_x is the regression class to be used for the input vector x,
k is the class identifier
i is the input vector index

$c_{k,i}$ is the i[th] element of the centre of class k
x_i is the i[th] element of the input vector
w_i is the input scaling factor of the i[th] element of the input vector

The purpose of the input scaling factors is to avoid that the predictors with the highest variance dominate the classification, typically the standard deviation within the training set is used.

ii. First Regression: The class identifies which set of linear regression coefficients to be applied. It consists of an offset vector $\bar{\boldsymbol{y}}$ and a regression operator, $\boldsymbol{R}$. A separate set of linear regression coefficients is available for each of the classes.The application of these coefficients produces the instance output vector $\boldsymbol{y}$ as

$$\boldsymbol{y} = \bar{\boldsymbol{y}} + \boldsymbol{RX} \qquad \textit{Eq. 95}$$

iii. Regression class refinement: For each retrieved parameter the value is compared to a sorted list of threshold values, to define the regression subclass. (n-1 threshold values for n regression subclasses.

iv. Regression: The regression formula (Eq. 148) is applied again. This time with coefficients $\bar{\boldsymbol{y}}$ and $\boldsymbol{R}$ corresponding to the subclass identified above

Finally the retrievals from the individual instances are averaged.

8.2.1.2.3 Moving window strategy

If the PWLR[3] 4x4 window were moved in a contiguous manner, as illustrated on the left-hand side of Figure 53, each dwell would be covered by 40 times 40 PWLR[3] retrievals of 4 by 4 groups of pixels. With this configuration, pixels such as the lower-right corner highlighted in purple on the figure would benefit from neighbouring pixels from only one side. To avoid this, the PWLR[3] window could be translated by one pixel at a time and retrievals be retained only for the centre pixel, which would effectively result in 25600 retrievals per dwell. To mitigate the computational overhead and still ensure that retrievals in individual pixels will benefit from adjacent information in all directions, overlapping groups of 4 by 4 retrievals will be organised, yielding more than one PWLR[3] retrieval for each pixel. For Day-1, we suggest to use overlapping 4 by 4 groups always shifted by two pixels in each direction, as illustrated on the right-hand side of Figure 53. In this way we end up with 79 times 79 basic PWLR[3] retrievals per dwell and all pixels, except at the edges of the dwell, will be a combination of 4 different retrievals. Of these four retrievals there will always be one in which the current pixel is one of the four centre pixels in the 4 by 4 group (green-window 3 on the right-hand side of Figure 53), there will be two where it is on the lateral edge but not corner (yellow- and blue-windows 2 and 4) of the 4 by 4 group and one where it is in the corner (red-window 1). The four individual retrievals for the current pixel as detailed in 8.2.1.2.2 will be averaged with weights 1/3, ¼, ¼ and 1/6 respectively to form the final retrieval for this pixel, to give more weight to the configuration where it sits in the middle of the window.

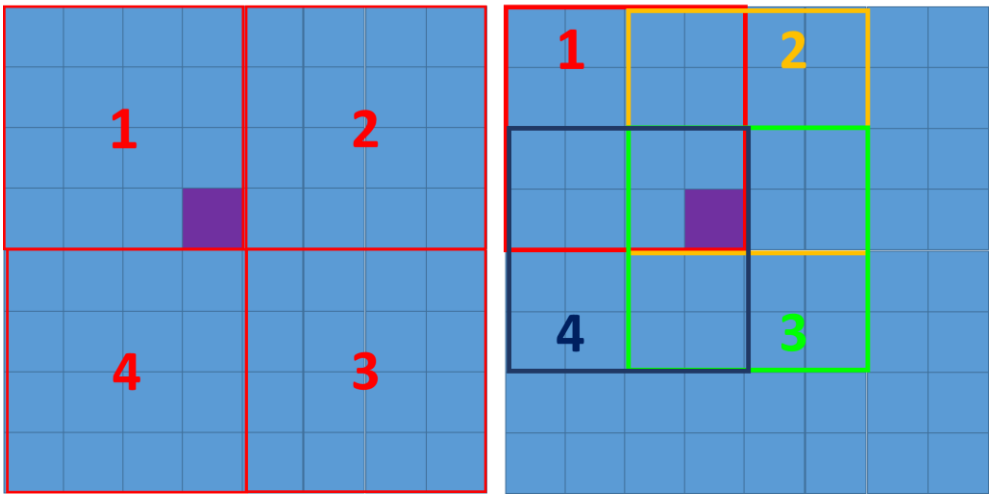

Figure 53: PWLR^3 moving window strategy illustrated on an 8 by 8 IRS-pixels subgrid of a dwell. Left: non-overlapping groups. Right: overlapping groups

8.2.1.3 Handling non-nominal situations

The regression assumes that all predictors, with which it was trained, are available and of good quality. This can cause problems, when one or more of the 16 adjacent pixels used in a PWLR^3 retrieval is missing or of bad quality. To overcome this problem we can use the remaining good pixels to predict the failed or missing pixels with linear regression and compute the PC scores of the predictors with predicted values of the missing predictors, which can be achieved with a simple update of the eigenvectors.

Let $\boldsymbol{E}$ be the matrix of eigenvectors, partitioned into rows corresponding to missing predictors $\boldsymbol{E_1}$ and rows corresponding to the remaining good predictors $\boldsymbol{E_0}$

$$\boldsymbol{E} = \begin{bmatrix} \boldsymbol{E_0} \\ \boldsymbol{E_1} \end{bmatrix} \qquad \textit{Eq. 96}$$

and let $\boldsymbol{C}$

$$\boldsymbol{C} = \begin{bmatrix} \boldsymbol{C_{00}} & \boldsymbol{C_{01}} \\ \boldsymbol{C_{10}} & \boldsymbol{C_{11}} \end{bmatrix} \qquad \textit{Eq. 97}$$

be the covariance matrix of all predictors compatibly partitioned.
To eliminate the use of the missing predictors, $\boldsymbol{E_1}$ must be set to zero in the updated eigenvectors and $\boldsymbol{E_0}$ must be replaced by

$$\boldsymbol{E_0} + \boldsymbol{C_{00}}^{-1}\boldsymbol{C_{01}}\boldsymbol{E_1} \qquad \textit{Eq. 98}$$

Using this principle, a total of 15 different sets of eigenvectors are needed for the computation of the PC score for groups of 2 by 2 pixels to cover all possible combinations of zero to three bad or missing pixels out of the four. Likewise, for the second step combining four groups of 2 by 2 into PC scores for a group of 4 by 4, we need 15 different set of

eigenvectors to be able to handle all possible combinations of missing 2 by 2 groups (except all four subgroups missing of course).

8.2.2 Heterogeneity index

The heterogeneity index is computed from the calibrated images. As mentioned in section 5.5, a proper absolute calibration seems difficult to achieve and what follows would need to be revised according to the output of the investigations on that issue.

The heterogeneity index HI_v per spectral band b is computed as the standard deviation of calibrated radiances $L^{EV}_{ii,jj}$ over the sub-pixels (ii, jj) of each IRS sounder pixel (i, j):

$$HI_v[i,j,b] = \frac{1}{N_{ii}N_{jj}}\left[\sum_{ii=1}^{N_{ii}}\sum_{jj=1}^{N_{jj}}\left(L^{EV}_{ii,jj}[i,j,b]\right)^2 - \left(\sum_{ii=1}^{N_{ii}}\sum_{jj=1}^{N_{jj}} L^{EV}_{ii,jj}\,[i,j,b]\right)^2\right] \qquad \textit{Eq. 99}$$

The average radiance per band and per pixel HI_M is given by:

$$HI_M[i,j,b] = \frac{1}{N_{ii}N_{jj}}\sum_{ii=1}^{N_{ii}}\sum_{jj=1}^{N_{jj}} L^{EV}_{ii,jj}\,[i,j,b] \qquad \textit{Eq. 100}$$

Its provision along with the heterogeneity index allows:

- the conversion of the index into brightness temperature;
- a first-glance discrimination of hot and cold scenes;
- the a posteriori evaluation of the heterogeneity index over an area extended to several IRS sounder pixels;
- an additional verification measure of the consistency between imaging and normal mode processing (comparing the average index with band-integrated IRS spectra).

The heterogeneity index as given above is in radiance units. Conversion in brightness temperature, that comes handy for some applications, can be performed as explained in appendix, section B.4.3, p. 174.

8.2.3 Dust Index

8.2.3.1 Introduction

The main objective of the dust index algorithm, is to provide a quality index, based on an estimation of the aerosol optical thickness (AOD) derived from the observations. The method is developed by [RD-14] and is a simple regression method which explores the channels in the 760 – 1210 cm^{-1} domain.

8.2.3.2 Method

The AOD estimation algorithm is a simple vector multiplication of a matrix $\boldsymbol{M}$ and the difference between the actual and a reference spectrum. Let R_d represent the estimated AOD and $\boldsymbol{L}_{ref}$ a reference spectrum then

$$R_d = \boldsymbol{M}\left(\boldsymbol{L} - \boldsymbol{L}_{ref}\right) \qquad \textit{Eq. 101}$$

The gain matrix $\boldsymbol{M}$ and the reference spectrum $\boldsymbol{L}_{ref}$ are determined using scenes which are free of dust and detailed radiative transfer calculations [RD-14]. Then if the AOD estimation exceed a threshold value

$$R_d > \mathrm{z}_{R_d} \qquad \textit{Eq. 102}$$

the dust index can be set to indicate the presence of elevated dust.

9 MODULES DECOMPOSITION

9.1 Day-1 modules decomposition

Figure 54 gives an overview of the baseline processing applied to the IRS level-0 products.

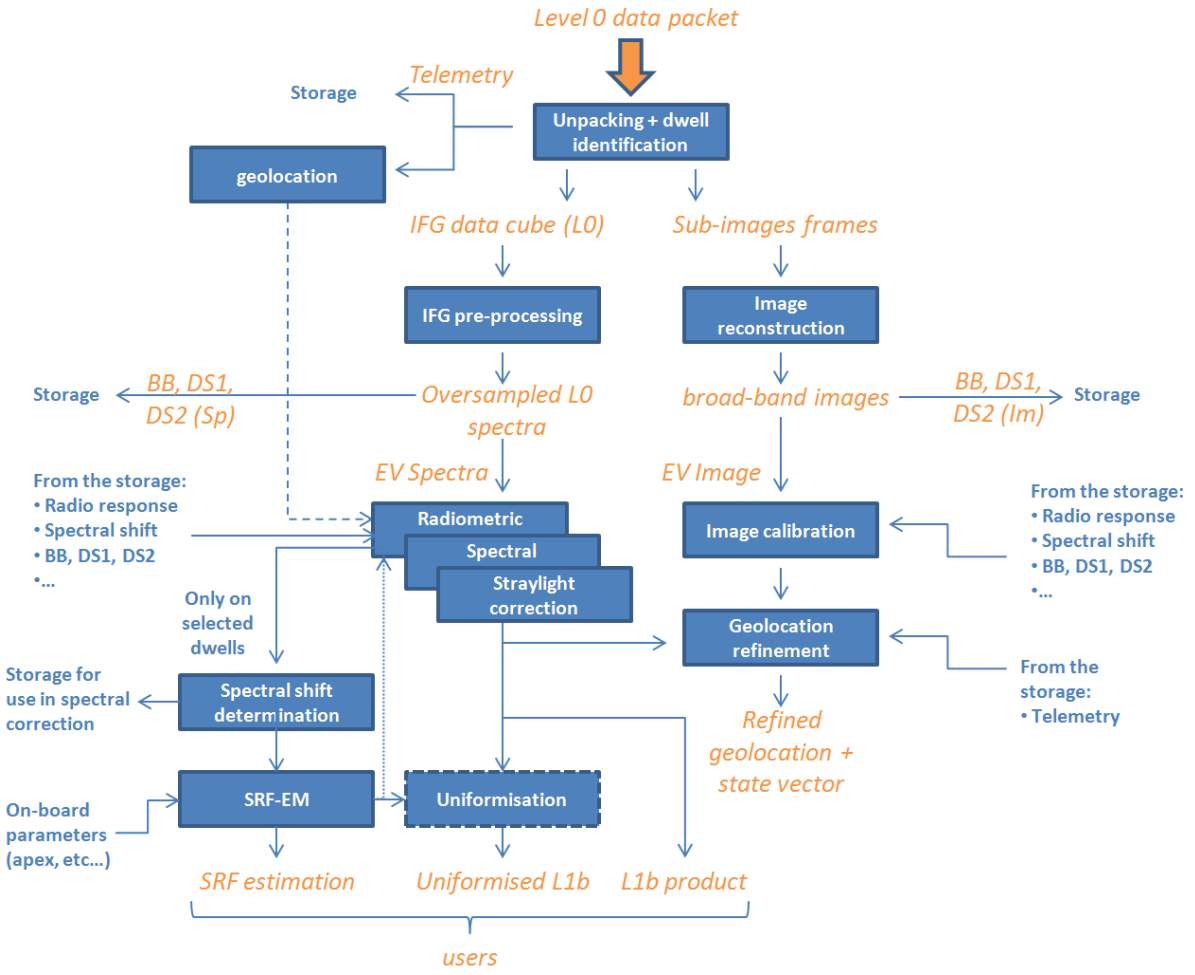

Figure 54: overview of the level-1 processing

9.2 Data flows

The nominal scan pattern has been presented in section 3.1.1: the dwells are scanned row by row, from South to North, in the sequential order as from the dwell number. A DS2 view is acquired at the beginning of each row. DS1 and BB views are acquired during the retrace time between two consecutive LACs, hence every fifteen minutes.

	EV *(Nominal Earth dwells)*	BB *(During retrace at the end of the LAC, after the last EV)*	DS1 *(During rally (at the beg of the LAC, before the first EV)*	DS2 *(After changing scanning row)*	Total
LAC 1	70	4	5	5	84
LAC 2	69	5	6	4	84
LAC 3	68	6	6	4	84
LAC4	73	3	3	5	84

Table 11: number of dwells of each type in the various LACs (EV: Earth View, DS1: deep space 1, DS2: deep space 2, BB: blackbody)

Because there are several types of calibration views that are furthermore not adjacent in time to the science data views, there is a complex data flow between the various dwells that is illustrated on Figure 55 that can be summarized as follow:

- Between two LACs (i.e. every 15 minutes), the radiometric response of the instrument is computed from the BB and DS1 views that are acquired at this time. The radiometric response will be stored and stay valid for all subsequent dwells until a new one becomes available (i.e. until the end of the considered LAC).
- At the beginning of each line, a new DS2 is acquired. It will be normalized by the radiometric response, stored and used to compute the coefficients of the linear fit together with the previous DS2(s). These coefficients will stay valid until a new useable DS2 is acquired, typically at the beginning of the next scan row (if there is not straylight contamination) i.e. for at most 3 minutes. It is worth to note that this does not mean that the estimated instrument background is constant during this time, only the coefficients are.
- The spectral shift is computed from Earth spectra acquired in a sub-region (covering several dwells) of LAC4. Processing is performed on these dwells as on the others Erath view dwells; but in addition radiometrically calibrated spectra are used for the spectral shift estimation. This value is then used for all subsequent dwells until this region is visited again i.e. every 30 minutes.

The validity duration of these various parameters is illustrated on Figure 56.

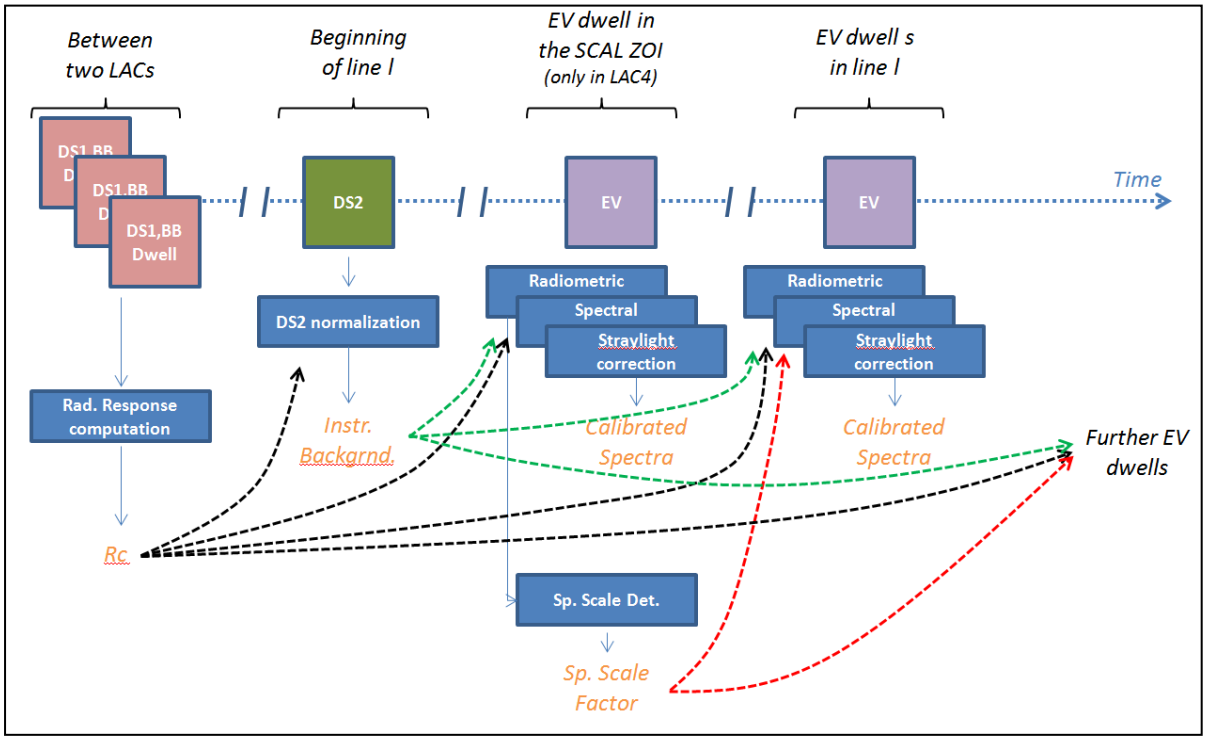

Figure 55: Main data flow between the various calibration and Earth view dwells. The symbol "Rc" stands for "Radiometric Response of the instrument", "Instr. Backgrnd." Is the normalized deep-space view that will be used to compute the instrument background, the "SCAL ZOI" is the region where the spectral shifts are estimated.

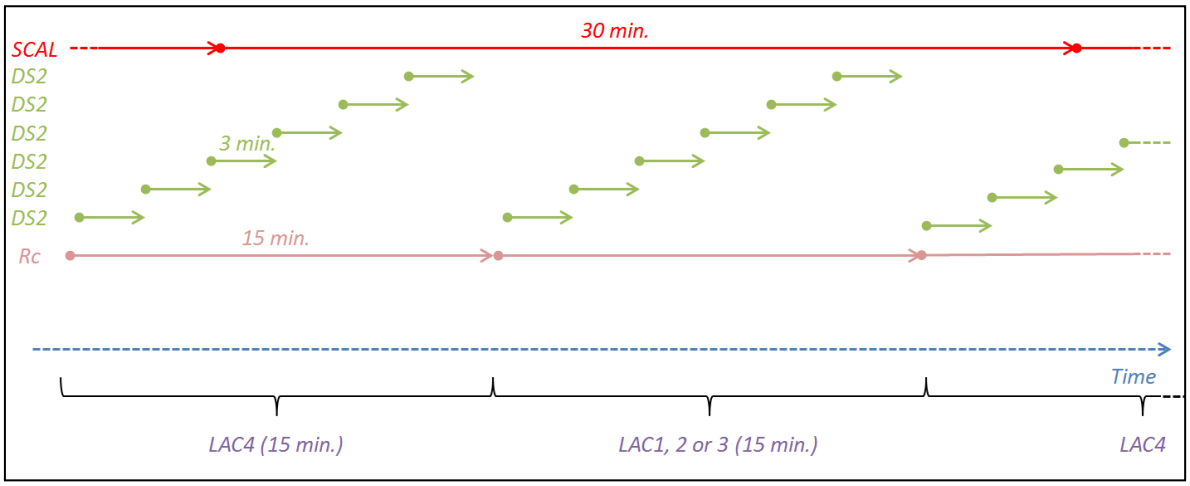

Figure 56: validity of various parameters over time; Rc: radiometric response 15 minutes (1 LAC). DS2: coefficients for the determination of the instrument background: at most 3 minutes. SCAL: spectral shif: 30 minutes (2 LACs).

Appendix A APPLICABLE AND REFERENCE DOCUMENTS

A.1 Applicable Documents

AD-1	MTG System Requirement Document [SRD]	EUM/MTG/SPE/06/0032
AD-2	MTG End User Requirements Document [EURD]	EUM/MTG/SPE/07/0036
AD-3	MTG Conventions and Terms Document [CONV]	EUM/MTG/DEF/08/0034

A.2 Reference Documents

RD-1	IRS Design and Technical Description	MTG-KT-IR-DD-0004
RD-2	IRS Performance and Calibration Analysis; Radiometric Performance Analysis	MTG-KT-IR-TN-0129
RD-3	IRS Scan Law Delivery Description	MTG-KT-IR-TN-0115
RD-4	Revercomb, H. E., *et al*. 1988. Radiometric calibration of IR Fourier transform spectrometers: solution to a problem with the High-Resolution Interferometer Sounder. *App. Opt.* **27**(**15**):3210-3218.	Doi: 10.1364/AO.27.003210
RD-5	Rodgers, C. D. 2000. Inverse Methods for Atmospheric Sounding: Theory and Practice. 2nd Ed. World Scientific.	
RD-6	Hultberg, T. 2016. IASI, CrIS, IASI-NG and MTG IRS PC compression – how to handle multiple detectors with different characteristics. 4th IASI Conference, Juan-les-Pins, France, 11-15 April 2016.	
RD-7	Cooley, J. W. and Tukey, J. W. 1965. An algorithm for the machine calculation of complex Fourier series. *Math. Of Comput.* **19**: 297-301.	Doi: 10.1090/S0025-5718-1965-0178586-1
RD-8	Blumstein, D., *et al*. 2007. In-Flight Performance of the Infrared Atmospheric Sounding Interferometer (IASI) on METOP-A. *Proc. SPIE* **6884**	doi: 10.1117/12.734162
RD-9	Lonjou, V., *et al*., "In-Flight Performance of IASI on Board METOP-A", ASSFTS 14, May 6-9, 2009	
RD-10	Knuteson, R. O., *et al*. 2005. On-orbit calibration of the Geosynchronous Imaging Fourier Transform Spectrometer (GIFTS). *Proc. SPIE* **5655**: 66-76.	Doi:10.1117/12.578992
RD-11	Tournier, B., *et al*. 2002. IASI Level 0 and 1	Doi:10.1117/12.578992

	processing algorithms description. ITSC-XII conference , Feb. 2002.	
RD-12	Tournier, B., *et al*. 2007. IASI on METOP-A Radiometric and Spectral Performances Measurement During Commissioning, 1st IASI conference, Anglet, France, Nov. 13-16, 2007	-
RD-13	Strow, L., *et al*. 2013. Spectral calibration and validation of the Cross-track Infrared Sounder on the Suomi NPP satellite. *J. Geophys. Res*. **118**, 12486-12496.	Doi: 10.1002/2013JD020480
RD-14	Clarisse, L., *et al*. 2013. A unified approach to infrared aerosol remote sensing and type specification. *Atmos. Chem. Phys*. **13**:2195 – 2221.	Doi:10.5194/acp-13-2195-2013
RD-15	Hanel, R. A. et al. 1970. The Nimbus-3 Michelson-interferometer. *Appl. Opt.* **9**:1767-1774.	Doi:10.1364/AO.9.001767
RD-16	Kempe, V. 1980. Satellite-Fourier-spectrometer for Meteor-25: design problems and mission. *Acta Astronaut.* **7**:893-902	doi: 10.1016/0094-5765(80)90078-8
RD-17	Gaucel, J.-M., *et al*. 2013. Metrology System and Method Applied to an Interferometer for remotely Analysing a Gaseous Compound. United States Patent Application Publication. Pub. No. US 2013/0044327 A1.	
RD-18	Hewison, T., et al.. 2013. GSICS Inter-Calibration of Infrared Channels of Geostationary Imagers Using Metop/IASI. *IEEE Transactions on Geoscience and Remote Sensing*, **51**(3), 1160-1170	doi:10.1109/TGRS.2013.2238544
RD-19	MTG-IRS L2 ATBD	EUM/RSP/TEN/17/935387
RD-22	Blumstein, D., *et al.* 2004. IASI instrument: technical overview and measured performances. *Proc. SPIE* **5543**, 196-207	doi:10.1117/12.560907
RD-23	Han, Y., *et al*. 2013. Suomi NPP CrIS measurements, sensor data record algorithm, calibration and validation activities, and record data quality, *J. Geophys. Res.*. **118**(22), 12734-12748	doi:10.1002/2013jd020344
RD-24	Elwell, J. D., et al. 2006. A Geosynchronous Imaging Fourier Transform Spectrometer (GIFTS) for Hyperspectral Atmospheric Remote Sensing: Instrument Overview & Preliminary Performance Results. *Proc. SPIE* **6297**, 62970S-1-62970S-12.	Doi: 10.1117/12.684135
RD-25	Yang, J. Z., *et al*. 2016. Introducing the new generation of Chinese geostationary weather satellites – FengYun 4 (FY-4). *Bull. Amer. Meteor. Soc*. (in press)	doi: 10.1175/BAMS-D-16-0065.1

RD-26 Davis, S., et al. 2001. Fourier Transform Spectroscopy. Academic press, San Diego, USA.

RD-27 Genest, J. and Tremblay, P., "Instrument line shape of Fourier transform spectrometers: analytic solutions for nonuniformly illuminated off-axis detectors", Applied Optics, 38 (25), 1999.

RD-28 Dall'Amico et al., "Meteosat Third Generation: Simulation and Level 1 Processing of Infrared Sounding Data", ESA Workshop on Simulation for European Space Program, Session 5: Future EGSE, ESA/ESTEC Noordwijk, 2015

RD-29 Dussarrat et al., "Correction of calibration ringing in the context of the MTG-S IRS instruments", https://arxiv.org/abs/2202.10149

Appendix B **NOTATIONS AND SYMBOLS**

B.1 Operators

$\{\ \}$	Routine or process arguments, e.g. $\mathrm{F}\{\mathrm{X}\}$
$(\ )$	Mathematical function argument, e.g. $\cos(\propto)$ and also range of mathematical vectors, e.g. $I(x)$, $S(\sigma)$
$[\ ]$	Index of numerical discrete arrays, e.g. $I[n]$, $S[m]$
$\langle\ \rangle$	Mean value, e.g. $\langle T \rangle$
$\tilde{Q}$	Complex quantity, as opposed to real quantity noted without tilde (~)
$\tilde{Q}^*$	Conjugate of the complex $\tilde{Q}$
$\mathrm{Re}\{\ \}$	Real part of a complex argument
$\mathrm{Im}\{\ \}$	Imaginary part of a complex argument
$\otimes$	Convolution
$\mathrm{F}\{\ \}$	Direct Fourier transform operator
$\mathrm{F}^{-1}\{\ \}$	Inverse Fourier transform operator
$\mathrm{FFT}\{\ \}$	Numerical discrete Fast Fourier Transform
$\mathcal{P}(\nu, T)$	Planck function

B.2 Notations referring to measurements

In general we have: $X_{sub}^{type}[i,j,k]$

B.2.1 Superscripts

EV	Earth View
BB	Blackbody
DS1	Deep space view 1
DS2	Deep space view 2

B.2.2 Subscripts

FIM	Flip_in Mirror
FS	Front Section

B.2.3 Indices

i,j	interferogram/spectrum spatial indices (pixel)	$0 \le i \le NPixx - 1$ $0 \le j \le NPixy - 1$

k	spectral sample index (range depends on the context)
l	Interferogram sample index (range depends on the context)

B.3 symbols

i	Complex unit	$i^2 = -1$
h	Planck constant	$h = 6.62607004 \,.\, 10^{-34}$ m^2 kg s^{-1}
k	Boltzman consant	$k = 1.38064852 \,.\, 10^{-23}$ m^2 kg s^{-2}K^{-1}
c	speed of light	$c = 299792458$ m s^{-1}

α	scan mirror angle
α^E	maximum eastward scan mirror angle during the characterization
α^W	maximum westward scan mirror angle during the characterization
ε_ν^{BB}	emissivity of the internal blackbody

d_{E-S}	Sun-Earth distance
d_{IRS-E}	Satellite-Earth center distance
γ_b	Correction to be applied to the straylight radiance to account for the baffle shadowing the scan mirror
γ_e	Correction to be applied to the straylight radiance to account for the Sun eclipse by the Earth disk

λ	Wavelength
ν	Wavenumber
δ	Optical path length
x	Optical path difference: $x = \Delta\delta$
T	Temperature
t	Time

η	Decimation factor
f_d	Decimation frequency
$\nu_{\min b}^{Filter}$ $\nu_{\max b}^{Filter}$	FIR filter limits

$\widetilde{S(\nu)}$	Raw spectrum
$A(\nu)$	Signal amplitude
$\varphi(\nu)$	Phase such that $\widetilde{S(\nu)} = A(\nu)e^{i\varphi(\nu)}$
$\varphi_{Las_l}(m)$	Phase of laser beam l and interferogram sample m
$L(\nu)$	Radiance
$I(\nu)$	Interferogram

$\widetilde{R_C}(\nu)$	Radiometric response
$SRF(\nu)$	Spectral response function
$SAF(\nu)$	Self-Apodisation function

$\widetilde{G(\nu)}$	Gain in the radiometric calibration equation
$\widetilde{O(\nu)}$	Offset in the radiometric calibration equation

L_ν^{EV}	Earth radiance
L_ν^{FS}	Radiance of the front section
L_ν^{CS}	Radiance of the core section
L_ν^{FIM}	Radiance of the flip-in mirror
L_ν^{BB}	Radiance of the blackbody
L_ν^{BG}	Radiance of the instrument thermal background
L_ν^{ext}	Radiance entering the blackbody cavity
$L_\nu^{stray}{}_0$	Straylight radiance without corrections
L_ν^{stray}	Straylight radiance including corrections for baffle shadowing and Sun eclipse
$\widetilde{S_\nu^{EV}}$	Measured complex spectrum of the Earth
$\widetilde{S_\nu^{DS2}}$	Measured complex spectrum of the DS2 (deep space through the main optical path)
$\widetilde{S_\nu^{DS1}}$	Measured complex spectrum of the DS1 (deep space through the secondary optical path)
$\widetilde{S_\nu^{BB}}$	complex spectrum of the blackbody
α	Scan angle of mirror M0 (scan mirror)
τ	Transmission (in general)
τ_ν^{FIM}	Flip-in mirror reflectivity
τ_ν^{CS}	Core section transmissivity
τ_ν^{FS}	Front section transmissivity
$\Delta\tau_\nu^{FS}$	correction of the front section transmissivity with the scan mirror angle
ϱ_ν^{FS}	maximal amplitude of the variation of the front section transmission with the scan mirror angle
$\theta_{sun}(i,j)$	Relative Line of Sight (LoS) elevation angle between the pixel (i,j) centre and the Sun centre
$\phi_{sun}(i,j)$	Relative LoS azimuth angle between the pixel (i,j) centre and the Sun centre
α_{sun}	Sun angle at which baffle shadowing starts
β_{sun}	Sun angle at which M0 is completely in the shadow
θ_{E-S}	Absolute elevation angle between the Earth centre and the Sun centre
ϕ_{E-S}	Absolute azimuth angle between the Earth centre and the Sun centre
$\mathbf{Z^{EV}}$	Measured broad-band image of the Earth
$\mathbf{Z^{DS1}}$	Measured broad-band image of the Deep-Space 1
$\mathbf{Z^{DS2}}$	Measured broad-band image of the Deep-Space 2
$\mathbf{Z^{BB}}$	Measured broad-band image of the Blackbody
$\mathbf{L^{EV}}$	Calibrated broad-band image of the Earth
$\mathbf{K}$	Detector Photo-Response Non-Uniformity

Npixc	Number of super-pixels along the x axis of the detector (160)
Npixl	Number of super-pixels along the y axis of the detector (160)
NsubPixc	Number of sub-pixels along the x axis of the detector (480)
NsubPixl	Number of sub-pixels along the y axis of the detector (480)
Nband	Number of spectral bands (2)

Nl1b Dimension of the nominal spectral grid
Nl1br Dimension of the oversampled spectral grid

B.4 Mathematical definitions

B.4.1 Fourier transform

Continuous:

$$S(\nu) = \int_{-\infty}^{\infty} I(x) e^{-2\pi i \nu x} dx$$

$$I(x) = \int_{-\infty}^{\infty} S(\nu) e^{+2\pi i \nu x} d\nu$$

Discrete:

$$S[n] = \Delta x \sum_{m=0}^{N-1} I[m] e^{-2\pi i m n / N}$$

$$I[m] = \Delta \nu \sum_{0}^{N-1} S[n] e^{+2\pi i m n / N}$$

B.4.2 Planck Function

$$\mathcal{P}(\nu, T) = \frac{2\mathrm{h}c^2\nu^3}{\exp\left(\frac{\mathrm{h}c\nu}{kT}\right) - 1} = \frac{c_1\nu^3}{\exp\left(\frac{c_2\nu}{T}\right) - 1}$$

with

$$c_1 = 1.19104.10^{-16}\ \mathrm{W\,m^{-2}\,sr^{-1}\,m^4}$$
$$c_2 = 0.0143877\ \mathrm{K\,m}$$

Conversely, the inverse Planck function is given by:

$$T(\nu, L) = \frac{c_2\nu}{ln\left(\frac{c_1\nu^3}{L}\right) + 1}$$

and its derivative with respect to temperature at T is:

$$\left(\frac{\partial \mathcal{P}(\nu)}{\partial T}\right)_T = \frac{c_1\nu^3}{\left[\exp\left(\frac{c_2\nu}{T}\right) - 1\right]^2} \exp\left(\frac{c_2\nu}{T}\right) \frac{c_2\nu}{T^2}$$

B.4.3 Images calibration units

After non-linearity correction, the linearized measured quantity is radiance [in W m-2 sr-1]. However, certain applications may favour a conversion in brightness temperature, even if the brightness temperature conversion for broadband channels inevitably involves further approximations.

Explicit brightness temperature conversion involves two steps:

(i) conversion into spectral radiance by means of an effective bandwidth;
(ii) conversion into brightness temperature by means of a central wavenumber.

The effective bandwidth $EdWn[b]$ is calculated through spectral integration of core section radiometric response after normalisation to its maximum value.

$$EdWn[b] = dWn \cdot \sum_{k=0}^{NL1A-1} R^{C}_{i,j,k}[b] / max_k\{R^{C}_{i,j,k}[b]\} \qquad \textit{Eq. 103}$$

The spectral radiance is given by the ratio of radiance and effective bandwidth:

$$N^{EV} = \frac{L^{EV}}{EdWn} \qquad \textit{Eq. 104}$$

The effective central wavenumber of the band $WnC[b]$ is given by the wavenumber integral weighted with the core section radiometric response:

$$WnC[b] = \sum_{k=0}^{NL1A-1} Wn_k[b] \cdot R^{C}_{i,j,k}[b] \Big/ \sum_{k=0}^{NL1A-1} R^{C}_{i,k,j}[b] \qquad \textit{Eq. 105}$$

The brightness temperature approximation is equivalent to the inverse Planck function of the spectral radiance, estimated at the central wavenumber:

$$T_b^{EV}[b] = InvPlanck\{N^{EV}[b], WnC[b]\} \qquad \textit{Eq. 106}$$

This formulation is approximate since it implicitly assumes flat spectra. Calculation of the central wavenumber should actually include a weighting with the spectrum itself which is not possible in practice. The effective variability of the central wavenumber with the spectrum shape introduces a non-linearity in the brightness temperature estimation, including for blackbody spectra due to the shape variation with temperature.

This type of non-linearity can be avoided using conversion look-up tables at a suitable sampling of the blackbody temperature T_{BB}. The broadband radiance L is given by:

$$L(T_{BB}) = \int Planck\{T_{BB}, \nu\} \cdot R^{C}(\nu) d\nu \Big/ \int R^{C}(\nu) d\nu \qquad \textit{Eq. 107}$$

with:

$$Planck\{T, \nu\} = \frac{c_1 \nu^3}{exp\left(\frac{c_2 \nu}{T}\right) - 1}$$

Brightness temperature conversion is obtained through a suitable regression function $\Re(L)$ such as:

$$R(L) = T_b \qquad \textit{Eq. 108}$$

Whatever the brightness temperature conversion approach, it is static only if the radiative transfer function is constant. It is expected that variations in time and between detectors are negligible at broadband level such that a unique brightness temperature conversion obtained upon some average radiometric response can be anticipated. This is nevertheless to be confirmed.

B.4.4 Noise Equivalent Temperature Difference at T_{ref} (NedT)

If a spectral difference in radiance is given by:

$$NEdL(\upsilon) = L(\nu) - L_0(\nu)$$

Then using the Planck derivative described in §B.4.2, the corresponding spectral Noise Equivalent Temperature Difference (NedT) is:

$$NEdT\left(\nu, T_{ref}\right) = \frac{NEdL(\nu)}{\left(\frac{\partial \mathcal{P}(\nu)}{\partial T}\right)_{T_{ref}}}$$

B.4.5 Residual Mean Squared Error (RMS)

$$\mathrm{RMS} = \frac{1}{N}\sqrt{\sum_{\mathrm{i=1}}^{\mathrm{N}} (\widehat{y_i} - y_i)^2}$$

B.5 Units

Radiance	W/(m^2.sr. m^{-1})
Angle	rad
Time	seconds
Wavenumber	m^{-1}
Wavelength	m
Temperature	K

Appendix C SPECTRAL GRIDS

C.1 L1Ar

The L1Ar grid on which is performed the radiometric calibration is defined as follow (LWIR, MWIR):

- Begin: 59200, 150000 m^{-1}
- End: 132167.2379295346, 227020.9733700643 m^{-1}
- Step: 8.908220965637232, 9.403122130394857 m^{-1}
- Length: 2^{13}, $2^{13} = 8192$

C.2 L1Ars

The L1Ars grid on which the spectra are interpolated at the output of the spectral calibration is defined as follow (LWIR, MWIR):

- Begin: 63145.47522279918, 155147.3883895242 m^{-1}
- End: 125868.7743934770, 226865.3251236365 m^{-1}
- Step: 60.310864587190252, 60.368633614572616 m^{-1}
- Length: 1041, 1189

C.3 L1B

The L1B grid on which the spectra are corrected in the uniformization processing is defined as follow (LWIR, MWIR):

- Begin: 67970.34438977440, 159976.8790786900 m^{-1}
- End: 121043.9052265018, 225054.2661151993 m^{-1}
- Step: 60.310864587190252, 60.368633614572616 m^{-1}
- Length: 881, 1079

NB: The L1B grid is a subset of the L1Ars grid, only some margins are removed.

Appendix D **ACRONYMS**

This section lists definitions for all acronyms used in this document.

ADC	Analogue to Digital Converter
AOCS	Attitude and Orbit Control System
AOD	Aerosol Optical Depth
APE	Application Processing Element
AMV	Atmospheric Motion Vectors
ASE	Acquisition Start/End
ASPKE	Absolute Sample Position Knowledge Error
ATBD	Algorithm Theoretical Basis Document
BB	Black Body
BTA	Back Telescope Assembly
BoL	Beginning of Life
BRDF	Bidirectional Reflectance Distribution Function
CCD	Coupled Charge Device (used for the detector)
CCM	Cube Corner Mechanism
CD	Cube Corner Direction
CDR	Critical Design Review
CFI	Customer Furnished Item
COM	Calibration and Obscuration Mechanism
CrIS	Cross-track Infrared Sounder
DA	Detection Assembly
DEA	Detector and Electronics Assembly
DOY	Day Of Year
DPPF	Data Processing Parameters File
DPU	Data Processing Unit (part of the DEA)
DS1	Deep Space spectrum (resp. interferogram) acquired through the DS1 port (i.e. excluding the front section), acquired at the beginning of each LAC)
DS2	Deep Space spectrum (resp. interferogram) acquired through the main telescope at the beginning of each line)
DSNU	Dark-Signal Non-Uniformity
ECEF	Earth Centered, Earth Fixed frame
ECMWF	European Centre for Medium-range Weather Forecasts
EURD	End-User Requirement Document
EXP	EXPERTISE mode
EoL	End of Life
ERA	ECMWF ReAnalyses
ESA	European Space Agency
EV	Earth View (science spectrum or interferogram)
FCI	Flexible Combine Imager on MTG-I
FDHSI	Full Disk High Spectral Imagery
FFT	Fast Fourier Transform
FIM	Flip-In Mirror
FIR	Finite Impulse Response (filter)
FOV	Field Of View
FPN	Fixed Pattern Noise

FS	Front Section of the instrument
FT	Fourier Transform
FTA	Front Telescope Assembly
FTS	Fourier Transform Spectrometer
FWHM	Full Width at Half Maximum
GIFTS	Geosynchronous Imaging Fourier Transform spectrometer
GIIRS	Geostationary Interferometric InfraRed Sounder
HF	High-Frequency
IA	Interferometer Assembly
IASI	Infrared Atmospheric Sounding Interferometer
IDPF-S	Instrument Data Processing Facility – Sounder
IDNE	Inter-Dwell Navigation Error
IERS	International Earth Rotation and Reference Systems Service
IFG	Interferogram
ILS	Instrument Line Shape
IM	Imager Mode
INR	Image Navigation and Registration
IQT	Instrument (IRS) Quality Tool
IPSF	Instrument Point Spread Function
IRDB	Instrument Reference DataBase
IRS	InfraRed Sounder
LAC	Local Area Coverage
LF	Low Frequency
LI	Lightning Imager
LoS	Line of Sight
LUT	LookUp Table
LWIR	Long Wave Infra-Red
MOF	Mission Operations Facility
MOPD	Maximum Optical Path Difference
MFG	Meteosat First Generation
MSB	Most Significant Bit
MSG	Meteosat Second Generation
MTG	Meteosat Third Generation
MTG-I	MTG imaging mission
MTG-S	MTG sounding mission
MWIR	Medium Wave Infra-Red
NM	Normal Mode (of the instrument)
NMP	NASA New Millenium Program
NWP	Numerical Weather Predicition
OPD	Optical Path Difference
PC	Principal Component
PCS	Principal Component Scores
PS	Processing Specification
PSF	Point Spread Function
PRNU	Photo-Response Non-Uniformity
RMS	Residual Mean-Square
RSPE	Relative Sample Position Error
RSPKE	Relative Sample Position Knowledge Error
RSF	Representative Spectral Feature

RSS	Rapid Scan Service
RTS	Random Telegraph Signal
SADT	Structured Analysis and Design Technique
SAF	Self-Apodisation Function
SCCDB	Satellite/Instrument Characterisation and Calibration Database
SRD	System Requirements Document
SRF	Spectral Response Function
SRF-EM	Spectral Response Function – Estimation Model
SSE	Spatial Sampling Error
SSP	Sub-Satellite Point
TBC	To Be Confirmed
TBD	To Be Defined
TM	TeleMetry
UTC	Coordinated Universal Time
UVN	Ultraviolet, Visible and Near-infrared spectrometer
VCU	Video Chain Unit
ZOI	Zone of Interest
ZPD	Zero optical Path Difference

Appendix E KALMAN FILTER FOR THE FORECAST OF THE INSTRUMENT BACKGROUND

The Kalman filter is an efficient way to get the best estimate (in a probabilistic sense) of the state of a dynamical system from a series of measurements provided that:

- Measurements are performed regularly;
- The physics of the system is known and can be described with a (linear) model;
- Measurement and model errors are known and are Gaussian.

The principles of the Kalman filter have been extensively described in the literature (see for instance RD-5). Basically, if **x** is the state vector representing the state of the considered system, **A** the matrices representing the physics of the system, **P** the state covariance matrix and **Q** the model error covariance, the state of the system at time t_i can be estimated from the state at time t_{i-1} from

$$\mathbf{x} = \mathbf{A}\mathbf{x}_{t_{i-1}}$$
$$\mathbf{P} = \mathbf{A}\mathbf{P}_{t_{i-1}}\mathbf{A}^{\mathbf{T}} + \mathbf{Q} \qquad \textit{Eq. 109}$$

In the same time interval, a vector **z** of measurements of the system is acquired, associated with a measurement error covariance matrix **R**. Then the best estimate of the state of the system at time t_i is:

$$\mathbf{x}_{t_i} = \mathbf{x} + \mathbf{P}\mathbf{H}^{\mathbf{T}}(\mathbf{H}\mathbf{P}\mathbf{H}^{\mathbf{T}} + \mathbf{R})^{-1}(\mathbf{z} - \mathbf{H}\mathbf{x})$$
$$\mathbf{P}_{t_i} = (\mathbf{I} - \mathbf{P}\mathbf{H}^{\mathbf{T}}(\mathbf{H}\mathbf{P}\mathbf{H}^{\mathbf{T}} + \mathbf{R})^{-1}\mathbf{H})\mathbf{P}_{t_{i-1}} \qquad \textit{Eq. 110}$$

where **H** is the observation matrix that transforms a state vector **x** into a measurement vector **z.**

Applying such a framework to the case of the IRS instrument background prediction has got implications that are listed below:

- The state and the measurement vectors are of dimension *NL1b* (≈ 2000) and the matrices are of dimensions *NL1b* x *NL1b* ($\approx 2000 \times 2000$). It is necessary to invert such a matrix for each of the 160×160 pixels whenever a new DS2 measurement is acquired. It could however be possible to reduce the dimensionality of the problem by:
  - Assuming that the covariance matrices are diagonal or at least band-diagonal (i.e. the model error and/or the measurement errors are uncorrelated which can be a source of error);
  - Compute the background for only a subsample of the 160×160 pixels (i.e. the background must then be spatially interpolated which can be another source of error).
- The elementary time step of the prediction is the time between two DS2 measurements. That means that using a Kalman filter does not remove the need for a time interpolation or extrapolation to estimate the instrument background of each dwell;
- The time evolution of the instrument background between two DS2 measurements is assumed to be linear: the model used for the prediction step is linear or should be

linearized if it is not; a complete model of the thermal behaviour of the instrument is needed in order to derive the matrix **A** under different conditions;

- It is necessary to estimate the model error covariance **Q** (as well as the measurement error covariance **R**).

The Kalman filter appears thus to be lacking robustness while bringing only a minor benefit (if any). It is thus not planned to use it for the prediction of the IRS instrument background.

Appendix F SPECTRAL CALIBRATION DETERMINATION SOLUTIONS

F.1 Solutions for LWIR

Representative spectral feature for all solutions in the LWIR:

F.1.1 General Solution

Reference position: 830.8391083 cm^{-1}

#	General Solution			#	General Solution	
	Wn [cm^{-1}]	Weight			Wn [cm^{-1}]	Weight
1	717.67830	1		16	750.62820	4
2	724.59828	1		17	754.35819	2
3	726.97827	2		18	756.52818	1
4	727.80827	2		19	757.32818	2
5	730.85826	1		20	759.58817	3
6	732.40825	1		21	760.38817	1
7	733.20825	3		22	791.75808	4
8	733.96825	1		23	798.62806	1
9	734.73825	1		24	1020.69740	2
10	737.04824	1		25	1041.24734	1
11	737.75824	1		26	1047.00732	1
12	738.55824	3		27	1047.82732	1
13	746.05821	1		28	1135.64706	2
14	746.84821	1		29	1187.00691	2
15	748.33821	4		30	1198.17688	3

F.1.2 Local Solution 1

Reference position: 739.7072046 cm^{-1}

#	Local Solution 1			#	Local Solution 1	
	Wn [cm^{-1}]	Weight			Wn [cm^{-1}]	Weight
1	715.08830	2		14	736.29824	1
2	717.67830	1		15	737.04824	2
3	724.59828	2		16	737.75824	3
4	726.18827	2		17	738.55824	4
5	726.97827	3		18	746.05821	1
6	727.80827	3		19	748.33821	4
7	730.12826	1		20	750.62820	4
8	730.85826	1		21	752.07820	1
9	732.40825	3		22	759.58817	4

10	733.20825	3		23	762.58816	2
11	733.96825	2		24	763.34816	2
12	734.73825	3		25	764.82816	2
13	735.50824	3				

F.1.3 Local Solution 2

Reference position: 850.5548684 cm^{-1}

#	Local Solution 2			#	Local Solution 2	
	Wn [cm^{-1}]	Weight			Wn [cm^{-1}]	Weight
1	777.04812	2		11	849.57791	2
2	778.12812	2		12	853.66790	1
3	784.45810	2		13	854.67789	2
4	790.51808	3		14	871.24784	4
5	793.88807	1		15	887.17780	3
6	794.80807	2		16	908.94773	4
7	795.86807	4		17	951.17761	3
8	802.08805	1		18	952.08760	2
9	803.30804	1		19	1001.35746	1
10	807.05803	4		20	1019.56740	1

F.1.4 Local Solution 3

Reference position: 1087.113038 cm^{-1}

#	Local Solution 3			#	Local Solution 3	
	Wn [cm^{-1}]	Weight			Wn [cm^{-1}]	Weight
1	1012.05743	1		13	1066.16727	1
2	1013.14742	1		14	1068.81726	2
3	1019.56740	3		15	1069.75726	2
4	1020.69740	1		16	1100.55717	1
5	1024.87739	1		17	1111.45713	2
6	1025.93739	2		18	1112.67713	1
7	1028.99738	1		19	1119.90711	3
8	1042.62734	1		20	1134.45706	1
9	1047.00732	1		21	1135.64706	3
10	1047.82732	1		22	1165.36697	3
11	1050.61731	4		23	1198.17688	4
12	1051.56731	1				

F.2 Solutions for MWIR

F.2.1 General Solution

Reference position: 1759.5757260 cm^{-1}

#	General Solution		#	General Solution	
	Wn [cm^{-1}]	Weight		Wn [cm^{-1}]	Weight
1	1601.10847	4	21	1784.91799	2
2	1602.15847	3	22	1805.15794	2
3	1603.26847	2	23	1807.69793	1
4	1607.00846	3	24	1810.53792	2
5	1608.25845	1	25	1817.47791	4
6	1609.52845	2	26	1825.18789	2
7	1627.83840	1	27	1837.20785	3
8	1640.30837	2	28	1846.58783	2
9	1641.34837	4	29	1852.36782	2
10	1642.38837	2	30	1858.45780	3
11	1689.15824	4	31	1889.547718	2
12	1690.16824	1	32	1895.207703	2
13	1691.33824	3	33	1903.067682	1
14	1704.37820	2	34	1904.377679	1
15	1710.22819	1	35	1907.83767	1
16	1722.32816	2	36	1908.907667	1
17	1723.53815	2	37	1961.18753	3
18	1731.26813	2	38	1998.937431	2
19	1750.06808	1	39	2017.757382	1
20	1775.69802	3	40	2041.30732	1

F.2.2 Local Solution 1

Reference position: 1680.7341458 cm^{-1}

#	Local Solution 1		#	Local Solution 1	
	Wn [cm^{-1}]	Weight		Wn [cm^{-1}]	Weight
1	1601.10847	1	13	1691.33824	4
2	1602.15847	1	14	1704.37820	2
3	1603.26847	2	15	1710.22819	3
4	1607.00846	2	16	1722.32816	4
5	1608.25845	2	17	1723.53815	1
6	1609.52845	4	18	1726.67814	1
7	1640.30837	3	19	1731.26813	2
8	1641.34837	4	20	1743.28810	3
9	1642.38837	3	21	1751.30808	1
10	1688.24825	2	22	1761.78805	4
11	1689.15824	3	23	1769.48803	1
12	1690.16824	4			

F.2.3 Local Solution 2

Reference position: 1812.2952759 cm^{-1}

#	Local Solution 2		#	Local Solution 2	
	Wn [cm^{-1}]	Weight		Wn [cm^{-1}]	Weight
1	1743.28810	2	13	1807.69793	4
2	1756.73807	2	14	1810.53792	3
3	1757.91806	1	15	1811.55792	1
4	1761.78805	3	16	1817.47791	4
5	1769.48803	1	17	1825.18789	2
6	1775.69802	4	18	1837.20785	4
7	1779.62801	3	19	1852.36782	2
8	1780.71800	1	20	1856.19781	2
9	1784.91799	4	21	1858.457799	4
10	1800.79795	1	22	1866.247779	1
11	1805.15794	2	23	1889.547718	4
12	1806.41794	2	24	1895.207703	1

F.2.4 Local Solution 3

Reference position: 1914.3805481 cm^{-1}

#	Local Solution 3		#	Local Solution 3	
	Wn [cm^{-1}]	Weight		Wn [cm^{-1}]	Weight
1	1852.36782	2	7	1904.37768	3
2	1856.19781	3	8	1907.83767	2
3	1858.45780	3	9	1908.90767	1
4	1866.24778	1	10	1961.18753	4
5	1889.54772	3	11	1998.93743	3
6	1895.20770	3	12	2041.30732	2

Appendix G SPECTRAL CALIBRATION BASELINE PARAMETERS

PARAMETER	*DESCRIPTION*	*BASELINE*	*MIN*	*MAX*
$A_{RSF,\min}$	Amplitude threshold for minimum spectral feature.	- 0.003 a.u. for LWIR		
		- 0.0003 a.u. for MWIR		
N_{ma_rev}	Moving average size of LAC 4 revisions for averaging before spectral scaling factor determination	3		
N_{L1B}	Number of spectral samples for the L1B product	N_{LW} for LWIR		
		N_{MW} for MWIR		
N_{L1Br}	Number of spectral samples to use for the spectral scale correction / interpolation process.	2^{13}		
N_{L1Brs}	Number of spectral sample after radiometric and spectral correction.			
N_{LW}	Number of spectral samples for the L1B product (LWIR band)	1127		
N_{MW}	Number of spectral samples for the L1B product (MWIR band)	1259		
N_{LFi}	Number of spectral samples to use for determination of spectral feature positions.	2^{17}		2^{20}
N_{SF}	Number of point to take around the nominal spectral feature positions to determine their location.			
Ω_{fit_pred}	Spectral scaling factor mode 2 predictor fit order	1		
t_{av_pred}	Time span for averaging of scaling factors (mode 1)	2.25 h		
t_{ex_red}	Extrapolation time after end of LAC 4 revision for mode 2 predictor	0.5 h		

Appendix H EXAMPLE CODE TO COMPUTE THE SAMPLE MEAN AND COVARIANCE WITH AN UPDATE FORMULA

```
struct Covariance {
  Covariance(int m) : M(m), N(0) {
    mean = new double[M]();
    deltamean = new double[M]();
    C = new double[M*(M+1)/2]();
  }

  ~Covariance() {
    delete [] mean; delete [] deltamean; delete [] C;
  }

  template <typename T>
  void addobs(T *x) {
      double invNp1 = 1/double(1+N);
      for (int i=0; i<M; i++) {
        deltamean[i] = x[i] - mean[i];
        deltamean[i] *= invNp1;
      }
      int k = 0;
      for (int i=0; i<M; i++) {
        for (int j=i; j<M; j++) {
          C[k] *= invNp1;
          C[k] += deltamean[i]*deltamean[j];
          C[k] *= N;
          k++;
        }
      }
      for (int i=0; i<M; i++) {
        mean[i] += deltamean[i];
      }
      N++;
  }

  int M,N;
  double *mean;
  double *deltamean;
  double *C;
};
```